UNIVERSITÀ DEGLI STUDI DI NAPOLI FEDERICO II

Dottorato di Ricerca in
Ingegneria dei Sistemi Idraulici, di Trasporto e Territoriali
XX Ciclo
Indirizzo Ingegneria Idraulica ed Ambientale

Experimental study on the hydrodynamic characteristics of a vegetated channel

dott. ing. Sergio De Felice

Tutors
Prof. ing. Guelfo Pulci Doria

Prof. ing. Paola Gualtieri

Coordinatore di Dottorato
Prof. ing. Bruno Montella

Anno accademico 2007/2008

INDEX

1. INTRODUCTION

1.1 Preface

The need to use natural and artificial flows to convey waters in order to irrigate, or to navigate, or to drain the land, has always driven the man to study the resistances to the flow faced by the current along the channel banks.

Such resistances to the flow are due both to the nature and type of the solid boundaries and to the development of the vegetation.

In particular, up until recently, the problem of the presence of the vegetation in the bed and along the banks was solved simply by means of scheduled maintenance of the channel, consisting in the weeding of the vegetation.

However, since the respect and the protection of the environment must be taken into consideration, it is no longer possible to work in such a way; but it is necessary to try to protect, however possible it may be, every form of flora, limiting to the minimum the damages caused by the human beings, in order to protect the survival of the aquatical fauna in its natural habitat, also considering that the bed vegetation influences the transport of nutritious and polluting solids.

Alwin Seifert is certainly one of the forerunners of the necessity of more sustainable use of natural and artificial flows, as he states in his essay of the year 1938 bearing the title "Naturnaherer Wasserbau" (literally "hydraulic engineering closer to nature").

In the last decades, such environmental needs have determined the birth and development of a different approach both to the planning and to the maintenance of the flows.

With particular reference to the latter aspect, for instance, it is interesting to remember that the restoration or the rehabilitation of a degraded aquatic ecosystem is often carried out by applying naturalistic engineering techniques.

1.2 The problem of currents flowing in vegetated beds and the different possible vegetation models

The study of the effects that the vegetation in the natural and artificial beds has on the characteristics of the stream flowing down in them (with particular reference to the flow resistance and to the flow rate) can be traced back to Chézy, who devoted himself to it at the end of the eighteenth century.

Typical examples of the effects of vegetation on water flow are the following ones: the decrease of the water velocity and the raising of the water levels i.e. the reduction of flow discharge capacity; the encouragement of the deposition of suspended sediment; the change of

the magnitude and the direction of the currents within the channel, causing or reducing local erosion; the interference with the use of the water for conveyance, navigation, swimming and fishing. Such effects depend mainly on height, density, distribution and stiffness and type of vegetation. These characteristics may change with the season, e.g. the flow resistance may increase in the growing season and diminish in the dormant season.

Much of the earlier studies on the hydraulic effects of vegetation were concentrated on determining roughness coefficient rather than obtaining a better understanding of the physical processes. Typically, a conventional method considered for head loss evaluation in vegetated channels was to select a suitable value of Manning's roughness coefficient *n*, which grouped all the sources of flow resistance, including vegetation (Chow, 1959). In his book "Open-Channel Hydraulics" published in 1959, Chow examines carefully the values to be ascribed to Manning *n*, showing tables and graphs, basing himself on numerous observations about the different types of vegetation, in order to point out possible planning and control methods. The vegetation is simply considered as bottom roughness in problems of verification, and this roughness reduces considerably the channel capacity to convey the flow, and it causes significant reductions in the current speed. Of course, such effects are linked to the type, height and density of the vegetation.

TABLE 5-6. VALUES OF THE ROUGHNESS COEFFICIENT *n* (*continued*)

Type of channel and description	Minimum	Normal	Maximum
C. EXCAVATED OR DREDGED			
a. Earth, straight and uniform			
1. Clean, recently completed	0.016	0.018	0.020
2. Clean, after weathering	0.018	0.022	0.025
3. Gravel, uniform section, clean	0.022	0.025	0.030
4. With short grass, few weeds	0.022	0.027	0.033
b. Earth, winding and sluggish			
1. No vegetation	0.023	0.025	0.030
2. Grass, some weeds	0.025	0.030	0.033
3. Dense weeds or aquatic plants in deep channels	0.030	0.035	0.040
4. Earth bottom and rubble sides	0.028	0.030	0.035
5. Stony bottom and weedy banks	0.025	0.035	0.040
6. Cobble bottom and clean sides	0.030	0.040	0.050
c. Dragline-excavated or dredged			
1. No vegetation	0.025	0.028	0.033
2. Light brush on banks	0.035	0.050	0.060
d. Rock cuts			
1. Smooth and uniform	0.025	0.035	0.040
2. Jagged and irregular	0.035	0.040	0.050
e. Channels not maintained, weeds and brush uncut			
1. Dense weeds, high as flow depth	0.050	0.080	0.120
2. Clean bottom, brush on sides	0.040	0.050	0.080
3. Same, highest stage of flow	0.045	0.070	0.110
4. Dense brush, high stage	0.080	0.100	0.140
D. NATURAL STREAMS			
D-1. Minor streams (top width at flood stage <100 ft)			
a. Streams on plain			
1. Clean, straight, full stage, no rifts or deep pools	0.025	0.030	0.033
2. Same as above, but more stones and weeds	0.030	0.035	0.040
3. Clean, winding, some pools and shoals	0.033	0.040	0.045
4. Same as above, but some weeds and stones	0.035	0.045	0.050
5. Same as above, lower stages, more ineffective slopes and sections	0.040	0.048	0.055
6. Same as 4, but more stones	0.045	0.050	0.060
7. Sluggish reaches, weedy, deep pools	0.050	0.070	0.080
8. Very weedy reaches, deep pools, or floodways with heavy stand of timber and underbrush	0.075	0.100	0.150

TABLE 5-6. VALUES OF THE ROUGHNESS COEFFICIENT *n* (*continued*)

Type of channel and description	Minimum	Normal	Maximum
b. Mountain streams, no vegetation in channel, banks usually steep, trees and brush along banks submerged at high stages			
1. Bottom: gravels, cobbles, and few boulders	0.030	0.040	0.050
2. Bottom: cobbles with large boulders	0.040	0.050	0.070
D-2. Flood plains			
a. Pasture, no brush			
1. Short grass	0.025	0.030	0.035
2. High grass	0.030	0.035	0.050
b. Cultivated areas			
1. No crop	0.020	0.030	0.040
2. Mature row crops	0.025	0.035	0.045
3. Mature field crops	0.030	0.040	0.050
c. Brush			
1. Scattered brush, heavy weeds	0.035	0.050	0.070
2. Light brush and trees, in winter	0.035	0.050	0.060
3. Light brush and trees, in summer	0.040	0.060	0.080
4. Medium to dense brush, in winter	0.045	0.070	0.110
5. Medium to dense brush, in summer	0.070	0.100	0.160
d. Trees			
1. Dense willows, summer, straight	0.110	0.150	0.200
2. Cleared land with tree stumps, no sprouts	0.030	0.040	0.050
3. Same as above, but with heavy growth of sprouts	0.050	0.060	0.080
4. Heavy stand of timber, a few down trees, little undergrowth, flood stage below branches	0.080	0.100	0.120
5. Same as above, but with flood stage reaching branches	0.100	0.120	0.160
D-3. Major streams (top width at flood stage >100 ft). The *n* value is less than that for minor streams of similar description, because banks offer less effective resistance.			
a. Regular section with no boulders or brush	0.025	.....	0.060
b. Irregular and rough section	0.035	.....	0.100

Fig. 1.1 – Some values of Manning's *n* from (Chow, 1959)

It is peculiar to observe how this type of empiric approach, that is to say the research of the most suitable value to attribute to the resistance coefficient n in the presence of vegetation, has remained unchanged till the eighties with few variations. However, this excluded the current hydrodynamic characteristics from the analysis, and there was no mention of the statistical characteristics of turbulence.

On the contrary, only in the last decades, thanks to both the development of new experimental investigation techniques applicable to the hydrodynamic studies, and following a research approach quite different from the previous one and developed in the field of the aeriform streams flowing on the earth vegetation (Raupach and Thom, 1981; Finnigan, 2000), the empiric approach has been replaced by a more physical approach.

Therefore, theoretical-experimental studies have been carried out that analyse the phenomenon, trying to find relations between the flow resistances and the measurable characteristics of a stream, among which the statistical ones.

The developments of this research topic have given raise to interesting effects regarding the hydraulic research on vegetated open-channel flows. First of all, roughness has been often considered following the more recent view of the equivalent sand roughness of Nikuradse within the Darcy-Weisbach equation. Moreover, numerous studies both experimental and numerical, have been carried out in order to examine closely not only the problems relative to the determination of the flow resistance of the streams on vegetated bottom, but also the main hydrodynamic characteristics of these streams, as the mean flow and the turbulent structures, and, therefore, the related transport processes of pollutants, heat, sediments.

With reference to the kind of vegetation, the investigations may be classified into two groups: the first one relative to rigid vegetation, the second one relative to flexible vegetation. Rigid vegetation may be modelled through wooden or metallic cylinders, or through natural plants; flexible vegetation may be modelled through plastic strips or through grass or other vegetation types. Moreover these models of vegetation may have different densities, and the effects of wholly or partially submerged vegetation may be examined.

Usually, these studies are concerned with uniform or steady flows.

In (Lopez and Garcia, 1997), a brief review of the works till the year of the paper concerning the interactions between vegetation and either atmospheric or free-surface flows is reported.

It has been deemed suitable to report a brief review of the more recent papers concerning the effects of fully submerged rigid vegetation on uniform or steady flows.

1.3 Literature review about rigid fully submerged artificial vegetation

As stressed in previous paragraph, here a brief review of the recent papers concerning the effects of fully submerged rigid vegetation on uniform or steady flows will be exposed. Sometimes also cases of partially emerging vegetation, or flexible vegetation will be also considered, if suitable to better clarify either the more important (for our sakes) previously considered cases or the specific authors' thoughts. The main part of the papers regards clearly artificial vegetation; only a few ones are devoted to natural like vegetation.

It is suitable to stress, once and for all, that in describing the different authors' papers, often their own words have been used, for the sake of signify their thought in the better way it would be possible.

Every paper that has been examined and deeply described is reported in the following through authors' names and publication year. Sometimes the actual papers description is preceded by a brief record of its background. The papers are referred in their temporal sequence, so that a kind of a vegetation researches history is generated.

(Tsujimoto *et al*., 1992)

The interactions between flow and vegetation differ for different species of water plant. When the vegetation layer over a bed is thin and the flow inside the vegetation is negligible, the bed may be treated as a rough bed. But, when the vegetation layer is thicker and the flow inside the vegetation cannot be neglected, the interaction between the faster flow over the vegetation and the slower flow inside the vegetation must play an important role in the turbulence.

In (Tsujimoto *et al*., 1992), this thicker vegetation case is investigated, as regards to rigid plants. The turbulence characteristics of a uniform flow developing in an open channel, with vertical rigid cylinders of the same diameter and height, set at equal spacing in a square pattern, as model of thicker rigid vegetation, are experimentally investigated in a laboratory flume. Based on the experimental data, the classical turbulence model (mixing-length model) is modified by focusing on the interaction between the flows over and through the cylinders to describe the velocity profile from the flume bed to the water surface.

In this study the "projected area of vegetation per unit volume of water in the flow direction" (dimensionally $[L^{-1}]$) is defined "so small" that the net and the apparent velocities of the flow in the vegetation layer can be considered equal**.**

The results obtained, neglecting the bottom shear stress in comparison with the additional resistance due to the vegetation, can be summarized as follows. When the flow depth is smaller than the vegetation height, there is a uniform velocity in the vegetation layer and the

Reynolds stress is zero; the turbulence intensity is not zero but it is very small.

When the flow depth is larger than the vegetation height, the turbulence characteristics in the free-surface flow region are little affected by the vegetation layer, while, the flow in the vegetation layer is strongly affected by the faster surface flows.

In particular, at the interface between the vegetation layer and the surface-flow region, the profiles of the velocity distributions show an elbow, the profiles of the turbulence intensity and Reynolds stress show a peak, indicating that the flow is characterized by the shear at this level, and suggesting an active momentum exchange there.

The profiles of the induced velocity and Reynolds stress in the vegetation layer are roughly approximated by exponential functions, with exponents respectively β and α representing the turbulent structure in the vegetation layer, and with the presence of two parameters, u_k and τ_k, representing, respectively the velocity and the shear intensity at the interface between the vegetation layer and the surface-flow region.

The β and u_k values also determine the boundary conditions for the velocity and the velocity gradient at the interface between vegetation layer and surface flow region.

With the induced velocity profile in the vegetation layer approximated by an exponential function, a method to correct the energy slope, which is difficult to determine experimentally, is proposed. This correction results in a reduction in the scatter of the data, showing the relations among α, β u_k and τ_k.

An analytical model describing the turbulence structure in the vegetation layer, which leads to relations among α, β and u_k was derived by assuming the Reynolds stress distributes exponentially in the vegetation layer

(Shimizu and Tsujimoto, 1994)

In (Shimizu and Tsujimoto, 1994), the characteristics of a turbulent flow developing over a submerged vegetated layer are numerically analyzed with a k-ε turbulence model.

In order to describe the boundary accurately, the flow within a vegetation layer cannot be treated as a two dimensional flow. Thus the equation governing the flow was spatially averaged as in a porous medium and the effect of individual roughness elements was taken into account, neglecting the geometry of individual vegetation elements, by an averaged local drag force (averaged in a calculation mesh). Therefore, the presence of individual vegetation elements was accounted for the spatially averaged drag force acting upon individual elements. Such a technique was introduced in analyzing canopy flow in the field of meteorology by (Wilson and Shaw, 1977).

Then the modified equations were obtained by adding the drag terms due to vegetation

not only to the momentum equation, but also to the k-ε turbulence model standard equations.

The calculations based on the present model were executed for uniform flow conditions in an open-channel vegetation, and the results were compared with turbulence measurements made in flume (Tsujimoto *et al*., 1992), in order to determine the numerical values of the parameters involved in the model, and to certificate the applicability of the model for flow over vegetation layers with different densities.

Not only the velocity profiles but also the statistical properties of turbulence can be described by the calculation based on the present model, where the specified model parameters can be rather universal, at least under the conditions of flow with idealized homogeneous vegetation. In fact, varying pattern of vegetation may bring about heterogeneous flow, often with secondary currents.

Moreover the calculated results were consistent with previous analysis, where an exponential distribution of the Reynolds stress in the vegetation layer was assumed, and the macroscopic force balance was considered in the vegetation layer, while a mixing length model was applied to the surface flow.

The present model was also applied to unestablished flow over a vegetation layer. In fact, when the flow is introduced to the vegetated bed, a transient process occurs where the turbulent characteristics change longitudinally until they reach an equilibrium state sufficiently downstream. The longitudinal changes of the profiles of mean velocity and Reynolds stress in the transient process were calculated by assuming, for simplicity, that the water surface elevation is parallel to the bed.

The comparison between calculated longitudinal change of the mean velocity profile and the measured data demonstrates the applicability of the model to non uniform flow conditions. The comparison of the calculated Reynolds stress distribution with the measured one shows that the present model can also explain the transient change of Reynolds stress distribution.

Therefore, the numerical results showed a good agreement with the measurements in the flume where the depth in the vegetated reach was tried to be kept as constant as possible and, therefore, the comparisons demonstrate the applicability of the model also to non-uniform conditions.

The study suggests that the proposed numerical model can be considered a good representation of flow over a vegetated bed.

(Kutija and Hong, 1996)

In (Kutija and Hong, 1996), a numerical model is described, developed to help in deepening the understanding of flexible submerged vegetation-induced resistances in steady

uniform flow, and, in particular, by following the effects of the various parameters involved. The basic model is a one-dimensional vertical mixing model which is coupled to the equation of conservation of momentum in the horizontal direction. It is used as a tool for investigating the influences of different parameters on the total resistance. The model addresses both rigid and flexible vegetation. In case of rigid vegetation, the most significant parameters are the properties of the height, the diameter and the density of the vegetation itself. In case of flexible vegetation, the role of the reed height is taken over by the effective reed height, which depends on the bending of the reed itself, due to the flow of the water.

The shear term is approximated within this model in two ways. In the surface flow layer, it is modelled as a turbulent shear stress approximated by a mixing length theory; in the vegetation layer, it is modelled according to the eddy-viscosity theory.

But comparing data from inflexible vegetation (Tsujimoto and Kitamura, 1990) with the results of the model, it became obvious that the eddy-viscosity approximation was not suitable for the whole height of the vegetation layer, especially near the tip of the reed, but only for a part (p) of the height of the vegetation layer, which is influenced by the density, the diameter and the stiffness of the reed. The rest of the height of the vegetation layer was modelled in the same manner as the surface flow.

In case of flexible vegetation, the effective height of any representative reed used in the evaluation of the drag force is influenced by the bending of the reed due to the flow of the water. The deflection of the reed can be calculated according to the standard cantilever beam theory (e.g. Timoshenko, 1955). As result of the bending, the effective height of vegetation is reduced, which means that the height over which the load is acting is also reduced and this reduced load causes less bending that would result with the full effective reed height: it is necessary to use an iterative procedure, which is stopped when a prescribed difference between the load height and the effective reed height is reached. It is obvious that in case of flexible vegetation the additional flow resistance is a result of more complex interactions than in case of rigid vegetation. Therefore, further study should be directed to establishing the interrelationship among the effective height of vegetation and the reed properties.

The additional force term due to vegetation, in the layer above the vegetation is equal to zero, while in the vegetation layer it is defined as a function of the density of reeds, the flow velocity, the drag coefficient, the diameter of one reed and the effective height of vegetation.

Some data from (Tsujimoto and Kitamura, 1990) were used for verification of the model with fixed, inflexible vegetation, due to the lack of experimental data relative to flexible vegetation.

In order to describe the influence of different parameters on the flow resistance, a simple

example is used, relative to conditions present in floods planes of the river Rhine in the Netherlands. The Authors observe that they do not introduce dimensionless combinations of the variables involved in the model, in order to leave all such possibility open at this stage. The influence of each parameter involved in the model is investigated by changing one parameter at time from the initial set of data and comparing the results with the ones obtained by the initial set of data. However not all these parameters are independent of each other. That means that when only a parameter is changed and all the others are kept constant, a not fully realistic situation might be obtained, which might lead to premature and possibly incorrect conclusions.

It results that the computational parameters as the grid step and the time step do not much influence the flow resistance; the hydraulic parameters as the water depth influences the flow resistance; the Chézy coefficient does not much influence it; the parameters connected with the turbulence model as p and α (an empirical coefficient) influence the flow resistance; the reed geometries and characteristics as the density, the height, the diameter and the stiffness are important parameters for assessing the flow resistance.

Once calibrated, the model can be added, as a module, into an existing two-dimensional nearly-horizontal flow model.

However, the model still needs to be verified using field measurements taken in presence of flexible vegetation.

(Klopstra *et al*., 1997)

In (Klopstra *et al*., 1997), results from studies on hydraulic roughness of vegetation reported in literature are used for development and verification of a physically based model of vertical flow velocity profile and hydraulic roughness of submerged tall vegetation such as reeds. The velocity profile of submerged vegetation is treated separately for the vegetation layer and the surface flow region. The two profiles are smoothly matched through boundary conditions at the interface.

For the vegetation layer, the Authors start from the momentum equation, assuming uniform and steady flow. The turbulent shear stress can be described by the concept of Boussinesq. In conformity with the turbulence models described in (Rodi, 1980) the eddy viscosity is assumed to be characterised by the product of a velocity scale and a length scale of the large scale turbulence, which is responsible of the vertical transport of momentum. In conformity with (Tsujimoto and Kitamura, 1990), the characteristic velocity scale is assumed to be represented by the flow velocity distribution. The characteristic length scale α is assumed to be independent of z. Transforming and solving the momentum equation, the

velocity profile for the vegetation layer is established. The only unknown parameter is the characteristic length scale α.

For the surface flow region the Prandtl's mixing length model is adopted, resulting in the well-known logarithmic velocity profile. The virtual bed level of such a profile does not coincide with the top of the vegetation but appears to lie under that level.

From the average flow velocity in the vertical, which follows from the integrals of the velocity distribution in the vegetation layer and in the surface flow region, the hydraulic roughness expressed as the value of Chézy coefficient, can be obtained, through a complex explicit expression, when vegetation characteristics, water depth and characteristic length scale α are known.

The model verification is assessed in two successive steps: 1) comparison with measured flow velocity profiles from flume experiments by varying the characteristic length scale α in such a way that the shape of the measured velocity is represented; 2) comparison with measured hydraulic roughness values from flume experiments.

The first verification step shows that the characteristic length scale α is not independent of z. To make the analytical model generally applicable, α has been correlated to hydraulic and vegetation characteristics as the water depth and the height of the vegetation elements. With this relation for α, the model is tested again and the comparison among the hydraulic roughness values calculated with the model and the corresponding ones measured from flume experiments reported in literature is good.

Models results for field situations show that, under certain conditions, e.g. α exceeds the values for which the relation for α was fitted, the calculated virtual bed level appears to lie up the top of the vegetation. This, in combination with the resulting low Chézy-values, shows the need for additional research either on the validity of the modelling concepts or on the relation for α. This study should be combined with a profound field measurement program (or on large scale flume experiments) so as to validate the study results.

(Meijer and van Velzen, 1998)

In (Meijer and Van Velzen, 1998), the physically based model developed by (Klopstra *et al*., 1997), that predicts the vertical flow velocity profile in the vegetation layer and in the surface flow region separately, and the hydraulic roughness of submerged vegetation, is considered. It is a physically based model, with one empirical parameter (the characteristic turbulence length scale α), to be determined by physical model tests. Different shear-stress descriptions are applied for the vegetation layer and the surface flow region. The analytical

model has been validated by results from literature, based on scale model tests. It had not been validated for field condition yet, due to the lack of data.

In this paper an extensive set of flume experiments on prototype-scale, carried out in 1997 and 1998, is discussed, in order to verify the applicability of the analytical model for fields conditions. Vegetation is simulated, respectively, in 1997 with steel bars, in 1998 with natural reeds, as verification in a more realistic situation. The density is defined as bars or reeds per m^2; their values were, respectively, 256 and 64 bars per m^2, and 256 reeds per m^2.

The results of the flow measurements carried out using steel bars show that the analytical model describes the measured flow profiles quite well and moreover, on the basis of the experiments, the prediction of the empirical parameter is improved. In particular, the dependence of α on the water depth and on the vegetation height, is confirmed, although through a different relation, while the α-value is proved to be independent of the vegetation density. The comparison among the Chézy hydraulic roughness values calculated with the model and the corresponding ones measured on prototype-scale flume experiments is good, due to the fact that the Chézy coefficients are relatively insensitive to deviations in α value. Therefore the α parameter is the empirical element in the analytical model with the highest uncertainty.

According to the Authors, the tests with the steel bars can be considered as fundamental research, whereas the tests with the natural reed should be regarded as a verification of a more realistic situation. The results of the flow measurements carried out using natural reed show that near the surface the velocities seem to be somewhat underestimated. It should be noticed some unresolved questions as that the α-function validated for steel bars, is not necessary valid for the natural reed and that an average reed height might not represent the varying reed height well.

Anyway, although the model does not incorporate the effects of variable diameters and heights, tufts and the bending of the reed stalks, the results seem to confirm the applicability of the model for the prediction of the hydraulic roughness of natural reed vegetation.

Moreover the Authors point out that in these studies only the average flow velocity in one direction was involved. There are still a lot of unused data available in the other two dimensions which can be used, e.g., for improving the α-function, involving the turbulent characteristics.

(Lopez and Garcia, 2001)

In (Lopez and Garcia, 2001), the ability of numerical algorithms, based on two equation closures of turbulence (k-ε and k-ω formulations), to model the mean flow and the turbulence

structure in open-channel flows with rigid, submerged vegetation is studied. From a mathematical point of view, the flow of water through and above vegetation presents new challenges due to the 3D nature of the turbulence, which represents a highly non homogeneous flow field. From an engineering perspective, a 1D description of the problem is commonly desirable.

A methodology to transform the 3D problem into an 1D framework, developed for atmospheric flows through plant canopies by (Raupach and Shaw, 1982), were applied to vegetated open channels. In particular, (Raupach and Shaw, 1982) proposed two schemes, by averaging the conservation equations over space and time.

In particular, in the first one (scheme I), the equations that describe the instantaneous flow field are locally time averaged over a horizontal plane large enough to obtain mean values independent of spatial variations due to the turbulence and the canopy structure. In the second one (scheme II), the three dimensional flow structures is first locally time averaged, to filter fluctuations due to the turbulence, and then spatially averaged to eliminate variations in space, due to the canopy structure.

With this methodology, drag related terms arise as a consequence of the averaging procedure, and it is clear that the simple addition of drag related to body forces in the momentum equation is incorrect, since the dispersive fluxes are not included. The budget of turbulent kinetic energy, irrespective of the averaging scheme, is composed of sources, sinks and transport terms. Two characteristic processes act as turbulent kinetics generators, i.e., transferring energy from larger scales (either mean flow or larger eddies) toward turbulent fluctuations in space or time at smaller scale: (1) the work of Reynolds and dispersive stresses against mean velocity gradients, which contribute to the generations of fluctuations in time and spatial perturbations of time-averaged velocities; (2) the work of mean flow or large eddies against pressure differences due to obstacles.

There are two limiting cases worth being analyzing. The first one is considered in the already remembered work of Raupach and Shaw (1982) and concerns the case when the length scale of canopy elements (and of their wakes, or in other words the scale of the wake-generated turbulence) is much larger then the Kolmogorov microscale, so that the viscous term becomes negligible. In this situation, the work of the mean flow against pressure differences becomes equal to the wake-production term for the turbulent fluctuations in time.

The second one concerns the case when the length scale of canopy elements (and of their wakes, or in other words the scale of the wake-generated turbulence) is much smaller (or even of the order of) than the Kolmogorov microscale. In this situation almost all the energy is spent in the generation of spatial fluctuations, and is therefore directly dissipated into heat. In

this situation, there is a negligible contribution from the wakes to the spatial average of the turbulent fluctuations in time.

The first one of these situations seems to be common to atmospheric flow, whereas the second situation is more common to water flows with relatively low plant concentrations. This is reasonable, considering the Kolmogorov microscale is smaller in air than in water. In addition, the characteristic length scales of canopy elements in atmospheric flows can be expected to be in general much larger than those found in water flows.

The numerical closure schemes selected for the study are the k-ε and the k-ω models. Following the common practice in turbulence closure schemes, it is assumed (and experimentally validated) that the total averaged vertical turbulent transport of longitudinal momentum, in the presence of vegetation, can be modelled using an eddy viscosity approach. Boundaries conditions at the bed account for the presence of vegetation, and algebraic expression to estimate the different components of the Reynolds stress tensor (proposed by (Rodi, 1976)), was slightly modified for the extra turbulence generation due to the plants.

Numerical results were compared to experimental observations on mean flow and turbulence structure of open channel with cylindrical wooden dowels (arranged in a staggered pattern with variable density, expressed as frontal area of obstructions per unit volume), to simulate rigid, submerged vegetation, made at the Ven Te Chow Hydrosystems Laboratory, University of Illinois.

Both models accurately predicted experimental observations on mean flow and turbulent quantities (up to the second-order statistics), and provided very good representation of the production, inertial diffusion, and dissipation terms in the turbulent kinetic energy budget. No significant difference was found between the numerical performance of either model. Flow resistance measured in terms of Manning's n, shows an almost constant value close to one corresponding to non-vegetated channels up to some threshold plant density. A linear increase is observed once this limit is exceeded. This work shows the need to average flow measurements taken in vegetated waterways in both space and time to obtain meaningful observations. The challenge for future work is to extend the predictive capabilities of the numerical models developed for "idealized" vegetation to the case of natural one.

(Stone and Tao Shen, 2002)

Well-established flow resistance formulas have long been used to analyze river flows. However, the resistance characteristics of relatively smooth boundaries roughened with large roughness elements is not well understood.

Flow resistance due to cylindrical roughness can provide a better understanding of the

resistance in vegetated channels. Many studies attempted to extend the conventional flow resistance formulas to account for the effect of vegetation with empirically determined resistance coefficients. However, those studies were not able to provide methods applicable to a wide range of vegetation conditions.

Moreover, the understanding of flow resistance in channels with rigid vegetation stems provides the basis for analyzing flow resistance with flexible stems. Kutija and Hong (1996), as already remembered, demonstrated that formulas developed for rigid vegetation could be extended to include the effects of stem flexure by an iterative method using a simple cantilever beam theory.

Recently, most studies focused on velocity profiles and turbulent characteristics of vegetated channel instead of developing resistance laws and conveyance formulas.

In this paper, the hydraulics of a flow in an open channel with circular cylindrical roughness is experimentally studied. The laboratory study consists of an extensive set of velocity profiles for flow with emergent and submerged cylindrical stems of the same height and of various diameters. The stems are distributed with staggered geometries, with different concentrations (defined as the number of stems per unit bed area).

Open channel flow with submerged cylindrical roughness can be envisioned as two interacting flow layers: the roughness layer or the stem layer, which is the lower layer containing the cylindrical stems, and the surface layer, above the stem layer, containing no part of the roughness.

An emergent condition can be considered as a limiting condition of a submerged one with no surface layer.

In general, the flow velocity in the stem layer is significantly smaller than in the surface layer, due to the drag imparted by the stems. The effect of the bed friction on the shape of the velocity profile is important only very near the bed where the profiles decrease to zero.

Due to the interaction of the surface and the stem layers, the submerged condition is much more complicated than the emergent condition.

Consider a steady, uniform, open channel flow with submerged cylindrical stems of equal length distributed uniformly over the channel bed. For a control volume of unit bed area extending from the bed to the water surface, the momentum balance in the streamwise direction gives that the streamwise component of the weight of the water mass can be given by the resistance due to the drag around the cylinders within the stem layer and the bed shear stress. The area concentration is the fraction of the bed area occupied by stems, expressed through the number of stems per unit plan area of bed and the stem diameter.

The stem drag force per unit bed area is expressed through the drag force for a single

cylinder in an array of identical cylinders, and the depth-averaged velocity of the constricted section in the stem layer. Therefore, the drag force is expressed in term of the velocity in the stem layer, instead of the often-used apparent vegetation layer velocity defined as the discharge in stem layer over the gross cross-sectional area. Moreover, in this study bed friction is included for completeness, although it is generally amounted to less than 3% of the total channel resistance.

Therefore, the friction slope of the channel flow may be considered as composed of contributions from bed resistance and stem resistance.

The expression of the apparent vegetation layer velocity can be rewritten in terms of the velocity in the stem layer. Moreover, it is hypothesized a relationship between the channel velocity (called apparent channel velocity) and the maximum velocity in the stem layer. Combining these expressions it is obtained a flow resistance formula based on the stem drag coefficient and a velocity coefficient.

Experimental data are used to determine these coefficients and to validate the preceding analysis.

In particular, the emergent flow data are used for drag coefficients calculations because there is no surface layer to complicate the analysis. An average value of the coefficient is determined. Moreover, it is used to calculate the apparent vegetation layer velocity and the results were compared with measured values for the emergent as well as submerged cases, obtained from this investigation and those from Fenzl (1962) and Tsujimoto and Kitamura (1990), including a wide range of roughness and hydraulic conditions. It is showed a generally close agreement between the calculated and the measured values of the apparent vegetation layer velocity values.

The velocity coefficient is calculated. An examination of the flume data suggested that it may be proportional to the wetted stem length/flow depth ratio. To verify this, all the data from the present study, as well those of Fenzl (1963) and Tsuijmoto and Kitamura (1990) are plotted together, using dimensionless variables, including both emergent and submerged conditions and a wide range of roughness and hydraulic conditions.

Therefore, a flow resistance formula is obtained for channels with cylindrical roughness, valid for both emergent and submerged cases.

The effect of vegetation flexibility is not considered in this study. Therefore, additional research would be desirable to validate the applicability of the rigid vegetation model developed in this study to flexible vegetation conditions.

(Cui J. and Neary V.S., 2002)

Vegetation causes flow resistance and affects local flow and turbulence properties, including the local streamwise velocity and the shear stress distribution.

Field and laboratory investigations have related vegetative resistance parameters, such as drag coefficients and Manning's n values, plant properties, including height, density and flexibility (e.g. Kouwen & Unny, 1973; Shimizu & Tsuijmoto, 1994). This information has aided the development of semi-empirical formulas for calculating bulk flow parameters and spatially averaged velocity profiles (Klopstra et a., 1997; Freeman et al., 1998).

Elucidations of more complex flow and transport processes requires more detailed investigations, namely measurements and modelling of vertical and transversal profiles of flow energy and turbulence properties. Such investigations require advanced experimental instruments (e.g. LDA and PIV) and CFD modelling techniques (e.g. Reynolds averaged Navier-Stokes (RANS) and Large Eddy Simulation (LES)).

Computational fluid dynamics (CFD) models that describe open channel flows with vegetative resistance have only recently been developed (Shimizu & Tsuijmoto, 1994; Lopez & Garcia, 1998; Tsuijmoto & Kitamura, 1998; Neary 2000, Fischer-Antze ed al., 2001).

These models close the RANS equations using two-equation isotropic turbulence models. With the exception of Neary (2000), who employed the near-wall k-ω model, the remaining investigators used the more popular k-ε with the near-wall functions. Such models provide detailed localized descriptions of the flow and the turbulence field, including profiles of the streamwise velocity and Reynolds shear stress, but provide only limited descriptions of the turbulence field.

The present work considers fully developed flow with simulated rigid vegetation as investigated by Shimizu & Tsuijmoto (1994) in their laboratory study. The objectives are: (1) to validate a LES model with the experimental measurements of Shimizu & Tsuijmoto (1994); (2) to investigate the effects of the vegetation layer on the turbulence field, including the turbulence intensities and the anisotropy of the Reynolds stresses.

The LES model developed by (Cui, 2000) is modified to include vegetative drag terms in the streamwise momentum equation. Near the bed and the edge of the vegetation layer, the mesh is densely distributed to resolve the step gradients of the mean flow and turbulence properties.

As with the RANS models, LES provides reasonably good predictions for the vertical velocity profiles and the Reynolds shear stress, when compared to the experimental measurements. LES also provides reasonably good results for the streamwise turbulence intensity. Neither model predicts the bulge in the measured streamwise velocity profile near

the bed. The bulge in the measured streamwise velocity profile near the bed is most likely due to the streamwise vorticity produced by individual vegetation elements, and can not be resolved with the present model representation. A refined model that solves the flow around individual vegetation elements should therefore provide better agreement in this region.

(Neary V.S., 2003)

Numerical modeling studies by Shimizu & Tsuijmoto (1994) and Lopez and Garcia (1997) are representative of recent attempts to simulate steady uniform flow through rigid submerged vegetation of uniform density.

These models close the RANS equations using the standard k-ε turbulence model with wall functions. They introduce a sink term representing vegetative drag to the RANS equations.

The k (turbulent kinetic energy) and ε (dissipation) transport equation were also modified by introducing the drag-related turbulence production terms.

Differences between these two numerical modelling studies relate to the treatment of the drag coefficient and the weighting coefficients. For the drag coefficient, Lopez and Garcia (1997) kept it constant; citing the experiments of Dunn et al. (1996) whereas Shimizu and Tsuijmoto (1994) adjusted its value in a range, to achieve a good fit with measured velocity and Reynolds stress profiles. For the weighting coefficients, Lopez and Garcia (1997) selected values (based on a theoretical argument first presented by Burke and Stolzebach (1983)) different from the corresponding ones selected by Shimizu and Tsuijmoto (1994) (based on calibration).

Comparing these two numerical model studies is somewhat arbitrary due to the different approaches used for selecting the model coefficients.

The objective of (Neary V.S., 2003) work is to develop and validate a CFD model that employs a near-wall k (turbulent kinetic energy) and ω (specific dissipation or dissipation per unit kinetic energy) turbulence closure that calculates the flow and turbulence properties all the way to the channel bottom. For vegetated waterways dominated by form drag, the k-ω closure offers no obvious advantage over the k-ε models with wall functions. However, the near-wall k-ω closure has been demonstrated to be the model of choice for predicting bed-shear stress over a wide range of roughness types (Patel and Yoon, 1995; Neary, 1995). Therefore, the model should yield more accurate predictions than the k-ε model with wall functions when both bed shear and form drag affect flow resistance.

However, an important question is to validate the use of the near-wall k-ω closure model for the case of steady uniform flow through rigid submerged vegetation of uniform density.

The detailed laboratory measurements of Shimizu and Tsuijmoto (1994) are used to compare model calculations.

A fully developed one-dimensional open-channel flow with submerged rigid vegetation is modelled within the portion of flow occupied by vegetation by adding a vegetative drag term to the x-momentum equation and additional turbulence production terms to the k-ω transport equations.

This study discusses both treatments of the model coefficients adopted by Shimizu and Tsujimoto (1994) and by Lopez and Garcia (1997), discussed above.

An evaluation of these two modelling strategies indicates that, for similar treatment of the model coefficients, the use of the near-wall k-ω model produces results similar to previous models that employed the standard k-ε models with wall functions.

Moreover, reasonable predictions of streamwise velocity and Reynolds stress profiles can be achieved by adopting universal values for all model coefficients, but the calculated energy gradient can have significant error. The study also indicates that predictions of streamwise turbulence intensity are significantly improved by adopting for the weighting coefficients, the calibrated values rather than the theoretically base ones.

(Uittenbogaard R., 2003)

The paper (Uittenbogaard, 2003) is dedicated to modelling the turbulent flow over and through vegetation in water of limited depth. The perspective of the paper is innovative at all, as it is based on the use of concepts relative to turbulent flow along and through porous media, considering the vegetation as it was a porous medium. A rather long paragraph is therefore devoted to a survey on turbulent flow along and through porous media. Some important differences are stressed relative to different volume-averaging methods, depending on whether the sub-pore scale of turbulent kinetic energy is considered or just the larger-scales that survive the volume averaging. Another observation regards the question if it is better to use a multi-scale k-ε turbulence model or a single k-ε turbulence model extended to all length scales, and the choice falls upon the last one. The last observation regards questions about the permeability or flow resistance.

Having the aforementioned literature at his disposal, and having also a vast experience with testing and applying a 3D shallow-water solver and in parallel with a simpler so-called 1 DV model, the author could realize a new model for turbulent flow over and through a current flowing over bed covered by submerged, rigid or flexible, vegetation. The complete model is based on two momentum equations for the orthogonal horizontal velocity components, possibly subjected to rotation. But, for comparison with straight channel experiments, the

model version which is presented is related to the Reynolds-averaged pore velocity in horizontal x-direction as a function of the vertical co-ordinate. The complete model includes a suite of eddy-viscosity based turbulence models, but in particular for the purpose of the paper only the k-ε model and a so-called low-Re version of the k-ε model are referred to. The essential limitation of the model is the assumption that the flow is uniform in horizontal direction.

After having developed the main characteristics of the model, the author presents some comparisons of its forecasts with the turbulence properties derived by the experiments referred in (Nepf and Vivoni, 2003) and also (López & Garcia, 2001) and (Meijer & Van Velzen, 1999). The first flume had a vegetation height of 160mm with a water depth of 440mm or of 280mm; the second flume of 120mm and 340mm respectively, the third flume of 900mm and 2090mm respectively. In relation to the first flume figures are presented in which, referring to some statistic properties of the current (local mean values of velocity, Reynolds stresses, turbulent kinematic viscosity, non dimensional turbulent kinetic energy), comparisons are performed between experimental data and modelled data.

In relation to the second and the third flume, only local mean values of velocity are considered. In the two last comparisons experimental and modelled data agree very well, whereas in the first comparisons agreement is worse: author attributes this partial lack of agreement to the circumstance that the flume of Nepf and Vivoni is too high in respect of its width (280mm).

In conclusion the author is rather satisfied with its model forecasts, even if he believes that some particular must be deepened.

(Choi S. and Kang H., 2004)

Stream flows over a vegetated bottom boundary are quite common in nature. Mean flow and turbulence characteristics of open-channel flows over rough boundary are studied either by laboratory measurements or numerical computations. In many engineering problems in fluid mechanics and hydraulics, the k-ε model has been widely employed perhaps due to the well-established empirical coefficients of the model. However, yet in 2004, none of the existing turbulence models were truly universal, and thus, each model needed to be tuned to specific flows. The k-ε model and similar models based upon the eddy viscosity concept made a basic assumption that the Reynolds stress is aligned with the velocity gradient. This assumption is valid only for simple shear flows. However, even for open-channel flows over a smooth bed, the bottom boundary and the free surface tend to reduce vertical turbulence intensity, and the decreased amount of turbulence intensity is redistributed to the ones in the

streamwise and the transverse directions (Nezu & Nakagawa, 1993). Therefore, it can be easily deduced that the vegetation layer will increase the level of non-isotropy of turbulence, which motivated the application of non-isotropic turbulence model to vegetated open-channel flows in the present study.

Shimizu and Tsuijmoto (1994) computed vertical distributions of mean and turbulent flow structures by using the k-ε model. Lopez and Garcia (1997) simulated flow structures of vegetated open-channel flows by using the k-ε model and compared the computed profiles with their experimental results. Neary (2003) simulated the open-channel flows with submerged vegetation using the k-ω model and suggested the weighting coefficients in the transport equations.

The considered study is an application of the Reynolds stress model (RSM) to vegetated open-channel flows, where cylinders of simulated vegetation are uniformly distributed. Averaged equations in both time and space dimensions are used. Assuming that the flow is at high Reynolds number in a wide open-channel, the momentum equation in the streamwise direction is expressed. The Reynolds stress due to the spatially fluctuating velocity is ignored because it is believed to be extremely small compared to the Reynolds stress due to the turbulent momentum transfer (Lopez and Garcia, 1997).

Now, beside the RMS model, three other turbulence models are considered in the paper for sake of comparison.

In the k-ε model, the values of the weighting coefficient for the drag due to vegetation suggested by Lopez and Garcia (1997) are used.

In the algebraic stress model (ASM), for the Reynolds stress, proposed firstly by Rodi (1979), the values of the empirical coefficients suggested by Shimizu and Tsuijmoto (1994), are used.

In the Reynolds stress model, for the computation of pressure-strain term, the Speziale, Sarkar and Gatsky's model (1991) is employed. For diffusion and dissipation rate of Reynolds stress, Mellor and Herring's model (1973) is used.

The turbulence models, previously introduced, are applied to plain open-channel flows over smooth bed and open-channel flows with submerged and emergent vegetation. Moreover, the suspended load transported by vegetated open-channel flows is evaluated by using the Reynolds stress model.

Measurement data from Lopez and Garcia (1997) are used for comparison with numerical simulations. It is seen that the RMS predicts the mean velocity and turbulence intensity better than the algebraic stress model or k-ε model, especially above the height of vegetation.

With reference to the Reynolds stress profile, over the entire depth, the simulated profile

by RMS and ASM are nearly the same and they match the measured data slightly better than the k-ε model.

With reference to the eddy viscosity profile, below the vegetation height, the eddy viscosity by the RMS is quite uniform except the region close to the bottom while the eddy viscosity by the k-ε model is the smallest, and the measured data lie between the profiles by the k-ε model and the RSM; above the vegetation height, the k-ε model and the ASM result in similar profiles, whereas the RMS yields larger values. Particularly, above the vegetation height, it can be said that the RSM simulates the eddy viscosity better.

However, more comparisons using another data set would consolidate the current finding.

For open channel flow with emergent vegetation, the RMS, the ASM and the k-ε model are employed in computation. Comparisons are made with experimental data by Nepf and Vivoni (2000). They used flexible cylinders with artificial stems to model vegetation. However, near the bottom, the RMS predicts the mean velocity profile best. Towards the slowly surface, all computed profiles are indistinguishable and agree well with measured data. The RMS simulates the turbulence intensity profile better than the ASM and the k-ε model. The Reynolds stress profile agrees well with measured data. The Reynolds stress profile is almost zero over the whole depth. All computed Reynolds stress profile agree well with measurements. The turbulent kinetic energy budget profile shows that the wake production balances dissipation rate over the entire depth except for the region close to the bottom where the shear production is dominant over the wake production.

However, more comparisons using another data set would consolidate the current finding. The challenges for the future of this model clearly include to extend it to natural vegetation.

(Poggi D., Porporato A., and Ridolfi L., Albertson J. D., Katul G. G., 2004)

In (Poggi et al., 2004) paper an innovative phenomenological model of the effect of vegetation density on canopy sub-layer (CSL) turbulence is established. The paper starts from the observation that the canonical form of atmospheric flow near the land surface, in the absence of a canopy, resembles a rough-wall boundary layer, whereas, in the presence of an extensive and dense canopy, the flow within and just above the foliage behaves as a perturbed mixing layer. Moreover the paper stresses the circumstance that up to 2004 no analogous formulation existed for intermediate canopy densities.

In order to create and validate the phenomenological model four steps were passed through.

The first step was an experimental one. Experiments were conducted in a re-circulating flume; the model canopy was composed of an array of vertical stainless steel cylinders with

densities from 67 rods m^{-2} (a very poor density) till 1072 rods m^{-2} (a very high density). The velocity was measured by using a two-component LDA: 11 measurement locations were used, and at each location a profile of 15 vertical measurement locations was established through runs of 300s every one at the sampling frequency of 2500-3000hz; finally a space and time mean was adopted in all the statistical analyses performed. Moreover, visualization experiments was conducted by injecting red rhodamine at several vertical layers which were lighted by a laser light split in a thin sheet to identify and photograph the dominant vortices at every level of canopies.

The second step was to perform statistics of the measured data. The performed statistics were first of all: mean velocity, variances, skewness and flatness factors, shear stresses. These statistics were presented for all the density cases, and the comparison clearly showed that, going from the less dense toward the most dense canopies, these statistics changed from rough-wall boundary layer type to perturbed mixing layer type, with all the intermediate possibilities. A second type of statistics was the quadrant analysis and the last type was the spectral analysis and visualization; these last analyses could show the vorticity characteristics of the flow: from both visualization and spectral analysis it was clear that the region inside the canopy, irrespective of density, is dominated by energetic motions controlled by length scales reflecting the local canopy geometry.

The third step was to create the phenomenological model. The created model decomposes the space within the CSL into three distinct zones: the deep zone in which the flow field is shown to be dominated by vortices connected with von Kármán vortex streets; the second zone, which is near the canopy top and presents a superposition of attached eddies and Kelvin-Helmoltz waves produced by inflection instability in the mean longitudinal velocity profile; the uppermost zone, where the flow follows the classical surface-layer similarity theory. In particular, in the second zone the flow is considered to be a superposition of a mixing layer and a rough-wall boundary layer with the superposition weights defined by canopy density. Finally the model equations were numerically integrated with suitable boundary conditions, and gave the possibility to obtain theoretic mean velocity and Reynolds stresses profiles.

The fourth final step was to compare the results obtainable from the model with the experimental data, and this comparison shows a good theoretic reproduction of mean velocity and Reynolds stresses profiles with the experimental data for a wide range of vegetation densities.

Authors conclude stating that with the advancement of remote sensing technology it is likely that broad space-time data mapping of canopy roughness densities should become

readily available and that the proposed model will provide a mechanistic bridge from the roughness density maps to vertical transport predictions.

(Keijzer M. *et al.*, 2005)

This paper presents a necessarily brief treatise about derivation of several equations to model the water depth dependant resistance induced by submerged vegetation in wetlands and floodplains. Two of the expressions of the roughness coefficient studied here were created through an analysis and a process of derivation upon the extensive literature on this subject. A third expression was obtained using a variant of genetic programming.

In case of submerged vegetation, the first expression is based on the method of the effective water depth, that models only two of the four zones that in the velocity profile can be observed: in particular, the zone inside the vegetation sufficiently away from the bed and from the top of the vegetation, and the zone above the vegetation. By summing up the discharge per unit width of each zone a general expression for the Chézy resistance coefficient can be derived.

The second expression is based on an analytical method that attempts to model the velocity inside the vegetation by analytically solving the momentum equation for flow through and over the vegetation, represented as rigid cylinders.

Solving the partial differential equation for the velocity profile inside the vegetation layer using boundaries conditions, at the bed and at the top of the vegetation, furthermore assuming a logarithmic velocity profile above the vegetation, connecting with the profile underneath, such second expression for the Chézy resistance coefficient can be obtained.

The third expression of the roughness coefficient was obtained using a variant of genetic programming. The data used for training the genetic programming created expression were generated by a 1DV turbulence model (Uittenbogaard, 2003). It can be argued that using such generated data defeats the purpose of finding an expression. But vegetation resistance is a typical 3-dimensional problem due to the water depth dependency. A full dynamical model thus operates on a 3D grid, which is computationally expensive. An analytical solution to the problem of resistance induced by vegetation, which includes water depth dependency, makes 2-dimensional, depth-averaged modelling possible, allowing for faster model computations and the possibility to apply the model to larger areas.

To ultimate test the created model, a dataset of laboratory flume experiments was collected from independent experimental studies. This data is not used for training, but kept aside to validate the created expression.

In particular, it can be seen that the expression based on the genetic programming results

are in better agreement with the experimental dataset, than the manually induced formulations, both on their performance on synthetic training and laboratory testing data, and in the economy of detail that needs to be modelled.

This means that the genetic programming engine can be used as a hypothesis generator in scientific discovery. Not only is genetic programming capable of producing equations that are comparable or better than their human derived competitors, but also it can produce expressions that are amenable to further analysis and manual improvement. The equation developed with the aid of genetic programming and modified using theoretical considerations is currently the most accurate and elegant formulation of resistance induced by submerged vegetation.

The authors conclude that, due to simplicity and accuracy of this formulation, a hydraulic engineering can simply calculate the resistance induced by vegetation using a simple expression, instead of setting up a complicated and computationally expensive model.

(Defina and Bixio, 2005)

A review of recent studies dealing with a one-dimensional flow through rigid vegetation, shows that there are two different approaches to determine the velocity profile through and above submerged vegetation: a two–layer approach, which separately describes flow in the vegetation layer and in the upper layer, and a suitable modified k-ε model, in which the drag due to vegetation is taken into account not only in the momentum equation, but also in the equations for k and ε.

In the study described here, these two models were revised and extended to consider plant geometry and drag coefficient variable with depth. In order to give a complete description of turbulence structure within and above the canopy, a turbulent kinetic energy budget equation was added to the two-layer model. In fact, the mixing length approach used to compute the eddy viscosity in the two-layer model provides limited information on the turbulence structure.

Numerical simulations were then performed with both models to reproduce the flow field in the presence of real and artificial vegetation. The results of these simulations were then compared with available experimental data reported in literature. These data were from laboratory experiments where vegetation was simulated using simple rigid cylinders, plastic plants, and real vegetation.

With reference to the mean flow structure, good agreement between the results of the models and experimental measurements was found for velocity and shear stress distributions along the vertical. Interestingly, for the plant prototypes used by Nepf and Vivoni (2000) and

the Spartina anglica used by Shi et al. (1995), the use of a variable with depth, vegetation density and drag coefficient, made it possible to improve the prediction of the velocity and the shear stress profiles inside the canopy. Furthermore, the s-.shaped velocity profiles characterized by the local maximum and minimum velocities along the vertical were accurately reproduced.

With reference to the turbulence structure, both models correctly predict the depth-averaged eddy viscosity. In fact, eddy viscosity profiles are fairly accurately predicted by the two-layer model. The k-ε model, on the other hand, does not accurately predict the behaviour of eddy viscosity within the vegetation layer. In this layer, the model predicts a parabolic profile and generally overestimates the experimental values. It is worth noting that the eddy viscosity is quite sensitive to average drag coefficient, while it seems unaffected by the assumption of constant or variable parameters.

The turbulent kinetic energy (TKE) budget illustrates the importance of the physical processes that govern turbulent fluid motions. The presence of vegetation adds a further dimension to the balance since new regions of turbulence production are created in the shear layer at the top of the canopy and in the wakes of the plant elements. The different length scales involved must be considered carefully. The wake-generated TKE has a length scale proportional to the dimensions of the elements in the canopy (i.e. the stem diameter), which is generally much smaller than the scale of the shear-generated turbulence, determined by the plant height. Therefore, when the scale of the wake-generated turbulence is smaller than the Kolmogorov microscale, which is commonly the case in aquatic flows with relatively low plant densities, most of the mean flow energy extracted by the plant drag is quickly dissipated into spatial fluctuations. So, in view of the above discussion, the TKE equation can be rewritten. Some terms of the TKE budget are represented together with the normalized TKE profile as calculated by the two models for an experiment developed by Nepf and Vivoni (2000). Two different sets of weighting coefficients suggested by Lopez and Garcia (2001) and Shimizu and Tsuijmoto (1994), respectively, were used in the calculations. Both the models overpredict the normalized turbulent kinetic energy when the first set of weighting coefficient is used, particularly in the vegetation layer. Slightly better results are obtained when using the second set of weighting coefficients. Nonetheless, neither model is able to predict the concave-shaped profile seen in the experimental measurements when approaching the bottom.

After the turbulent kinetic energy k and the dissipation rate ε are computed, the streamwise turbulence intensity can be calculated using an algebraic stress model. Both the proposed sets of weighting coefficients lead to unsatisfactory results from the two models. In

fact, most of the available experimental data clearly show concave-shaped profiles of streamwise turbulence intensity within the vegetation layer, while the models always show convex-shaped profiles. This discrepancy is probably due to the highly non isotropic character of the flow, which cannot be described by present models. However, there is also some uncertainty in the experimental data because measuring flow velocity in the presence of vegetation is quite difficult given that the spatial variation of the mean flow field makes it necessary to consider a large number of measurements location.

Nepf and Vivoni (2000) observed that the flow through a submerged canopy can be divided into two regions: the "vertical exchange zone" in the upper canopy, where the vertical turbulent exchange with the overlying water has a significant influence on the momentum balance, and the "longitudinal exchange zone", near the bottom, where the vertical turbulent transport of momentum is negligible and the pressure gradient is balanced by the vegetative drag. The distance from the bottom of the limit between the two zones is called penetration depth. The penetration depth of turbulent stress inside the canopy was estimated according to different criteria, based on the analysis of vertical profiles of Reynolds stress, velocity and total transport of turbulent kinetic energy. The results of the two models confirmed the experimentally observed trend of the penetration depth, although with some limits.

To sum up, both models proved to be effective in predicting velocity and shear stress, but not quantitative turbulence. Future research efforts should focus on modelling the turbulence generated by the interaction between flow and vegetation.

(Ben Meftah M. *et al.*, 2005)

Most efforts to study vegetal effects on a current have concentrated on analyzing rigid and flexible submerged vegetation. For a large part, research on vegetated open channels has focused on flow resistance due to vegetation, in particular on the determination of the friction factor and the drag coefficient in the flow resistance law, by means of analytical models and laboratory flumes.

Less is known about the local effect of the vegetation when it is characterized by a very low concentration. Indeed, in this condition, it is not possible to consider the flow field homogeneous and so assign constant values to parameters such as the resistance index, the bed-friction velocity and/or the drag force, for the whole channel.

The rood topic of the present work is the investigation of the hydrodynamic effects of both rigid and flexible vegetation on a cross flow, in terms of velocity and turbulence distribution. The research is limited to the case of relatively low current velocities and flow depth higher than the height of vegetation, which is identical for both rigid and flexible type,

in absence of current.

Different configurations as vegetation type, flow depth and velocity were investigated in the laboratory flume. In particular, metallic cylinders with rough lateral surface were used to simulate rigid plants, while commercial broom acted as surrogate of the flexible vegetation. For all the configurations the vegetation was taken submerged; different relative submergences have been considered.

Emphasis is put on assigning a minimal density to the artificial plants, as it is expected that in non-uniform, bed-friction conditions in the channel, a local analysis is needful for better understanding the phenomenon. Therefore, to capture spatial variability within the array, multiple measurements points were set between each two consecutive elements on the three principal directions.

Therefore, in order to study the variations of the velocity distribution around both rigid and flexible individual elements, several analysis of the velocity component data into the flume have been carried out, along longitudinal and horizontal sections. To better highlight the local effect of the artificial vegetation on the crossflow, velocity, data have been processed and plotted either at different longitudinal distances from the plants, or on horizontal planes at different levels.

In the vegetation layer, the current is subject to a strong slow motion due to the presence of the close elements. Near the top of the vegetation, both the local velocity and its gradient increase progressively, producing at the vertical profile an evident inflection point and the typical S shape, as reported in literature. Upon the vegetation, the velocity gradient decreases, with the concavity directed upward. These differences decrease as we move away upstream or downstream from the stem, and are particular evident for rigid elements.

It is noticeable that the isolevel contours around the rigid plants are not circular but elliptical with major axis parallel to the longitudinal direction, which reveals the anisotropy of vegetation stem effects over the hydrodynamic flow distribution. Moreover, the current is particularly delayed by the presence of flexible elements, while with rigid cylinders the normalized flow velocity at the middle longitudinal section of two arrays reach the unit value or slightly larger, which means the negligence of the vegetation stem effects as long as going away from it.

Nevertheless, the aim of the research at this stage has been the investigation of the particular hydraulic path of the flow inside the vegetated zone, and just on its top, and the detection of different behaviour due to the particular kind of plants. The normalized longitudinal velocity component profiles obtained around the flexible elements match those related to rigid ones, with minimum velocity values in proximity of each stem, while away

from the stem, the velocity tends to rich the average value of the current in the flume in absence of vegetation. As a first remark, this result can be justified by a particularly low vegetation density chosen for the experimental work. On the contrary, at the top of vegetations, the flow pattern is quite different, and the presence of rigid elements seems to not disturb the current, which means that velocity values keep constant along the whole transversal section, while the flexible vegetation branches make the horizontal velocity profiles more irregular.

With reference to the turbulent characteristics, turbulence intensity and Reynolds stresses distributions have been obtained, with the intention of highlighting the influence of different kind of vegetation on the turbulent behaviour of the current. However, a different behaviour is recognizable for the kinds of artificial vegetations. In particular, for rigid rods, non-dimensional values of turbulence intensity peak just below the rod top, maintaining same maximum independently of the hydraulic flume conditions. On the contrary, the maximum streamwise turbulence occurs above the element tops for the flexible canopy situation, particularly when the relative submergence is small. In fact, for small and intermediate relative submergence, coherent structures cannot develop their whole size.

Moreover, the vertical Reynolds stress distributions in the channel with flexible and rigid vegetation have been plotted. Again, the flexible vegetation shifts the Reynolds stress peak at higher level in the flow, above the canopy, than the single rigid element.

As final analysis, the transversal Reynolds stress distributions in the channel with flexible and rigid vegetation have been plotted. Alternate of positive and negative transversal Reynolds stress distribution, between stems, implies the formation of clocks and anti-clockwise vortices.

(Huthoff F. *et al.,* 2006)

For open channel flow over rough surfaces, several relations exist that relate the average flow velocity to a roughness height that reflects the resistance of the bed. However, when the bed is covered with large roughness elements such as vegetation, or cylindrical elements, these methods are theoretically no longer valid.

In the current work, flow over vegetation is described by an average-velocity model where distinct flow characteristics are attributed to two separate flow layers. These two regions will be referred to as the surface layer and the resistance layer.

In this paper, a two-layer scaling model is proposed that treats the flow field above and in between the roughness elements separately, and, when combined, gives a description of the depth-averaged velocity of the entire flow field.

When a flow field is penetrated by vegetation, turbulent vortices are created in the wake behind the protruding stems. Consequently, in addition to the resistance at the bed, drag effects around the individual plant stems cause the flow to slow down. This is the case of emergent vegetation.

Whenever cylindrical elements become submerged, the flow in the surface layer has a higher average velocity than in the resistance layer, because in this layer no drag due to the stems is experienced. The energy losses in the surface layer are entirely due to the shear stress near the top of the resistance layer, which balances the gravitational force that drives the flow. Subsequently, the shear stress between surface and resistance layer (i.e. the interface shear) also causes the flow in top of the resistance layer to speed up (i.e. the characteristics S shape velocity profile). The force balance, with an extra component due to the surface layer, yields for the scaling expression of the average velocity in the resistance layer, in case that the stems are submerged.

Based on physical principles and scaling assumptions, the well-known Manning/Strickler equation can be derived for the case of rough channel flow (Gioia and Bombardelli, 2002). The main principles behind the derivation are: a simple force balance, scaling of turbulent fluctuations to the average flow velocity, and the concept of a constant energy dissipation rate when large eddies break down into small ones (known as Kolmogorov scale). The Authors follow the same line of reasoning to describe the depth-averaged flow over submerged rigid cylinders, i.e. for the surface layer, arriving to a scaling expression of the average velocity in the surface layer, including an unknown scaling length in terms of measurable geometric parameters, which can be specified from comparison with laboratory experiments.

When comparing the derived scaling expression of the average velocity in the resistance layer to results from flume experiments, very good agreement is found.

With reference to the scaling expression of the average velocity in the surface layer, several combination of available length scale was attempted. It is turn out that the spacing between the cylindrical stems gives the best agreement between calculated data and measured ones of the scaling expression of the average velocity in the surface layer. It is expected that this is no longer the case when the height of the cylinders is smaller than the distance between them. Future work of the authors will be focussed on the characteristics of such a scaling length when geometric variability among the resistance elements exists. Eventually, the aim will be to describe flow over natural vegetation, which involves further complications as stems flexibility, or leaves and side branches that individual plants may have.

(Ghisalberti M. and Nepf H., 2006)

In this paper flume experiments were conducted with rigid and flexible model vegetation to study the structure of coherent vortices (a manifestation of the Kelvin-Helmhotz instability) and vertical transport in shallow vegetated shear flows. This is a relatively innovative approach to the topic, as takes into account the non steady phenomena. In particular the vortex coherent structures are taken into consideration.

The rigid model canopies consisted of circular wooden cylinders arranged randomly in holes drilled plexiglas boards. Velocity measurements were taken simultaneously by three 3D acoustic Doppler velocimeters (ADV) and the vertical profiles consisted of 30 ten-minute velocity records collected at a sampling frequency of 25 Hz. The flexible model vegetation was designed to mimic eelgrass. Each model plant consisted of a stem region and six thin blades, based on the typical morphology of Massachusets. Bay eelgrass: wooden dowels were used to mimic the eelgrass stem. In this case the experimental technique hold four 3D ADV and also a digital video camera used to determine the maximum plant height and the monami (phenomenon that will be described afterwards) amplitude. Finally, to characterize the impact of plant flexibility on the flow, the oscillatory nature of both the velocity field and the plant height had to be characterized, so that series of $u'v'$ and together oscillations of three particular blades, coloured red, green and blue, were considered.

As for qualitative experimental results, the vortex street generated in flows with submerged vegetation creates a pronounced oscillation in the velocity profile, with the velocity near the top of a model canopy varying by a factor of three during vortex passage. This oscillation, and the vortex structures themselves, did not encompass entire thickness of the shear layer (in particular do not arrive till the flume bottom, but only till a particular lower limit of the vegetation height), which is the contrary unconfined by the free surface. However, the mixing length of momentum varies little in the entire flow overlying the canopy and, relative in particular to flows over rigid vegetation, within canopy geometry the oscillation has the effect of decreasing the amount of turbulent vertical momentum transport in the shear layer. In turn, this velocity oscillation drives the coherent waving of flexible canopies so that in case of flexible submerged aquatic vegetation, the response of the full system to the steady stronger currents is a progressive, synchronous, large-amplitude waving, termed monami by Ackerman and Okubo (1993).

This last phenomenon allows to use the flexible vegetation to study the vortex cycle: using a waving plant to determine the phase in the vortex cycle, each vortex is shown to consist of a strong sweep at its front (during which the canopy is most deflected), followed by a weak ejection at its rear (when the canopy height is at a maximum). Whereas in

unobstructed mixing layers the vortices span the entire layer, they encompass only 70% of the flexibly obstructed shear layer studied here.

Generally speaking, measurements distinguished among four zones: above shear layer zone, upper shear layer zone, exchange zone, wake zone; moreover measurements distinguished also among the three cases of rigid canopy, still flexible canopy and waving canopy. Profiles of mean velocities, shear stresses, vertical mixing length, turbulence intensities, and also oscillations of bin-averaged values of plant height and of velocity profiles, are considered, and these quantities are studied also within a quadrant analysis.

Finally, remembering that, by using a waving plant to determine phase in the vortex cycle, each vortex is shown to consist of a strong sweep at its front followed by a weak ejection at its rear, the Reynolds stress generation by the vortex appears to respond to the oscillating instantaneous plant height: that is, the greatest penetration toward the bed of large-scale turbulence occurs when the canopy is at its most prone. Accordingly, it is imperative that the motions of the fluid and canopy are coupled in models of flow over flexible vegetation. The last remark is that the highly structured vertical transport within both rigid and flexible canopies is dominated by sweeps (to a degree dependent upon the drag density), while that in the unobstructed flow is dominated by ejections.

(Nezu I., *et al.*, 2006)

There are a lot of knowledge and valuable data in air flows over and within the vegetation canopies. In contrast, the vegetated rivers and the open-channel flows have only recently been investigated.

In particular, while the friction law and resistance of vegetation have in past decades studied intensively, a lot of uncertainties remain concerning the coherent structures, dispersive effects and turbulent energy transport properties.

These topics have been highlighted in this experimental work, where turbulence measurements in the whole depth region from the bottom-bed to the free surface, in a vegetated canopy open-channel flows have been conducted, in order to investigate dispersive properties and turbulence structure, by varying the vegetation density.

To reveal the effects of vegetation on turbulent structure, it is of essential importance to consider the horizontal space averaging in the time averaging Navier-Stokes equations.

The main findings obtained in the present study are as follows.

The streamwise velocity is varied significantly in the spanwise direction within the canopy, due to the local deceleration behind the vegetation. This trend is more remarkable in the denser vegetation. In contrast, over the canopy, the lateral variations become smaller,

because the local effects of vegetations become negligibly small.

The vertical profiles of the space-averaged streamwise velocity reveals that the typical drag effects of vegetation decelerate the streamwise velocity more largely in the canopy layer as the vegetation density becomes larger. Consequently, a significant inflectional point appears near the canopy edge, the feature of which is consistent with that of plant canopy flows. The measured shear length scale decreases with an increase of the vegetation density Furthermore, a second peak is observed near the bottom-bed, which may be caused by three-dimensional dynamics of wakes.

The friction velocity was evaluated as the peak value of the Reynolds stress, which is consistent with the method of plant canopy flows as reviewed by Finnigan (2000). The results suggest that the bed friction becomes larger with an increase of the vegetation density.

The vegetation has much significant effects on the space-averaged velocity and Reynolds stress within the canopy rather than over the canopy. Therefore, a universal formula, i.e. the log-law, may be applied to the velocity profiles over the canopy.

It is inferred from the inflectional profiles of velocity as well as the Reynolds stress profiles that coherent eddies are generated by the velocity shear near the vegetation edge, and, consequently, they cause large momentum exchanges between the low-speed flow within the canopy and the high-speed flow over the canopy. In order to evaluate these properties quantitatively, the quadrant conditional analysis was conducted for the instantaneous Reynolds stress. It revealed that the sweep event was greater than the ejection event, near the canopy edge.

The sweep and ejection events are related with skewness. It was found from the skewness distributions that there were noticeable coherent structures within the canopy, and the significant momentum exchange occurs between the within-canopy and the over-canopy.

In over-canopy layers, the spectral distributions obey the Kolmogoroff's power law in the inertial subrange. Within the canopy, the spectral distribution fits to the Kolmogoroff's power law in a narrower range, and the spectrum increases in the high frequency range. This suggests that there may be a turbulence energy supply caused by the wake eddies generated behind the vegetation elements. This property is more remarkable nearer the bottom bed, whereas the spectral profile nearer the free surface is closer to that of boundary layer since the effects of coherent motions are smaller farther from the vegetation layer.

The turbulent kinetic energy (TKE) budget was examined in order to reveal the dispersive contributions of turbulence due to vegetations. Of particular significance is that the turbulent fluctuations are generated strongly near the vegetation edge and the wake generation is comparable or larger than the shear generation. This suggests that the wake generation plays

an important role on the turbulence generation within the canopy.

Furthermore, it is demonstrated significantly that the coherent motion, such as sweeps, transports high-speed momentum toward the inner vegetation layer, causing significant energy loss.

2. AIM AND STRUCTURE OF THE THESIS

The aim of this Doctoral thesis is to analyse experimentally, by using measures of instantaneous velocity carried out through a laser Doppler anemometer, the behaviour of streams flowing on a rigid vegetated bottom, realized by means of brass cylinders, and characterized by different height and density. A particular attention has been paid to the effects that such a type of vegetation has both on the flow resistance and on the distributions of the main statistical quantities of the turbulence, such as local mean velocity, and variance, skewness, kurtosis of the fluctuating velocities, and finally longitudinal integral length scales obtained through the autocorrelation function. Measurements are carried out both in boundary layer and in uniform flow currents.

As for the structure of the thesis, this is constituted by a first methodological part which can be subdivided into two sections (A−Introductory section, B−Laboratory facilities section) and a second scientific substantial part which can be subdivided into three sections (C−Boundary layer section, D−Roughness measurements section, E−Statistical quantities in uniform flow section) and a Conclusion (F). Within each section the theme is developed in chapters. The first part contains ten chapters and the second part contains eight chapters.

A−The Introductory section holds an account of the problem and a long state of art. Moreover it holds the present chapter relative to aim and structure of the thesis.

B−The Laboratory facilities section refers to the accurate description of the experimental plants and instrumentations that have been used in the thesis. The experimental plants consist fundamentally of two channels of different sizes, used the first one for boundary layer measurements and the second one for uniform flow measurements. The first channel was already disposable at the beginning of the thesis' work whereas the second channel did not exist at all at this beginning and has been wholly realized within this thesis. The instrumentations consist fundamentally of a laser doppler anemometer (LDA) system of Polythec for instantaneous velocity measurements and a LabView system of National Instruments for processing of the previously obtained data. Here too the LDA was already disposable at the beginning of the thesis' work whereas the LabView software has been implemented during this thesis.

C−The Boundary layer section deals with the interaction between a boundary layer current with turbulent free stream, developing within a channel, and the rigid vegetated bottom, realized through cylinders of different height and density. The aim of the study is to determine the effects of the vegetated bottom on some of the main statistical quantities of the

boundary layer, such as the thickness and the distributions of the local mean velocity, developing a comparison with the condition of smooth bottom. In the hydrodynamic condition with vegetated bottom, the experimental investigations were carried out by making local mean velocity measurements in different positions with respect to the cylinders. Non dimensional distributions of the local mean velocity were obtained by using the velocity value in the free stream and the suitable values of the boundary layer thickness in the subsequent sections taken into consideration.

D−In the Roughness measurements section, the experimental results obtained with reference to the boundary layer flowing on vegetated bottom were used to define a simplified methodology to measure the absolute roughness of the vegetated bottom itself. This methodology allows to obtain the absolute roughness of a current, using experimental surveys relative only to the boundary layer reach, thus permitting a considerable simplification of the experimental facilities. The validity of the methodology was checked through experimental data both found in literature and obtained through other experimentations carried out afterwards during the thesis' work.

E−In the Statistical quantities section, the distributions of the main statistical quantities of the turbulence with reference to a uniform stream flowing on a rigid vegetated bottom are analysed. In particular, beginning from the acquisitions of the instantaneous velocities, the distributions of the local mean velocity, and variance, skewness, kurtosis of the fluctuating velocities, and finally longitudinal integral length scale obtained through the autocorrelation function were determined. Preliminarily, the study of the distributions of such statistical quantities was carried out referring to a single cylinder, in the section D. Afterwards, the study was extended to a mesh of cylinders, characterized by a geometry similar to one used in the case of the boundary layer.

F−Finally, in this section, the partial results previously obtained are presented all together in the Conclusion.

As to the single chapters, the thesis is divided in such a way:

A−Introductory section

The first chapter deals with the type of problems that will be developed and describes a long literature review.

The second chapter illustrates the aim and the structure of the thesis.

B−Laboratory facilities section

The third chapter describes the system used to measure the instantaneous velocities values.

The fourth chapter describes the experimental channel used to study the boundary layer. This channel was already disposable at the beginning of the thesis.

The fifth chapter reports the building of the experimental channel used to study the uniform flow. This channel did not exist at the beginning of the thesis.

The sixth chapter describes the calibration of the orifice placed on the feeding pipe of the channel.

The seventh chapter describes the check of the working of the channel with smooth bottom.

The eighth chapter reports how the vegetated bottom has been made.

The ninth chapter describes the calibration of the measurement system of the instantaneous velocities in the channel.

The tenth chapter describes the implementation within the National Instruments LabView system of the software necessary for calculating the turbulence statistical quantities, giving also, briefly, definitions and physical meaning of these quantities.

C−Boundary layer section

The eleventh chapter describes the tests carried out on the boundary layer and the results obtained through a classic methodology of non-dimensional representation.

The twelfth chapter describes the results obtained through a new methodology of non-dimensional representation.

The thirteenth chapter describes new tests carried out on the same boundary layer but changing the position of the measurement points within the current, and refers the consequent improved results.

D−Roughness measurements section

The fourteenth chapter relates the procedure to obtain the absolute roughness starting from measurements in the boundary layer.

The fifteenth chapter verifies and calibrates the above methodology with experimental data obtained in the second channel and compares the obtained results with literature data.

The sixteenth chapter reports the results concerning the aforementioned statistical quantities obtained in the wake of a single cylinder in order to explain some peculiar results relative to the previously obtained absolute roughness values. These measurements and consequent data processing have been performed also to test the system, and to have a background with respect to the analogous measurements to be afterwards performed in the uniform flow.

E−Statistical quantities in uniform flow section

The seventeenth chapter reports the results relative to the tests carried out with the bottom

completely vegetated. Here too all the previously remembered statistics were performed, having also at disposal the previous experiences carried out in the wake of a single cylinder.

F−Conclusions

The eighteenth chapter relates the general conclusions of the thesis.

3. LDA SYSTEM FOR DATA ACQUISITION

3.1 Introduction

The Laser Doppler Anemometer (LDA) is an instrument that allows to obtain velocity measurements of a fluid.

The characteristics of this instrument are:

- the non-interference with a measurement fluid, or rather the measurement does not depend on the type of liquid;
- no need for calibration;
- the possibility of obtaining measurements just about precise.

Anyway, the use of the LDA presents two limitations:

- the need to inseminate the current with very small particles, because, while being dragged by the current, they will reflect the display lights coming from the laser;
- the walls of the pipe shall be transparent in order to allow the crossing of the laser beam.

3.2 Theoretical analysis

The working principles is based on the Doppler effect; it is a physical phenomenon, that is characteristic of the wave propagation, which shows itself in the presence of a relative motion between a source of waves and a receiver (fig. 3.1).

Let's say that the source emits a light signal with frequency:

$$f = \frac{c}{\lambda}$$

where c is the light velocity and λ is the wavelength.

The light signal arriving at the receiver will have a frequency f_R which depends on the type of the relative motion; in fact, it is proved that:

$$f_R = f\left(1 - \frac{\hat{v}\cdot\hat{n}}{c}\right) \tag{3.1}$$

in case it is the receiver to move with respect to the source and:

$$f_R = \left(\frac{f}{1 - \frac{\hat{v}\cdot\hat{n}}{c}}\right) \tag{3.2}$$

in case it is the source to move with respect to the receiver.

The product $\hat{v}\cdot\hat{n}$ represents the component part of the relative velocity in the direction

identified by the joining line between receiver and source, and *n* is the versor directed from the source towards the receiver, in both cases.

The difference f_D between the frequency registered and the emitted one is the frequency called Doppler frequency:

$$f_D = f_R - f$$

3.3 Configuration of the optical scheme (Differential Doppler)

The laser beam is sent to the B optical system (beam splitter) which, through a series of reflections, splits it in two; the two beams obtained are focused by a lens, and their intersection identifies the measurement volume.

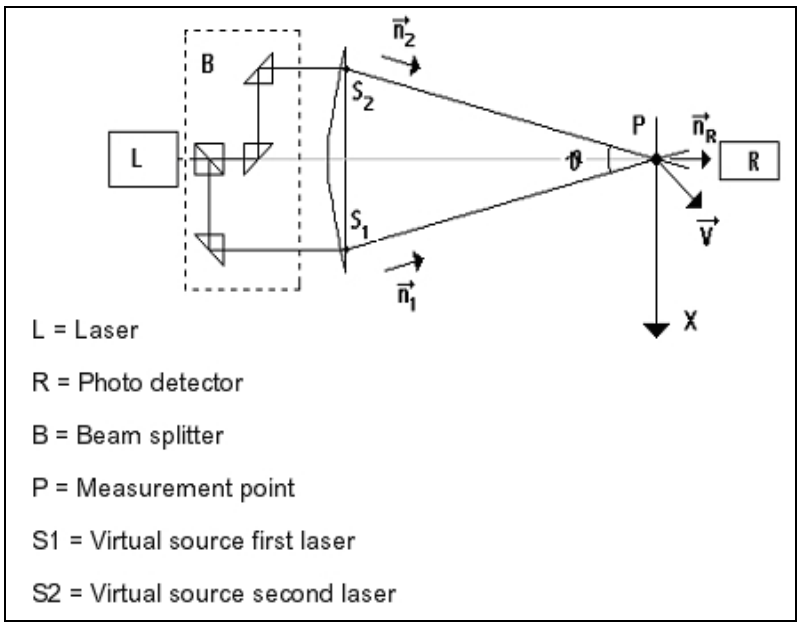

Fig. 3.1 - Optical scheme

When a particle crosses the measurement volume, a first Doppler effect takes place, due to the relative motion between the particle and a virtual source, as if it were in the points S_1 and S_2, respectively for the first and second beam.

Besides, since the particle is in relative motion, it takes place a second Doppler effect also respect to the receiver.

By using the (3.1) and (3.2) it is possible to trace the two frequencies that the photodetector (R) receives for each signal:

$$f_{R1} = \frac{\frac{c}{\lambda}}{1 - \frac{\hat{v} \cdot \hat{n}_1}{c}} \left(1 - \frac{\hat{v} \cdot \hat{n}_1}{c} \right) \tag{3.3}$$

(3.4) $$f_{R2} = \frac{\frac{c}{\lambda}}{1 - \frac{\hat{v} \cdot \hat{n}_R}{c}} \left(1 - \frac{\hat{v} \cdot \hat{n}_2}{c} \right)$$

The respective Doppler frequencies are:

(3.5) $$f_{D1} = f_{R1} - f = \frac{\frac{c}{\lambda}}{1 - \frac{\hat{v} \cdot \hat{n}_R}{c}} \left(1 - \frac{\hat{v} \cdot \hat{n}_1}{c} \right) - \frac{c}{\lambda} = \frac{\frac{\hat{\nu}}{\lambda}}{1 - \frac{\hat{v} \cdot \hat{n}_R}{c}} \left(\hat{n}_R - \hat{n}_1 \right)$$

(3.6) $$f_{D2} = f_{R2} - f = \frac{\frac{c}{\lambda}}{1 - \frac{\hat{v} \cdot \hat{n}_R}{c}} \left(1 - \frac{\hat{v} \cdot \hat{n}_2}{c} \right) - \frac{c}{\lambda} = \frac{\frac{\hat{\nu}}{\lambda}}{1 - \frac{\hat{v} \cdot \hat{n}_R}{c}} \left(\hat{n}_R - \hat{n}_2 \right)$$

where $\hat{n}_R$ represents the versor in the direction "point of measure-photodetector".

Since the velocity of the particle is negligible compared with the velocity of the light "c" by which the signals are propagated, with a good approximation, it is possible to assume the relations:

(3.7) $$f_{D1} = \frac{\hat{\nu}}{\lambda} \cdot \left(\hat{n}_R - \hat{n}_1 \right)$$

(3.8) $$f_{D2} = \frac{\hat{\nu}}{\lambda} \cdot \left(\hat{n}_R - \hat{n}_2 \right)$$

Assuming $f_{D1} > f_{D2}$ we have:

(3.9) $$\Delta f = f_{D1} - f_{D2} \qquad \text{where } \Delta\omega = 2\pi\Delta f$$

(3.10) $$f_0 = \frac{f_{D1} + f_{D2}}{2} \qquad \text{where } \omega_0 = 2\pi f$$

After indicating with $\Delta\omega$ and ω_0 the relative pulses, we have:

(3.11) $$\omega_{D1} = \omega_0 + \frac{\Delta\omega}{2}$$

(3.12) $$\omega_{D2} = \omega_0 - \frac{\Delta\omega}{2}$$

and consequently the photodetector will receive two signals given by:

(3.13) $$S_1 = A\cos\left(\omega_{D1} t\right) = A\cos\left(\omega_0 + \frac{\Delta\omega}{2} \right) t$$

(3.14) $$S_2 = A\cos\left(\omega_{D2}t\right) = A\cos\left(\omega_0 - \frac{\Delta\omega}{2}\right)t$$

in which the A amplitude of the signals is supposed to be equal.

In fact, the photodetector cannot distinguish the two signals, and therefore it receives the sum of the two:

(3.15) $$S = S_1 + S_2 = A\left[\cos\left(\omega_0 + \frac{\Delta\omega}{2}\right)t + \cos\left(\omega_0 - \frac{\Delta\omega}{2}\right)t\right] = 2A\cos\left(\frac{\Delta\omega}{2}t\right)\cos\left(\omega_0 t\right)$$

Such signal turns out to be basically a light signal with pulse ω_0 and then with f_0 frequency, with modulate amplitude:

(3.16) $$2A\cos\left(\frac{\Delta\omega}{2}t\right)$$

The luminous power arriving at the photodetector is supplied instant by instant by the square of the amplitude, which is worth:

(3.17) $$4\mathrm{A}^2\cos^2\left(\frac{\Delta\omega}{2}\mathrm{t}\right) = 4\mathrm{A}^2\frac{1\text{-}\cos\left(2\frac{\Delta\omega}{2}\mathrm{t}\right)}{2} = 2\mathrm{A}^2\left[1+\cos\left(\Delta\omega\,\mathrm{t}\right)\right]$$

and then it is clear that, beyond a constant medium value, this term presents a fluctuation about this medium value of pulse $\omega_D=\Delta\omega$ and then of frequency $f_D = \Delta f$.

Such frequency value is assumed as conclusive value of Doppler frequency, since it seems to be the frequency of the signal coming out of the photodetector and is worth:

(3.18) $$f_D = \Delta f = f_{D1} - f_{D2} = \frac{\hat{\nu}}{\lambda}\cdot\left(\hat{n}_R - \hat{n}_1\right) - \frac{\hat{\nu}}{\lambda}\cdot\left(\hat{n}_R - \hat{n}_2\right) = \frac{\hat{\nu}}{\lambda}\cdot\left(\hat{n}_2 - \hat{n}_1\right)$$

Then, being:

(3.19) $$\hat{n}_2 - \hat{n}_1 = 2\,\mathrm{sen}\left(\frac{\vartheta}{2}\right)\hat{i}$$

and replacing in the (3.18), we have:

(3.20) $$f_D = \frac{\hat{\nu}}{\lambda}\cdot 2\,\mathrm{sen}\left(\frac{\vartheta}{2}\right)\hat{i} = \frac{\nu_x}{\lambda}2\,\mathrm{sen}\left(\frac{\vartheta}{2}\right)$$

Indicating with:

$$\beta = \frac{\lambda}{2\,\mathrm{sen}\left(\frac{\vartheta}{2}\right)}$$ Calibration factor

which is intrinsic of each optical system and laser beam wavelength, it is possible to sum up that:

(3.21) $$\nu_x = \beta f_D$$

and then to note that the measurement is independent of the position of the photodetector. The calculation of β is bound by the knowledge of the technical data of the laser used, and particularly by the θ convergence angle of the two laser beams (it can be expressed in terms of the focal length (d_f) and of the length of the two beams (d_r) at the exit of the convergence lens from the relation:

(3.22) $$\vartheta = 2\,arctg\frac{d_r/2}{d_f}$$

and by the laser beam wavelength.

To sum up, we have:

$$\beta = \frac{\lambda}{2\,\mathrm{sen}\left(arctg\frac{d_r/2}{d_f}\right)}$$

3.4 Interference fringes

It is possible to arrive at the relation number (3.20) also through a different way, that is by geometrical considerations on the interference fringes that are formed by the intersection of the two beams, therefore, irrespective of the Doppler effect.

The superimposition of the two laser beams is, in fact, constructive in some points, and destructive in others; as a consequence, in the volume of measurement, it creates some regions where the luminous intensity is maximum, spaced out by dark areas or by areas with a very low luminous intensity.

The system of fringes can be represented as in fig. 3.2 a), when there is a generic plane parallel to the one of propagation of the two beams.

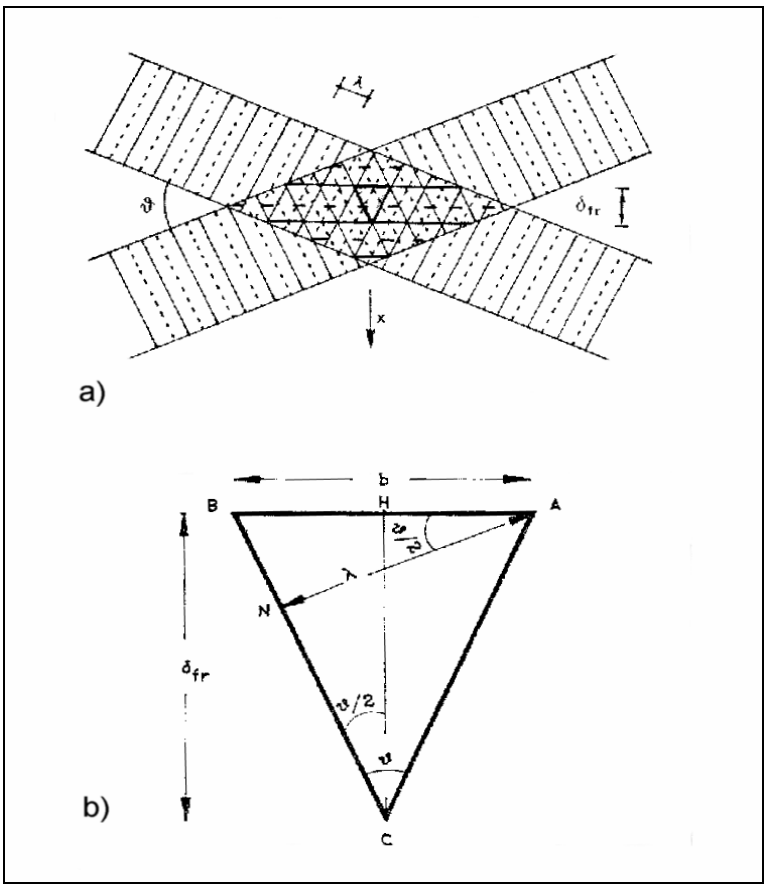

Fig. 3.2 - Interference fringes

The relative maxima and minima of the light wave are represented for each beam; they are λ far from each other. The intersection of two maxima or of two minima generates points of maximum luminous intensity (in absolute value). These points are placed on the lines obtained by linking the intersection points of the couples of the following maxima or minima (they are the horizontal segments represented in figure).

The distance δ_{fr} among the light fringes is constant. On widening a triangle, for convenience, (as in Fig. 3.2 b), we can note that the angles $B\hat{A}N = H\hat{B}C = \frac{\vartheta}{2}$ since the BAN and HBC triangles are alike.

Besides, we get:

$$\delta_{fr} = \frac{b}{2} cotg\left(\frac{\vartheta}{2}\right) \quad \text{and} \quad \mathrm{b} = \frac{\lambda}{\cos\left(\frac{\vartheta}{2}\right)}$$

replacing:

$$\delta_{fr} = \frac{\lambda}{2\,\mathrm{sen}\left(\frac{\vartheta}{2}\right)}$$

A particle crossing the measurement volume with a component part of velocity v_x constant, generates a recurrent light signal of T period, equal to the time spent to cover the space between two fringes, exactly δ_{fr}:

$$T = \frac{\delta_{fr}}{v_x}$$

The frequency, then, is:

$$f_D = \frac{1}{T} = \frac{v_x}{\delta_{fr}}$$

from which, replacing the expression found by δ_{fr}:

$$f_D = \frac{v_x}{\lambda} 2\,\mathrm{sen}\,\frac{\vartheta}{2}$$

and it exactly the expression (3.20), quod erat demonstrandum.

The expression (3.20), then, constitutes a fundamental equation for the LDA system.

3.5 Measurement volume

The measurement volume is the area identified by the intersection of the two beams coming from the beam splitter.

In order to define this measurement volume, it is necessary to identify the transversal dimension of a beam laser.

The intensity I of the light follows a Gaussian distribution, along a diameter of the beam laser:

(3.23) $$I(r)=I_0\, e^{-\frac{1}{2}\left(\frac{r}{\sigma}\right)^2}$$

where:

r = distance from the beam axis

σ= standard deviation

I_0= maximum value of the luminous intensity which can be reached for r = 0.

Then, it is agreed to assume as reference diameter d* of the laser beam, the double of the distance from the axis of the laser beam next to it, the power is of $1/e^2$ of the power relative to the axis.

As to the intensity, it means that $I(r^*) = I_0/e$

We obtain from the (3.23) expression that:

$$d^* = 2\sqrt{2}\sigma$$

The intersection of the two defined laser beams is spatially formed by an ellipsoid of a Cartesian equation:

$$x^2 \cos^2\left(\frac{\vartheta}{2}\right) + y^2 + z^2 \operatorname{sen}^2\left(\frac{\vartheta}{2}\right) = 2\sigma^2$$

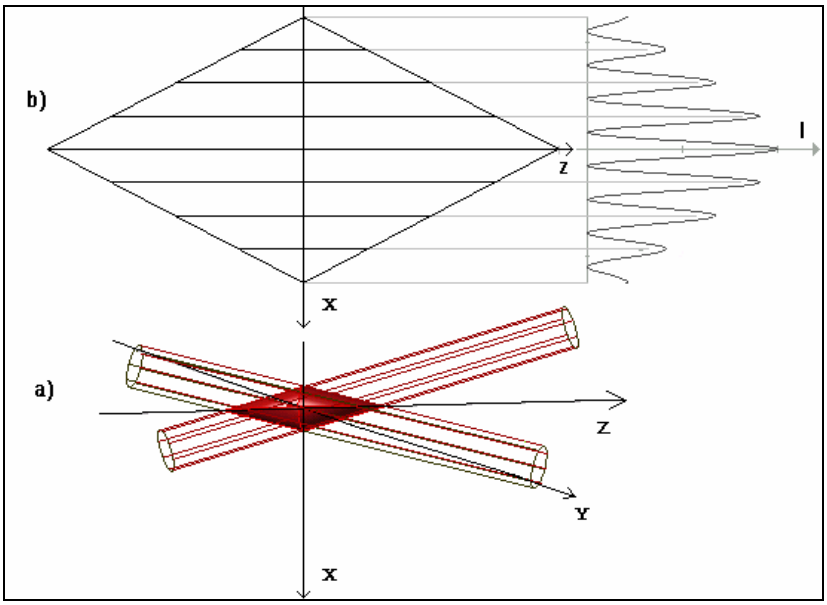

Fig. 3.3 - Measurement volume

It is proved that the axial dimensions of the measurement volume are:

(3.24) $$d_x = \frac{2\sqrt{2}\sigma}{\cos\left(\frac{\vartheta}{2}\right)} \qquad d_y = 2\sqrt{2}\sigma \qquad d_z = \frac{2\sqrt{2}\sigma}{\operatorname{sen}\left(\frac{\vartheta}{2}\right)}$$

In Fig. 3.3 b) the x-z section of the measurement volume is represented with fringes and relative luminous intensities.

3.6 The measurement point position

The measures are referred to the point P of intersection of the two laser beams.

If we consider the fluid under examination separated from the laser source by a transparent wall, the distance of the P point from the internal plane of the wall depends on a series of geometrical factors, as well as on the fluid nature and on the nature of the wall.

In fig. 3.4 there are represented the two laser beams with bisectors orthogonal to the wall

(the reason for such condition will be explained in the next paragraph); they focus on the P point crossing the air, wall and fluid.

We can define the following parameters:

ϑ = angle formed by the two beams in the air;

α = angle formed by the two beams in the wall;

ϑ'= angle formed by the two beams in the fluid;

d_r = distance between the two beams at the exit from the lens;

d_1= distance of the wall external surface from the lens;

s = thickness of the wall;

d_3 = distance of the measurement point from the wall internal surface.

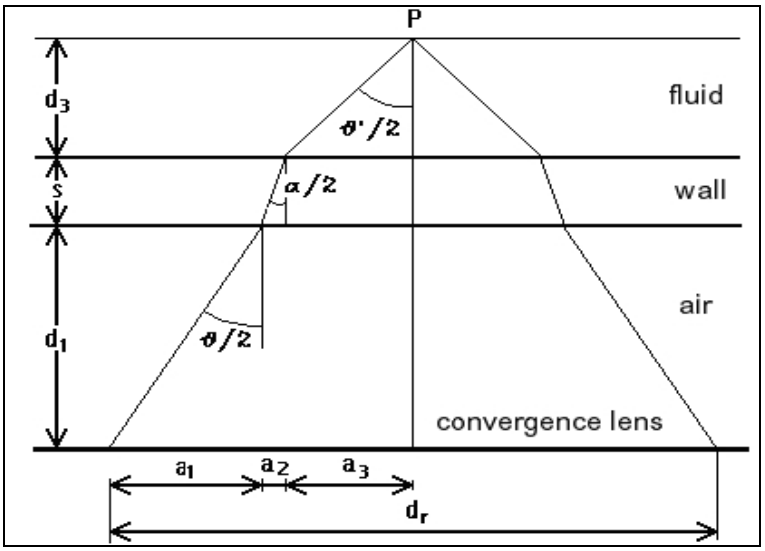

Fig. 3.4 - Scheme of the direction of the laser beam

We obtain:

$$d_1 = \frac{\frac{d_r}{2} - s \cdot tg\left(\frac{\alpha}{2}\right) - d_3 \cdot tg\left(\frac{\vartheta}{2}\right)}{tg\left(\frac{\vartheta}{2}\right)} \qquad (3.25)$$

This expression gives the distance d_1 of the wall external surface from the lens; it is necessary to place the lens at that distance in order to obtain a defined position of the measurement point.

The d_1 magnitude is in terms of the distance between the beams at the exit from the lens (d_r) and their angle of incidence in the air (ϑ), which are parameters characteristic of optical system.

Besides, the d_1 magnitude depends on the thickness *s* of the wall and on the angles ϑ and

α that are function of the indexes of reflection in the relative means (fluid and wall).

Some of these parameters might not be known, then it is possible to modify the d_1 like that, let's write:

(3.26) $$A=\frac{\frac{d_r}{2}-s\cdot tg\left(\frac{\alpha}{2}\right)}{tg\left(\frac{\vartheta}{2}\right)} \quad \text{and} \quad B=\frac{tg\left(\frac{\vartheta'}{2}\right)}{tg\left(\frac{\vartheta}{2}\right)}$$

therefore expression (3.25) becomes:

(3.27) $$d_1=A-Bd_3$$

This is the equation of a line, in order to be able to identify it, it is enough to know two points belonging to it.

If we consider a liquid current flowing in a channel with vertical walls, we can carry out two experimental tests; from which we note down (manually) two measures of d_1, one by fixing the measurement volume on the first wall internal surface (d_3=0), the other one by fixing the measurement volume on the second wall internal surface (d_3=D, internal width of the canal).

We obtain the points:

P_1: d_3=0, d_1(0)

P_2: d_3=D, d_1(D)

These points allow to draw a segment belonging to the line identified by the equation (3.27).

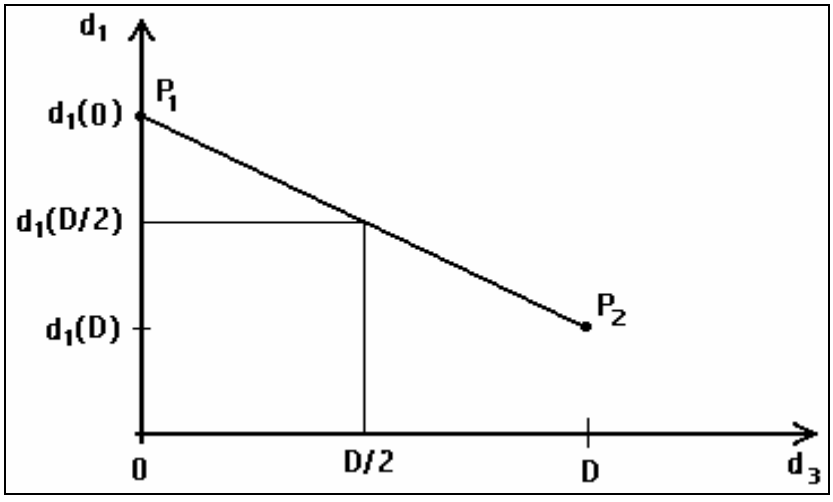

Fig. 3.5 - Practical determination

Very often, the measures to be performed are the ones concerning measurement volumes equidistant from the walls (afterwards we will use the expression median longitudinal section of the current); therefore, in our case a $d_3=D/2$; to know $d_1(D/2)$ it is enough to calculate the arithmetic mean of the values $d_1(0)$ and $d_1(D)$ already obtained:

$$d_1\left(\frac{D}{2}\right)=\frac{d_1(0)+d_1(D)}{2} \tag{3.28}$$

3.7 Observations about the calibration factor

We noted that the velocity we have to measure is proportional to the Doppler frequency through the Beta constant, called calibration factor and given by:

$$\beta=\frac{\lambda}{2\,\mathrm{sen}\left(\frac{\vartheta}{2}\right)} \qquad \text{Calibration factor}$$

On passing from one means to another, the wavelength of a bright beam changes, as well as the angle of incidence. It would be necessary, then, to consider how λ and ϑ change.

However, it is proved that, in case the bisector ϑ is orthogonal to the wall that separates it from the fluid, the value of β remains unchanged.

According to Snell's law, we have (referring to Fig.3.4):

$$\frac{\mathrm{sen}\left(\frac{\vartheta}{2}\right)}{\mathrm{sen}\left(\frac{\vartheta'}{2}\right)}=\frac{\lambda}{\lambda'} \tag{3.29}$$

Multiplying both members by $2\mathrm{sen}\left(\frac{\vartheta'}{2}\right)\Big/2\mathrm{sen}\left(\frac{\vartheta}{2}\right)$ we obtain:

$$1=\frac{\frac{\lambda}{2\mathrm{sen}\left(\frac{\vartheta}{2}\right)}}{\frac{\lambda'}{2\mathrm{sen}\left(\frac{\vartheta'}{2}\right)}}=\frac{\beta}{\beta'}$$

that is β=constant, quod erat demonstrandum.

3.8 Back-scattering and forward-scattering

While the type of signal registered is independent of the photodetector position as to the measurement point, on the contrary, the signal intensity changes according to its position sensibly.

A particle that generally has irregular surface and form, on crossing the interference fringes, causes a series of phenomena of reflection and refraction of the incident light, radiating it in all directions.

Such a process can be defined as ”diffusion” or “scattering”.

The spatial distribution of the light intensity spread by a spherical particle shows a rather complex trend, characterized by a maximum in the direction of the propagation of the incident light, and a minimum in the opposite one.

Then, the process of “forward-scattering” takes place when the photodetector is set so that it can intercept the scattering light forward, the process of “back-scattering” takes place when the photodetector is set so that it can intercept the scattering light backward. In the first case, it is possible to use a lower power laser; but, when it is physically impossible to set the photodetector beyond the measurement point, it is necessary to use the back-scattering, which makes it useless to carry out the pointing of the photodetector again, whenever the measurement point is changed, (since the photodetector is integral with the laser).

In fact, as it is pointed out in fig. 3.6, the light signal starts from the P point, is incident on the semi-transparent glass at 45° (this too is integral with the optical system) and arrives at the photodetector, which always remains focused on the measurement volume.

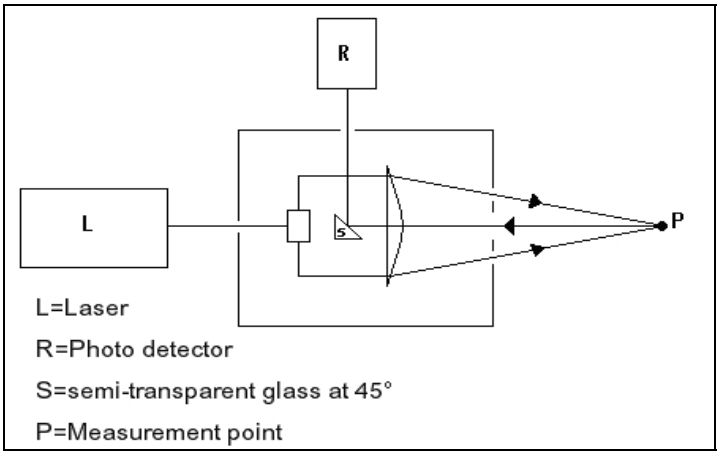

Fig. 3.6 - Scheme of a back-scattering

3.9 The photodetector

The photodetector generates a correspondence between the light signal, at Doppler frequency, and a tension variable according to the same law: as a consequence, a light signal

is converted into an electric one.

It must be pointed out that the photocurrent generated contains a fictitious particle, due to a random emission of electrons; this fact causes a background noise that, owing to the random characteristics of the phenomenon generating it, can be found in a wide field of frequencies, including the Doppler frequency. Therefore, the noise cannot be eliminated by means of filters, since it is near the Doppler frequency.

3.10 The frequency Shifter

The signal coming from the photomultiplier cannot be defined yet univocally for two reasons:

- ambiguity about the ν_x sign;
- presence of an interference signal which is called pedestal signal.

As regards the first problem,. the Doppler frequency ν_x/β has always a positive value (owing to the frequency definition) apart from the ν_x sign; this causes the above ambiguity.

It is clear how this fact can create a lot of difficulties should the direction of the flow change in time (wave-motions) or in space (circular motions).

As regards the second problem, the pedestal signal frequency is the inverse of the crossing time of the whole measurement volume, while the Doppler signal frequency is the inverse of the crossing time of a single interference fringe. Thus, the pedestal signal has usually a lower frequency than the Doppler signal.

Evidently, the signal arriving at the photodetector is the sum of two contribution, the Doppler one, and the pedestal one.

Let's assume to have ten interference fringes inside our measurement volume, and let's assume that the particles taken into consideration have a velocity $V=\overline{V}\pm\Delta V$ along the X axis.

We can say that $V_{Max}=\overline{V}+\Delta V$ and $V_{Min}=\overline{V}-\Delta V$.

Since there is proportionality between velocity and frequency $\nu_x = \beta f$, we obtain the maximum Doppler frequency $f_{D,Max}$ from the first expression and the maximum pedestal frequency $f_{p,Max} = f_{D,Max}/10$ from the second one similarly.

Besides, it is possible to identify respectively the Doppler frequency and the pedestal one calculate at $\overline{V}$ by the symbols $\overline{f}_D$ and $\overline{f}_p = \overline{f}_D/10$.

The difference $f_{D,Min} - f_{p,Max}$ depends on ΔV; it is possible to define a limit value for

ΔV such as the pedestal signal does not influence the field of Doppler frequencies, therefore it can be easily filtered:

$$\Delta V_{\lim} = \overline{f}_D - \overline{f}_p = \overline{f}_D - \frac{1}{10}\overline{f}_D = \frac{9}{10}\overline{f}_D \quad (3.30)$$

On the contrary, if $\Delta V \geq \Delta V_{\lim}$, the pedestal signal gets into the field of Doppler variable signal and it cannot be filtered, because a meaningful part of the same signal would be lost.

It is possible to solve the problem, as well as the problem about the ambiguity of the velocity sign, with the use of the frequency shifter.

The frequency shifter consists of an optical shift, that can be found inside the same laser, and by an electronic shift.

The optical shift is necessary to obtain a Doppler signal also when the flow velocity is null.

It is used to let one of the two beams pass through an optical device, called Bragg's cell, which increases its frequency by a f_B=40MHz value. This fact involves that the interference fringes will not be stable in the measurement volume, because the frequency of the two beams is different, but the fringes will move with βf_B velocity in the direction of the X axis supposed to be negative (according to which beam has increased its frequency).

A particle moving in the measurement volume with ν_x velocity in the positive direction of the X axis gives a frequency signal:

$$f_B + \frac{\nu_x}{\beta} \quad (3.31)$$

At this point it is necessary to process this frequency sending it to a mixer that arranges for removing the f_B from it and for mixing another f_s frequency supplied by a further shift, which is electronic this time.

The frequency coming out will be:

$$f_u = \left| \left(f_B + \frac{\nu_x}{\beta} \right) - \left(f_B + f_S \right) \right| = \left| \frac{\nu_x}{\beta} - f_S \right| \quad (3.32)$$

which is always positive by frequency definition.

The f_s can be easily changed and we can both remove and add it; the only condition that f_s must satisfy is that its absolute value must be greater than the value of ν_x / β:

$$|f_s| > \left| \frac{\nu_x}{\beta} \right| \quad (3.33)$$

In this situation, the frequency coming out $\nu_x/\beta - f_s$ turns out to be always of the same sign (the sign opposite to the chosen one for f_s) ant there cannot be any interpretation ambiguity.

Besides, in any case, the frequency coming out proves to be increased as to the pure Doppler frequency, (being $|f_S|$ sufficiently raised), so allowing the separation of the pedestal frequency from the Doppler one easily.

The (3.32) can be divided like that:

- if $f_s<0$:

$$f_u = \frac{\nu_x}{\beta} - f_S \qquad \frac{\nu_x}{\beta} - f_S > 0 \quad \text{from which} \quad \frac{\nu_x}{\beta} = f_u + f_S$$

or more synthetically $\frac{\nu_x}{\beta} = f_u - |f_s|$

- if $f_s>0$:

$$f_u = f_S - \frac{\nu_x}{\beta} \qquad \frac{\nu_x}{\beta} - f_S < 0 \quad \text{from which} \quad \frac{\nu_x}{\beta} = f_S - f_u$$

or more synthetically $\frac{\nu_x}{\beta} = -f_u + |f_s|$.

3.11 The frequency Tracker

The Doppler frequency obtained is conveyed to another instrument, called “frequency tracker”. This instrument supplies a tension proportional to the Doppler frequency at the exit; besides, it can give the medium value of the velocities obtained directly on a digital display, (it is possible to choose the time through a control), after inserting the calibration factor β a priori.

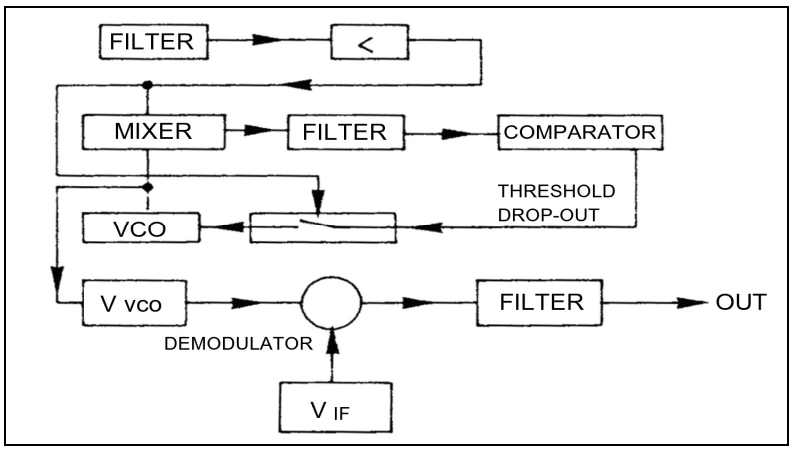

Fig. 3.7 - Operating scheme of the tracker

In the previous block diagram is shown the operating principle of the tracker. The entry signal f_{in} is filtered so as to remove a part of the noise, as well as the pedestal frequency.

After being filtered and simplified, this signal is sent to a mixer that combines it with another signal coming from the VCO (Voltage Controlled Oscillator), that supplies a tension with a certain frequency f_{VCO}; therefore, the mixer receives two tensions changeable according to time with sinusoidal law, and, putting them together, ($f_0 = f_{VCO} - f_{in}$) sends them to another filter, called IF (Intermediate Frequency), which is a narrow band filter, centred around an f_{IF} frequency, fixed a priori.

In particular, the VCO looks for a frequency value f_{VCO} that might guarantee that the f_0 may be able to pass through the IF.

Therefore, the f_0 is sent to a comparator to compare it with the f_{IF}; if f_0 turns out to be equal to f_{IF}, we say that "the tracker hooked on" and the f_D is equal to $f_{VCO} - f_{IF}$.

On the contrary, if $f_0 \neq f_{IF}$, this is not possible, and then a tension V_c is emitted from the comparator; it is called feedback, because it is sent to the VCO which changes its own frequency according to its own value and the sign of V_c, till f_0 is equal to f_{IF}: we say that the VCO "has chased and reached" the $f_D + f_{IF}$ frequency.

Now, two frequency modulators supply two exit tensions proportional, respectively, to f_{VCO} and f_{IF} which are sent to a subtracting circuit which supplies an exit tension proportional to f_D:

$$\Delta V_u = K f_D$$

and, therefore, the velocity is given by:

$$v_x = \frac{\lambda}{2K\,\mathrm{sen}\left(\frac{\vartheta}{2}\right)} \Delta V_u$$

In this process, downstream the comparator, there is a drop-out circuit that interrupts the processing of the signal in the following cases:

- when the signal intensity at the exit of the amplifier does not exceed a certain threshold value; this happens if the amplifier is not well regulated;
- when there are some few particles in the measurement volume, or they do not have suitable sizes: in that case, it is necessary to go on with an adequate insemination; (it has been carried on with lime during this experimentation);
- when the value of f_0 is too far from f_{IF}.

Then, in these cases, the tracker emits a constant signal equal to the last frequency hooked, until the instrument succeeds in “hooking again”; of course, this happens when the above conditions are lacking.

4. BOUNDARY LAYER: DESCRIPTION OF THE EXPERIMENTAL CHANNEL

4.1 Experimental plant

For the carrying out of the experimental researches concerning a boundary layer stream flowing on a rigid submerged vegetated bed the used experimental plant is shown in the following figures.

Fig. 4.1 - Overall view of the plant

Fig. 4.2 - LDA during the acquisition

Fig. 4.3 - Acquisition system

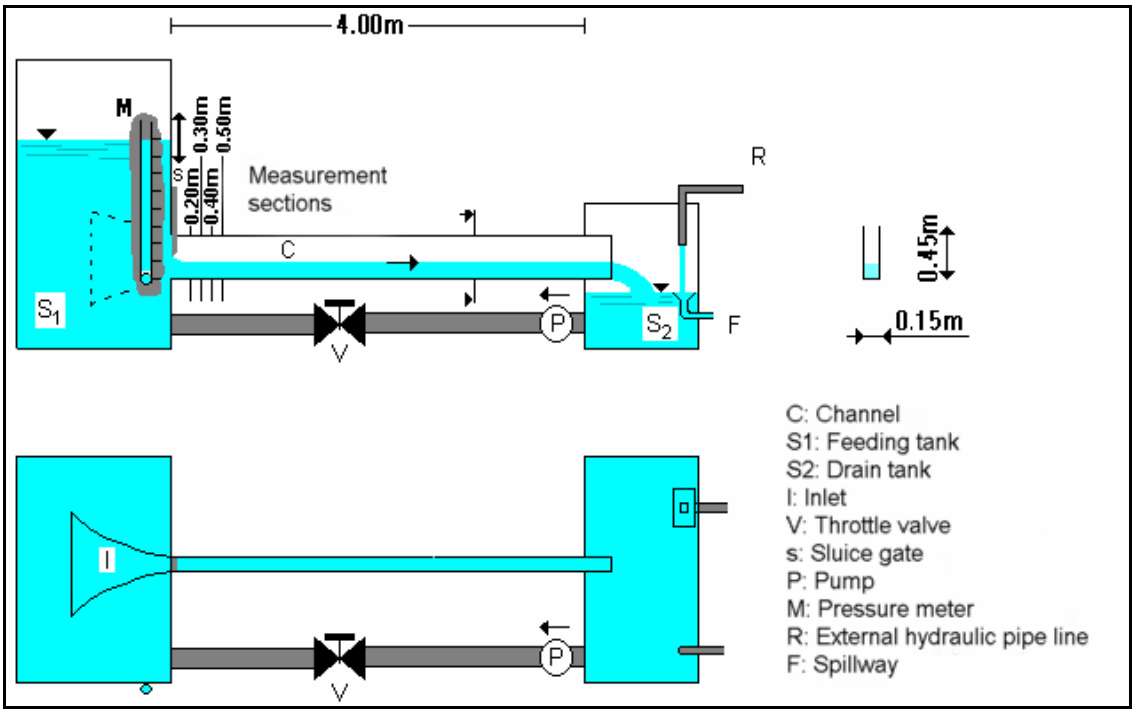

Fig. 4.4 - Geometry of the experimental plant

The main device of the experimental plant is a channel 4 metres long and 15 cm. wide with variable slope, plexiglas walls and bottom, with a feeding tank supplied by a circulation pump, which takes water from the drain tank downstream. The feeding tank feeds the channel through a rectangular adjustable sluice gate. A plexiglas inlet, well shaped and moulded directs the flow towards the sluice gate.

In this plant, it is possible to measure the flow depth in the tank, the height of the sluice gate, the channel slope, as well as the flow depth in all the cross-sections of the channel itself.

Fig. 4.5 - Moulded inlet

In the first sections of this channel, a boundary layer stream is generated on the bottom.

The boundary layer rises in the subsequent sections until its thickness reaches the same value as the depth of the circulating flow, at a distance from the inlet of the channel depending on the dynamic characteristics of the flow itself.

In a theoretic boundary layer, the thickness of the external stream should be very high (in theory endlessly high) and the stream should be very large (in theory endlessly large): as a consequence, the flow in the channel might not be considered as a real boundary layer.

This method of creating a boundary layer stream has often been used. In previous papers issued, the following concept has been strengthen, that is, the distributions of the main statistical turbulence quantities developing in the water, were in agreement with the corresponding ones described in literature, with reference to boundary limit streams developing in the air.

In any case, in a recent paper, it was definitely proved, through systematic experimental studies, that this stream can be really considered a boundary layer one.

The measures of instantaneous velocity have been carried out through the LDA technique.

It was used a compact new generation LDA system.

The laser beam has a frequency out of the field of the visible (invisible beam): for this reason, it was decided to use an infrared camera, by which it was possible to monitor, at any moment, the position of the measurement point effectively.

The optical system works in backscattering, with Bragg cell and frequency shifter.

The sampling system consists in frequency tracker that processes also the data mean value (with an average of the times that can be chosen freely), so as to obtain, in real time, the mean

value of the local mean velocity in every measurement point.

Each value of the local mean velocity was obtained through a mean time of 200 s, which was considered sufficient to reduce the main fluctuations of the turbulent velocity to the minimum.

4.2 Vegetation modelling

The experimental tests were carried out with the superimposition of a suitable plate on the bed channel. The plate was 1.20 m long, 15 cm large and 1 cm thick. The first 20 cm of the plate length were placed before the channel inlet, and were conveniently moulded.

Particularly, the first 10 cm were rounded off from 0 to 1 cm, in order to let the water get in the channel without any trouble, even if there was the plate.

Therefore, the plate extends along 1 m starting from the channel inlet.

This length is sufficient to get the boundary layer to develop as far as the section where its thickness reaches the flow depth.

After the plate, the stream meets a 1cm step and it becomes irregular; this fact does not influence the upstream current, since it is a fast current.

Seven types of removable flat plates were prepared so as to simulate different types of vegetated bottoms.

The first plate was perfectly smooth, so as to be able to reproduce a classic boundary layer.

The vegetation was modelled by small brass cylinders with a 4 mm diameter, on the other six plates.

Particularly, the second, third and fourth plates were made rough by means of cylinders of different height (h_1 = 5mm, h_2 =10mm, and h_3 =15 mm) arranged according to the scheme shown in fig.4.6.

Along the flow direction, the rows of the cylinders are 5 cm far from one another; along the orthogonal flow direction, the rows of the cylinders are 2.5 cm far from one another and are 1.25 cm far from the side walls.

The first row was placed at 2.5 cm from the inlet of the channel (section of the sluice gate).

The meshes formed by the cylinders are rectangular, of 5x2.5 cm^2 (single density, or type "A").

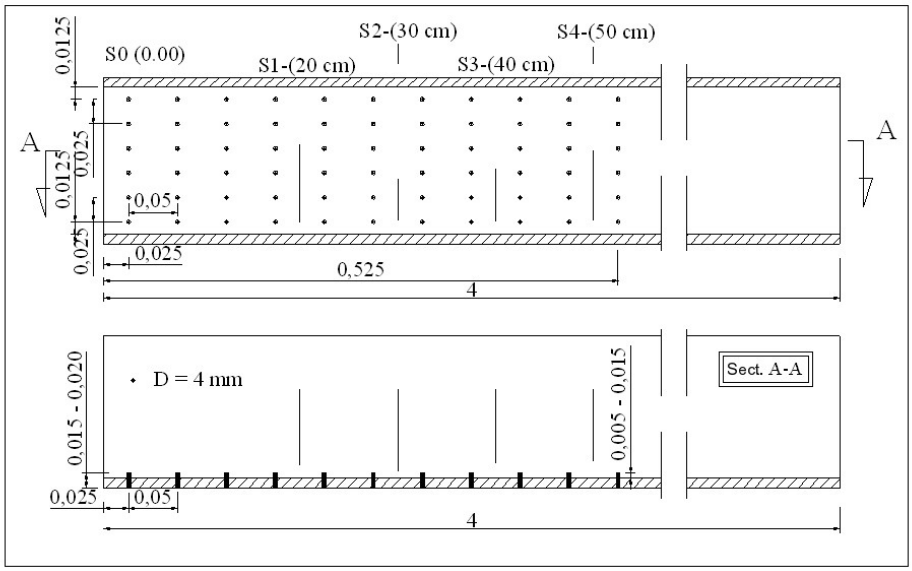

Fig. 4.6 - Geometry of the sheet with cylinders 5.10 or 15 mm high with single density (Type "A")

The fifth, sixth and seventh plates were made rough by cylinders of different height (respectively h_1 = 5mm, h_2 = 10mm and h_3 = 15 mm), arranged according to the scheme shown in Fig.4.7.

Along the flow direction, the rows of the cylinders are 2.5 cm far from one another; along the orthogonal flow direction, the rows of the cylinders are 2.5 cm far from one another and 1.25 far from the side walls.

The fist row was placed at 1.25 cm from the inlet of the channel (section of the sluice gate).

The meshes formed by the cylinders are, therefore, square of 2.5x2.5 cm^2 (double density or Type "B"). In fig.4.8 a view of the cylinders 15 mm high double density is given as example.

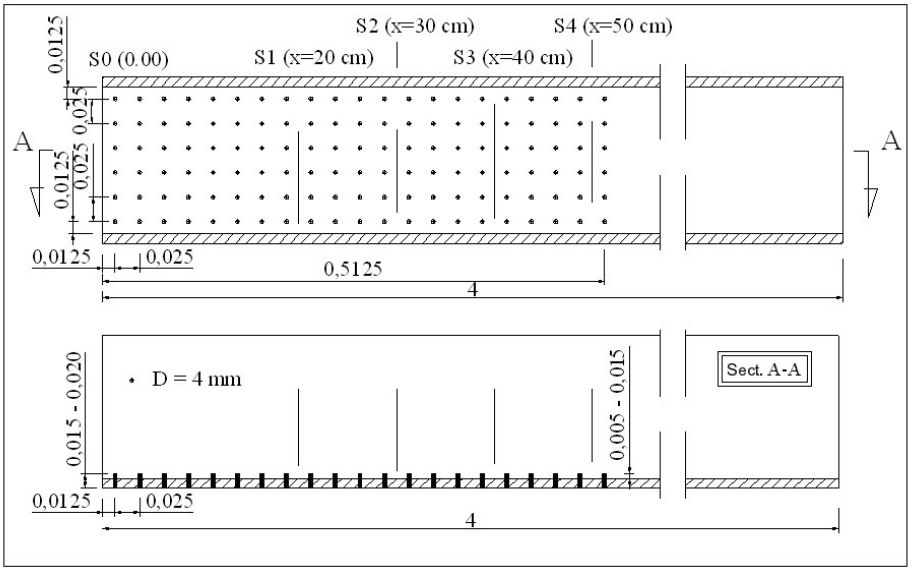

Fig. 4.7 - Geometry of the sheet with cylinders 5, 10 or 15 mm high with double density (Type "B")

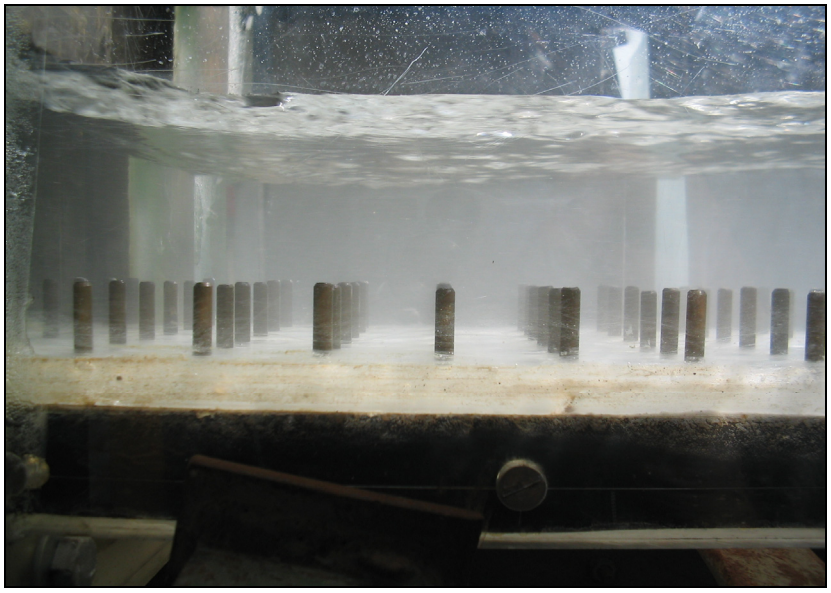

Fig. 4.8 - View of cylinders 15 mm high with double density (Type "B") at the inlet of the channel

This way, the whole arrangement of the cylinders was symmetrical, the central line of the bed channel was free (there were no cylinders) and it was possible to measure the velocity distribution along this vertical line (from the bottom to the free surface).

Particularly, four test sections were chosen measuring 20 cm, 30 cm, 40 cm and 50 cm respectively from the section of the channel inlet.

These test sections were placed between two rows of cylinders, so that the vertical line occurred, in any case, exactly at the centre of each rectangular or square mesh.

5. BUILDING OF THE NEW EXPERIMENTAL CHANNEL

5.1 Introduction

The study of the interactions between vegetated bottoms and uniform water currrents implies the basic building of a new hydraulic experimental plant, starting from the planning of the channel, followed by its building, by the calibration of the orifice placed on the water pipe feeding the channel, by the definition of the hydraulic arrangements, and, finally, by the calibration of the anemometer laser-doppler, frequency shifter and frequency tracker system, to measure the instantaneous velocity of the flow.

The channel, whose characteristics will be described afterwards, is fed by a discharge tank connected to the hydraulic network of the Laboratory of the Department of Hydraulic, Geotechnical and Environment Engineering of the University of Naples Federico II.

At the exit of the channel, there is a tank from which the water flows through a system of free surface channels straight into the tanks of the Laboratory.

In particular, the water is taken (through a system of pumps with nominal capacity from 25 to 75 l/s) from one of the backwater tanks of the laboratory, and is sent to a feeding tank, whose overflow fixes the hydraulic load on the experimental plants fed by the tank itself.

The water flows from this tank towards a pipe which ramifies in three pipes with diameters of 100, 200 and 300 mm respectively, (each of them having an orifice for the measurement of the flow rate); the three pipes feed the plants through subsequent pipes.

In particular, the pipe feeding the loading tank of the channel has a diameter of 150 mm, and it is connected to the 200 mm pipe on which the orifice is placed.

The building and setting of this new hydraulic plant inside the Laboratory were suitably weighed up, so that they might be consistent with the plants already existing.

Hereafter there is a layout showing the position of the channel in the Laboratory.

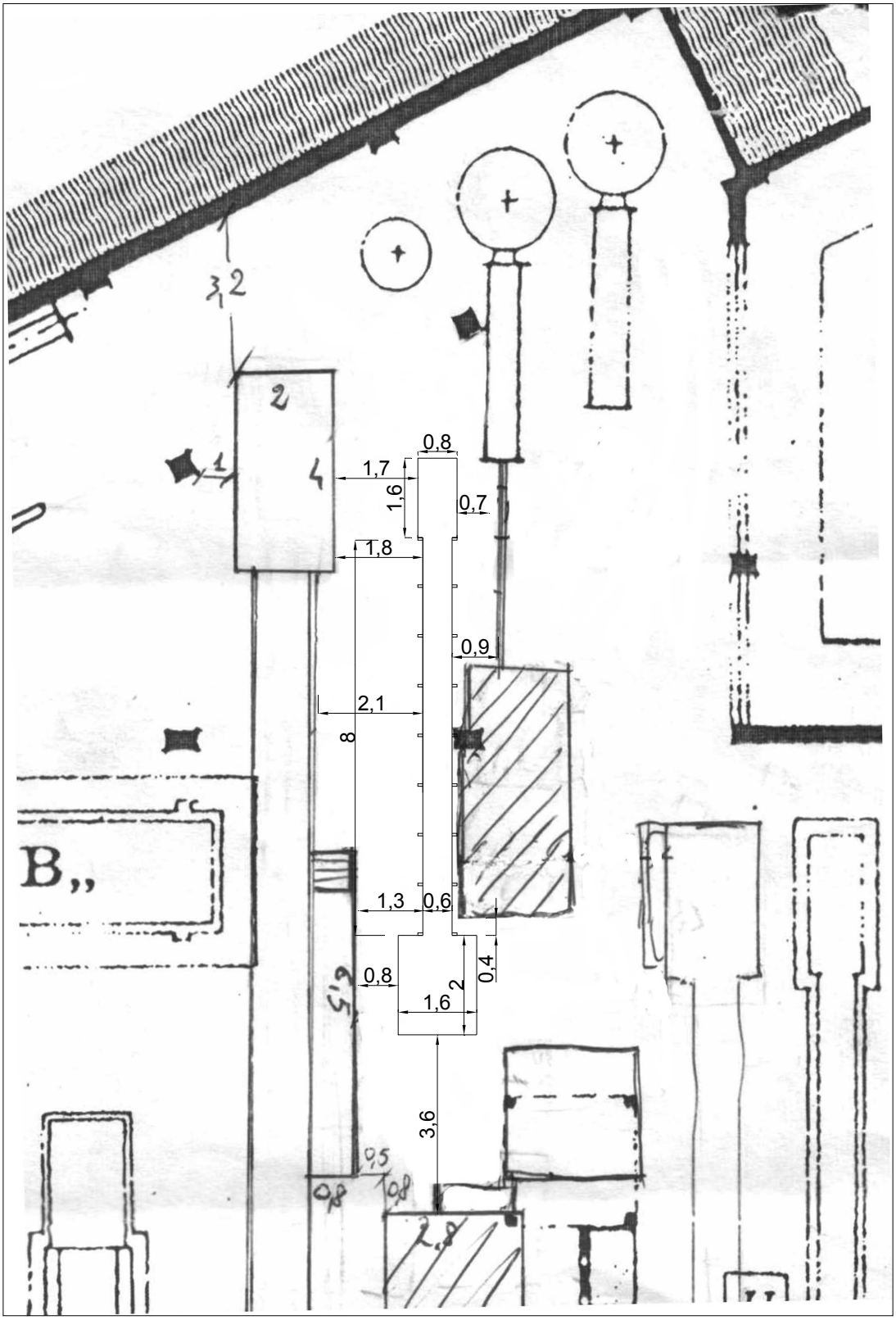

Fig. 5.1 - Position of the channel in the laboratory

Fig. 5.2 - A view of the channel: in the foreground the discharge tank, behind the feeding tank

5.2 Realization of the channel

The channel has plexiglas walls and bottom, is 40 cm large, 8 m long and its walls are 40 cm high.

Fig. 5.3 - Plexiglas channel

Originally, the channel should have been horizontal; therefore it had been placed on a grid made with Innocenti tubes (the name is derived from their inventor Ferdinando Innocenti).

As a consequence, the connection between the channel and the feeding tank was rigid, because it was made by bolted iron flanges, as it is shown in the following figures.

Fig. 5.4 - Rigid fixing by bolted flanges

Fig. 5.5 - Fixing system (inside view)

5.3 Adjustment of the channel to make it reclining

Afterwards, in order to obtain a greater flexibility of the plant, it was decided to make the channel reclining, so as to be able to realize numberless working conditions (both in uniform and permanent flow), regulating its slope at the right moment.

Therefore, it was necessary:

- to modify the channel rigid connection to the feeding tank;
- to build a terminal support for the channel;
- to foresee a new support for the channel along its whole length.

The channel was set on two steel girders hinged to support placed at the entrance of the channel itself.

The terminal support of the channel was realized through a mechanical sliding female screw jack, by manual activation, with 1/28 reduction ratio, which allows to fix at will the channel slopes within the 3% of maximum slope.

Practically, the channel rigid support was replaced with hinged girders upstream, and set on the jack downstream.

The rigid connection between the channel and the feeding tank was replaced with a flexible rubber gasket that guarantees wet seal.

First of all, a preliminary research was carried out in order to choose the most suitable type of rubber and its fittest thickness. This research was necessary to realize how much the rubber might lengthen in order to have the channel maximum slope foreseen, as to 3%.

The limit of slope is due, on the one hand, to the mechanical tensile strength, on the other hand also to the layout of the draining tank which does not allow a greater slope of the channel.

Fig. 5.6 - Mechanical jack

Fig. 5.7 - Rubber gasket

Fig. 5.8 - Upstream support

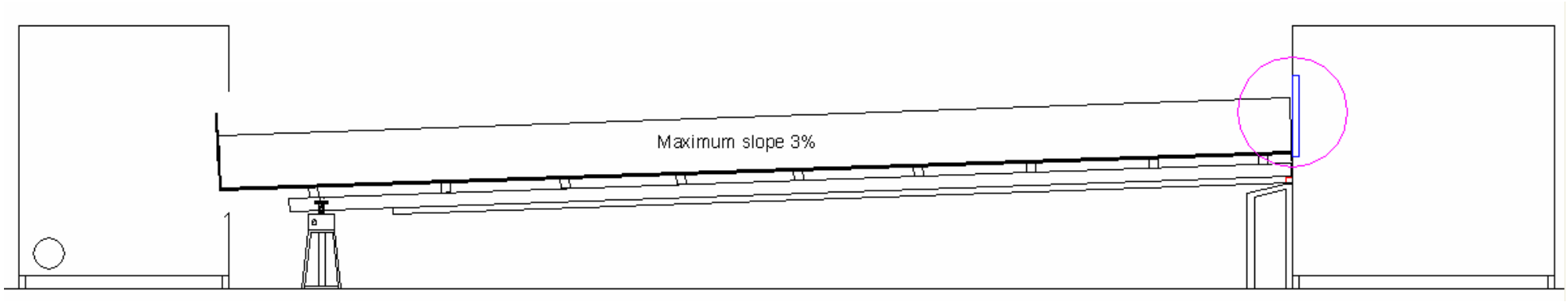

Fig. 5.9 - Channel changeable slope

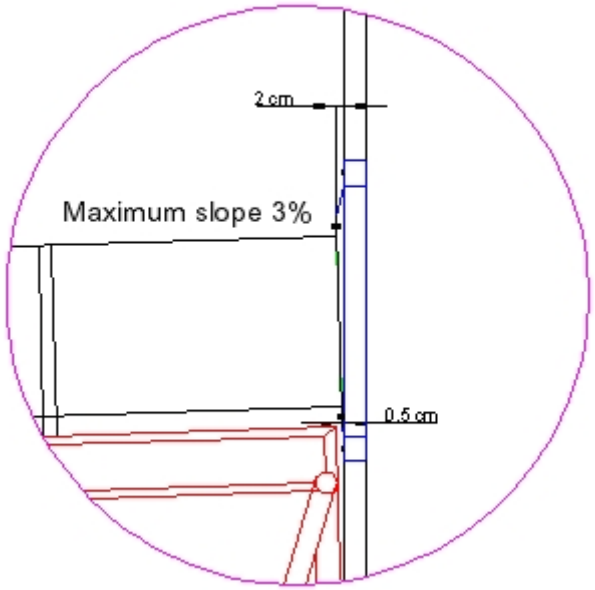

Fig. 5.10 - A detail of the reclining channel

When the channel is completely filled with water and in use, it was necessary to foresee also an intermediate support of the channel, in order to avoid the breaking of the channel made of plexiglas (in fact, the plexiglas has a reduced flexibility, also in relation to thickness that is about 1 cm), owing to the remarkable bending direction generated.

Fig. 5.11 - Central support

5.4 Static calculation of the steel girders

The check on the girders was carried out by taking into consideration a beam only rested and evaluating its maximum inflection

Fig. 5.12 - Girders

In order to limit the bending to a few mm when the functioning is very heavy, that is when the channel is filled with water, it was necessary to realize a beam on three supports.

Of course, it occurred also the inflection when the channel was empty. Since it was consistent with the flexibility of the plexiglas, the procedures of the channel slope control

were made easier, allowing to remove temporarily the central support during this phase. So it was possible to operate only on the downstream jack for the necessary control.

5.5 Realization of a shaped draft

The first surveys about the flow within the channel brought out that it was necessary to realize both a well shaped draft inside the feeding tank (Fig. 5.13 and Fig. 5.14) in order to limit very clear troubles, and a floodgate at the outlet (Fig. 5.15), so as to make the plant more flexible from the point of view of the hydraulic layout that might be realized.

In particular, the equation used for the planning of the draft to be placed inside the feeding tank is the equation of a parabola.

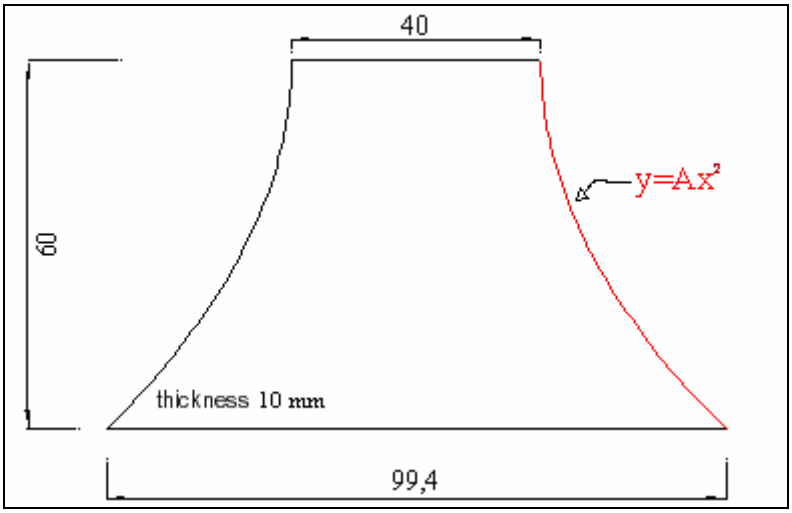

Fig. 5.13 - Shape of the plexiglas plate to be made at the inlet

Fig. 5.14 - Shaped draft

Fig. 5.15 - Downstream outlet

5.6 Improvement of the discharge

Two pipes were planned in the discharge tank for its emptying, because the preliminary tests had pointed out that the channel maximum flow could not be discharged easily with only one pipe.

Before this change, it was possible to discharge a flow rate of about 30l/s; after this change, on the contrary, it was possible to discharge a flow rate of about 60l/s, that is the maximum channel flow rate.

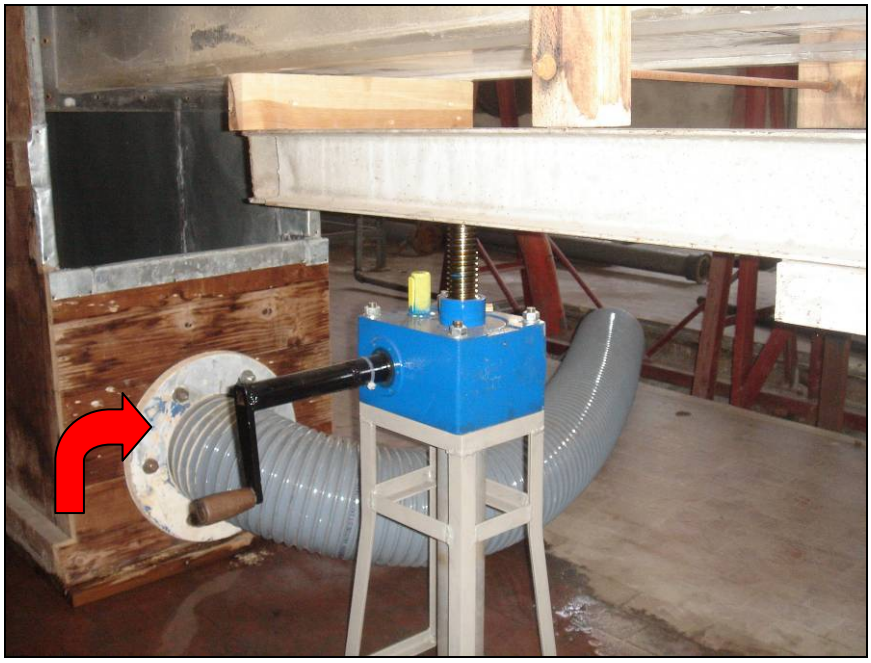

Fig. 5.16 - Bottom discharge added

The two following figures show the complete channel from two different angles.

Fig. 5.17 - View of the channel (1)

Fig. 5.18 - View of the channel (2)

6. ORIFICE CALIBRATION

6.1 Volumetric method

In this chapter it is described the method used to calibrate the orifice set on the feeding pipe of the tank. The channel feeding tank is fed by a pipe with nominal diameter of 150mm; in its turn, this pipe is connected to the main feeding system of the Laboratory, through a pipe with a nominal diameter of 200mm.

The orifice is set on this last pipe, connected to an air-water differential manometer, in order to measure the channel flow rate.

From the point of view of a complete setting up of the experimental plant, it was opportune to calibrate the orifice through a classical method, that is the volumetric one, that is always valid and, perhaps it is one of the most reliable.

This method relates to the definition itself of the flow rate expressed as a ratio between the volume drained and the time spent for its outflow.

Since it was impossible to make changes on the pipe on which the orifice was set, after the channel had been made and already functioning, it was decided to use the channel feeding tank itself as a volume to be filled.

Thus, the feeding tank was analysed thoroughly and the procedure was carried on like that.

The channel inlet was sealed with a floodgate, in order to increase the volume of the tank to be filled.

It was considered a part of the total volume between two heights at 57cm and 97cm, from the bottom of the tank.

The value of the first height was defined owing to the anomaly found during the filling of the feeding tank at the lower heights, of about 40cm. Such an anomaly was due to the shape of the feeding pipe of the tank. In fact, the end of the pipe has some rows of holes for a length of about 25cm. Their function was to regulate the feeding of the tank; but they caused big concentrated head losses, changeable according to their working condition (partially or totally submerged). This circumstance invalidated actually reading of the air-water differential manometer connected to the orifice. This problem occurred as far as the height of 40cm; therefore, the choice of the height of 57cm guaranteed the complete absence of this effect.

The value of the second height was defined owing to the necessity to obtain a measurement volume great enough to allow longer filling times. Moreover it would have been difficult to perfectly seal the channel inlet beyond the height of 97cm of filling of the tank.

Fig. 6.1 shows the plan of the feeding tank; the elements whose volumes were added to or subtracted from the volume used to apply the volumetric method are highlighted with progressive numbers.

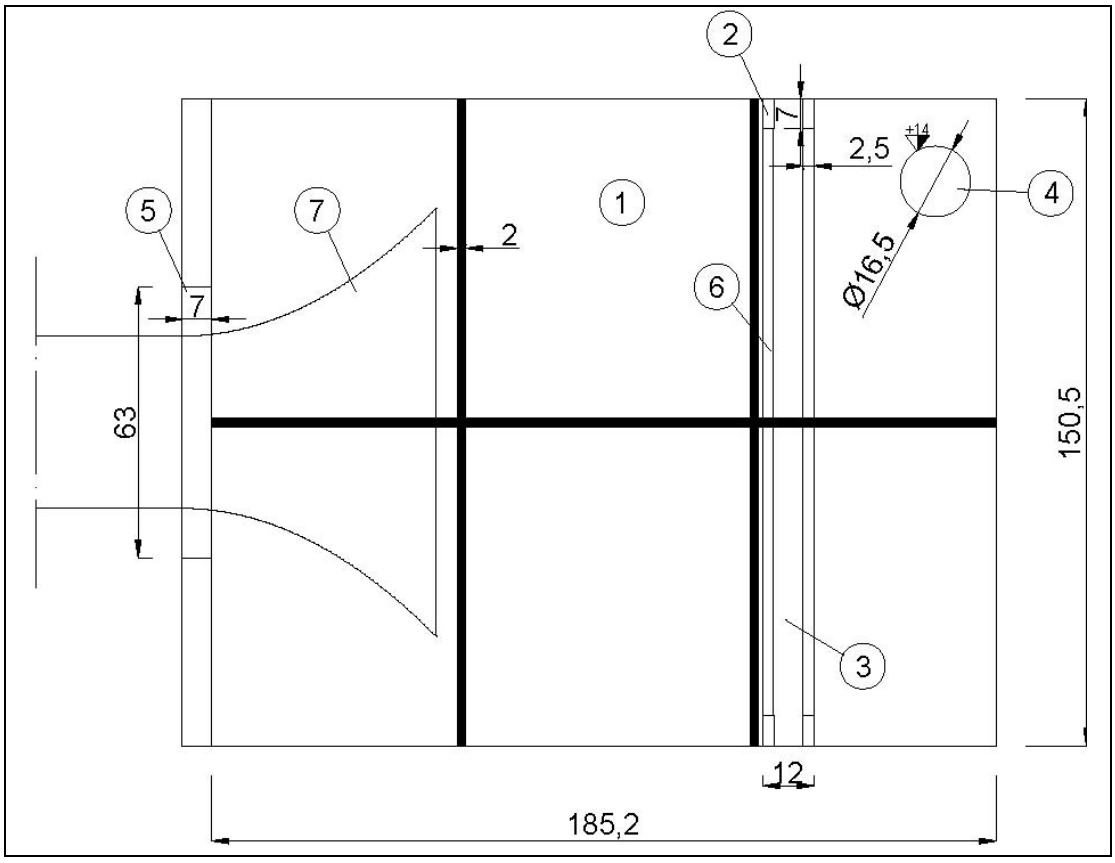

Fig. 6.1 - Plan of the upstream basin

Hereafter, it is cleared how the volume of each element of the tank was calculated, and then the total volume used for the volumetric method:

1. Gross area: 2.8 m^2
2. Area of the wooden splints of the base: 0.07 x 0.02 x 4 = 0.0056 m^2
3. Internal area of the base: 0.07 x 1.505 x 0.2 = 0.02107 m^2

   The factor 0.2 appearing before represents the percentage of area occupied by the elements of the base; such a value was inferred from a careful analysis of their geometry.
4. Area of the pipe: (3.14 x 0.1652) / 4 = 0.0214 m^2
5. Set off volume: 0.07 x 0.62 x 0.32 = 0.01141 m^3
6. Volume of the horizontal wooden splints : (0.025 x 1.365 x 0.07) x 2 = 0.00478 m^3
7. Volume of the channel shaped draft : 0.36 x 0.01 = 0.0036 m^3
8. Volume subtracted from le walls, the flange of the draft and the floodgate : 0.0009 + 0.00143 + 0.0022 = 0.0045 m^3

9. Net area among the heights 12.00 cm and 62.00 cm : 2.8 – 0.0056 – 0.02107 – 0.0214 = 2.75193 m^2
10. Total volume between the heights 57.00 cm and 97.00 cm : 2.75193 x 0.4 + 0.01141 – 0.0036 – 0.00478 – 0.0045 = 1.099 m^3.

6.2 Calibration curve

In order to obtain the best calibration of the orifice with the volumetric method, it was carried a series of measurements of the filling time of the above total volume, changing, from time to time, the opening of the sluice gate placed on the feeding pipe of the tank (that is to say, by changing the inlet flow rate) and reading the corresponding value of Δh on the air-water differential manometer connected to the orifice.

The following steps were:

1. the sluice gate of the pipe feeding the tank was opened and the tank was filled as far as the fist level, that is up to 57 cm;
2. as soon as the height was reached, the timer was activated to measure the time taken by the water to fill the volume as far as 97 cm high;
3. on the air-water differential manometer, the Δh, corresponding to a half of the filling fixed in advance, was read, in order to be able to take in account the head and flow variations that take place when the water level changes in the tank;
4. once the tank had been emptied (through an orifice located at the bottom of the tank), the sluice gate placed on the feeding pipe of the tank was opened again with a quantity every time different from the previous one, and the experimental procedure was repeated.

The results obtained are shown here below by a table as well as by graph and they point out the reliability of the measurements carried on and of the method used.

Table 6.1 - Calculation of the flow rate

Volumetric Method				
Volume [mc]	**Time [s]**	**Δh [cm]**	**√(Δh)**	**Q [l/s]**
1,099	358,53	0,30	0,548	3,065
	169,87	1,20	1,095	6,470
	112,16	2,70	1,643	9,799
	84,78	4,80	2,191	12,963
	68,75	7,70	2,775	15,985
	56,28	11,10	3,332	19,527
	49,56	14,40	3,795	22,175
	43,69	19,00	4,359	25,154
	39,59	22,60	4,754	27,760
	35,72	27,60	5,254	30,767
	33,37	32,00	5,657	32,934
	31,00	36,65	6,054	35,457
	29,37	41,00	6,403	37,419
	26,81	48,00	6,928	40,992
	25,44	53,30	7,301	43,200
	23,72	64,4	8,025	46,332
	22,28	74	8,602	49,327
	20,85	82,5	9,083	52,710
	20,28	86	9,274	54,191

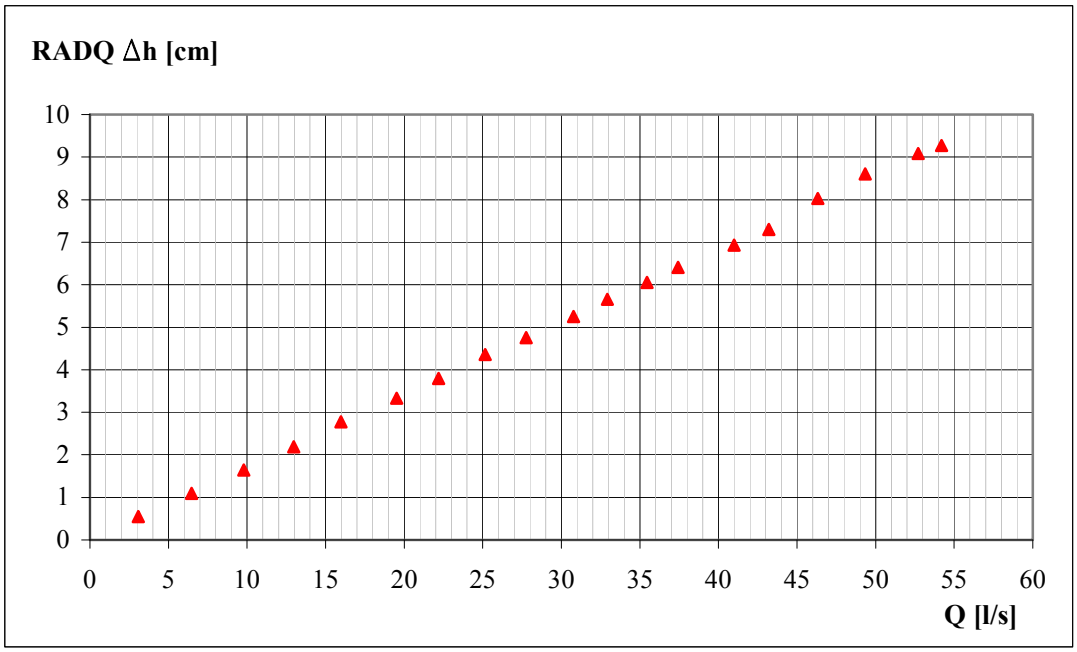

Fig. 6.2 - Representation of the data obtained through the volumetric method

As it is pointed out in the graph, the points seem to arrange themselves on a line, unless of natural losses in the high part, due, of course, to casual errors in the reading of the Δh (due to its fast fluctuations) and in the time measures (that are very short).

This loss is justified by the circumstance that the orifice is more sensitive to big flow rates than to the smaller ones, as it is clear in its calibration curve in Fig. 6.3.

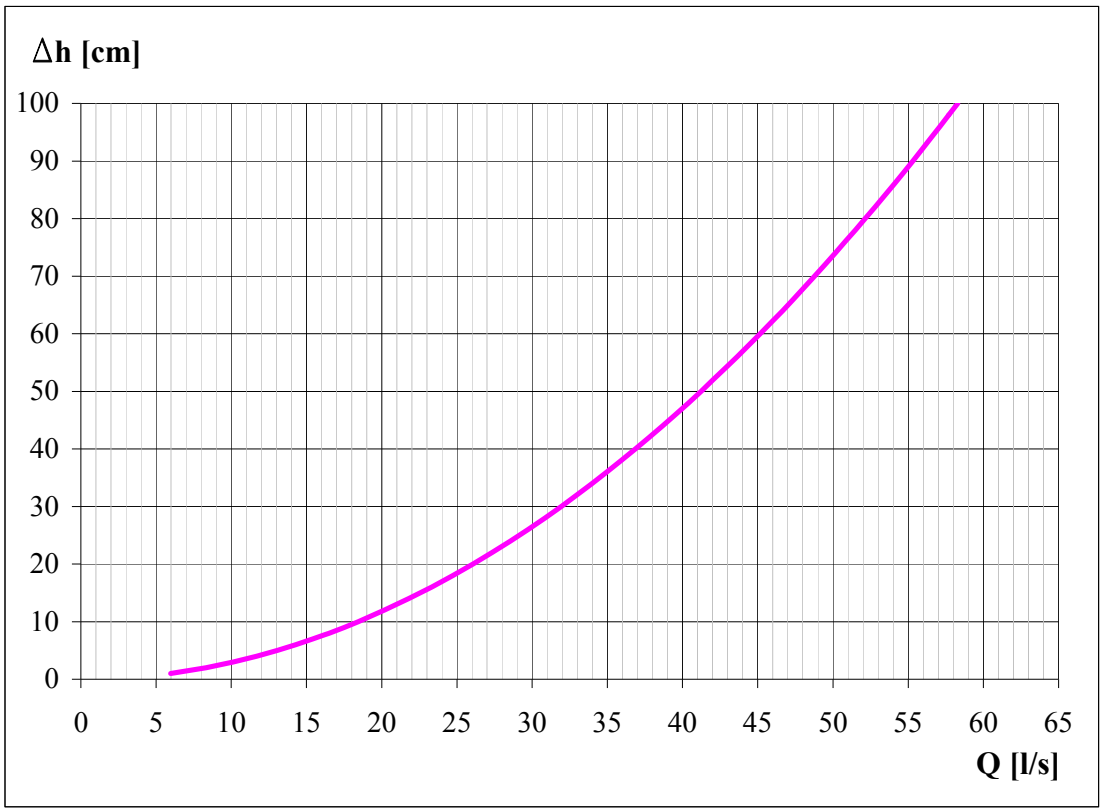

Fig.6.1 - Calibration curve

The experimental data concerning the orifice calibration are represented in a chart (first graph of Fig. 6.4) where in abscissa, in logarithmic scale, there are the Reynolds numbers relative to the different flow rates calculated through the volumetric method; in ordinate, the corresponding values of the ratio $Q/\sqrt{\Delta h}$.

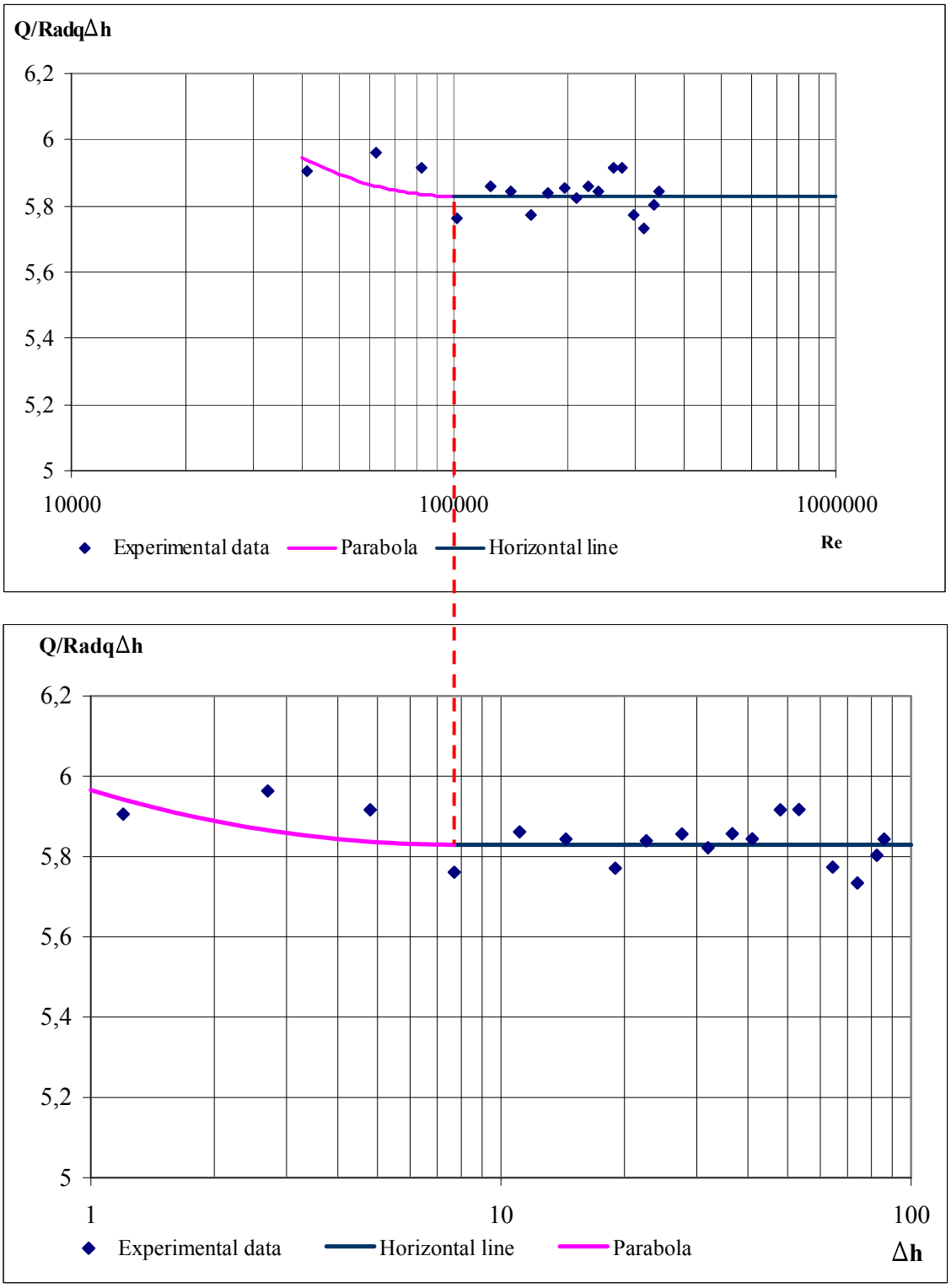

Fig. 6.4 - Theoretical-experimental curve

First of all, it is noticed that the trend of the experimental data is undoubtedly congruent with the one described in studies conducted on the orifices (Fig. 6.5); they point out that the C contraction coefficient is a function of Reynolds number Re and the ratio of throttling A_0/A_1.

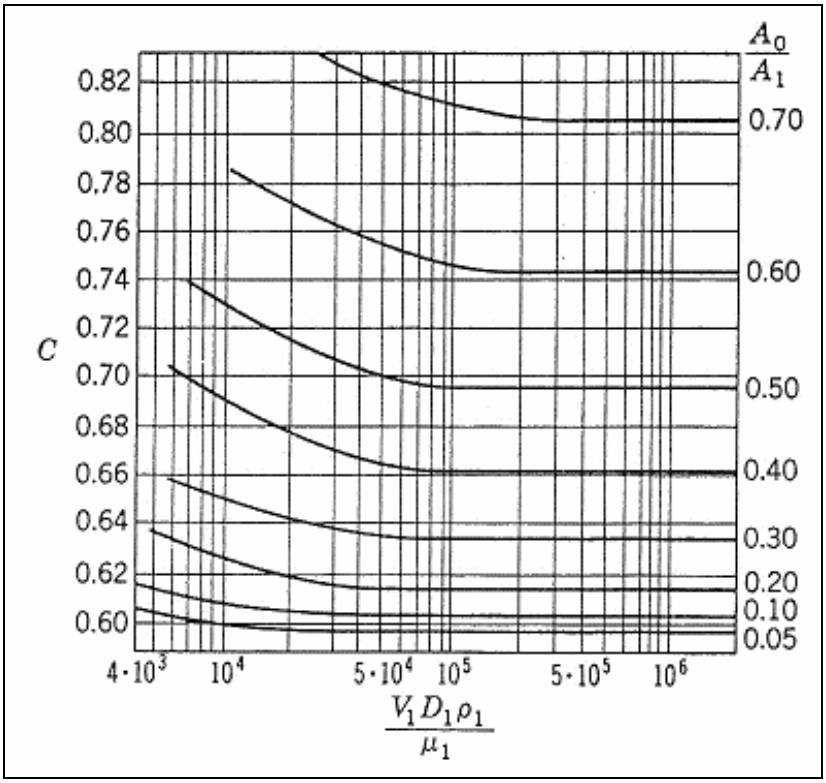

Fig. 6.2 - Curves representing some studies carried out on orifices

Furthermore, (first graph of Fig. 6.4) it is possible to assume that the trend of the experimental data characterized by values of the Reynolds number up to 100000, might be reproduced by a parabola; while the trend of the experimental data characterized by values of Reynolds number bigger than 100000, might be reproduced by a horizontal line. In particular, a quadratic equation of the type $\eta = B + A\xi^2$ is assigned to the curve of the first stretch, while the curve of the second stretch is a line parallel to the axis of the abscissa.

In the second graph of Fig. 6.4 a similar representation is shown; this time it does not report the Reynolds numbers, but the corresponding values of Δh (the correspondence is pointed out with the red line outlined). This way of representation allows to obtain the expression of the complete curve given by the following equations:

$$Q=\left[5.83+0.173\cdot\log^2\left(\Delta h/7.7\right)\right]\sqrt{\Delta h} \qquad \text{Equation of the parabola}$$

$$Q=5.83\sqrt{\Delta h} \qquad \text{Equation of the line}$$

The value of the angular coefficient of the line $\hat{\mu} = 5.83$ has been obtained as the mean of the ratios $Q/\sqrt{\Delta h}$ calculated excluding the first data regarding the curved stretch.

The equation of the parabola can be written as:

$$y-\hat{\mu}=A\left[\log x-\log 7.7\right]^2$$

where y represents the ratio $Q/\sqrt{\Delta h}$ e $\hat{\mu}=5.83$ represents the mean of the ratios $Q/\sqrt{\Delta h}$ calculated excluding the first data regarding the curved stretch.

The value of the A parameter is obtained through statistical elaborations, or minimizing the function of mean square deviation (method of the minimum squares):

$$\sum\left(\eta-A\xi^2\right)^2=\min \rightarrow 2\sum\left(\eta-A\xi^2\right)\left(+\xi^2\right)=0$$

$$\sum\eta\xi^2-A\sum\xi^4=0\rightarrow A=\frac{\sum\eta\xi^2}{\sum\xi^4}$$

and it is A = 0.173.

To conclude, again it is reported the calibration curve (Fig. 6.3) of the orifice to be used to evaluate the flow rates flowing into the channel.

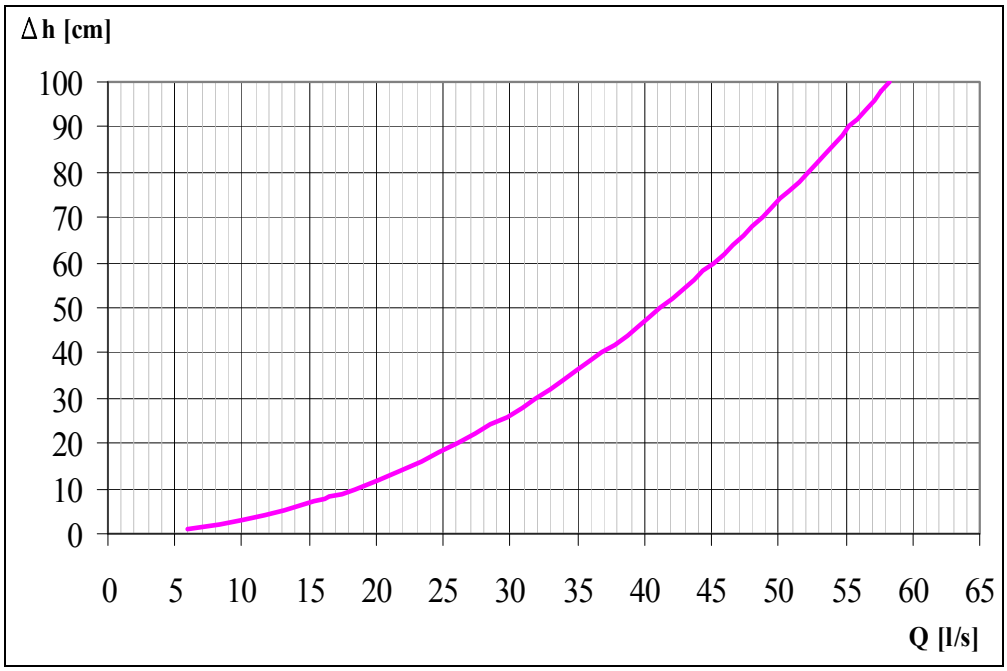

Fig.6.3 - Calibration curve

7. HYDRAULIC CHECK OF SMOOTH BOTTOM CHANNEL

7.1 Introduction

The aim of this work is to lay the basis for the study of the interactions between the vegetated bottom and uniform flows.

After calibrating the orifice, it was necessary to carry out a hydraulic check of the flow conditions in the channel with smooth bottom.

The Darcy-Weisbach equation was used to define the resistances to the flow in the flow profile determination:

$$J = \frac{f}{D} \cdot \frac{V^2}{2g} = \frac{f}{4R} \cdot \frac{V^2}{2g} \tag{7.1}$$

in which it was assumed D=4R that is valid for rectangular channels.

The Colebrooke-White equation was used for the f friction factor expression. In this resistance law, it is opportune to consider the influence of the section shape (Marchi, 1961), by multiplying the R hydraulic radius, that appears in the expressions of the relative roughness and of Reynolds number, by the coefficient of shape ψ:

$$\frac{1}{\sqrt{f}} = -2.0 \log\left(\frac{2.51}{\mathrm{Re}_{\psi} \sqrt{f}} + \frac{\varepsilon}{3.71(4R_{\psi})} \right) \tag{7.2}$$

In particular, in the case of a rectangular section large enough, it is possible to assume for ψ the value of 0.83.

That being stated, the channel hydraulic check was started according to the following phases:

- choice of the channel slope and of the flow rate;
- determination of the flow profile experimentally, that is to say by measuring the flow depth in the subsequent sections of the channel by means of a hydrometer equipped with a twentieth nonius;
- determination of the flow profile analytically, by the well known method of the finite differences;
- comparison between the two flow profiles obtained.

This procedure was applied to the two different types of current that can be established in the channel, that is to say supercritical flow and subcritical flow.

7.2 Profile of a supercritical flow

The method described was applied to the case of a supercritical flow.

The Fig. 7.1 represents the comparison between the experimental flow profile (green points) and the theoretical flow profile (blue curve).

However, in order to obtain a better alignment between experimental points and theoretical curve, it was necessary to consider an ε bottom absolute roughness value not null, but equal to 0.05mm, which is a value that improves the alignment of the theoretical curve to the experimental points, even if it appears negligible (as it must be, since the bottom is practically smooth).

The red curve represents a theoretical curve in the presence of a hypothetical rough bottom, with ε equal to 1 cm; this value is assumed as reasonable order of the absolute roughness size on the basis of results obtained from the experimentations described in chapters n.14, n.15 and n.16.

This curve aims at showing that, with the same slope and flow rate, in the case of ε equal to 1 cm, the uniform motion is reached at a distance shorter than the channel length; on the contrary, in the case of ε equal to 0.05mm (smooth bottom), the uniform flow would be reached at about 30 m from the inlet (therefore at a distance longer that the channel length).

Fig. 7.1 - Supercritical flow profile

7.3 Profile of a subcritical flow

Different considerations have been made in the case of subcritical flow.

In the case of subcritical flow, the uniform flow would be reached upstream, where the effects due to the development of the boundary layer would be still strong (above all when the bottom is vegetated with heavy roughness).

Therefore, the only possibility of being able to study the uniform flow far from the entrance is to obtain a steady uniform flow along the whole channel: this is possible with the use of a sluice gate at the exit of the channel.

Then, the problem arises about the definition of the height to attribute to the orifice under the sluice gate, so that it is possible to start the condition of uniform flow immediately upstream the sluice gate and along the whole channel.

This result can be obtained through experiments, after defining the channel slope and the flow rate, by changing the height of the orifice under the sluice gate, and measuring the upstream flow depth with a hydrometer, till the reaching the uniform flow depth h_u.

In the hydraulic condition examined (channel slope and flow rate fixed), the result is:

- h_u = 14,8 cm
- a = 10,3 cm

Besides, the problem arose about the definition of the value of the coefficient of discharge μ for this type of orifice.

At regards this problem, the following remarks were made:

- the ratio h_u/a is little greater than 1; therefore, it is predictable that the coefficient of discharge μ is greater than 0.615, (a value defined experimentally for an orifice on the bottom);
- the outflow is particular compared with the classical outflow from an orifice on the bottom, since downstream of the orifice, a stretch of the channel is lacking.

We infer from the literature (De Marchi, 1986) that experimental values of the coefficient of discharge μ greater than 0.615, correspond to this particular typology of outflow from an orifice on the bottom.

In order to evaluate, even if roughly, the coefficient of discharge μ, we thought we could apply, to this type of orifice the correlation between the depth of the subcritical flow (in this case, the depth of the uniform flow h_u) immediately upstream the sluice gate, and the depth of the supercritical flow in the contracted cross section immediately downstream the sluice gate, since the height of the orifice is known.

To this end, we proceeded as follows:

- the curve $H_f(h)$ has been made, and the value of the hydraulic load on the bottom H_f corresponding to h_u has been identified;
- the hydraulic load on the bottom H_f being equal, it has been calculated the corresponding depth of the supercritical flow downstream the sluice gate, which represents the flow depth in the contracted cross section.
-

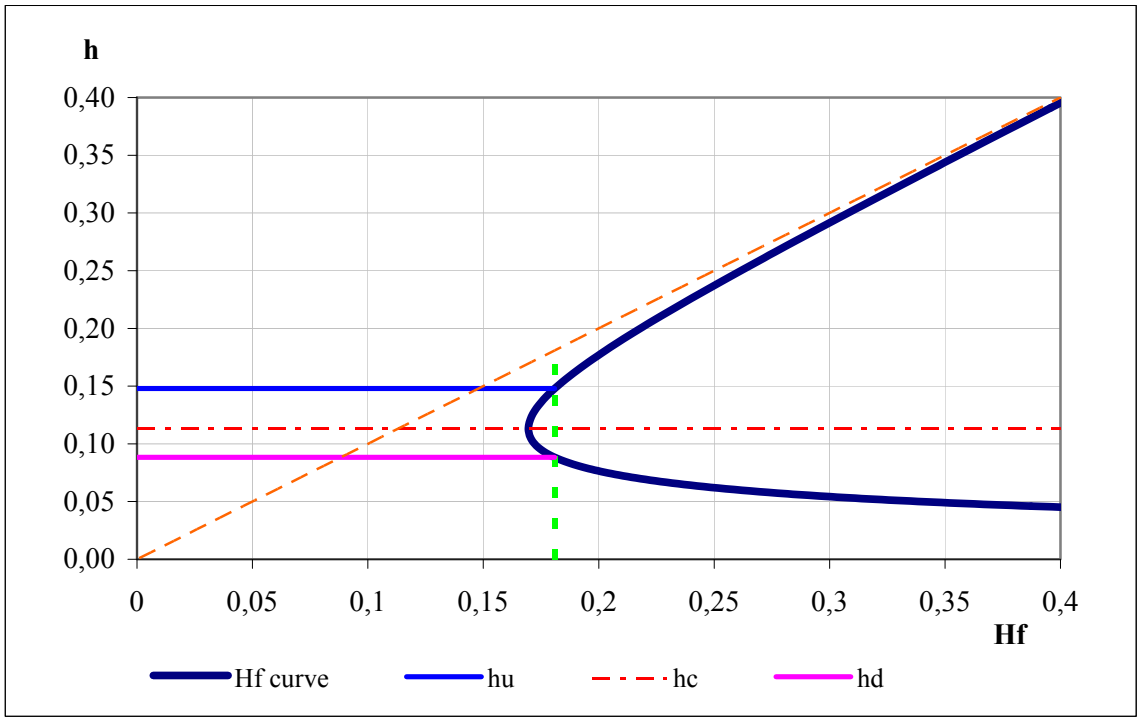

Fig. 7.1 - Definition of the height of the orifice

The ratio between the flow depth in the contracted cross section and the height of the orifice allows to define the value of the coefficient of contraction, that, practically, correspond to the value of the coefficient of discharge μ, which is equal to 0.86. This value has been considered important in relation to the above comments.

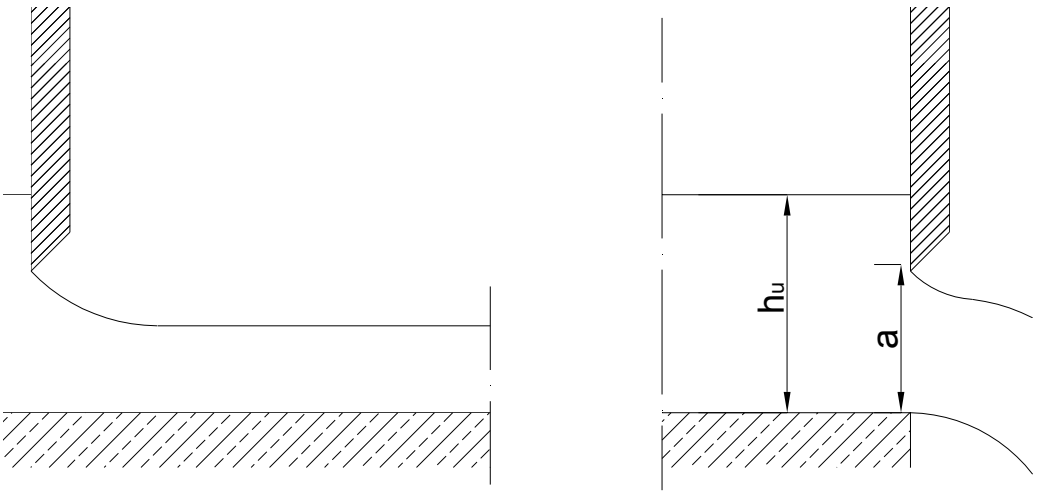

Fig. 7.3 - Classic bottom opening (to the left) and the experimental channel outlet in use (to the right)

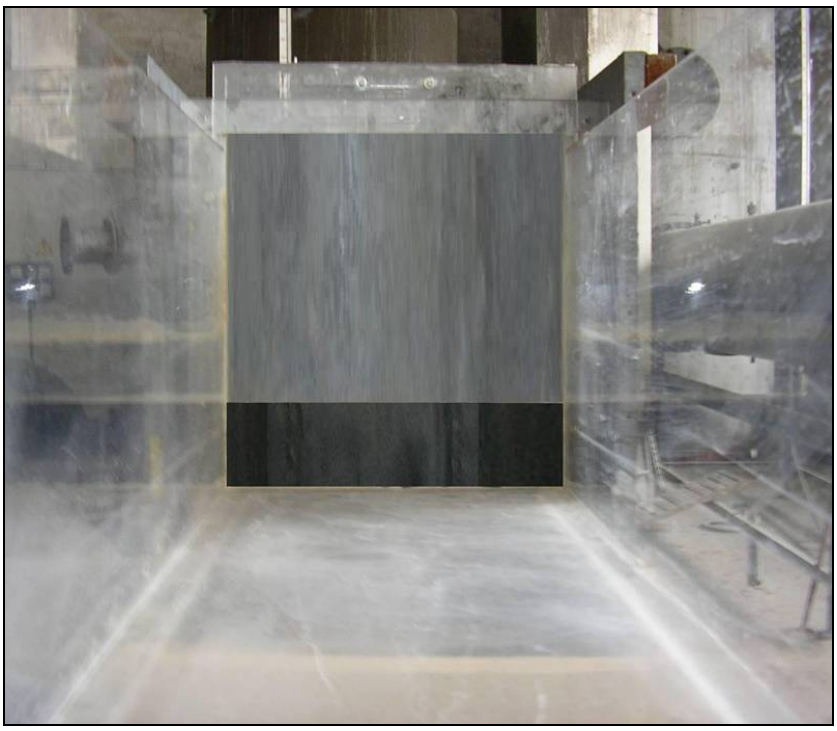

Fig. 7.4 - The channel outlet

By comparing the experimental flow profile (green points) and the theoretical flow profile (blue curve) represented in Fig. 7.5, it is possible to assume, approximately, that the aim of realizing the uniform motion along the whole channel has been reached.

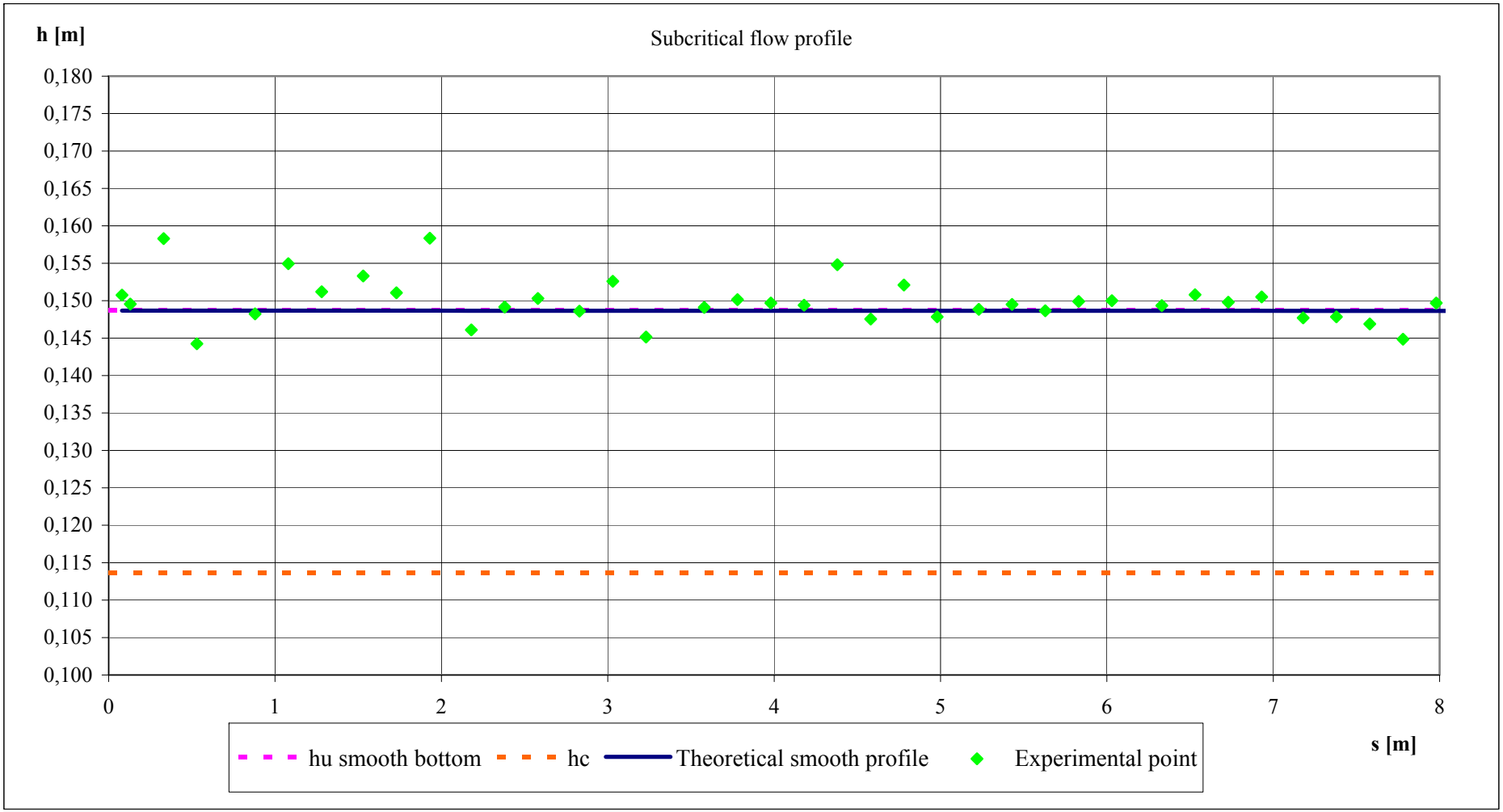

Fig. 7.5 - Subcritical flow profile

7.4 Comments about the definition of the channel slope

The channel slope, as well as its real rectilinearity, is a very important parameter, therefore particular attention has been paid to their measures.

In order to guarantee a precise value of the slope and rectilinearity in each shaping, it is necessary to proceed to their measures according to the following method:

- a first attempt is made to fix the slope, close to the slope required;
- the whole channel is sealed and filled with water;
- the slopes of the first stretch of the channel are measured, from the entrance to the central support, and of the channel second stretch from the central support to the scale and finally of the whole channel from the entrance to the scale;
- in case there is a difference in the measures, we proceed to a gradual lowering or rising of the final stretch by working on jack, repeating the procedure until the difference among the slopes in the different stretches is almost null.

8. DEFINITION OF THE VEGETATED BOTTOM

8.1 Preparation of the Plexiglas plates

In order to model the submerged rigid vegetation, we thought of the most suitable way that might permit us to put in the cylinders to schematize the vegetation itself.

The solution that guarantees the greatest flexibility is the following.

In short, we chose to cover the channel bottom with Plexiglas plates, conveniently drilled with a very precise laser system, so that it was possible to put the brass cylinders into the holes easily.

At this point some problems arose, both of technical nature (drilling of the plates), and of hydraulic nature (number and size of the holes and their hydraulic resistance).

It was advisable to make eight plates to cover the whole channel, whose structural typology is shown in the figure below.

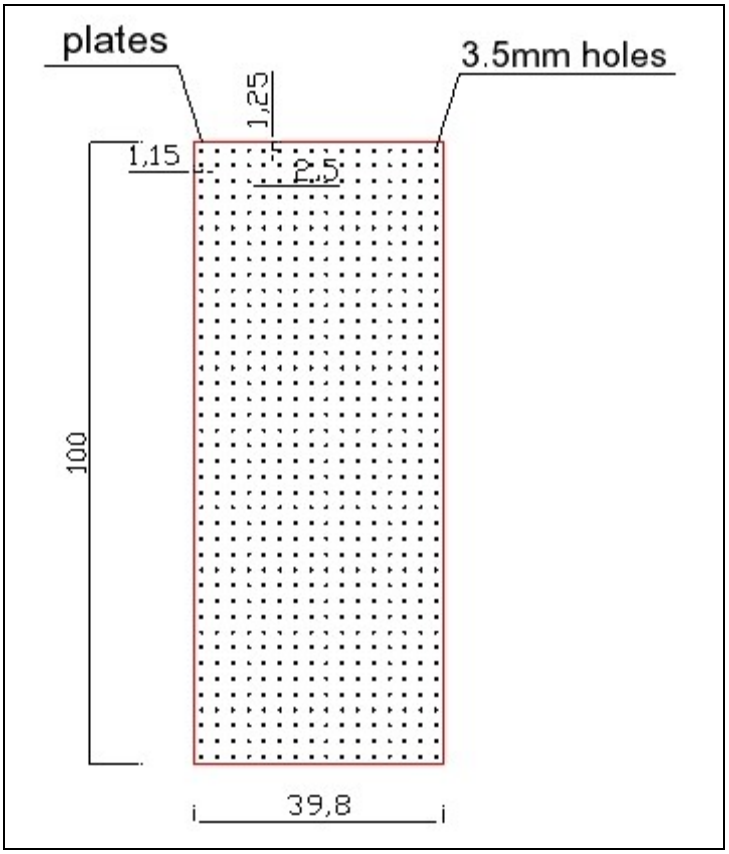

Fig. 8.1 - Plexiglas plates

The plate is 1cm thick and 1m long, while the width is according to the channel width, that is 40 cm.

As shown in the figure, it was made a square net of 2.5x2.5 cm^2, in such a way as to succeed in modelling any rigid vegetation, but, above all, this choice was necessary so that it

was possible to go back to the tests relative to a boundary layer current with cylinders arranged as “double density”, (Type “B”) or a square net of 2.5x2.5 cm^2.

To complete the vegetated bottom and to avoid a step at the entrance, it was necessary to realize a plate with the same sizes as the draft, but not drilled, since it was useless to create vegetation in that area.

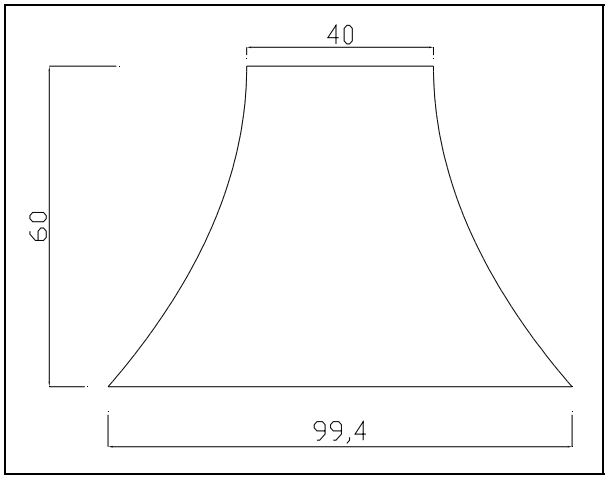

Fig. 8.2 - Bottom entrance

After making the plates, it was necessary to find a way to fix them to the test channel. At first, it was sufficient to use a double-sided tape.

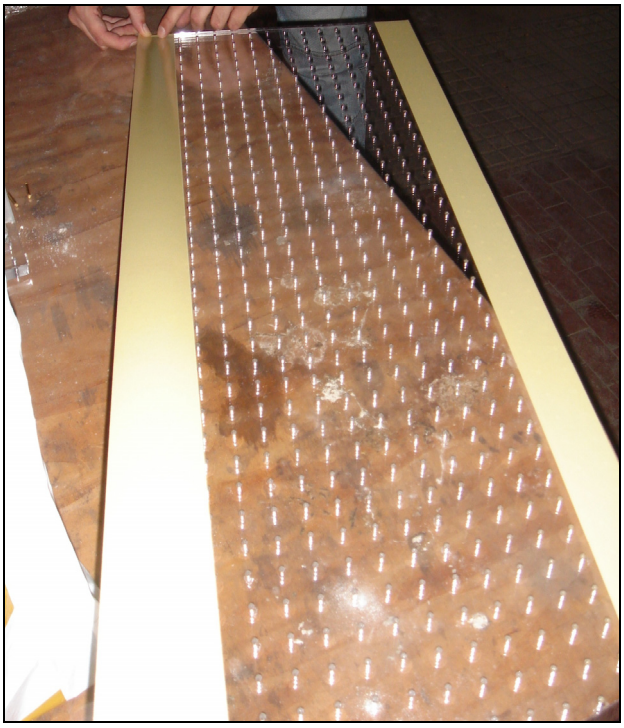

Fig. 8.3 - Fixing with double-sided tape

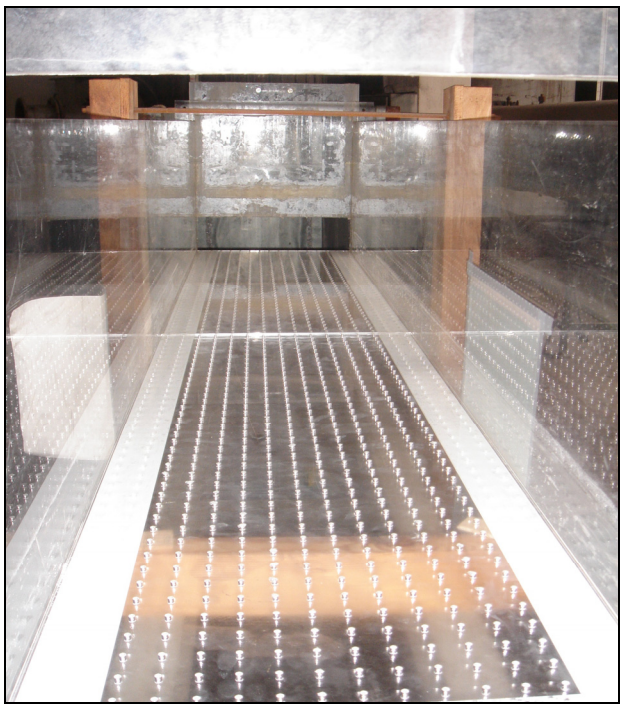

Fig. 8.4 - Plates situated in the channel

The next seal tests showed that the plates tended to rise owing to the hydraulic pressure.

So, the most suitable method chosen was to fix the plates with flat-headed screw on the bottom, so as to reduce the resistances to the motion to the minimum.

Further studies have proved that their influence on the resistances is negligible.

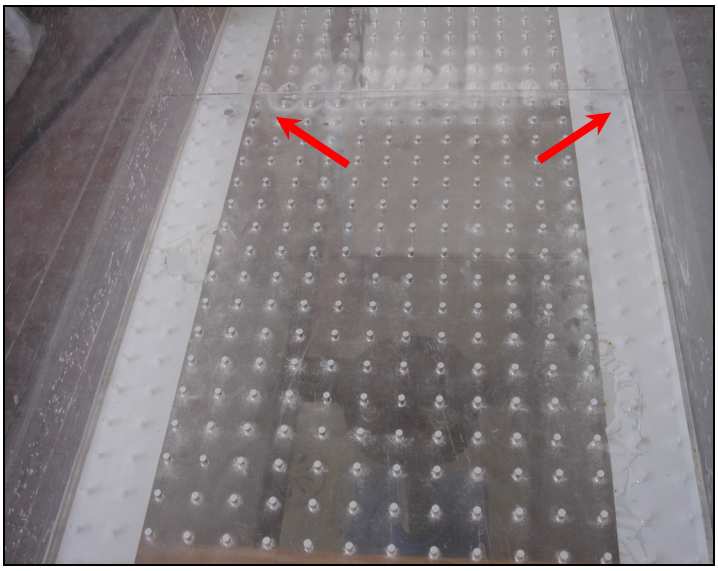

Fig. 8.5 - Fixing with screws

Of course, the sizes of the holes made on the plates depend on the cylinder sizes, considering that they will have to be put in and taken off.

Easily, but they must also resist to the water pressure.

The cylinders are brass cylinders, their diameter is 4 mm, while their height ranges from 2.5 cm to 7.5 cm.

8.2 Realization of the rigid vegetation

From the photo here below it is possible to have an overall view of the channel with the vegetation schematized with the cylinders.

The schematization adopted for the vegetation we chose a regular rectangular net, with the side 2.5x5 cm^2, already defined during the tests carried out on the boundary layer current as "single density" (Type "A"), with cylinders 2.5 cm high, coming out from the bottom of 1.5 cm.

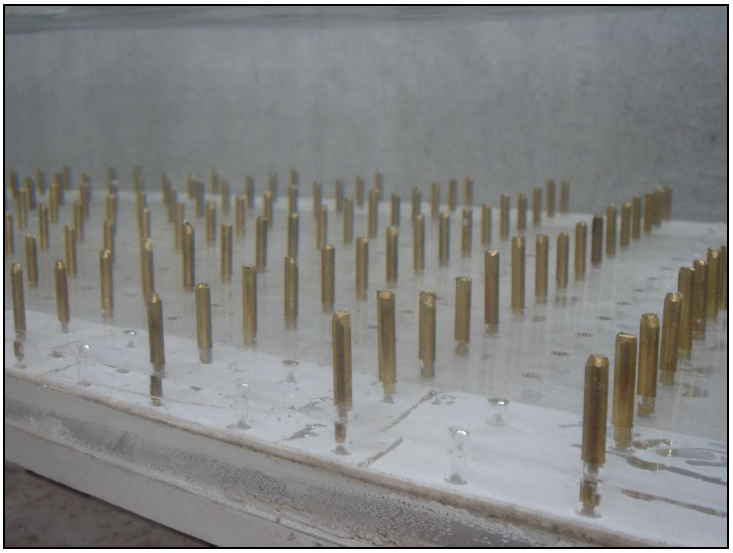

Fig. 8.6 - Vegetation chosen for the experimentation

Fig. 8.7 - Channel ready for the experimentation

9. NEW CALIBRATION OF THE LDA SYSTEM

9.1 Introduction

The aim of the work described in this chapter is the calibration of the system of measure of the instantaneous velocity carried out on the channel smooth bottom.

In the experimentations carried out on the boundary layer currents (chapter n.11, n.12 and n.13), the system had already been calibrated, obtaining a calibration constant equal to 0.9882.

On the contrary, since it was noted that on the experimental channel described in chapter n.5 the frequency ranges were very changeable, we wanted to verify the congruity, on changing the frequency field, of the calibration constant already used in the experimentations relative to the boundary layer currents.

In order to be able to go on with this operation, it is necessary to establish preliminarily:

- the type of current (subcritical or supercritical);
- the slope of the experimental channel;
- the flow rate;
- the range of acquisition of the frequency tracker;
- the shift frequency;
- the measurement position.

The procedure of survey of the local mean velocity profile in the measure section chosen is the following:

- the laser is placed in the high part of the current in correspondence with the free surface (till a good signal is guaranteed, whose quality can be controlled on the oscilloscope);
- the acquisition is launched for a prearranged time (in our case 2 minutes and 15 seconds);
- afterwards we carry on the measurements of the values of the local mean velocity in the next points of the measure section, lowering of quantities ranging from 1 mm to 5 mm towards the channel bottom.

Thus, the whole profile of the local mean velocities is obtained with sufficient precision.

In order to set up the position of the acquisition point, two graph paper strips are placed on the walls, to the channel hydraulic left and right respectively, on which the positions of the acquisition point as regards the bottom are read, so as to calculate the position of the acquisition point with an adequate ratio.

Due to the power of the laser source, it was not possible to acquire on the axis as the current, but only at a distance from the wall placed to the channel hydraulic left of 12 cm, as shown in Fig. 9.1.

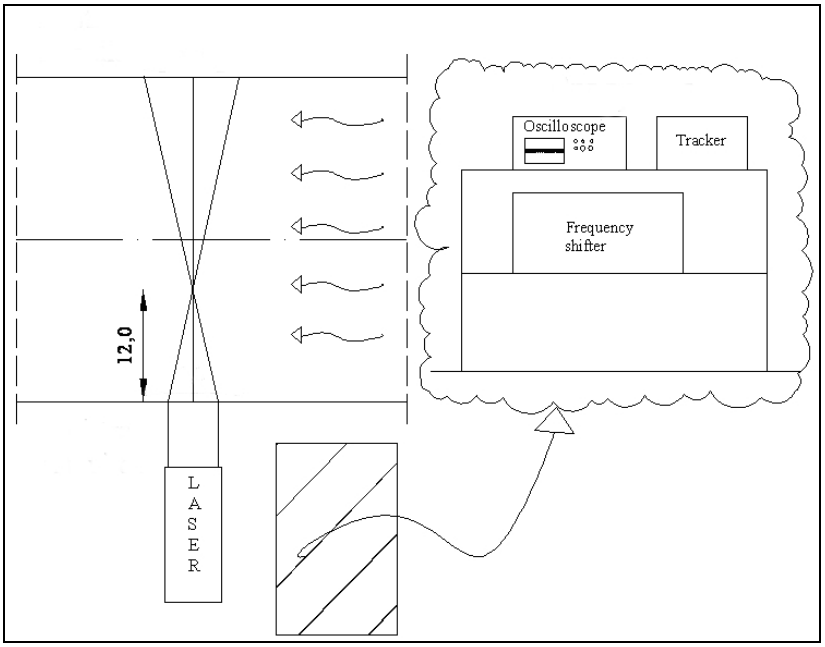

Fig. 9.1 - Diagram of laser positioning

9.2 Experimental measures

For each series of measures, we fix in advance the channel slope, with the method previously described at the 7.4 paragraph, the flow rate, obtained by reading on the air-water differential manometer the Δh and the corresponding value of the flow rate Q_T on the orifice calibration curve; the frequency interval of the frequency tracker; the value of the shift frequency.

We want to focus on the methodology used to obtain each value of the local mean velocity.

As a matter of fact, the frequency tracker does not give directly the value of the local mean velocity, but the value of the Doppler frequency not yet detracted from the shift value stated at the beginning.

Therefore, to obtain the local mean velocities, the frequencies tracker are reported on a calculation sheet, and the shift frequency is added or subtracted (depending on whether this frequency has been set with a negative or positive sign on the shifter frequency); the frequency Doppler obtained must be multiplied by the calibration factor, in the case of our LDA system it is equal to 4.489.

Preliminarily, a test was made consisting in the survey of a single velocity profile, relative

to a distance from the inlet equal to 6.61m, in a supercritical current in a channel with a steep slope, with a flow rate value from the orifice calibration curve (hereafter called theoretical flow rate) equal to 47.52 l/s.

Such a velocity profile has been measured six times, changing the shift frequency value every time.

The measures carried out during this first test are reported hereafter with the relative local mean velocities profiles achieved (Figs. from 9.2 to 9.8).

Table 9.1 - List of First Test measurements

Stage	Fr. Tracker [MHz]	Fr. Shift [kHz]	h [cm]	Slope
1	0,1-1	20	6,88	1,72%
2	0,1-1	60	6,88	1,72%
3	0,1-1	100	6,88	1,72%
4	0,1-1	-20	6,88	1,72%
5	0,1-1	-60	6,88	1,72%
6	0,1-1	-100	6,88	1,72%

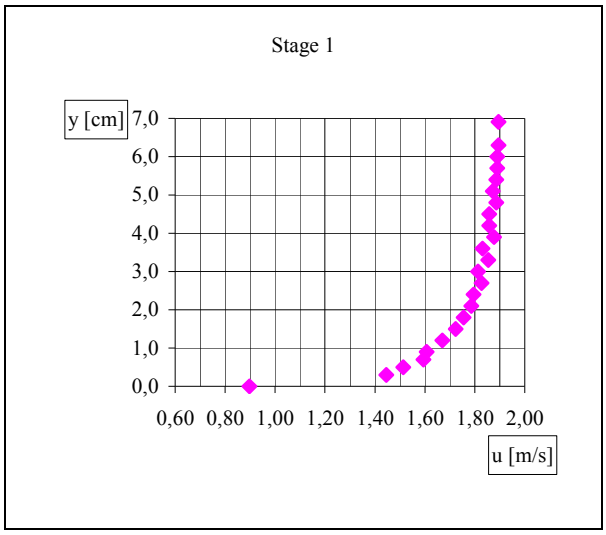

Fig. 9.2- I Test – Stage 1

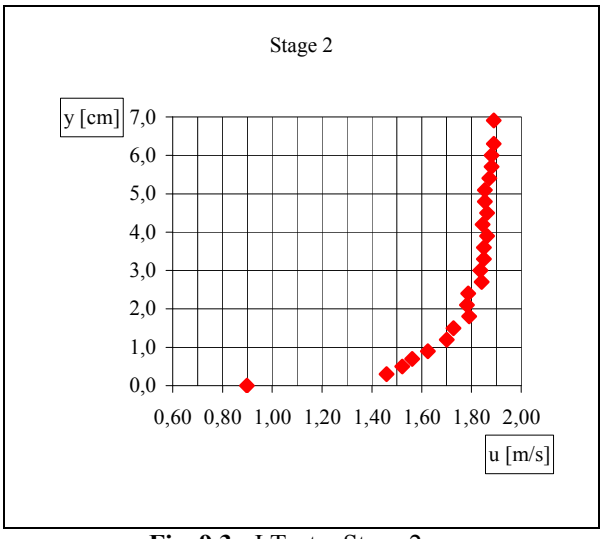

Fig. 9.3 - I Test – Stage 2

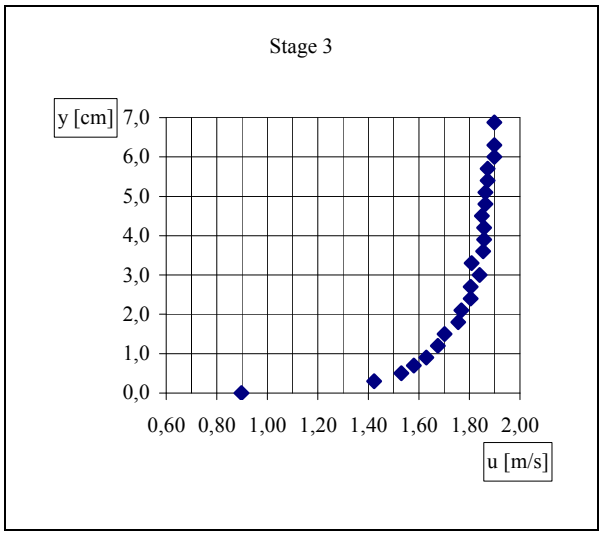

Fig. 9.4 - I Test – Stage 3

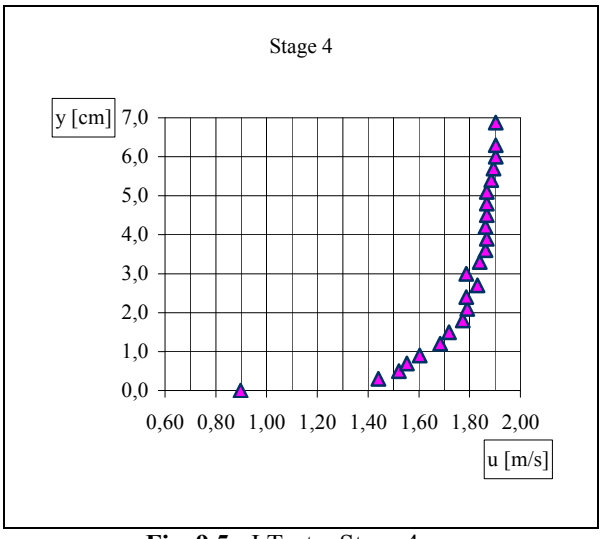

Fig. 9.5 - I Test – Stage 4

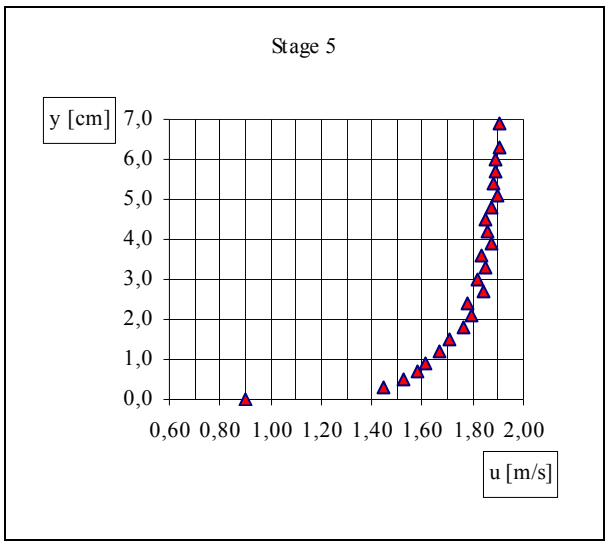

Fig. 9.6 - I Test – Stage 5

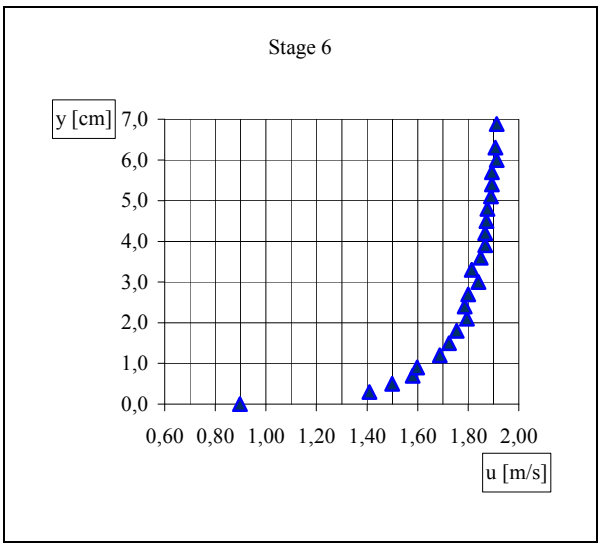

Fig. 9.7 - I Test – Stage 6

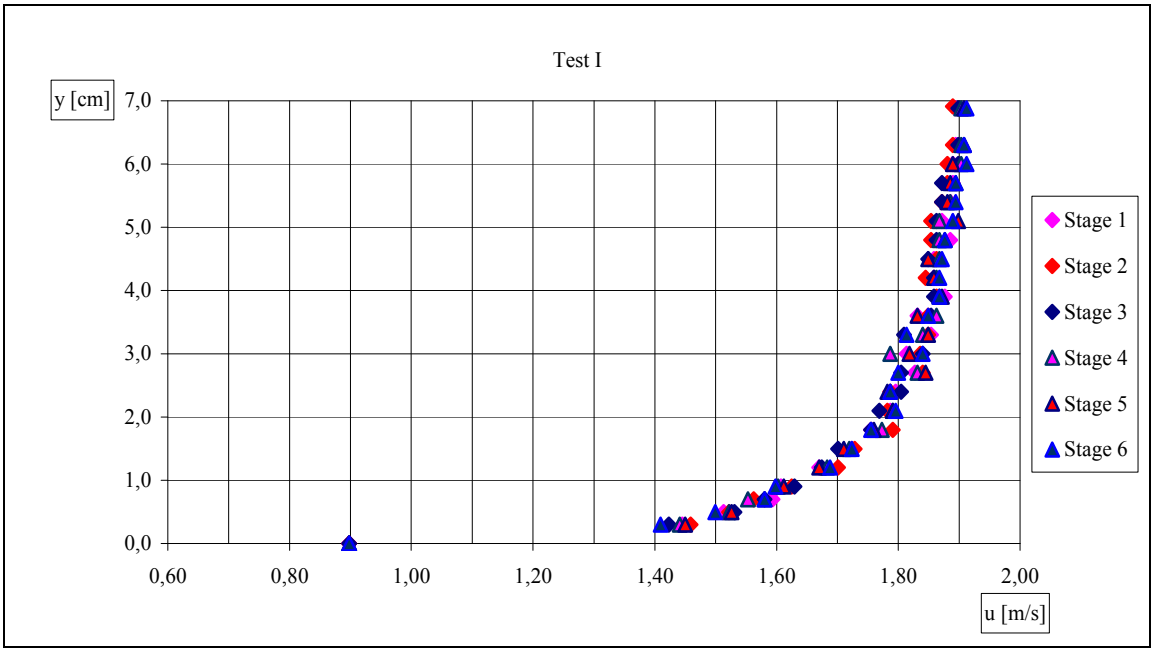

Fig. 9.8 - Superimposition of the six previous stages

The value of the velocity at 0.00cm (i.e. on the bottom) is different from zero, since, for the flow rate calculation, starting from the velocity profile, a null value assigned would cause an underestimate of the integral area, considering that the velocity profile tends quickly to zero very near the bottom, and certainly it is not measurable with the LDA equipment. On the contrary, the assignment of a positive value, inferred from the single velocity profile, certainly causes a minor mistake.

Watching the global final graph summarizing all the measures carried out (fig.9.8), it is possible to notice that, when the Doppler frequency changes (that is the velocity changes) there is an inversion of the experimental points detected in the measures with different shift frequencies, or rather the points that arrange themselves on the right above, on the contrary, in

the lower part they arrange themselves on the left.

Being about acquisitions in the same conditions, flow depth being equal, this tendency must not be attributed to shift frequency, (moreover constant), but to the different values, in the same measure point, of the Doppler frequency, that, therefore, is the only element which must be considered for the calibration. That is to say, the calibration factor varies with the measured Doppler frequency, therefore, it is not a "calibration constant" but a "calibration line" we are looking for.

For this reason, in this Doctoral thesis we do not speak of "calibration constant", but of "calibration line", because the value of the calibration factor to be looked for is changeable with the measured Doppler frequency.

Therefore, in order to understand this variability, in the next experimental tests, two o three series for each velocity profile (corresponding to the same flow rate) were acquired: in each series, choosing in each point of the same series the appropriate shift frequency, all the points of the same series were made to correspond to about the same tracker frequency.

Hereafter, there are the hydraulic characteristics of each test subsequent the one previously illustrated (Table 9.2).

Table 9.2 - List of measurements

Test	Flow type	Range Fr. Tracker [kHz]	h [cm]	Slope	Theoretical Flow rate [l/s]	Stage	Fr. Shift [kHz]
II	Accelerated supercritical	100-1000	6,92	1,72%	47,86	1 2	70 10
III	Accelerated supercritical	100-1000	5,61	1,72%	27,35	1 2	70 10
IV	Accelerated supercritical	100-1000	6,93	1,72%	47,51	1 2 3	From -10 to +90 From -50 to +50 From -100 to -10
V	Accelerated supercritical	100-1000	5,80	3,03%	47,97	1 2 3	From -10 to +100 From -50 to +80 From -100 to +30
VI	Accelerated subcritical	33-333	8,98	0,12%	27,72	1 2 3	From -30 to -10 From -60 to -20 From -90 to -50
VII	Accelerated subcritical	100-1000	9,05	0,12%	28,02	1 2 3	100 200 300
VIII	Accelerated subcritical	33-333	11,37	0,12%	40,09	1 2 3	From -30 to +10 From -60 to -10 From -90 to -30
IX	Accelerated supercritical	100-1000	5,99	1,80%	40,39	1 2	From +10 to +70 From -100 to -40
X	Accelerated subcritical	33-333	8,87	0,15%	27,84	1 2 3	From -30 to +20 From -60 to -10 From -90 to -40
XI	Accelerated subcritical	33-333	11,27	0,15%	40,31	1 2 3	From -30 to +30 From -60 to -10 From -90 to -30

For example, we show the acquisition data table concerning the IV test – Stage 1, from which it is evident as the changing of the frequency shift permits to have a tracker frequency almost unvaried (Table 9.3).

Table 9.3 - Data of IV Test – Stage 1

Fr. fixed on Frequency Shifter	h	Tracker Frequency	Fr. Shift	Real LDA Frequency	Velocity
	[cm]	[MHz]	[kHz]	[kHz]	[m/s]
-	**0**	**0,195**	0	0,195	0,875
90	**0,30**	**0,415**	-90	0,325	1,459
70	**0,50**	**0,411**	-70	0,341	1,531
60	**0,70**	**0,419**	-60	0,359	1,612
50	**0,90**	**0,412**	-50	0,362	1,625
40	**1,20**	**0,414**	-40	0,374	1,679
30	**1,50**	**0,417**	-30	0,387	1,737
20	**1,70**	**0,410**	-20	0,390	1,751
20	**1,80**	**0,419**	-20	0,399	1,791
10	**2,10**	**0,403**	-10	0,393	1,764
10	**2,20**	**0,410**	-10	0,400	1,796
10	**2,40**	**0,419**	-10	0,409	1,836
10	**2,60**	**0,415**	-10	0,405	1,818
10	**2,70**	**0,413**	-10	0,403	1,809
10	**3,00**	**0,421**	-10	0,411	1,845
-10	**3,30**	**0,401**	10	0,411	1,845
-10	**3,60**	**0,407**	10	0,417	1,872
-10	**3,90**	**0,409**	10	0,419	1,881
-10	**4,20**	**0,412**	10	0,422	1,894
-10	**4,50**	**0,408**	10	0,418	1,876
-10	**4,80**	**0,413**	10	0,423	1,899
-10	**5,10**	**0,414**	10	0,424	1,903
-10	**5,40**	**0,412**	10	0,422	1,894
-10	**5,70**	**0,413**	10	0,423	1,899
-10	**6,00**	**0,415**	10	0,425	1,908
-10	**6,30**	**0,413**	10	0,423	1,899
-	**6,93**	**0,413**	10	0,423	1,901

Hereafter, we report the global graphs concerning every test, in which it is possible to note how the differences among the single local mean velocity values, measured at the same flow depth, but with different shift frequencies, and in particular with different values of the tracker frequency, are not completely unimportant.

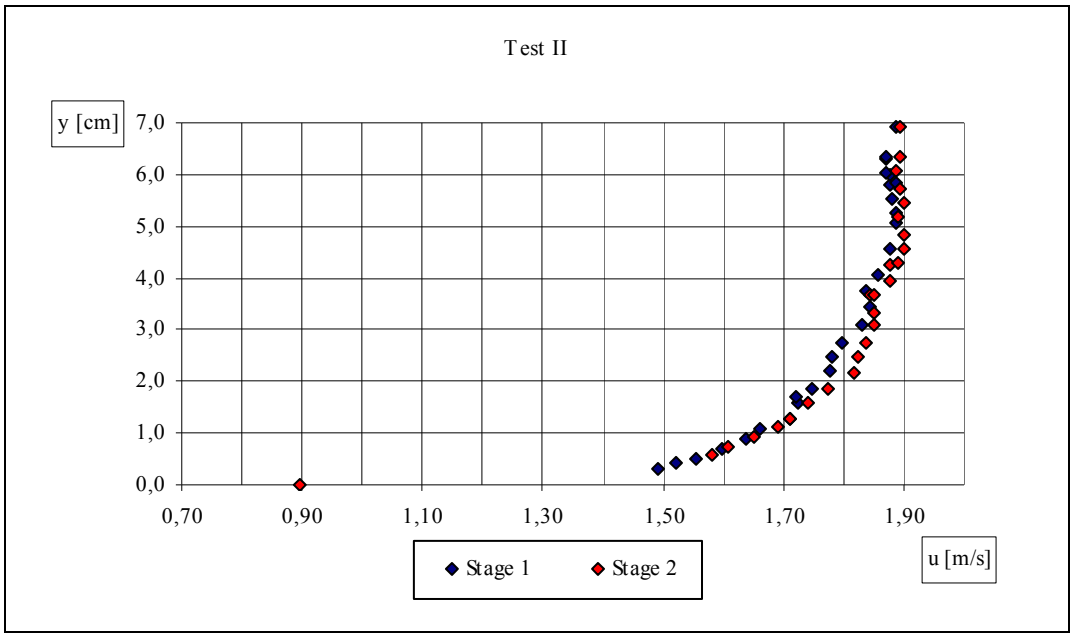

Fig. 9.9 - Local mean velocity profiles - Test II

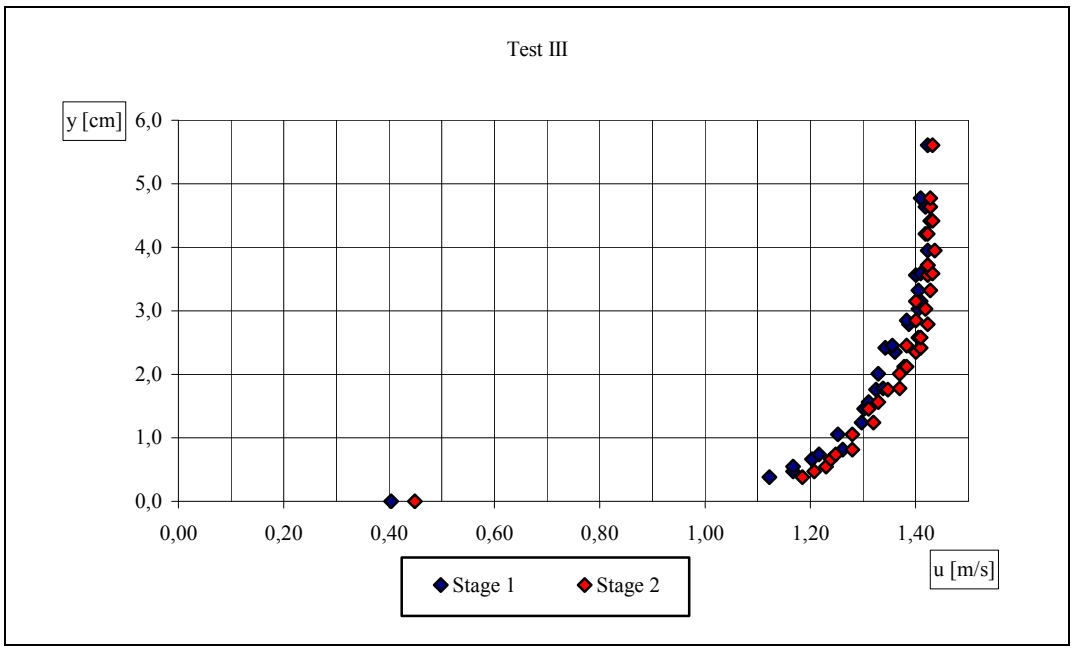

Fig. 9.10 - Local mean velocity profiles - Test III

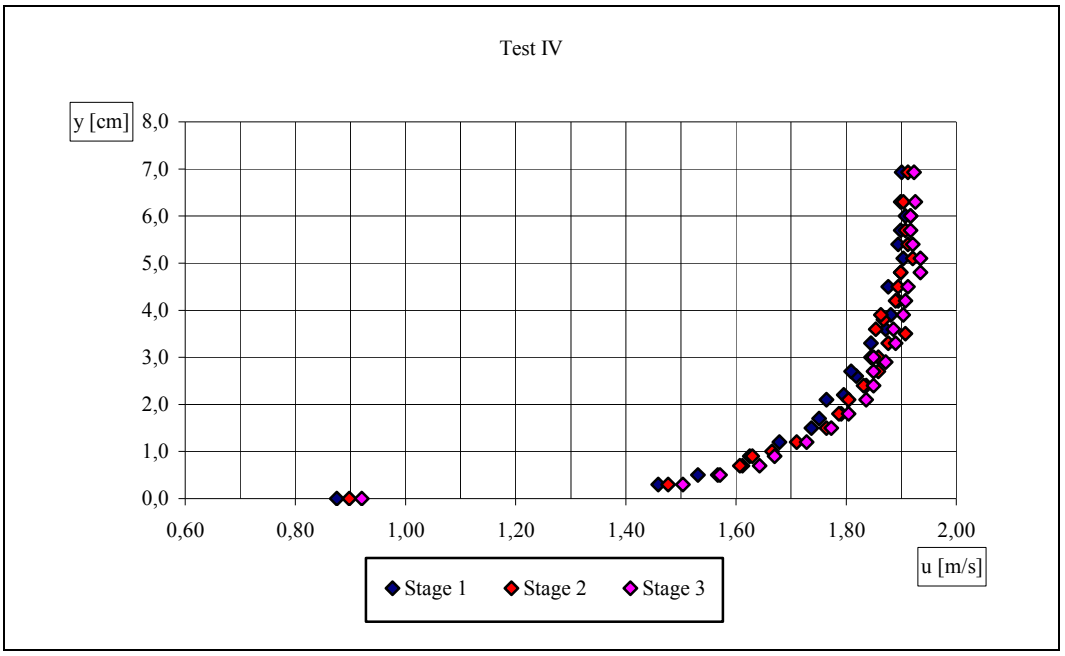

Fig. 9.11 - Local mean velocity profiles - Test IV

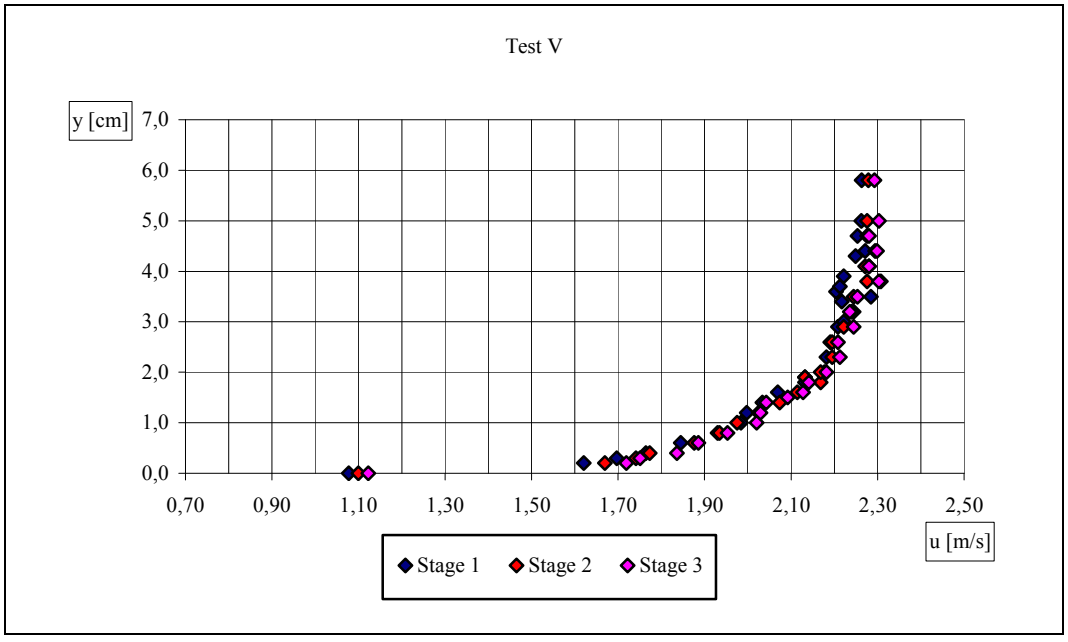

Fig. 9.12 - Local mean velocity profiles - Test V

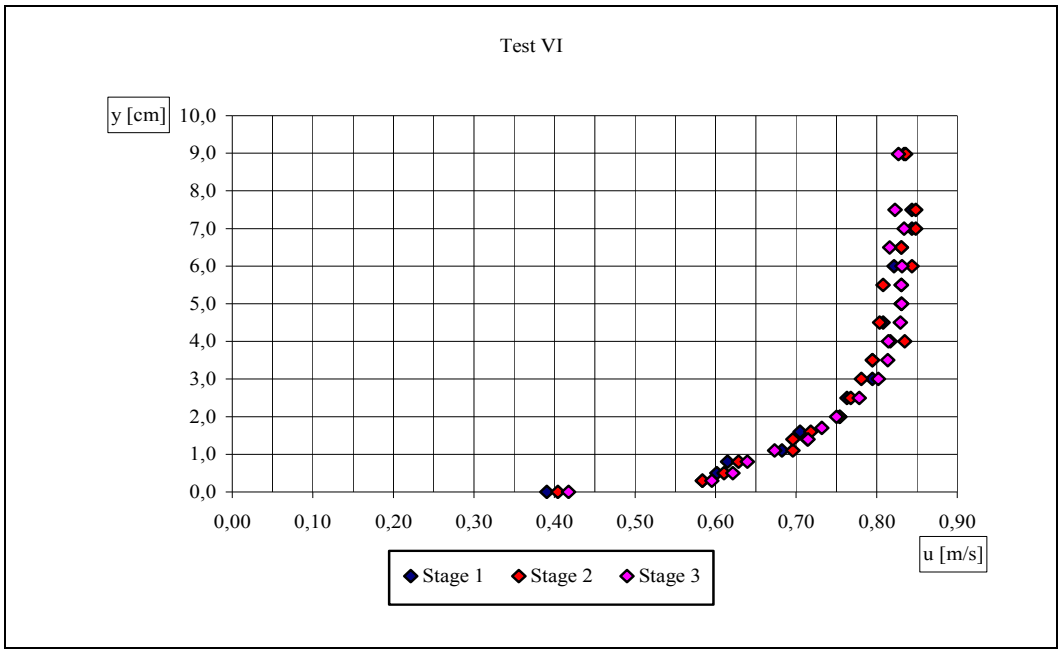

Fig. 9.13 - Local mean velocity profiles - Test VI

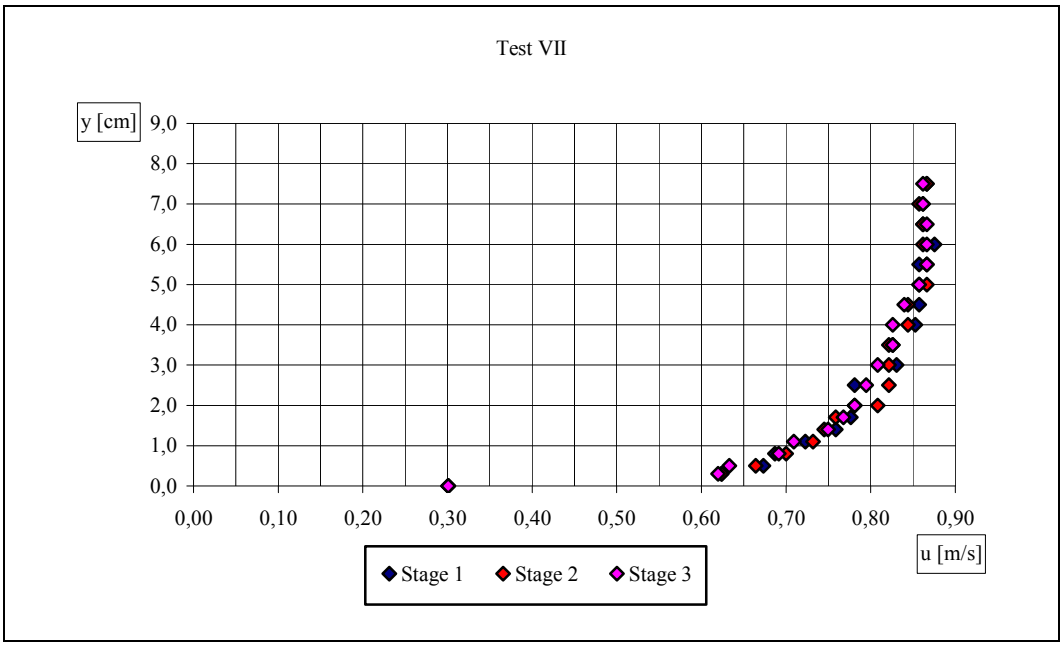

Fig. 9.14 - Local mean velocity profiles - Test VII

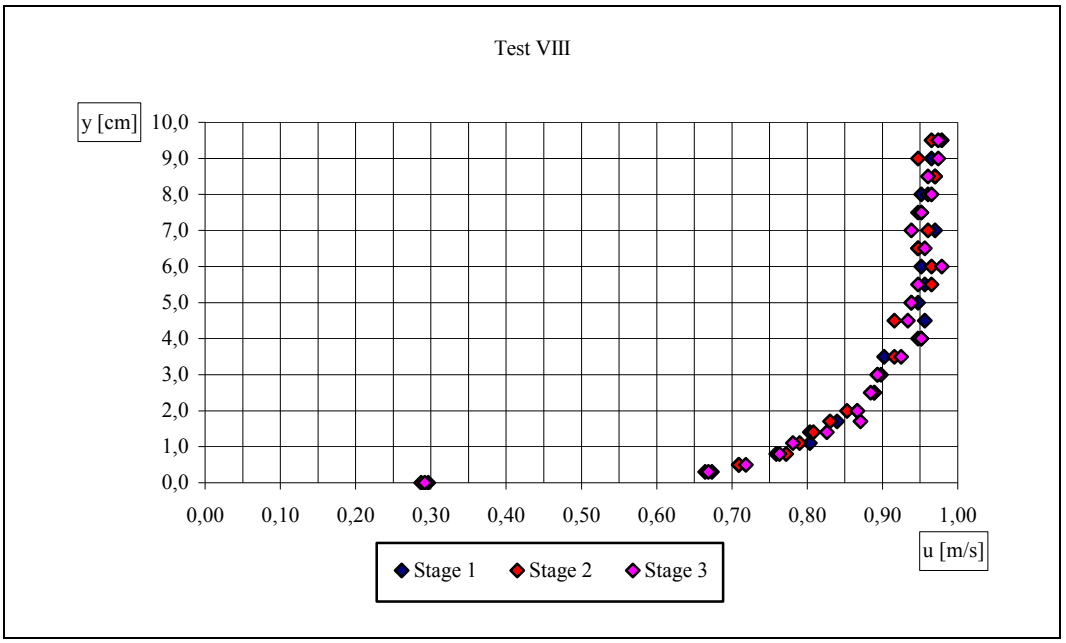

Fig. 9.15 - Local mean velocity profiles - Test VIII

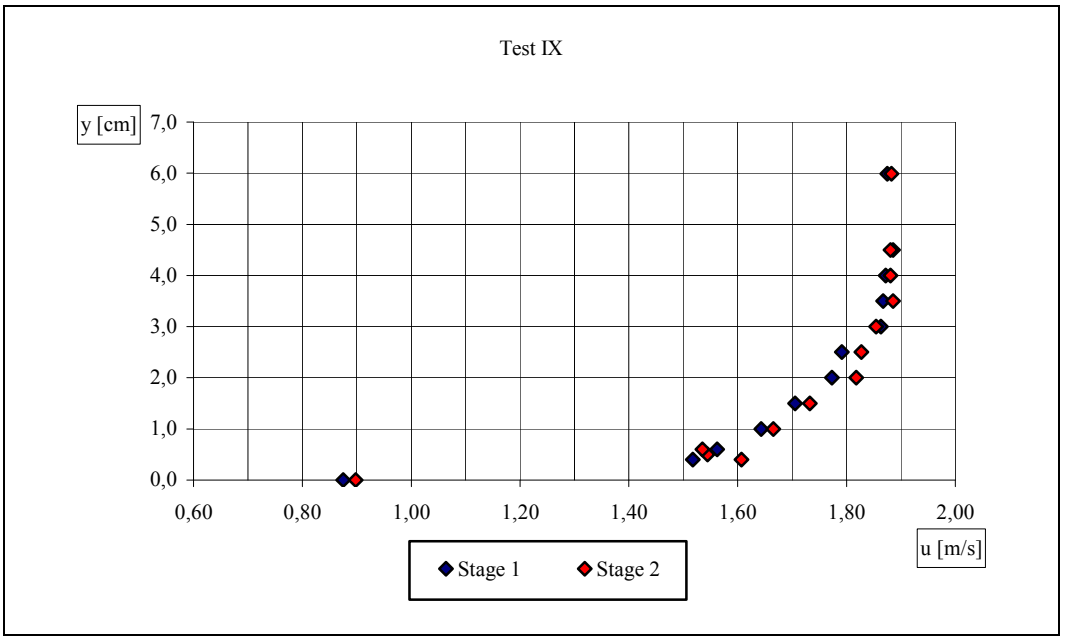

Fig. 9.16 - Local mean velocity profiles - Test IX

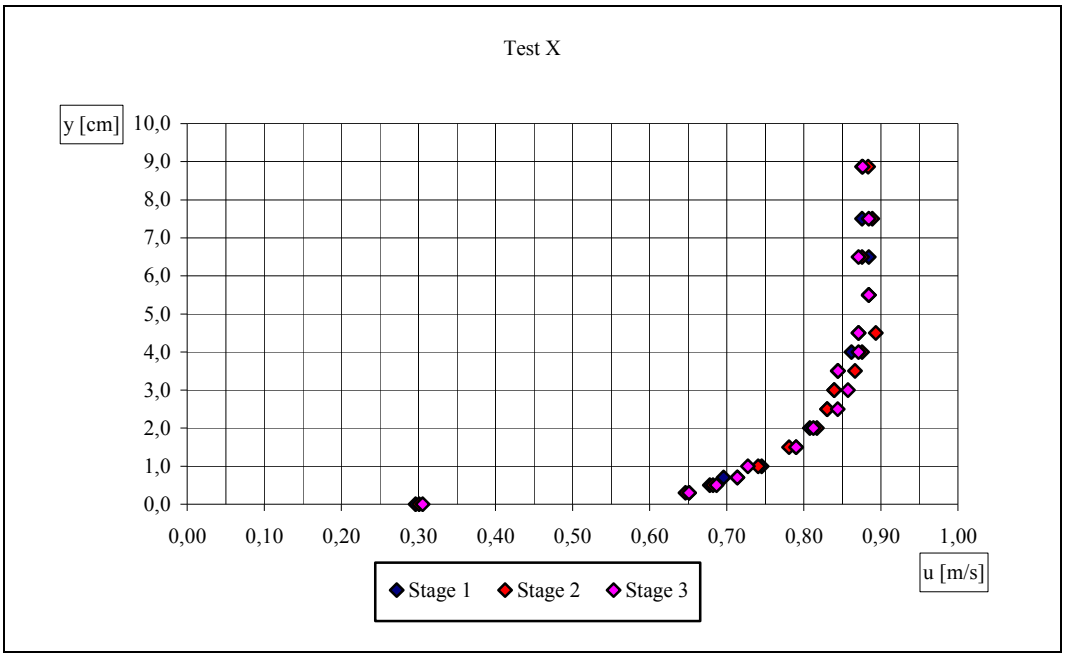

Fig. 9.17 - Local mean velocity profiles - Test X

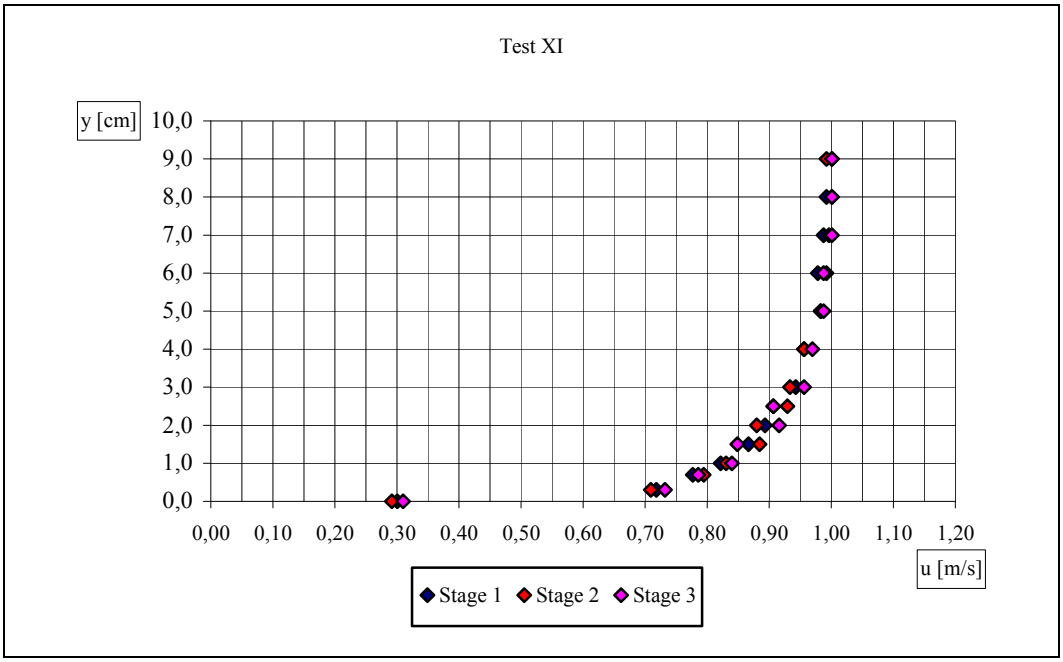

Fig. 9.18 - Local mean velocity profiles - Test XI

9.3 Observations on free surface position and roughness coefficient

The evaluation of the experimental flow rate (that is the one calculated starting from the velocity profiles), compared to the theoretic one (that is the one calculated starting from the orifice calibration curve), gives the value of the calibration constant (to be corrected later with further considerations), and is strongly influenced by the evaluation of the free surface position.

Fluctuations in the free surface position evaluation, even if very low, involve important variations in the experimental flow rate evaluation, thus causing the change of the calibration constant value.

For this reason, it is necessary to develop a close examination of the choice of the exact value of the free surface position.

The possibilities offered for the resolution of the problem are two:

To use, for each test, the free surface position measured through the hydrometer;

To build the flow profile for each test and choose as free surface position the theoretic one corresponding to the measurement section, placed at a distance of 6.61 from the inlet.

The first method is influenced by some experimental measure difficulties with the hydrometer in a current with a very wavy free surface.

The second method is influenced by possible mistakes in calculating data such as the real value of the flow rate and the real value of the roughness coefficient of the bottom, that, perhaps, are not known exactly.

It is impossible to choose a priori which is the best solution; therefore, it is opportune to carry out a comparison between experimental and theoretical values of the free surface position.

The building of the flow profiles was carried out through the method of the finite differences, both for supercritical current and subcritical one.

By way of example, hereafter, we report the supercritical flow profile tending to downstream uniform flow relative to the fifth test, that is with steep slope channel (S=0.0303).

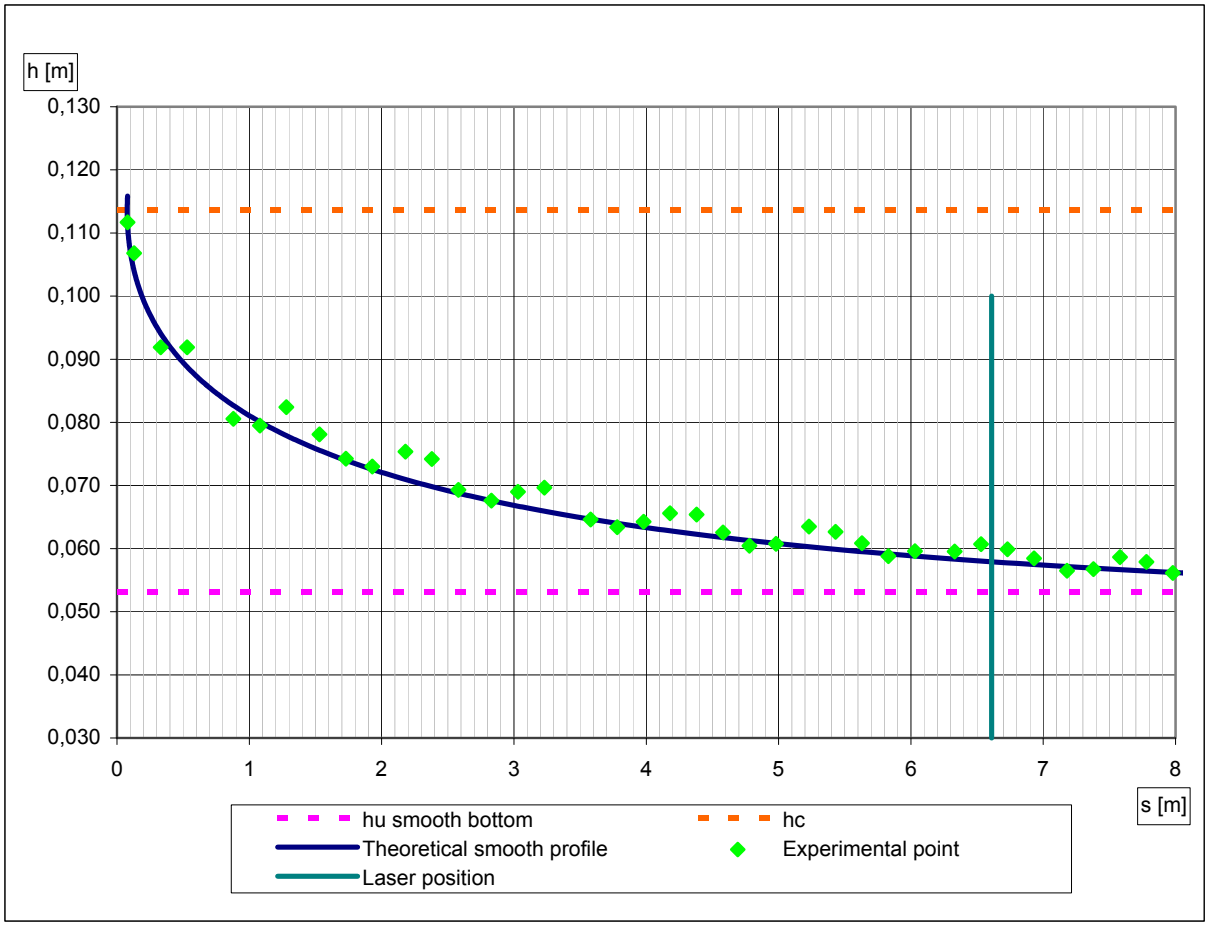

Fig. 9.19 - Profile of supercritical flow for V Test

In the above figure, it is represented the comparison between the experimental flow profile (green points) and the theoretic flow profile (blue curve).

The waving of the experimental flow profile is to be ascribed to surface rippling that are produced at the inlet, in spite of the well shaped draft; afterwards, flowing along the current they spread laterally, being reflected on the walls of the channel.

Therefore, assuming as free surface position value the experimental one read with the hydrometer exactly in the measure point might invalidate the flow rate evaluation and the calibration constant calculations. On the contrary, it was more appropriate to assume the theoretic value of the free surface position.

However, the experimental flow profile is very important for the control of the existence of a mean superimposition between experimental and theoretic data; that is to say, to be able to control the roughness coefficient value assigned to the channel (which is the most sensible datum).

In order to obtain a better adaptation between experimental points and theoretic curve, (as shown in chapter 7, paragraph 7.2) it was necessary to consider a bottom absolute roughness value ε not null, but equal to 0.05mm. This value may appear to be negligible (as it must be,

since it concerns a smooth bottom), but it is a value that improves the adaptation of the theoretic curve to the experimental points.

To prove the waving of the free surface, we built a part of it (XI Test, for example) which pointed out the strong variability of the free surface when the longitudinal and transversal position changed.

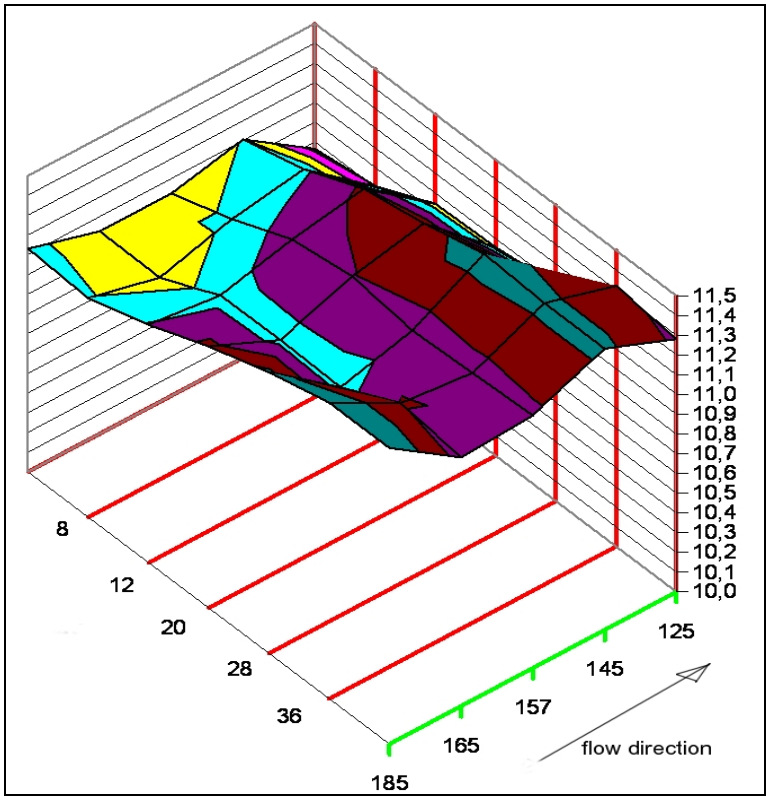

Fig. 9.20 - Example of 3D free surface

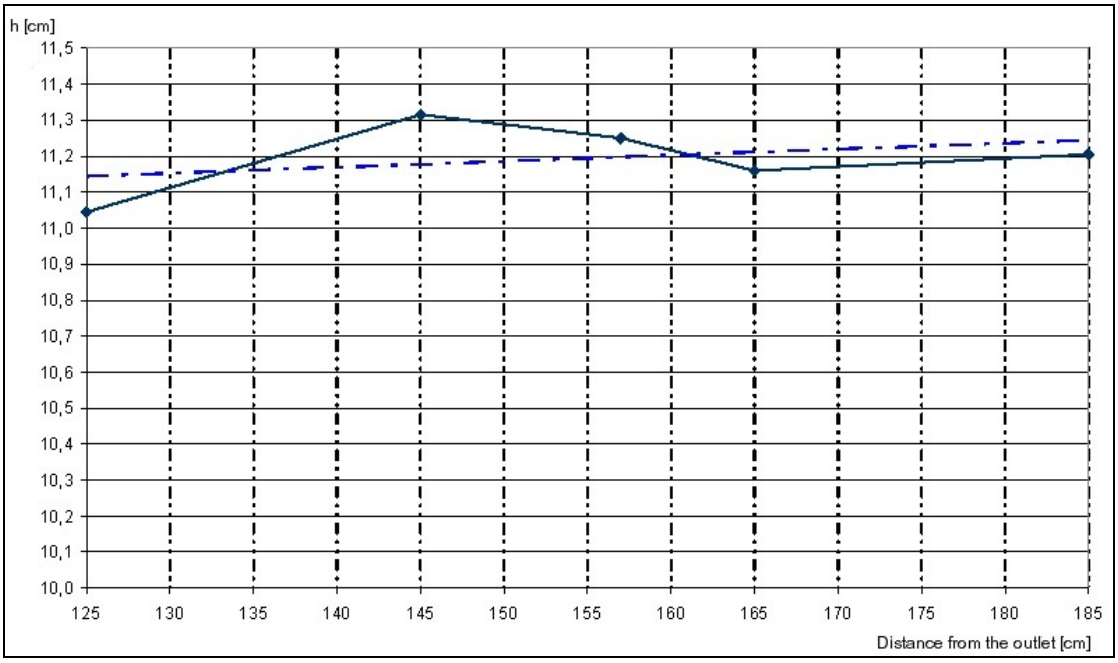

Fig. 9.21 - Longitudinal profile at 12 cm from the hydraulic left

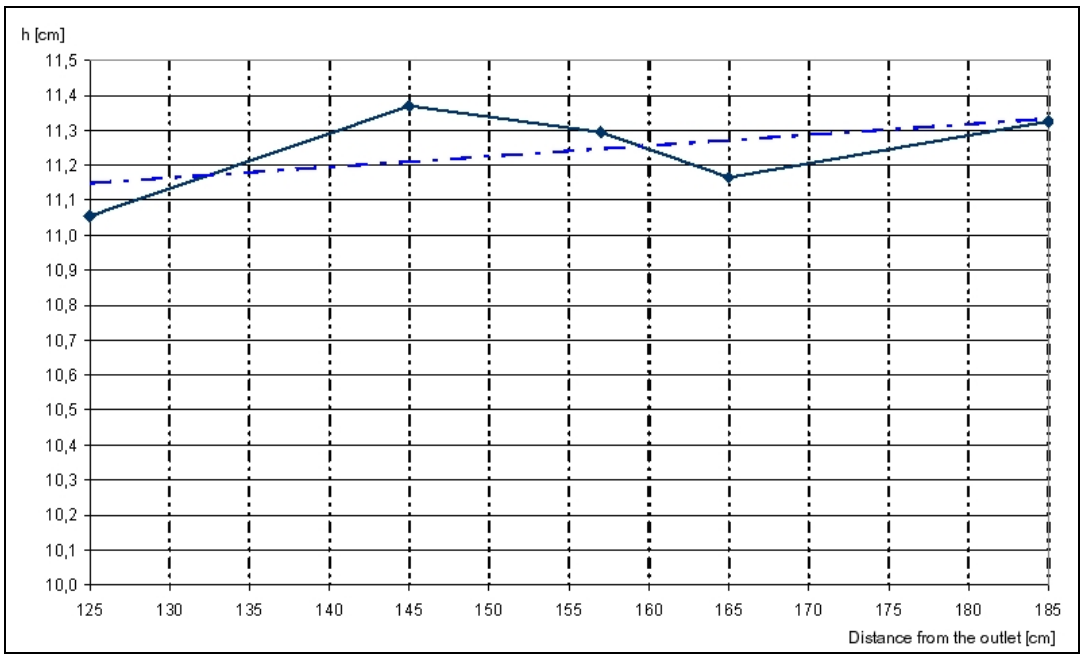

Fig. 9.22 - Longitudinal profile in axis of the flow

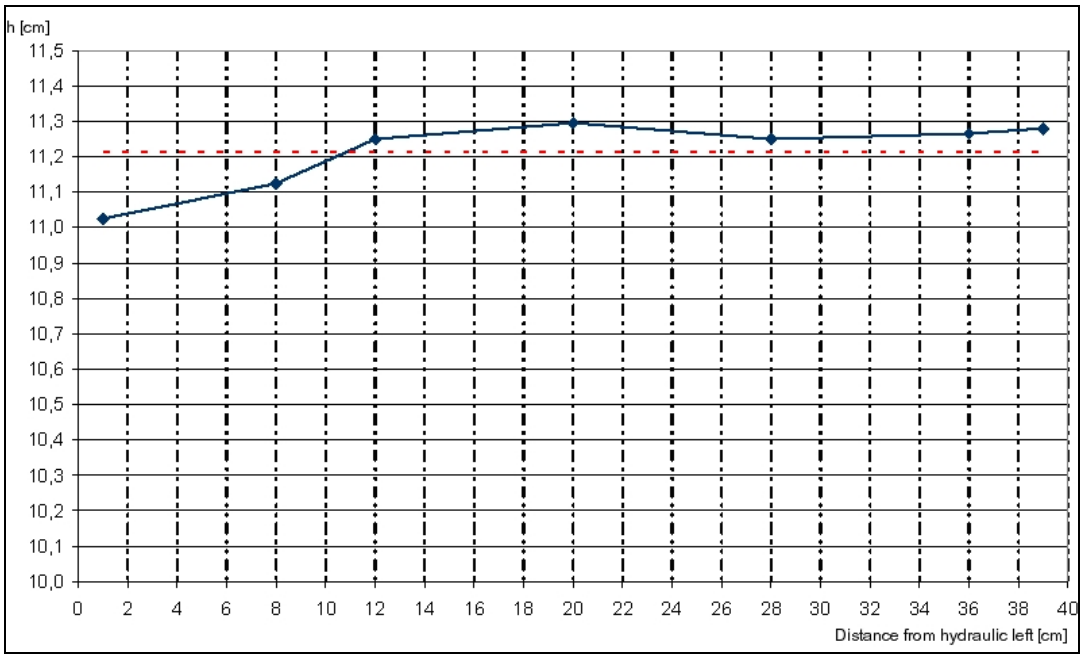

Fig. 9.23 - Transversal profile of the flow

9.4 Calculation of the calibration constant

Now all the necessary data are available for the definition of the calibration constant, for which we got along as follows:

- the data concerning the local mean velocity values were arranged in ascending order as regards the distance of the acquisition points from the channel bottom, as it was made in all the tables;
- for every couple of points the difference of distance was calculated (indicated with $\Delta y_i = y_{i+1} - y_i$);
- this difference was multiplied by the mean velocity $(V_i + V_{i+1})/2$, where V_i indicates the local mean velocity of the generic point at y_i distance from the bottom, and V_{i+1} the velocity of the point placed at the upper distance y_{i+1}.

Then, by summing the products $(V_i + V_{i+1}) \cdot \Delta y_i / 2$ we obtain the flow rate per unit of width Q/b.

This procedure is the discretisation of the integral of the velocity profile.

A point of the calculation to highlight is the influence of the datum of the free surface position, dealt with above.

The last point of velocity measure cannot coincide with the free surface position, since the LDA system is not able to read a clean signal.

So, the last measure point is placed about at 0.5 cm from the free surface.

On the other hand, in order to carry out the complete discretisation of the velocity profile, it is necessary to insert one last virtual point in the table, placed right on the free surface, to which we assign a velocity value obtainable from a velocity profile extrapolation, even if only visual.

The possible error in the velocity calculation does not cause important errors in the flow rate calculation.

On the contrary, a possible error in the free surface position evaluation causes final errors in the experimental flow rate evaluation; they might reach about 2% for every mm of error, which is not negligible.

The flow rate per width unit achieved is multiplied by the channel width (equal to 40 cm) and we obtain a first estimate of the experimental flow rate in the channel, as it is shown in the following table.

Table 9.4 - Experimental flow rate

Test	Stage	h [cm]	Slope	Theoretical Flow rate [l/s]	Experimental Flow rate [l/s]
I	1 2 3 4 5 6	6,88	1,72%	47,51	49,12 48,90 48,76 48,91 48,94 48,94
II	1 2	6,92	1,72%	47,86	49,12 49,34
III	1 2	5,61	1,72%	27,35	29,66 30,14
IV	1 2 3	6,93	1,72%	47,51	49,64 50,03 50,49
V	1 2 3	5,80	3,03%	47,97	49,21 49,60 49,94
VI	1 2 3	8,98	0,12%	27,72	27,97 28,06 28,05
VII	1 2 3	9,05	0,12%	28,02	29,42 29,44 29,22
VIII	1 2 3	11,37	0,12%	40,09	41,42 41,26 41,46
IX	1 2	5,99	1,80%	40,39	42,19 42,57
X	1 2 3	8,87	0,15%	27,84	29,44 29,64 29,53
XI	1 2 3	11,27	0,15%	40,31	42,37 42,51 42,72

9.5 Correction of the calibration constant

After calculating the experimental flow rate, it is possible to estimate a “rough” calibration constant given by the ratio between theoretic flow rate and the experimental one just defined.

However, the values of this constant cannot be considered quite careful, since the experimental flow rate has been estimated multiplying the specific one (Q/b) by the channel width. This is an approximation that underestimates such a ratio, because it is as if we considered the local mean velocities distribution to be steady along all the channel width; this causes an overestimation of the experimental flow rate, with a subsequent decrease in the constant calibration value.

In short, it is not even considered the wall resistances of the channel (Fig. 9.24).

As we can see, owing to the wall resistances, a curve velocity profile is generated along each transversal horizontal line of the cross section, unknown a priori, for a certain part of the

whole transversal length; therefore, the problem is in the definition of the length *x* in Fig. 9.24.

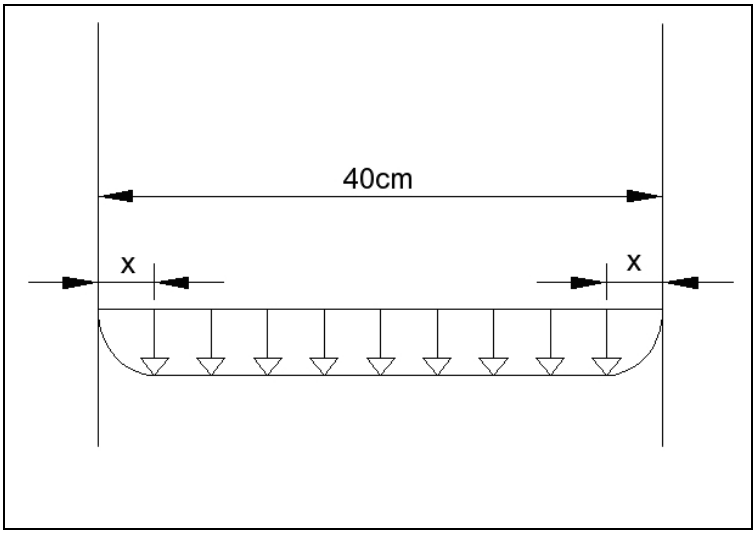

Fig. 9.24 - Profile of transversal velocity distribution

A valid approximation to achieve a good evaluation of this length *x*, since the bottom and the walls are both smooth, is to assume, for each horizontal distribution as a value for *x*, the distance from the bottom where the local mean velocity distribution is not any longer vertical, or where the curvature of the velocity profile begins (or it becomes more definite).

Therefore, once it was clear how to schematize the vertical and transversal velocity profiles, we proceed as follows for defining the calibration constant:

- the *x* position is fixed, representing the separation point between the curvilinear tract and the vertical one in the vertical velocity profile;
- at first the area A_1 is calculated relative to the curved tract as $\sum_{i \le x} v_i * \Delta h_i$ with:
    - i generic point
    - V_i local mean velocity relative to the i^{th} point
    - Δh_i difference of distance between two successive points
- then the A_2 is calculated as $\frac{\left(\sum_{i>x} v_i\right)}{n_i} * h_x$ with:
    - h_x depth at the distance *x*;
    - n_i number points above the position x fixed;
- the ratio A_1 / A_2 is estimated; this ratio represents, in substance, a kind of contraction coefficient;
- according to the oversimplification adopted, the flow rate is given by:

$$Q_{eff} = \frac{Q_{mis}}{b} * (b - 2x) + \frac{Q_{mis}}{b} * 2x * A_1 / A_2$$

where Q_{mis} shows the flow rate measured with rough methodology;

- therefore, the corrective coefficient of the calibration constant is:

$$R = \frac{Q_{mis}}{Q_{eff}} = \frac{b}{(b - 2x) + 2x * A_1 / A_2}$$ with b channel width.

Finally, the right calibration constant is given by $C=R*c$, being C the rough calibration constant.

Hereafter, the results obtained are reported, for each test, through the methodology detailed above.

Table 9.5 - Right calibration constants

Test	Stage	h [cm]	Slope	Right Calibration Constant
I	1	6,88	1,72%	0,9860
	2			0,9886
	3			0,9932
	4			0,9908
	5			0,9900
	6			0,9914
II	1	6,92	1,72%	0,9901
	2			0,9933
III	1	5,61	1,72%	0,9228
	2			0,9399
IV	1	6,93	1,72%	0,9840
	2			0,9754
	3			0,9661
V	1	5,80	3,03%	0,9929
	2			0,9848
	3			0,9881
VI	1	8,98	0,12%	1,0192
	2			1,0158
	3			1,0133
VII	1	9,05	0,12%	0,9785
	2			0,9765
	3			0,9869
VIII	1	11,37	0,12%	0,9954
	2			0,9999
	3			0,9939
IX	1	5,99	1,80%	0,9757
	2			0,9650
X	1	8,87	0,15%	0,9694
	2			0,9628
	3			0,9652
XI	1	11,27	0,15%	0,9788
	2			0,9761
	3			0,9703

9.6 Statistical processing of the results achieved

In the previous paragraphs the estimate of the calibration constant was made; however, it was valid only for every single test.

The aim of this paragraph is to reach the estimate of a unique law to calibrate the velocity values achieved through the LDA measurement tool.

It is clear that, since we have a great number of data available, as shown in the previous pages, it is convenient to carry out a statistical analysis of the data, trying to use also the ones coming from the experimentation carried out on the boundary layer currents (the calibration constant was set at the unique value of 0.9882 for them).

A synthetic outline is reported in the following table.

Table 9.6 - Significant values of each test

Test	Stage	Mean Fr.	Range Lower Extr.	Ratio	Calibration Constant	Slope	Diff. Ratios Extr.
I	1	0,377	0,100	3,773	0,9860	0,0172	
	2	0,338	0,100	3,376	0,9886	0,0172	
	3	0,297	0,100	2,974	0,9932	0,0172	
	4	0,417	0,100	4,173	0,9908	0,0172	
	5	0,457	0,100	4,573	0,9900	0,0172	
	6	0,496	0,100	4,962	0,9914	0,0172	1,988
II	1	0,415	0,100	4,148	0,990	0,0172	
	2	0,466	0,100	4,659	0,993	0,0172	0,511
III	1	0,314	0,100	3,137	0,923	0,0088	
	2	0,368	0,100	3,685	0,940	0,0088	0,548
IV	1	0,4126	0,100	4,126	0,9840	0,0172	
	2	0,3773	0,100	3,773	0,9754	0,0172	
	3	0,3310	0,100	3,310	0,9661	0,0172	0,816
V	1	0,4876	0,100	4,876	0,9929	0,0303	
	2	0,4538	0,100	4,538	0,9848	0,0303	
	3	0,4019	0,100	4,019	0,9881	0,0303	0,857
VI	1	0,1445	0,033	4,378	1,0192	0,0012	
	2	0,1182	0,033	3,581	1,0158	0,0012	
	3	0,0903	0,033	2,736	1,0133	0,0012	1,642
VII	1	0,2784	0,100	2,784	0,9785	0,0012	
	2	0,3785	0,100	3,785	0,9765	0,0012	
	3	0,4769	0,100	4,769	0,9869	0,0012	1,985
VIII	1	0,1768	0,033	5,358	0,9954	0,0012	
	2	0,1492	0,033	4,523	0,9999	0,0012	
	3	0,1207	0,033	3,657	0,9939	0,0012	1,700
IX	1	0,3119	0,100	3,119	0,9757	0,0180	
	2	0,4183	0,100	4,183	0,9650	0,0180	1,064
X	1	0,1642	0,033	4,976	0,9694	0,0012	
	2	0,1361	0,033	4,125	0,9628	0,0012	
	3	0,1056	0,033	3,201	0,9652	0,0012	1,775
XI	1	0,1903	0,033	5,767	0,9788	0,0012	
	2	0,1613	0,033	4,888	0,9761	0,0012	
	3	0,1328	0,033	4,026	0,9703	0,0012	1,741
Boundary layer test	-	0,331	0,100	3,31	0,9882	var.	

Therefore, after obtaining a certain number of constants, it was advisable to chart them in terms of the ratio between mean frequency value of each stage and maximum frequency value of the acquisition range.

At this point, it is possible to process the data statistically, according to the following phases:

- for every series of tests, the tendency line is built of the experimental points, such as $y=ax+b$, with relative regression coefficient R^2 and values of the a and b terms;
- in order to obtain a global line of calibration, it is necessary to carry out a weighted mean of all the lines obtained as described previously.
- in order to be able to go on in this operation, it is necessary to calculate an a_m at first, and then a b_m (afterwards we will explain these terms);
- to build variation ranges of the line of the previous point through the estimation of the mean square deviations;
- to create charts from which it was possible to obtain conclusive considerations relative to the calibration problems of the measurement tool.

Let's ignore the description concerning the first point (that is rather banal), it is necessary to think about the next points.

Since every test series is basically different from the point of view of number of data available and from the hydraulic point of view, in order to be able to group them, it is necessary to evaluate the importance of a test compared to another one by the introduction of different weights, that in our case are two:

- the number of data of every series of test, that we will indicate with p'_a;
- the difference among the extremes of the *Mean Frequency Value/Range extreme bottom* ratios reported in the Table 9.6 for every series in order to consider the width of the acquisition field, that we will indicate with p''_a.

Since we think that the constant is influenced not by the type of current but by the acquisition range (0.1-1 MHz and 33-333 kHz), this study has been carried out separating the series of tests executed in the two different methods.

Hereafter, the results concerning the definition of the constant a are reported.

Table 9.7 - Definition of constant a_m for Range 0.1-1 MHz

Test	a	p'_a	p''_a	$p'_a * p''_a$	$a*(p'_a * p''_a)$
I	-0,00002	6	1,987826	11,92696	-0,00024
II	0,02940	2	0,510971	1,021943	0,03005
III	0,01360	2	0,547813	1,095625	0,01490
IV	0,02080	3	0,816141	2,448423	0,05093
V	0,01800	3	0,808102	2,424306	0,04364
VI	0,00440	3	1,985263	5,955789	0,02621
IX	0,00940	2	1,063889	2,127778	0,02000
				weighted mean	**0,00687**

Table 9.8 - Definition of constant a_m for Range 33-333 kHz

Test	a	p'_a	p''_a	$p'_a * p''_a$	$a*(p'_a * p''_a)$
VI	0,00320	3	1,642394	4,927182	0,01577
VIII	0,00100	3	1,700132	5,100395	0,00510
X	0,00220	3	1,775152	5,325455	0,01172
XI	0,00480	3	1,741126	5,223377	0,02507
				weighted mean	**0,00280**

Now it is possible to estimate the value b_m relative to each series of measures through the expression $b_m = \frac{\sum_i (y_i - a_m * x_i)}{N}$ where:

- b_m is the intercept on the y axis of the mean line;
- i ith test
- x_i the value of the ratio between mean frequency and extreme bottom of the range relative to the ith test;
- y_i the value of the calibration constant relative to the ith test;
- a_m angular coefficient of the mean line;
- N number of points.

This formula means to find the b_m as mean of single b that can be found for each of the experimental points, once the a_m of reference have been fixed.

Table 9.9 - Definition of constant b_m for Range 0.1-1 MHz

Point	x	y	fixed a_m	b
I,1	3,772609	0,990773	0,00687	0,969466
I,2	3,376087	0,990018		0,970951
I,3	2,974348	0,991374		0,974575
I,4	4,173043	0,98602		0,962452
I,5	4,573478	0,988561		0,962731
I,6	4,962174	0,993197		0,965173
II,1	4,1476	0,990104		0,96668
II,2	4,658571	0,99325		0,96694
III,1	3,136875	0,922845		0,905129
III,2	3,684688	0,939906		0,919096
IV,1	4,126308	0,984023		0,960719
IV,2	3,772692	0,975443		0,954136
IV,3	3,310167	0,966124		0,947429
V,1	4,876276	0,992926		0,965386
V,2	4,537652	0,984833		0,959206
V,3	4,068174	0,977736		0,954761
VII,1	2,784	0,978471		0,962748
VII,2	3,785368	0,976474		0,955095
VII,3	4,769263	0,986914		0,959978
IX,1	3,119444	0,964978		0,94736
IX,2	4,183333	0,97567		0,952043
			Mean	**0,956288**

Table 9.10 - Definition of constant b_m for Range 33-333 kHz

Point	x	y	fixed a_m	b
VI,1	4,378485	1,019222	0,00280	1,006953
VI,2	3,580606	1,015837		1,005805
VI,3	2,736091	1,013301		1,005634
VIII,1	5,357576	0,995375		0,980363
VIII,2	4,52253	0,999892		0,98722
VIII,3	3,657444	0,993929		0,98368
X,1	4,975758	0,969368		0,955425
X,2	4,124848	0,962845		0,951287
X,3	3,200606	0,965156		0,956188
XI,1	5,766667	0,978849		0,962691
XI,2	4,887879	0,976115		0,962419
XI,3	4,025541	0,970312		0,959032
			Mean	**0,976391**

Afterwards, we define the ranges within which the mean line can change through the calculation of the root mean square that will be illustrated hereafter.

After evaluating the a_m and b_m parameters, for the construction of the ranges within which the line representative the calibration constant can change, it is necessary to estimate:

- The mean square deviation as $RMS = \sqrt{\frac{\sum_n \Delta y^2}{n-2}}$ with:

- Δy vertical distance of the experimental points from the equation line $y=a_m x+b_m$;
- n number of points;

- the mean RMS as $RMS_{mean} = \frac{RMS}{n}$;
- the lines representative of the range at 66% as $y = a_m x + b_m \pm RMS_{mean}$;
- the lines representative of the range at 95% as $y = a_m x + b_m \pm RMS_{mean}$^2;

This reasoning can be considered complete for the range 33-333 kHz, and the results obtained are reported hereafter by a graph with relative equation of the line representative of the calibration for the above range.

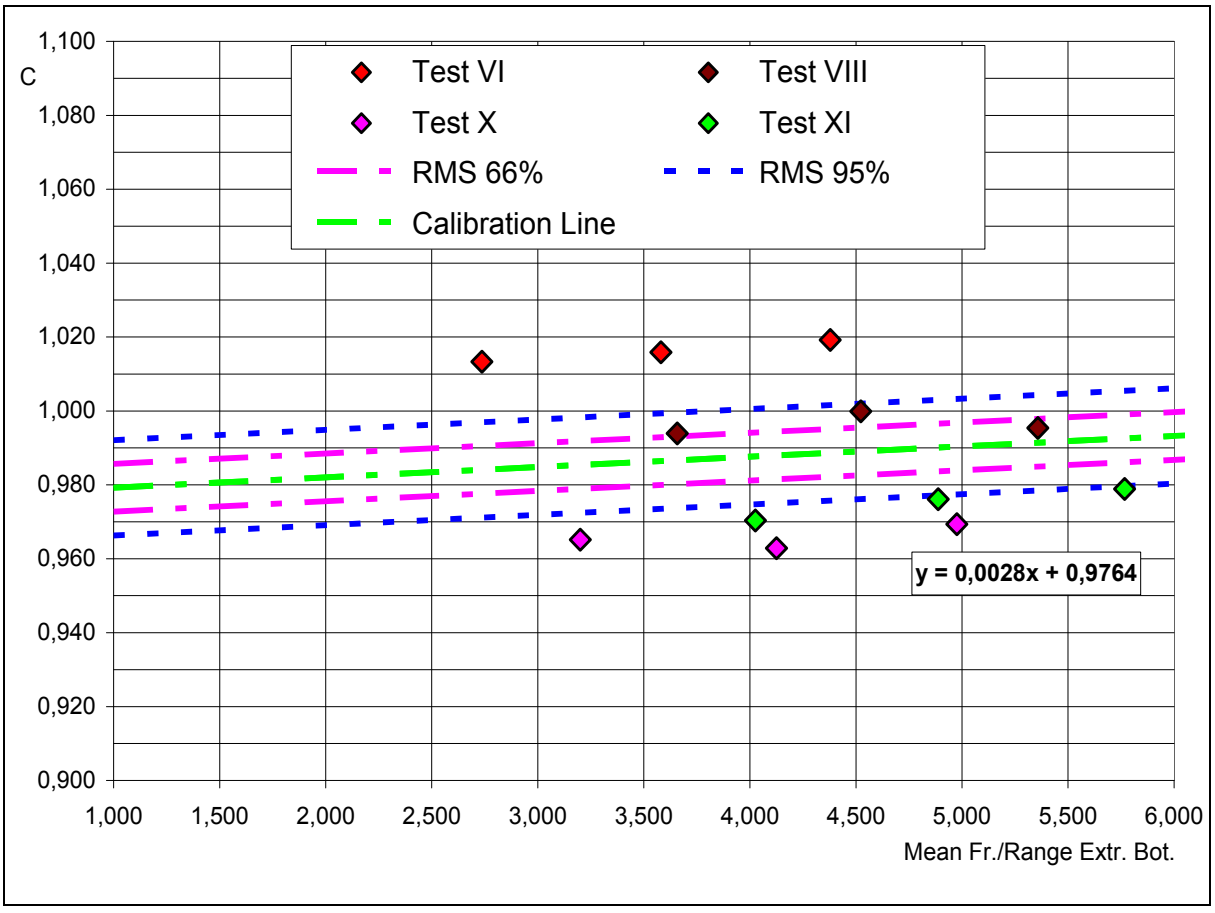

Fig. 9.25 - Equation of the line representative of the calibration constant for the range 33-333 kHz

As to the range 0.1-1 MHz, the processing cannot be complete, since it is necessary to add the calibration constant estimated in the previous experimentation, carried out on the channel described in chapter n.4, that is the value adopted with regard to the tests carried out on the boundary layer currents.

In order to be able to define a line that may consider also what previously said, it is

necessary to attribute to the previous calibration constant (equal to 0.9882 and equal to a value of *b* equal to 0.966) a weight in order to be able to process it together with the other experimental points.

The best method to compare these points is to weigh the variances of the two experimentations:

- for the recent data, by definition, it is enough to square the RMS mean;
- on the contrary, in order to weigh the calibration constant equal to 0.9882, it is necessary to go on with an intermediate statistical working out.

The error that can be made about the estimate of the tests carried out on the boundary layer channel concerns only the reading of the value of hydraulic load at the piezometer, situated in the feeding tank, as well as to the estimate of the channel free surface in the contracted section, for this reason:

- this error $\eta_{\max}$ can be estimated at 1.5 mm on 10.34cm read, therefore, its percentage value is of 1.5%;
- the standard deviation on the maximum error, according to a statistical method approved, can be estimated as $\sigma = 0{,}4\eta_{\max}$;
- to estimate the standard deviation on the velocity measured as $\sigma_v = \frac{\sigma}{2}$, since the velocity $v = \sqrt{2gh}$, considering that the square root halves the error;
- finally, the variance on the velocity measured is estimated as $VAR[v] = \sigma_v^2$.

At this point, for the construction of the line and of the actual ranges, it is necessary to estimate a b_{eff} weighted as to the inverse of the variances just calculated, and an effective variance that may considers also the weight of the calibration constant equal to 0.9882.

Thus, we calculate:

$$b_{eff} = \frac{\left(\frac{1}{VAR\left[y = a_m x + b_m\right]} \cdot b_m + \frac{1}{VAR[v]} \cdot b_{red} \right)}{\left(\frac{1}{VAR\left[y = a_m x + b_m\right]} + \frac{1}{VAR[v]} \right)}$$

being:

$b_{red} = y_{red} - a_m x_{red}$ with (x_{red}; y_{red}) the coordinates of the point representing the calibration constant equal to 0.9882;

$$\frac{1}{VAR\left[y = a_m x + b_{eff}\right]} = \left(\frac{1}{VAR\left[y = a_m x + b_m\right]} + \frac{1}{VAR[v]} \right);$$

$RMS_{eff} = \sqrt{VAR\left[y = a_m + b_{eff}\right]}$.

The line representative of the range at 66% is calculated as $y = a_m x + b_{eff} \pm RMS_{eff}$.

The line representative of the range at 95% is calculated as $y = a_m x + b_{eff} \pm RMS_{eff}\text{^}2$.

The results obtained are reported afterwards with a draft with the relative equation of the line representative of the calibration for the range 0.1-1 MHz.

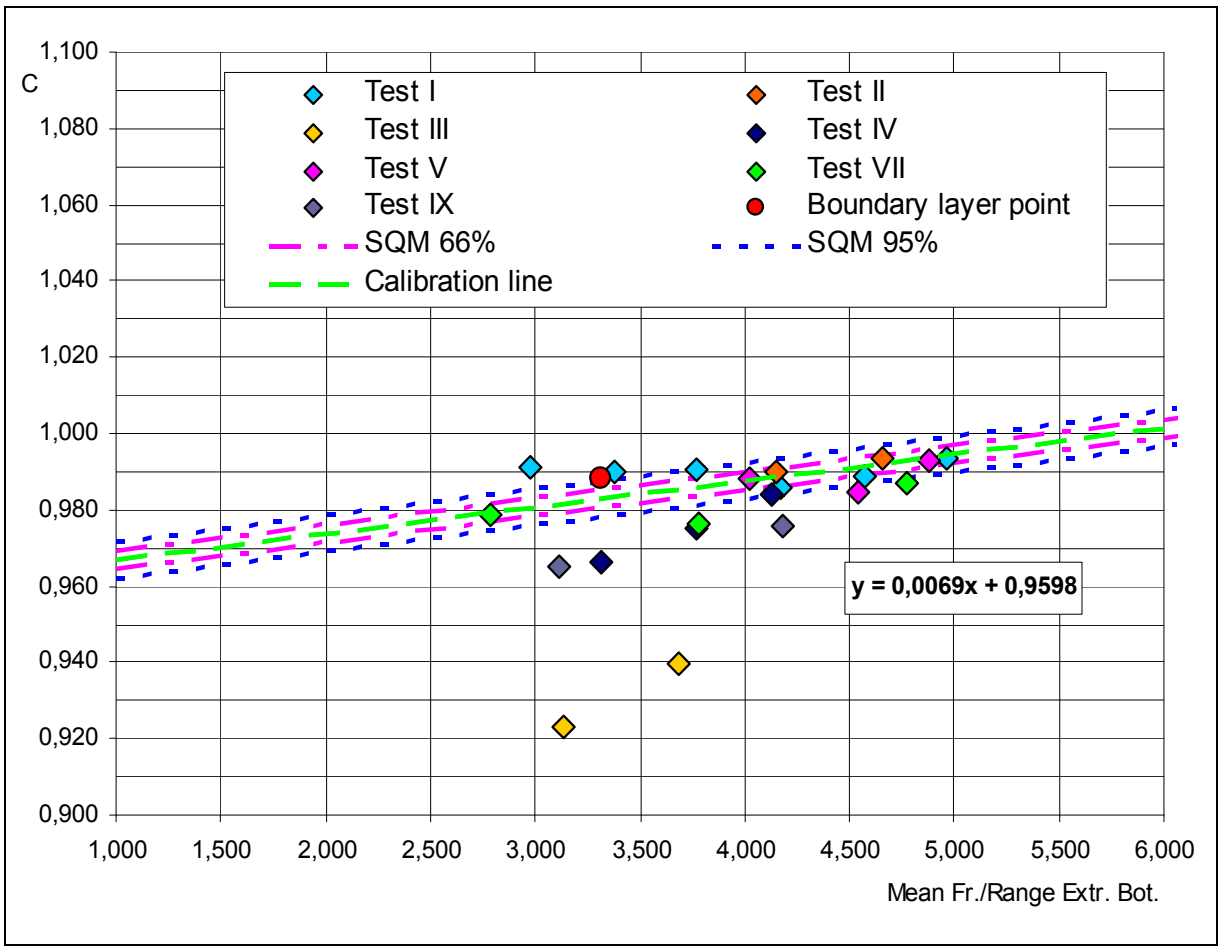

Fig. 9.26 - Equation of the line representative of the calibration constant for the range 0.1-1 MHz

Ultimately, we came to the definition of two equations representative of the calibration lines, that is:

$$C_1 = 0{,}0028\frac{Freq.}{Range\ Extr.Bottom} + 0{,}9764$$ for a frequency range 33-333 kHz;

$$C_2 = 0{,}0069\frac{Freq.}{Range\ Extr.Bottom} + 0{,}9598$$ for a frequency range 0,1-1 MHz.

These equations are representative of a value changing when the frequency changes, therefore it will be unique for each Doppler frequency value measured.

10. IMPLEMENTATION OF LABVIEW ACQUISITION AND DATA PROCESSING SOFTWARE

10.1 Introduction

The implementation of a suitable software in order to evaluate the turbulence statistics (specifically local mean velocity, variance, skewness, kurtosis, integral length scales) from the instantaneous velocity data collected was one of the fundamental aims of this Doctoral thesis.

This implementation has been a very noteworthy work and only its main characteristics will be briefly described in the second paragraph.

Obviously, on the contrary, the turbulence statistics will be very largely presented in the subsequent chapters, and a few definitions of these statistical terms will be reported in the third paragraph.

10.2 LabView software

In order to evaluate the turbulence statistics, the LabView software with the DAQmx Assistant, was used: with this integrated system it was possible, in real time, to acquire, to analyze and to present the data collected.

In particular, the implemented software permits to evaluate, in real time, local mean velocity, variances, skewness, kurtosis, starting from the acquisition of instantaneous velocities; thus being able to monitor the progress of the experimentation and to check possible faults.

In addition it is possible, through a second Virtual Instrument, to develop separately a successive data processing, and so, to be able to carry out the analysis of the integral length scales that also will be presented in the subsequent chapters.

The interface of the Virtual Instrument created ad hoc for this Doctoral thesis is shown in the following figure.

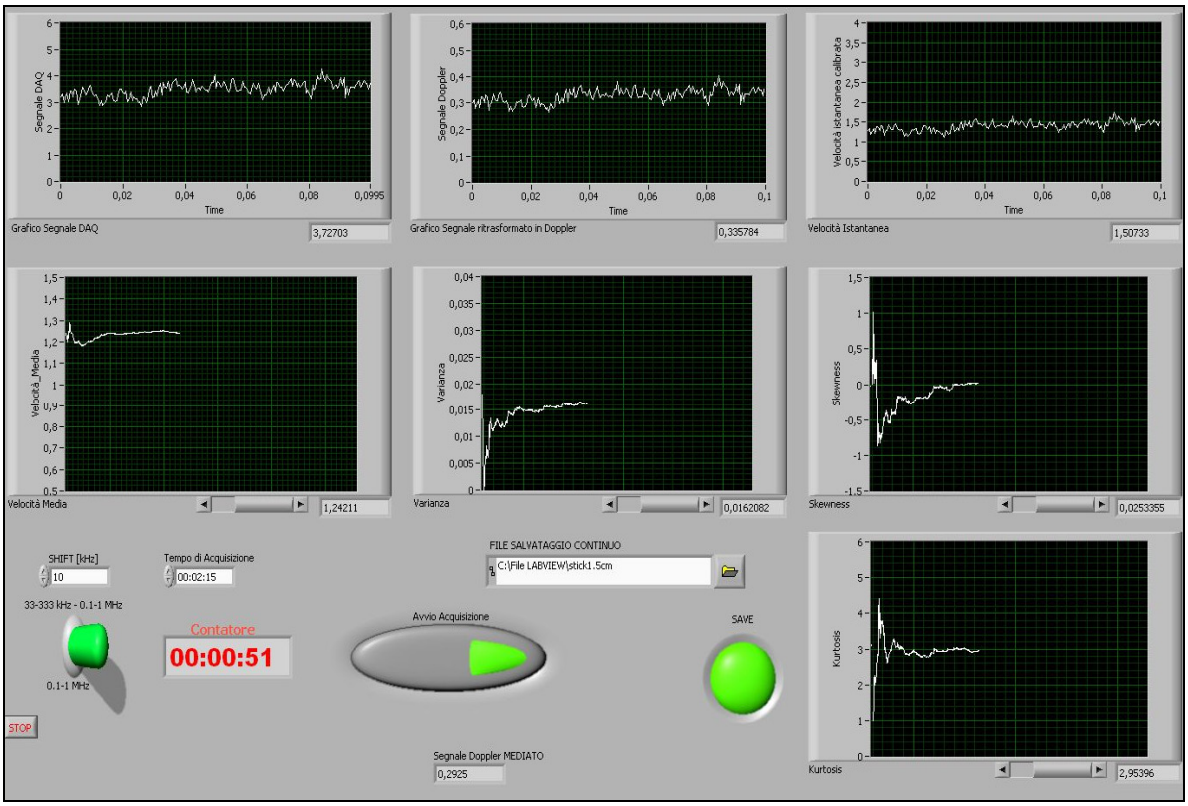

Fig. 10.1 - Real Time Virtual Instrument interface

Of course, as every acquisition system, also for the LabView it was necessary a calibration to compare the data obtained by the LabView software itself to the corresponding ones evaluated by the data analyzing system previously used, as to say the frequency tracker.

For this purpose, a repeated acquisition, extended in the time, was carried out in the same measurement point with different shift frequencies, reading the values supplied by the frequency tracker and the ones obtained by the LabView software.

By charting the data and carrying out a linear regression on such data, we obtained a transformation law (with a comparison coefficient equal to 0.9994) of the Doppler (frequency tracker) signal into current voltage (expressed in Volt, supplied by the acquisition chart DAQmx).

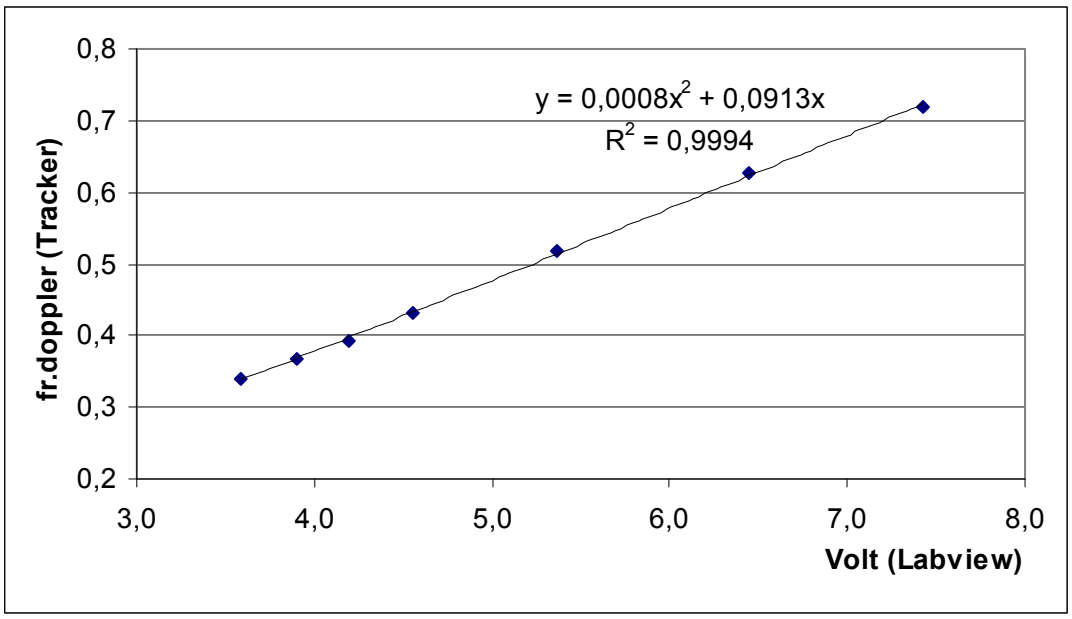

Fig. 10.2 - Transformation of the Doppler signal

The real advantage to use an acquisition system as the LabView lies in the possibility of storing all the time series of the data collected.

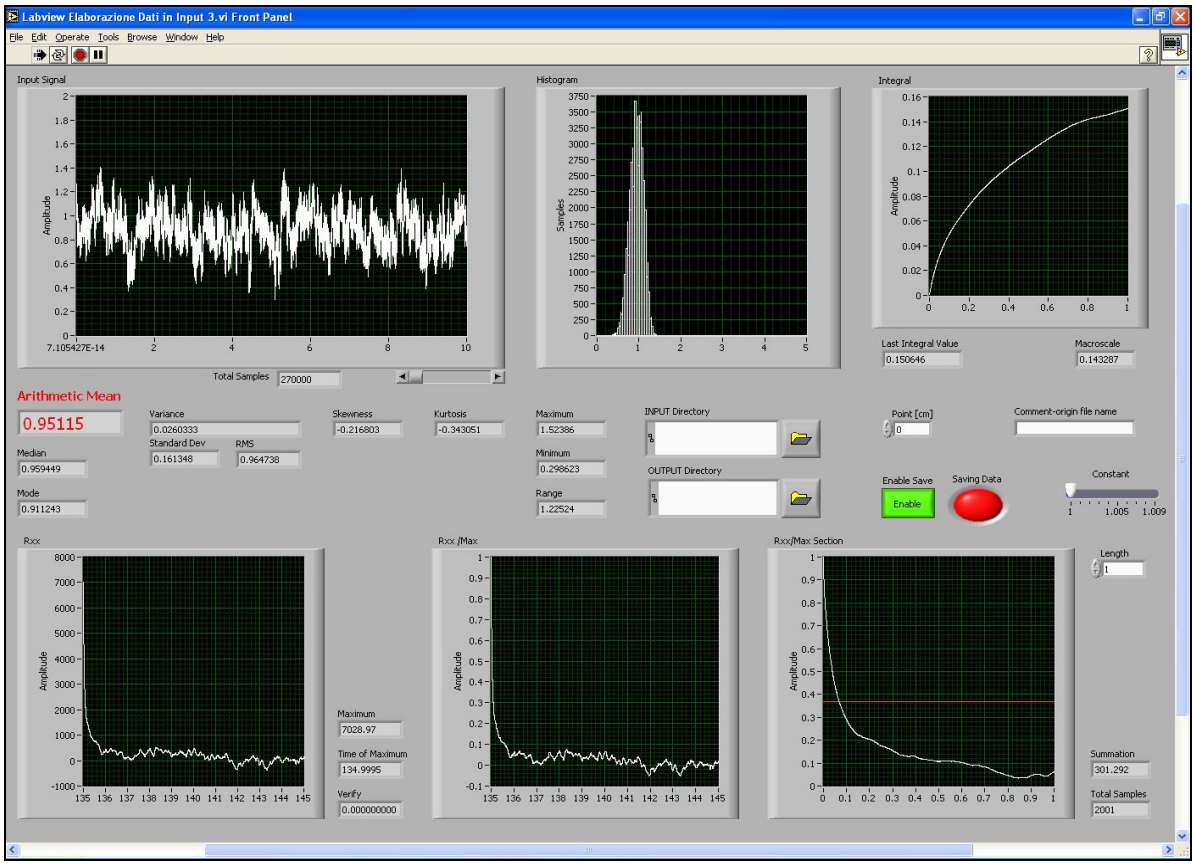

Fig. 10.3 - Virtual Instrument for stored data processing

10.3 Statistical basic concepts

A turbulent motion is a motion where chaotic motion superimpose to the main transport motion of a current, so that it happens that: $\vec{V} = \vec{V}(t)$.

Let's consider now an x axis coincident with the axis of the current. In this case the instantaneous value of the x component of the velocity (that in this paragraph we call U) appears as in Fig.10.4

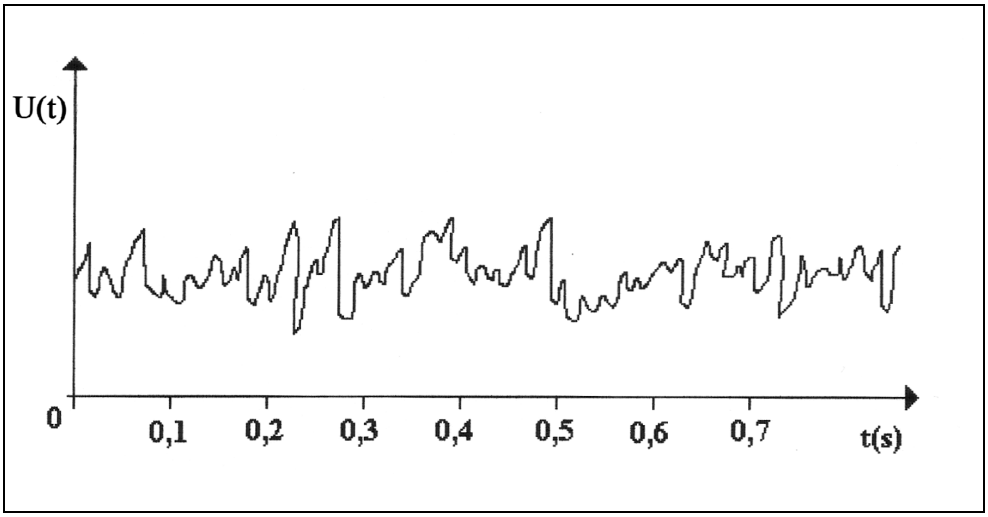

Fig. 10.4 - Instantaneous velocity function

Now we can in each instant t carry out the mean:

$$U_{mean} = \frac{1}{T}\int_{t-T/2}^{t+T/2} U(\theta)d\theta$$

In this mean the integration time T must be sufficiently large. In this case the mean will be called the "local mean value of U".

Now we can consider a new time function, i.e. the difference u'(t) between the whole instantaneous velocity U and its local mean value U_{mean} or also $\overline{U}$ that is called the "fluctuating component of U":

$$u'(t) = U(t) - \overline{U}$$

As a direct consequence of its definition, the local mean value of u'(t) is necessarily equal to 0.

A statistical quantity that defines the amplitude of the velocity fluctuations is the Variance V of the fluctuating x component u'(t). This Variance is defined as the local mean value of the squares of the instantaneous velocity fluctuation, i.e.:

$$V = \frac{1}{T}\int_{t-T/2}^{t+T/2}\left[u'(\theta)\right]^2 d\theta$$

Moreover two further statistical quantities are often considered always with regard to the fluctuating x component u'(t), i.e. the Skewness:

$$S_d = \frac{1}{T}\int_{t-T/2}^{t+T/2}\left[u'(\theta)\right]^3 d\theta$$

that represents the asymmetry of the u'(t) function with respect to its origin, and the Kurtosis:

$$K_d = \frac{1}{T}\int_{t-T/2}^{t+T/2}\left[u'(\theta)\right]^4 d\theta$$

that represents the deviation of the u'(t) function from Gaussian, in sense that u'(t) functions having large Kurtosis values are more sharply picked than are Gaussian distributions, and conversely.

Variance, Skewness and Kurtosis are expressions of the more general definition of Moment of order n of a time fluctuating function:

$$M_d = \frac{1}{T}\int_{t-T/2}^{t+T/2}\left[u'(\theta)\right]^m d\theta$$

In both definitions of Skewness and Kurtosis the suffix *d* is used to remember that the considered definitions are "dimensional" definition.

It is also possible to define Skewness and Kurtosis in a non dimensional way, dividing them by suitable powers of the Variance:

$$S = S_d / V^{3/2}$$

$$K = K_d / V^2$$

Lastly it must be stressed that the value of S in case the u'(t) has a Gaussian amplitude distribution is just 0, whereas the value of the Kurtosis in case of Gaussian distribution of u'(t) amplitudes is just 3. Due to this result, often a new Kurtosis definition is given, i.e.:

$$K = K_d / V^2 - 3$$

In such a way also the Kurtosis will be equal to 0 with a Gaussian distribution. This is the shape of the Kurtosis that will be implemented in this work.

Another relevant statistical quantity is the longitudinal integral length scale. Its definition starts from the autocorrelation function definition:

$$\varphi_{11}(\tau) = \frac{1}{T}\int_{-T/2}^{T/2} u'(t)u'(t+\tau)dt$$

Autocorrelation is a function that provides a measure of how well a signal "remembers" its temporal or spatial values (in this case, temporal); it is an integral over time (or space, in this specific case over time) of a value of the signal (in this specific case the function u'(t)) at a given time, multiplied times a copy with shifted time (or space, in this specific case time) argument. In the specific case the considered function is u'(t).

Here too, this is a dimensional definition. The correspondent non dimensional definition is the following one:

$$\varphi_{11n}(\tau)=\frac{\varphi_{11}(\tau)}{\varphi_{11}(0)}=\frac{\overline{u'(t)u'(t+\tau)}}{\overline{u'(t)u'(t)}}$$

The general shape of the non dimensional autocorrelation is shown in the following Fig. 10.5.

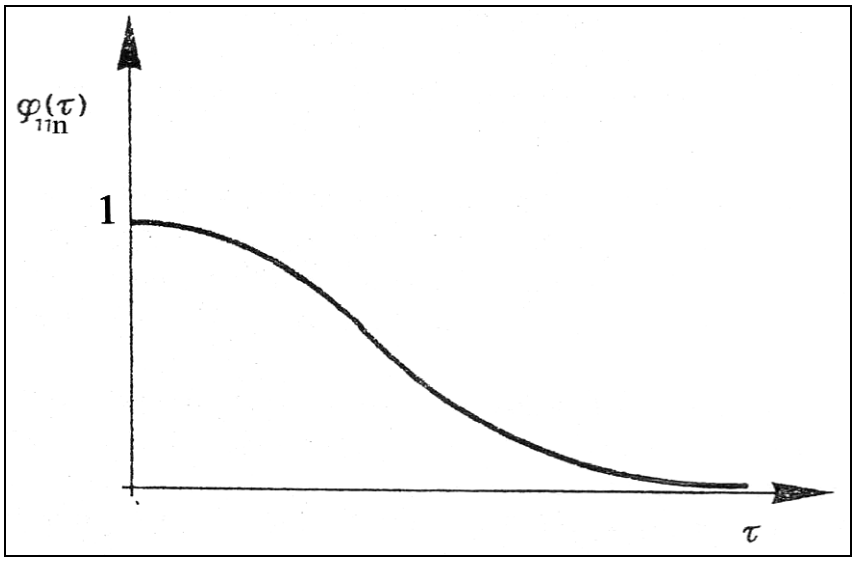

Fig. 10.5 - Space autocorrelation function

Now the Taylor's hypothesis states that in a turbulent flow for which the magnitude of the fluctuations is not too great, it is possible to deduce spatial turbulence quantities from time series measured at a single point of the flow.

If we use the Taylor's hypothesis and consequently we change the τ time variable in the ξ=Uτ longitudinal length variable, then the autocorrelation becomes:

$$\varphi_{11}(\xi)=\frac{1}{L}\int_{-L/2}^{L/2}u'(x)u'(x+\xi)dx$$

And the non dimensional autocorrelation becomes:

$$\varphi_{11n}(\xi)=\frac{\varphi_{11}(\xi)}{\varphi_{11}(0)}=\frac{\overline{u'(x)u'(x+\xi)}}{\overline{u'(x)u'(x)}}$$

And the shape of the curve will be as in Fig 10.6.

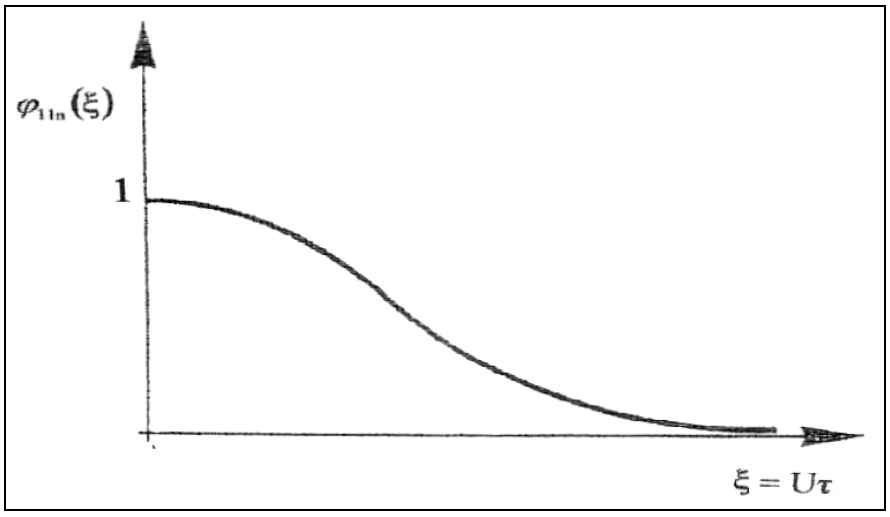

Fig. 10.6 - Time autocorrelation function

The area under the longitudinal autocorrelation curve is lastly defined as the longitudinal integral length scale of the turbulent motion.

It is noteworthy that, due to some problem in the integration operation, in this work, as suggested in some literature paper, the longitudinal integral length scale will be computed through the integration not performed till $+\infty$ but only till the abscissa where the non dimensional autocorrelation attains a value equal to 1/e.

11. TESTS ON A BOUNDARY LAYER CURRENT: CLASSICAL METHODOLOGY TO MAKE EXPERIMENTAL DATA NON DIMENSIONAL

11.1 Description of the tests with measurement points coaxial to the mesh of the cylinders

The experimental tests, carried out on vegetated bed as described in the fourth chapter, were conducted according to the following hydraulic conditions, kept identical to each configuration in order to allow a suitable comparison:

- the height of the sluice gate that is 7.49 cm,
- the load on the vena contracta is 10.34 cm,
- the velocity of the external stream is 1.424 m/s,
- and the flow rate is 9.85 l/s.

So as to have an equilibrium boundary layer, that is with the piezometric gradient head constant (in particular null and so free surface horizontal) along the flow direction, it was necessary to rise the slope of the channel further on with respect to quoted previous experimentations: this was due to the increase of head losses, generated by the growth in the height of the cylinders.

In the following table a comparison among the experimentations is showed.

Table 11.1 - Slopes used in different cases

	Smooth	**Rough 5 mm**	**Rough 10 mm**	**Rough 15 mm**
Single Density	0.25%	0.92%	1.6%	**2.27%**
Double Density	0.25%	1.15%	2.05%	**2.95%**

In each test section many mean velocity values (from 20 to 30) have been measured along its central vertical, so as to obtain suitable local mean velocity distributions.

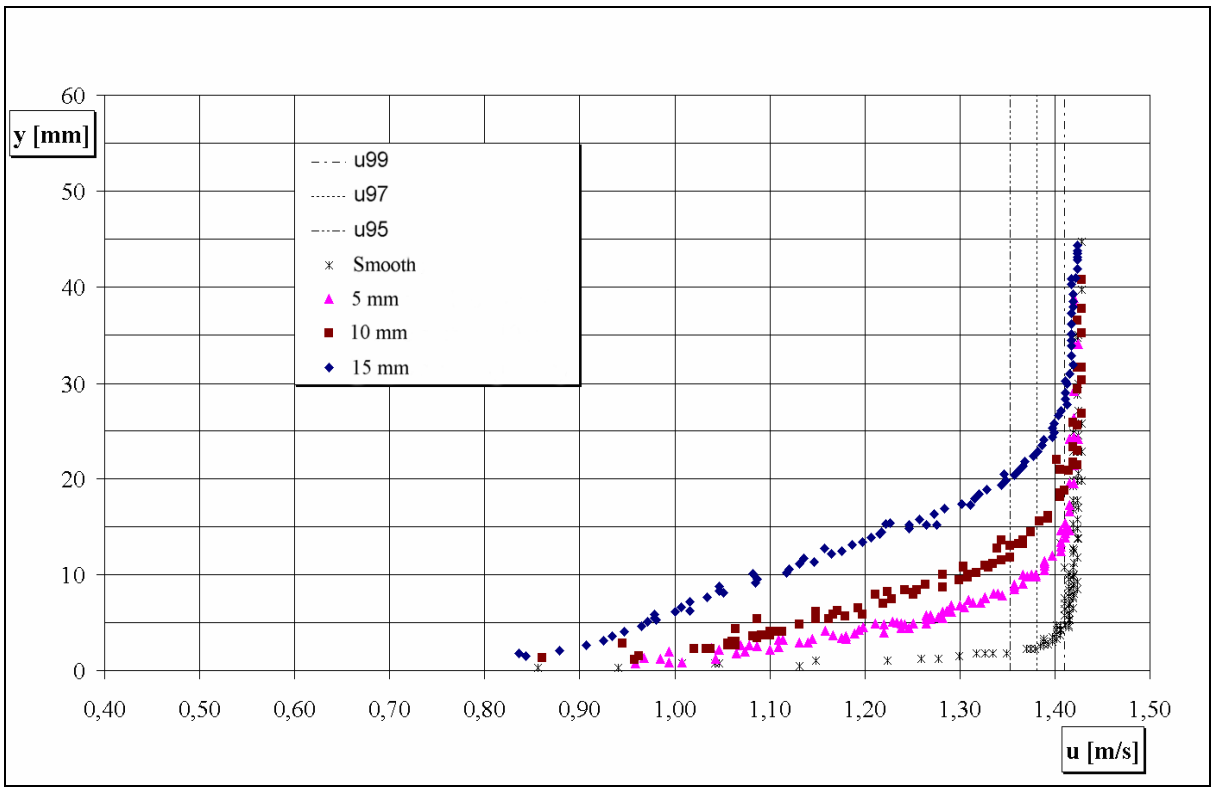

Fig. 11.1 - Local mean velocity distributions in test section n.1 (single density)

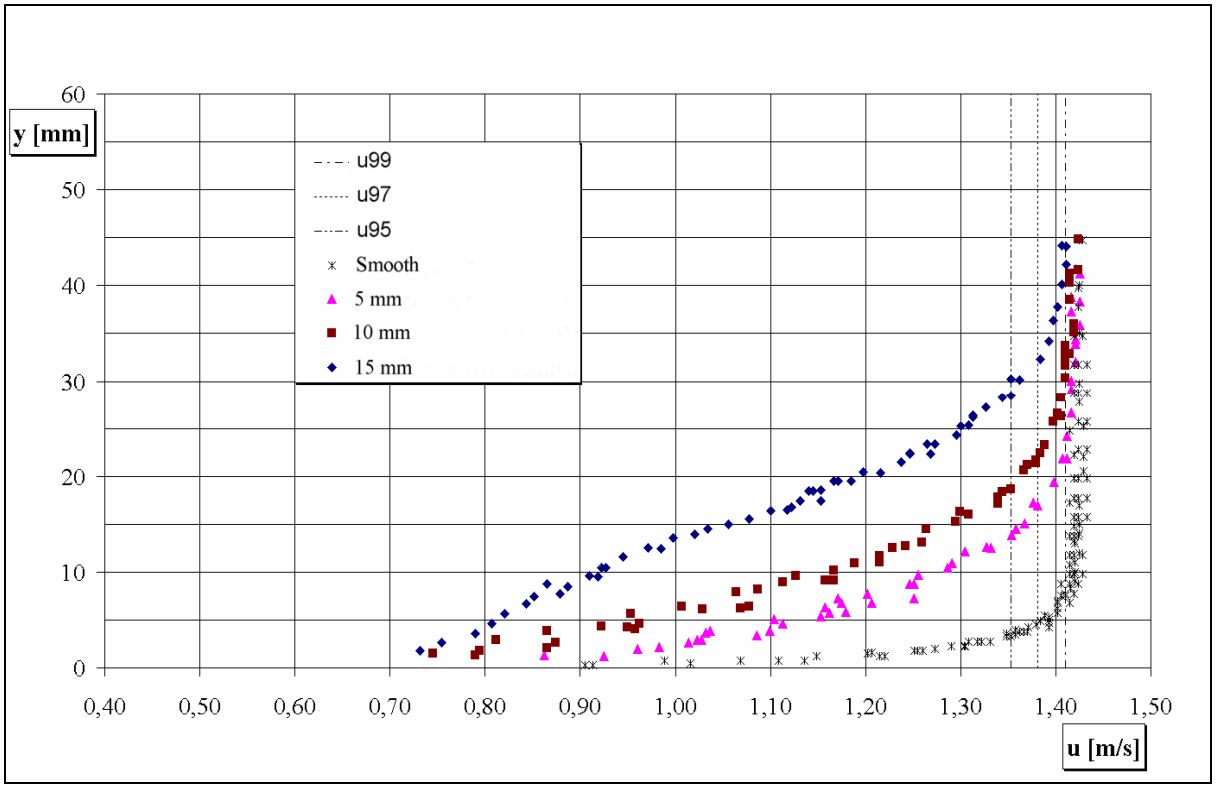

Fig. 11.2 - Local mean velocity distributions in test section n.2 (single density)

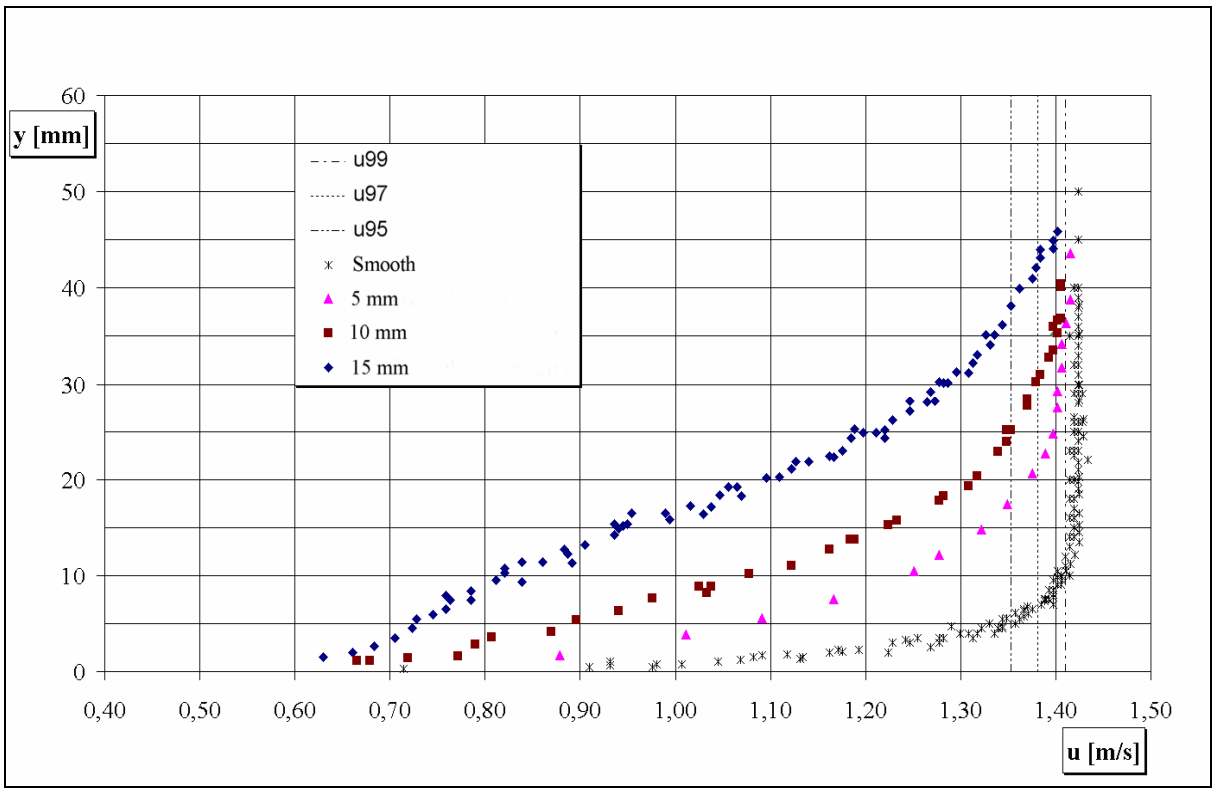

Fig. 11.3 - Local mean velocity distributions in test section n.3 (single density)

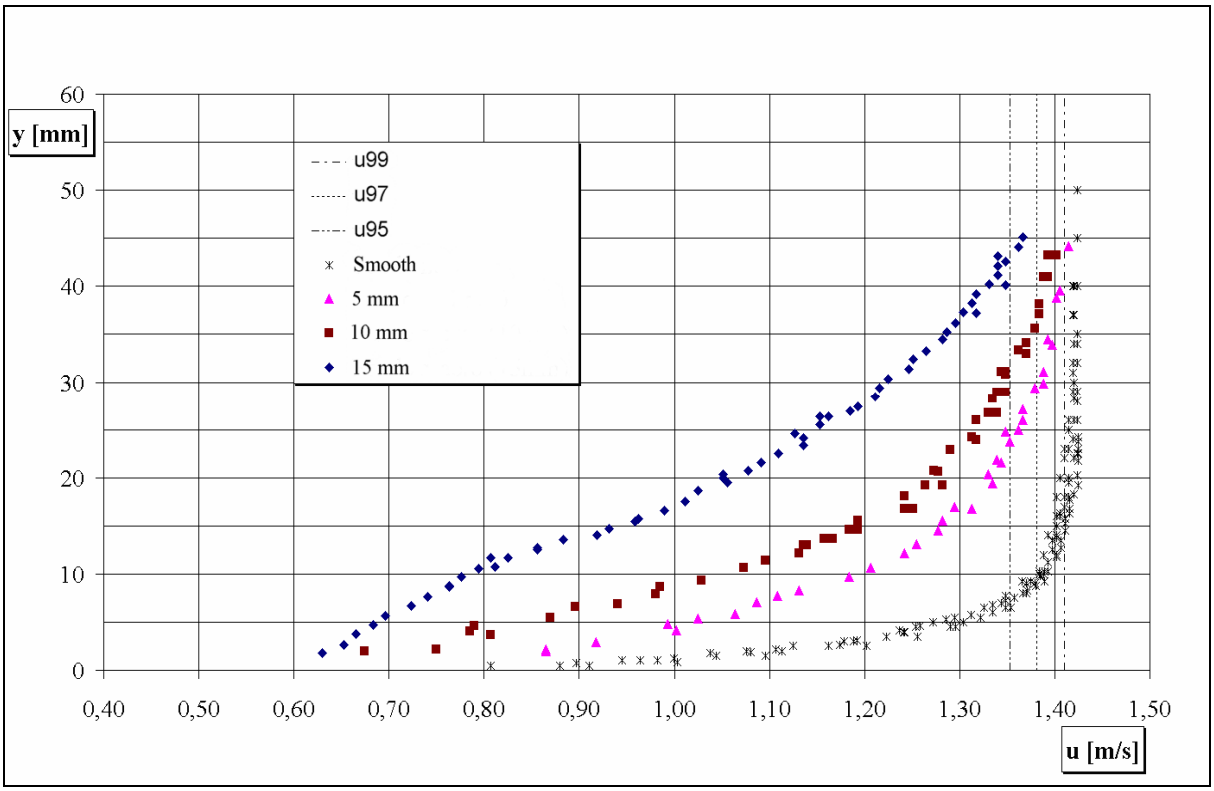

Fig. 11.4 - Local mean velocity distributions in test section n.4 (single density)

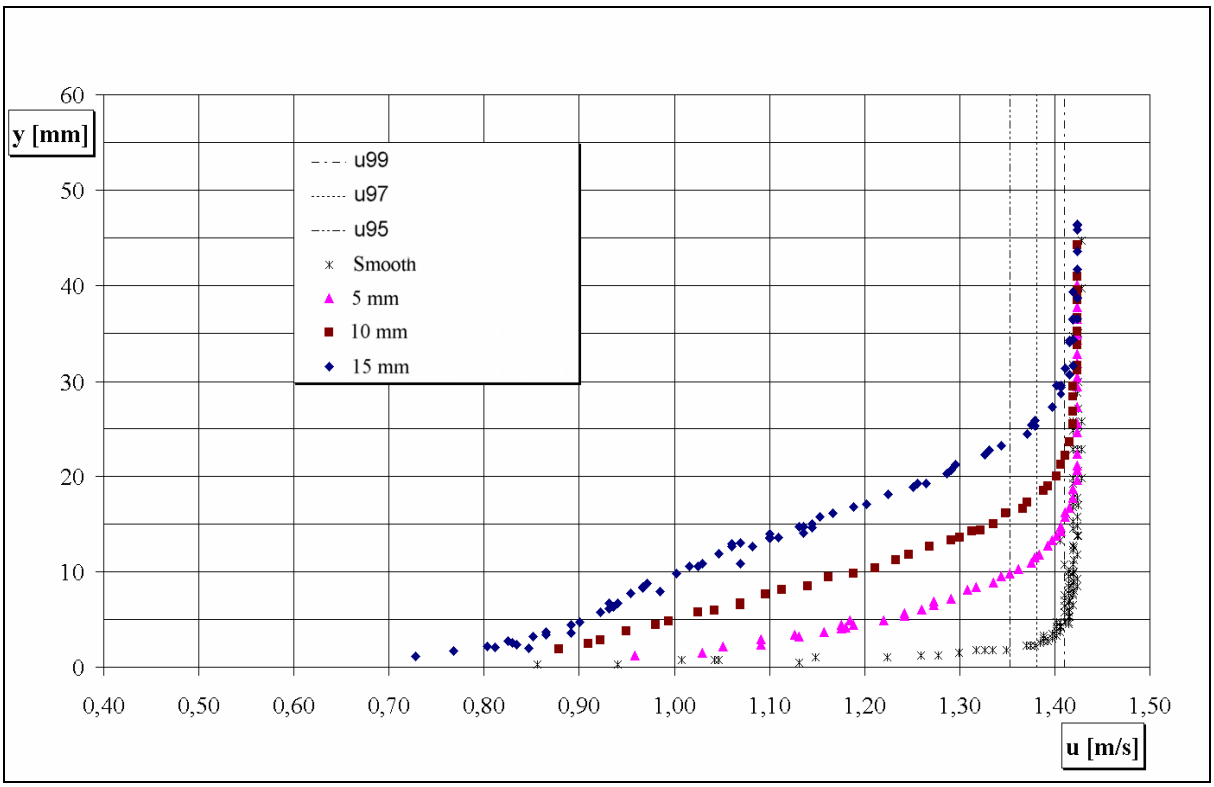

Fig. 11.5 - Local mean velocity distributions in test section n.1 (double density)

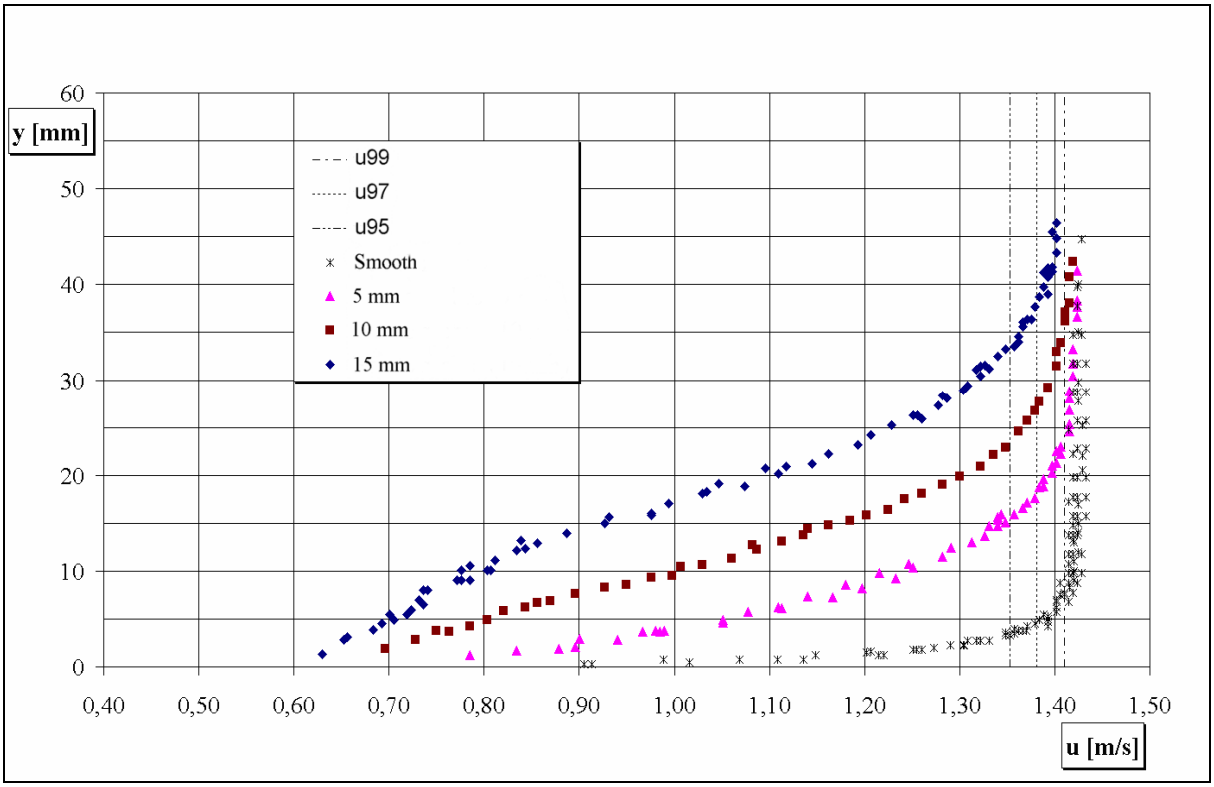

Fig. 11.6 - Local mean velocity distributions in test section n.2 (double density)

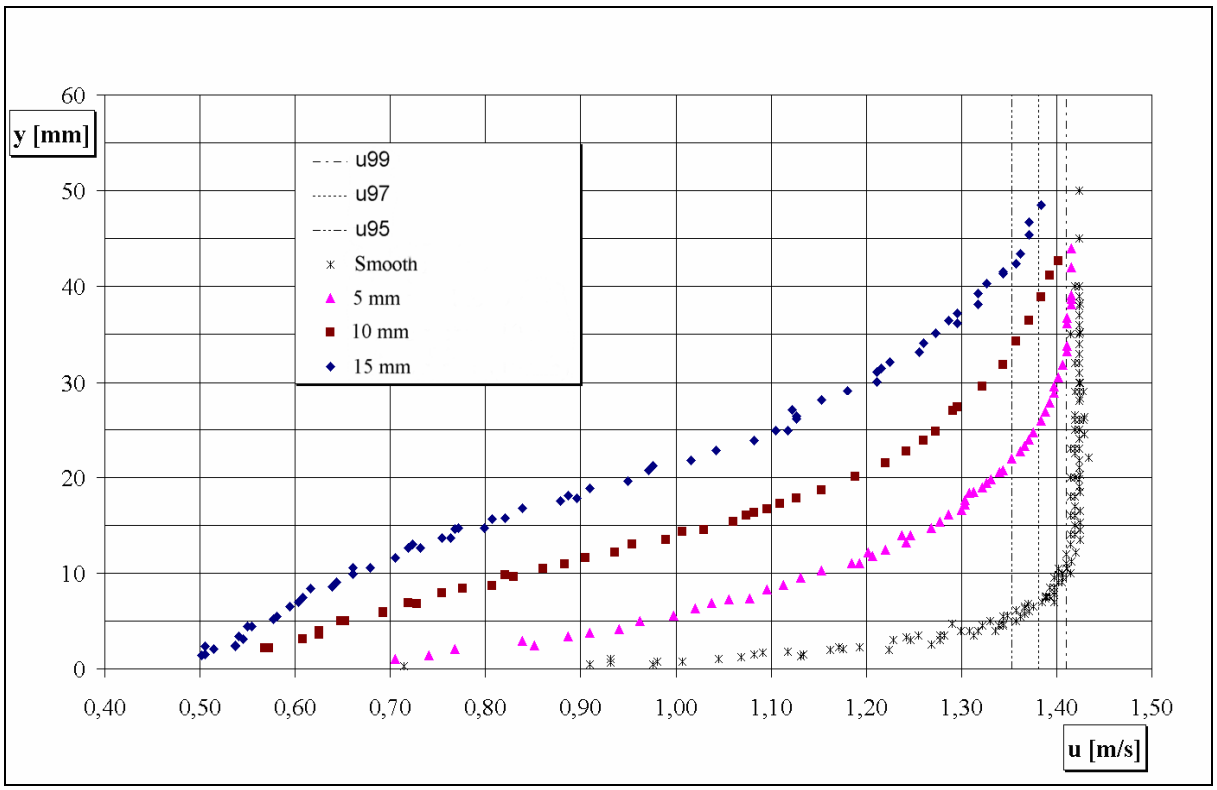

Fig. 11.7 - Local mean velocity distributions in test section n.3 (double density)

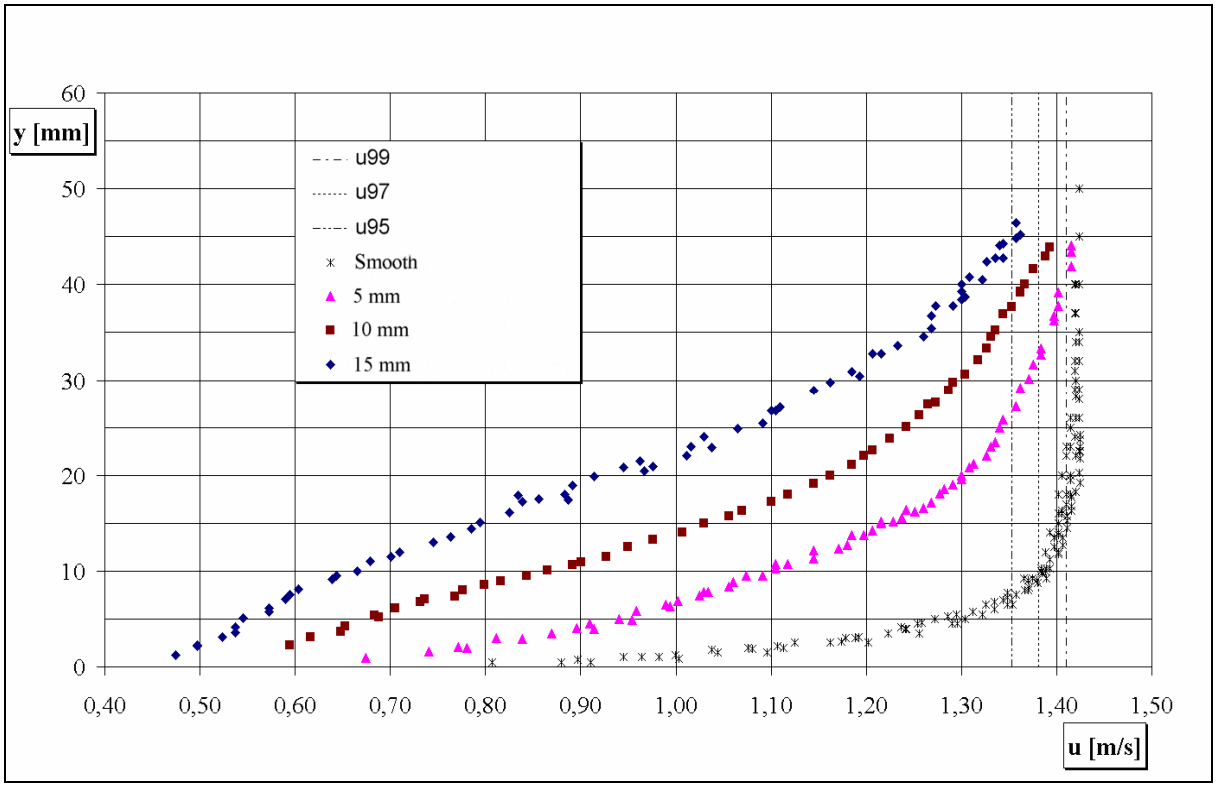

Fig. 11.8 - Local mean velocity distributions in test section n.4 (double density)

11.2 Calculation of the boundary layer thickness

From the local mean velocity distributions, the values of the thickness of the boundary layer shown in the Tables 11.2 and 11.3 have been obtained.

However, it is important to point out that the direct reading of the δ_{99} is not possible in all the local mean velocity distributions: therefore it was necessary to adopt a method of computing the δ_{99} based on the readings of the δ_{95}.

Obviously δ_{99} and δ_{95} are, respectively, the boundary layer thickness based on 99% and on 95% of the external stream velocity.

Table 11.2 - Thickness of the boundary layers (single density)

Thickness of the boundary layer	Smooth	Rough 5 mm	Rough 10 mm	Rough 15 mm
δ_{S1} (mm)	3.8	14.6	20.0	**29.5**
δ_{S2} (mm)	7.1	25.6	31.4	**43.5**
δ_{S3} (mm)	10.9	32.0	42.1	**56.8**
δ_{S4} (mm)	13.5	42.2	51.3	**64.1**

Table 11.3 -Thickness of the boundary layers (double density)

Thickness of the boundary layer	Smooth	Rough 5 mm	Rough 10 mm	Rough 15 mm
δ_{S1} (mm)	3.8	16.0	22.0	**31.5**
δ_{S2} (mm)	7.1	26.3	33.9	**45.5**
δ_{S3} (mm)	10.9	35.1	47.7	**56.7**
δ_{S4} (mm)	13.5	44.0	52.4	**62.2**

The method used was the following one:

- the values of the δ_{99} were read with much more precision in the sections where it was possible in the condition of single and double density;
- the values of the δ_{95} in both density conditions were read;
- the ratio δ_{99}/δ_{95} were calculated whenever possible. If the boundary layer, in any flow condition, is an equilibrium boundary layer, the above ratio must be, in each condition, equal in all test sections. Probable differences are to be ascribed to reading errors, above all about the δ_{99} values;
- in order to minimize such reading errors the mean of these ratios were computed,

separately for the two types of density.

The obtained mean values multiplied by the δ_{95} were considered as the real δ_{99} and the ones shown in Tables 11.2 and 11.3 in boldface.

Perhaps, it is useful to underline the fact that sometimes the thickness shown in Tables 11.2 and 11.3 exceed the thickness of the flow, and therefore, it must be considered as "virtual thickness".

The concept of "virtual thickness" can be found also in previous works about the boundary layer and it has the following meaning. The "virtual thickness" represents the "scale" to make non dimensional the heights of the points corresponding to the local mean velocities values when the boundary layer "breaks" the free surface of the current.

In particular the local mean velocity distributions obtained for each test section and each flow condition can be changed into non dimensional ones, taking into consideration the ratio between the local mean velocity measured and the velocity in the external layer (the latter being constant in every flow condition), and the ratio between the height of the measurement point and the thickness of the boundary layer (the latter being different in each test section and in each flow condition), shown in Tables 11.2 and 11.3.

11.3 Non dimensional velocity profiles

The non dimensional velocity distributions are shown in Figs. 11.9 - 11.15.

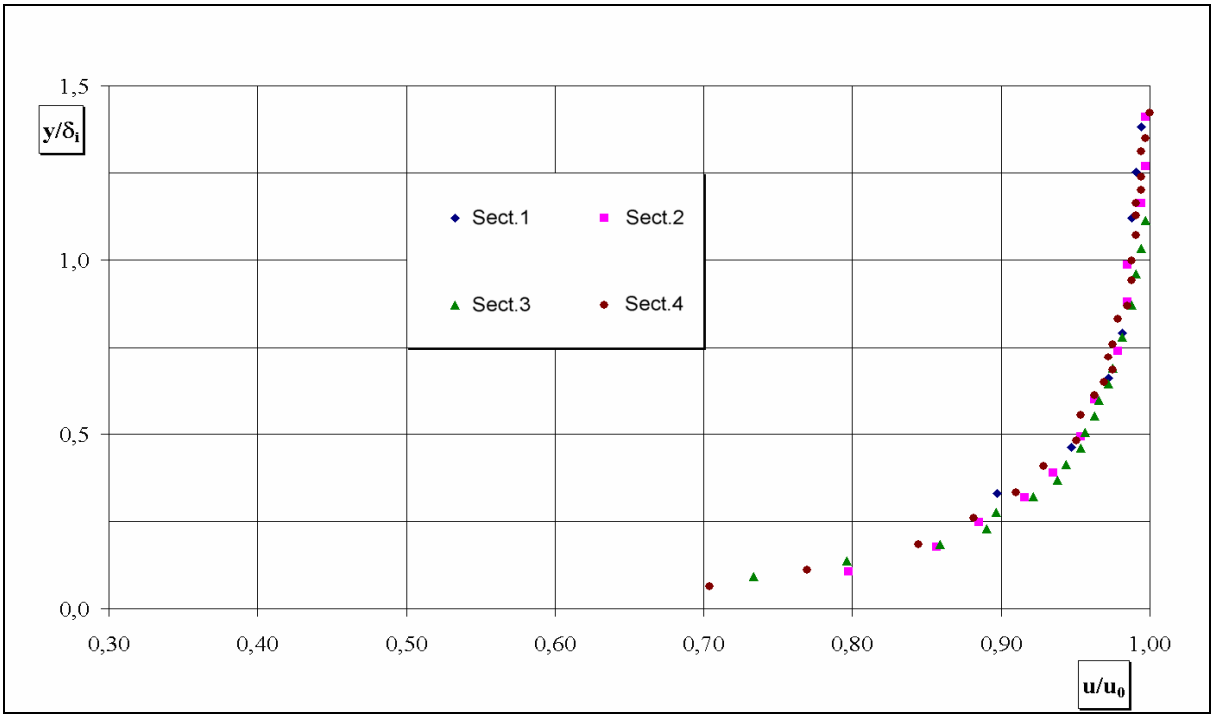

Fig. 11.9 - Non dimensional local mean velocity distributions: smooth bottom

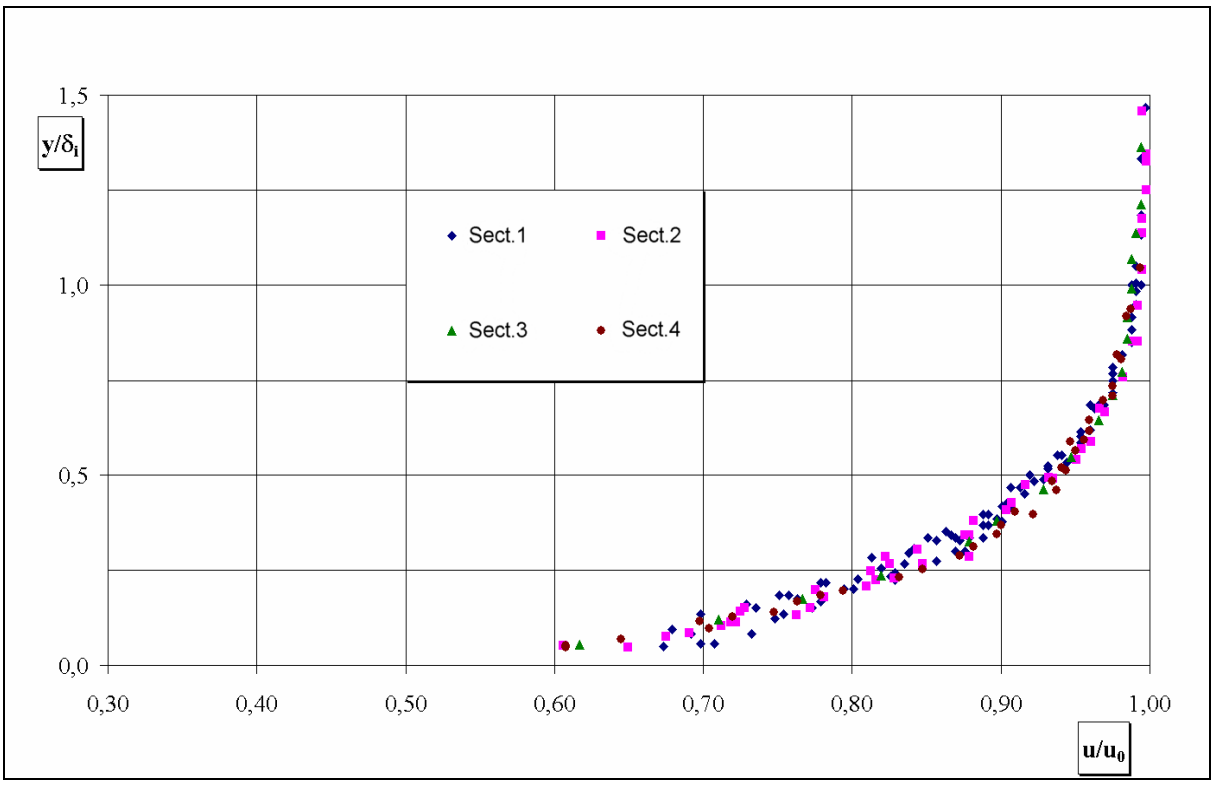

Fig. 11.10 - Non dimensional local mean velocity distributions: 5 mm cylinders single density

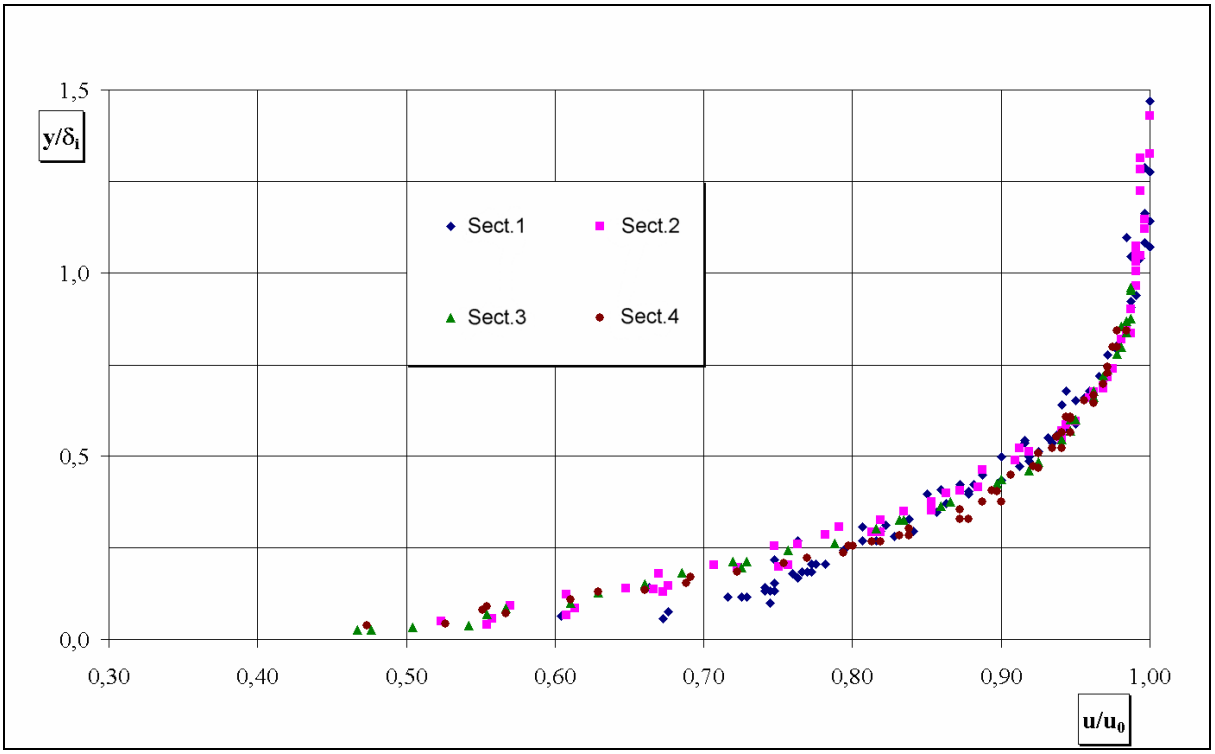

Fig. 11.11 - Non dimensional local mean velocity distributions: 10 mm cylinders single density

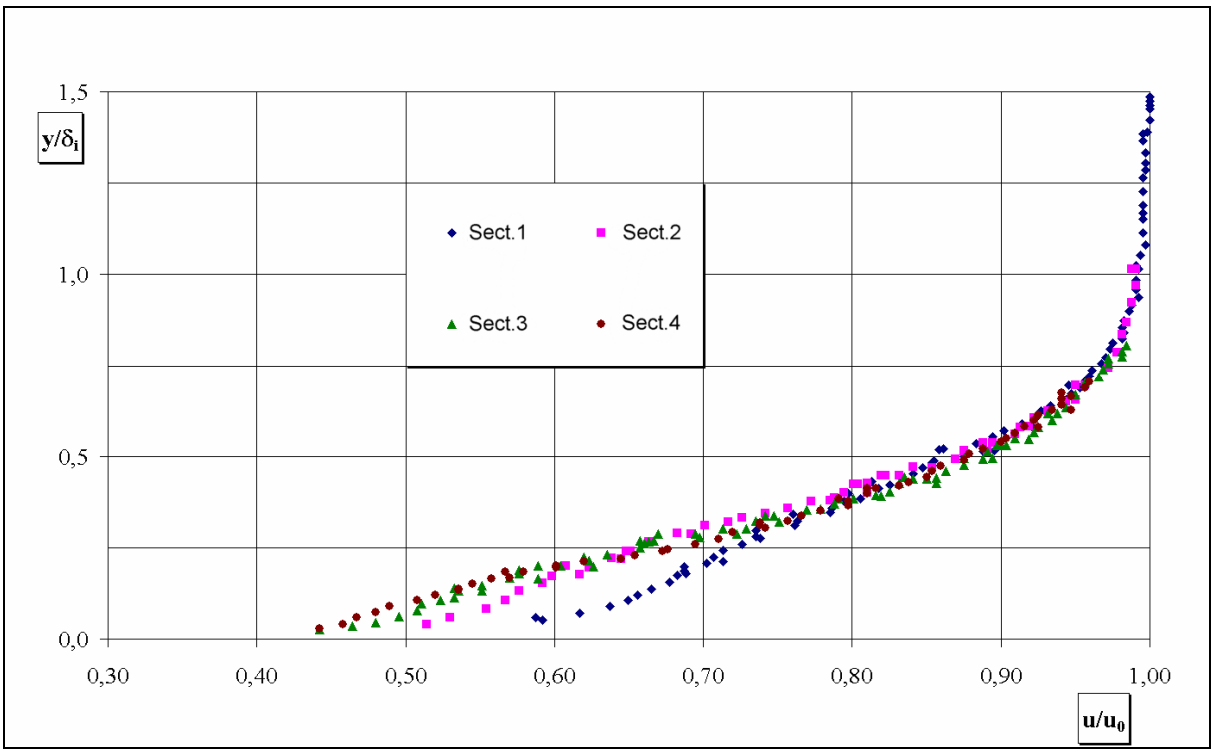

Fig. 11.12 - Non dimensional local mean velocity distributions: 15 mm cylinders single density

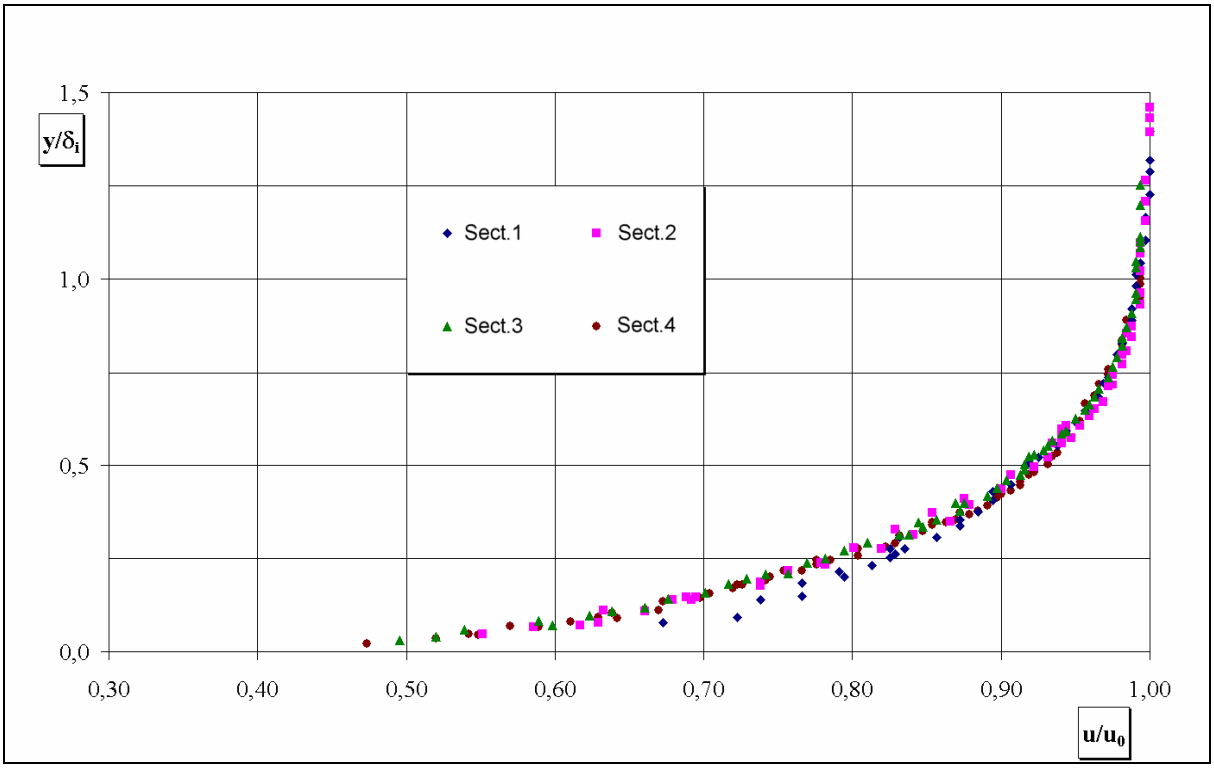

Fig. 11.13 - Non dimensional local mean velocity distributions: 5 mm cylinders double density

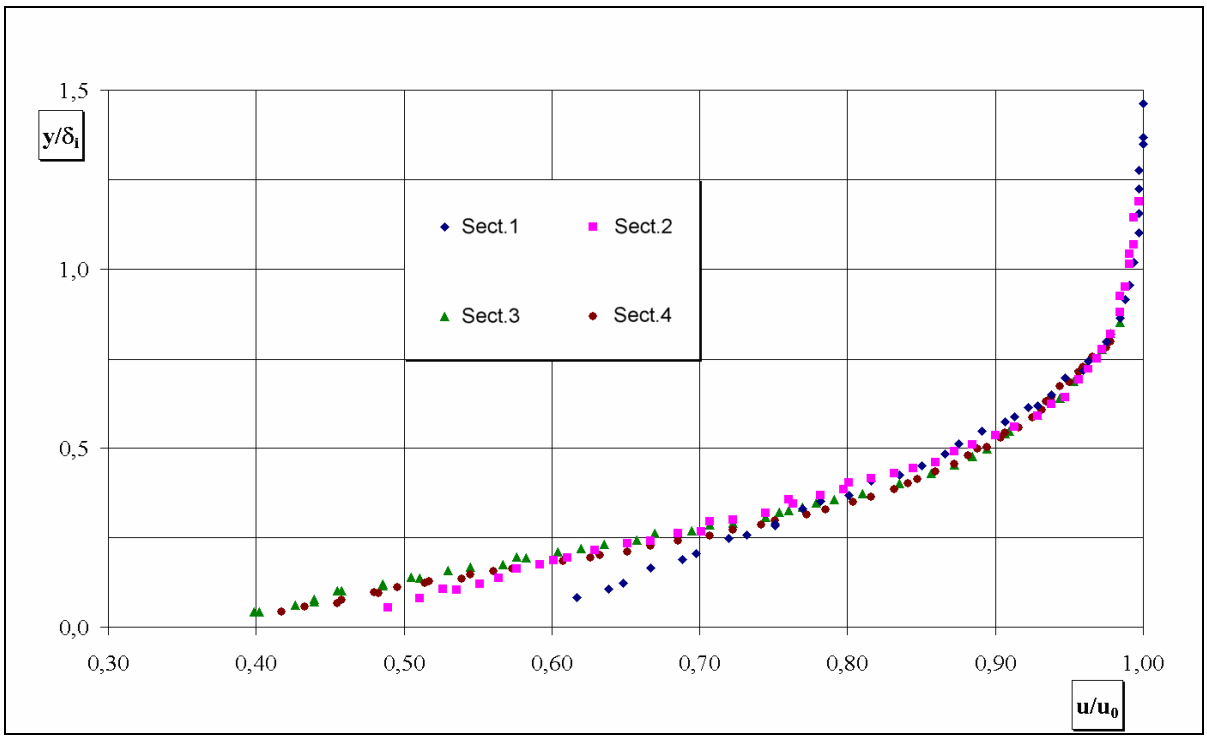

Fig. 11.14 - Non dimensional local mean velocity distributions: 10 mm cylinders double density

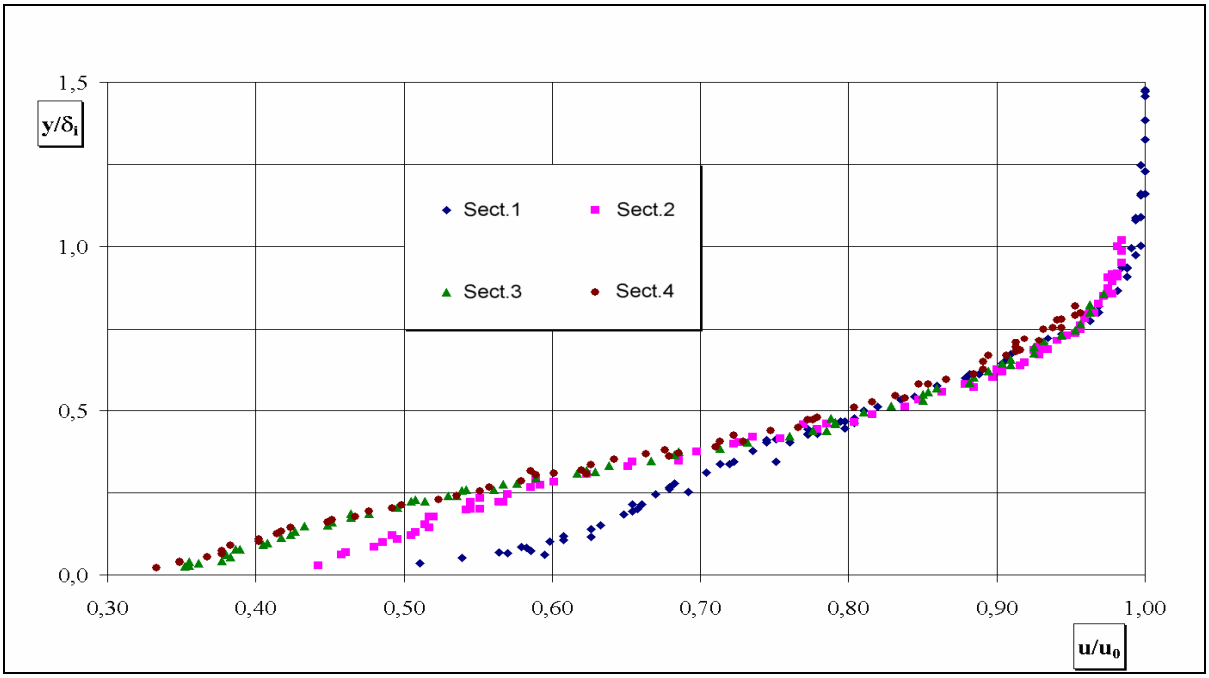

Fig. 11.15 - Non dimensional local mean velocity distributions: 15 mm cylinders double density

While in the smooth and 5 mm cases the non dimensional local mean velocity distributions relative to the different test sections tend to be superimposed one upon another, in the 10 and 15 mm ones, on the contrary, it is clear that, below a certain value of the y/δ ratio, they tend to separate visibly, with particular reference to the distributions concerning the first two sections.

This circumstance does not make it possible any longer to speak about a "total" equilibrium state of the boundary layer; it would be more opportune to speak about a "partial" equilibrium, in order to consider the different behaviour according to the change of y/δ ratio.

In order to realize why in some sections there is not superimposition any longer, it is convenient to create a new table, Table 11.4, where the ratio among the heights of the boundary layer and of the cylinders are shown.

Table 11.4 - Ratio between thickness of the boundary layer and height of cylinders

	20 cm	**30 cm**	**40 cm**	**50 cm**
5 mm single density	2.92	5.12	6.40	8.44
10 mm single density	2.00*	3.14	4.21	5.13
15 mm single density	**1.97***	**2.90***	**3.79**	**4.27**
5 mm double density	3.20*	5.26	7.02	8.80
10 mm double density	2.20*	3.39*	4.77	5.24
15 mm double density	**2.10***	**3.03***	**3.78**	**4.15**

An asterisk marks the cases where such superimposition disappears. As it is evident particularly in the experimentations made with cylinders 15 mm high, this happens in the 20 cm and 30 cm sections.

From the Table 11.4 it is possible to evaluate a limit value of the ratio, depending on the density of the cylinders, below which the anomaly pointed out in the non dimensional distributions appears.

Such limit value has been estimated about 2.9 for the single density, and about 3.6 for the double density, which are the mean values of the following ranges: 2.90 and 2.92 for the single density, and 3.39 and 3.78 for the double density.

Besides, the Table 11.5 shows the ratios between the values of the Table 11.4 and the limit values previously estimated.

Table 11.5 - Ratio between values of the Table 11.4 and corresponding limit values

	20 cm	**30 cm**	**40 cm**	**50 cm**
5 mm single density	1,01	1,77	2,21	2,91
10 mm single density	0,69*	1,08	1,45	1,77
15 mm single density	**0,68***	**1,00***	**1,31**	**1,47**
5 mm double density	0,89*	1,46	1,95	2,44
10 mm double density	0,61*	0,94*	1,33	1,46
15 mm double density	**0,58***	**0,84***	**1,05**	**1,15**

It is possible to notice clearly that, where the anomaly is scarcely visible, the ratio is about 1; when the anomaly becomes more evident, the ratio decreases, and the smaller the ratio is the more evident the anomaly is. In short, it is possible to conclude that, in any case, according to the density of the cylinders, as long as the height of the cylinders is enough smaller than the thickness of the boundary layer, the boundary layer seems to be of "total" equilibrium; while, when the height of the cylinders is a considerable fraction of the thickness of the boundary layer, this loses the characteristic of "total" equilibrium and becomes a "partial" equilibrium.

Moreover it is interesting to notice that where the anomaly is evident the dimensional local mean velocity distributions too show some irregularities at the height of the cylinders.

In Figs. 11.16 and 11.17 are reported together the four non dimensional local mean velocity distributions concerning the smooth plate and vegetated plate with 5, 10, 15 mm high cylinders respectively relative to single and double density, after eliminating the points relative to the non equilibrium conditions from each distribution.

It is clearly visible that in each figure the four distributions are not superimposed among them, but they follow distinct laws.

Besides, if we compare the two figures, it is possible to observe that, apart from the distributions concerning the smooth plate, which are the same in both, there is not superimposition even between distributions relative to the same height of the cylinders, but of different densities.

In confirmation of this last remark, in Figs. 11.18, 11.19 and 11.20 the non dimensional local mean velocity distributions concerning vegetated plates with 5, 10 and 15 mm high cylinders, with single and double density, have been reported.

Actually, it is noted that the non dimensional curves do not superimpose one upon another even in this second way of representation.

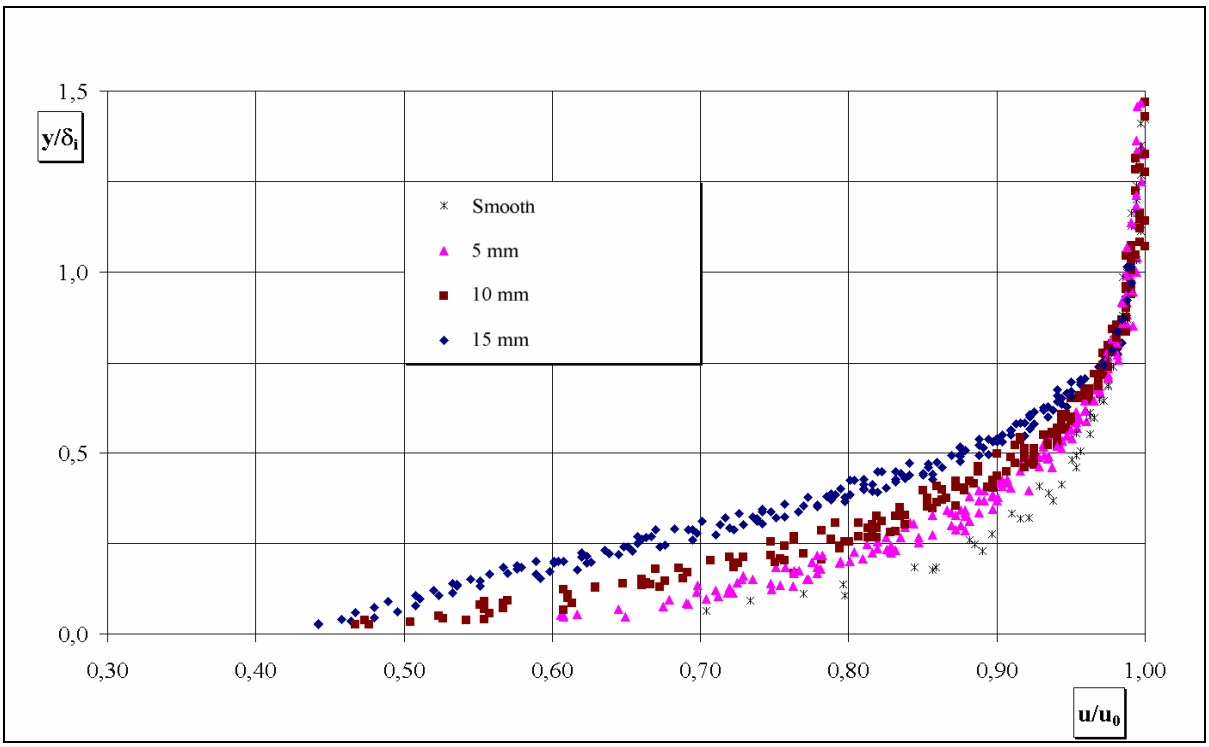

Fig. 11.16 - Non dimensional local mean velocity distributions (0, 5, 10, 15 mm single density)

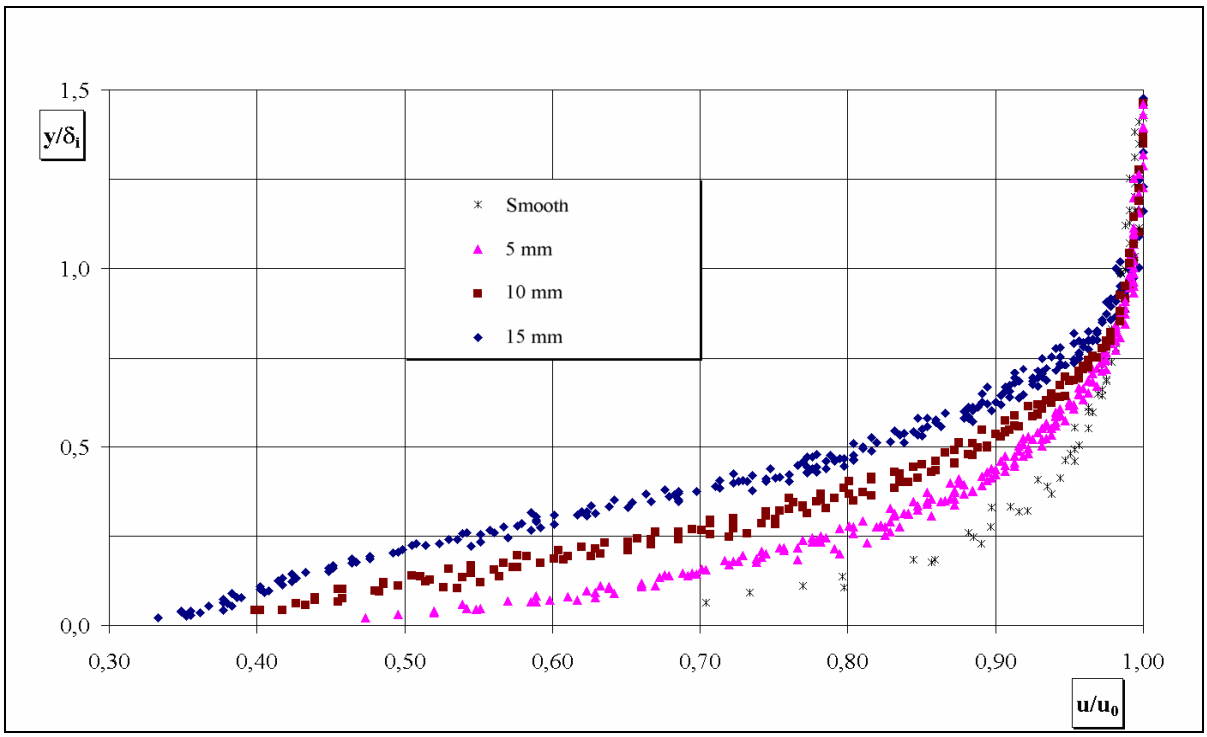

Fig. 11.17 - Non dimensional local mean velocity distributions (0, 5, 10, 15 mm double density)

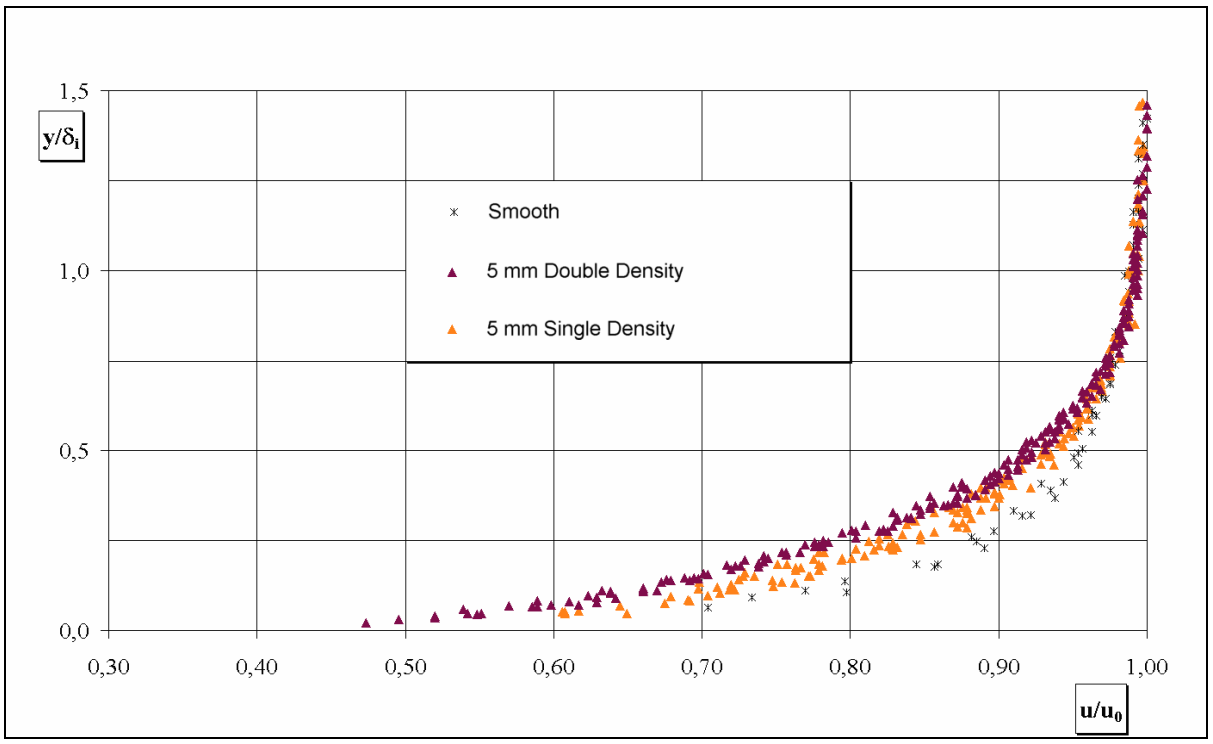

Fig. 11.18 - Non dimensional local mean velocity distributions (5 mm single and double density)

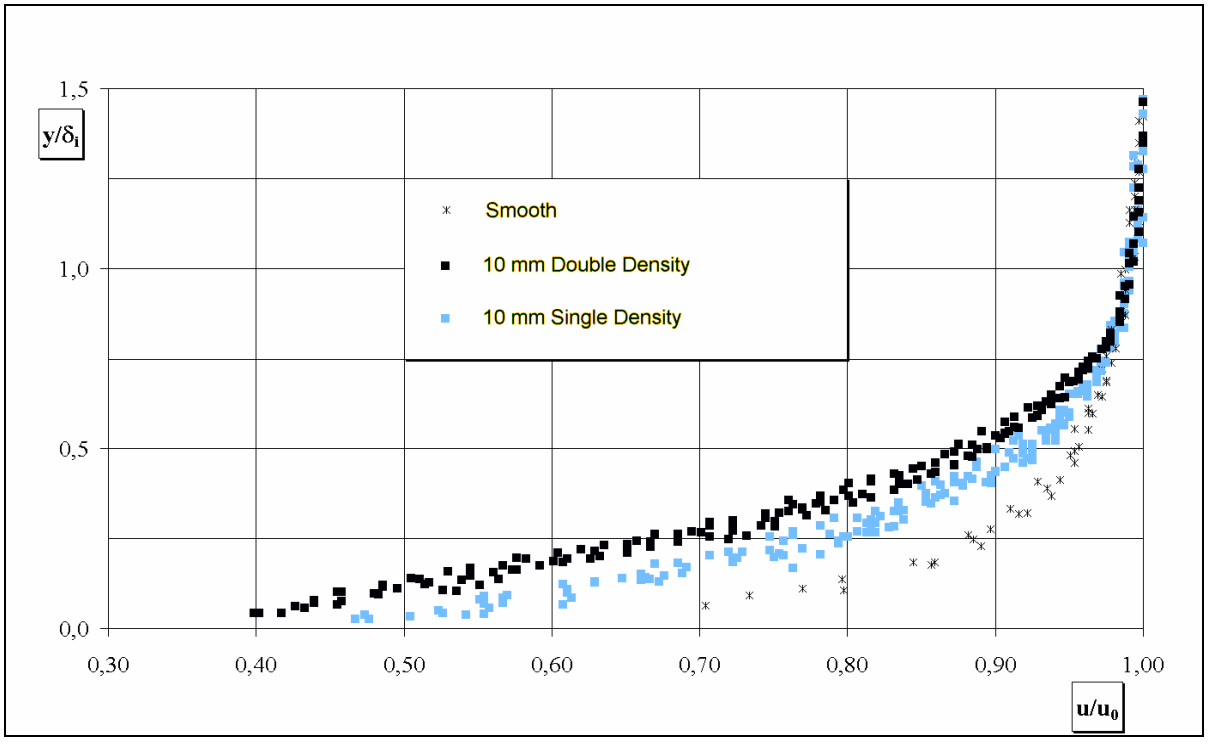

Fig. 11.19 - Non dimensional local mean velocity distributions (10 mm single and double density)

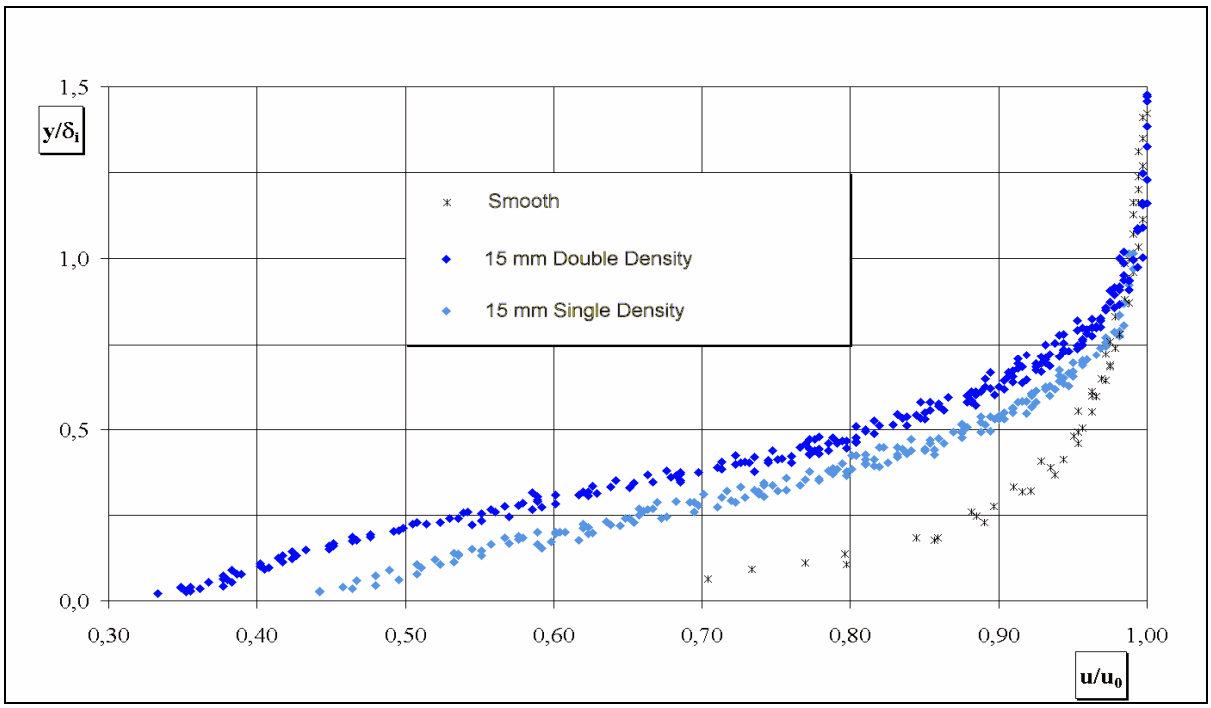

Fig. 11.20 - Non dimensional local mean velocity distributions (15 mm single and double density)

It is possible to infer that the presence of vegetation has an influence in any case, on the general course of the non dimensional local mean velocity distributions, even when it does not influence the dimensional local mean velocity distributions at the height of the cylinders in an evident way. This influence is connected both with the height of the cylinders and their density.

11.4 Shape factor and comparisons between the boundary layer thickness

Finally, to complete the processing about the shape of the non dimensional local mean velocity distributions, the mean values of the ratios $\delta_{99}/\ \delta_{77}$ for each height and density of the cylinders have made it possible to identify a "Shape Factor" shown in the following table.

Table 11.6 –Different Shape Factors for the various flow conditions

	Zero Density	Single Density	Double Density
Height 0	1.65	1.65	1.65
Height 5 mm	1.65	1.50	1.38
Height 10 mm	1.65	1.40	1.25
Height 15 mm	**1.65**	**1.32**	**1.20**

From it, it is evident that the Shape Factor is a function both of the height and the density of the cylinders. Such function of two variables can also be represented by a 3D-histogram (Fig. 11.21).

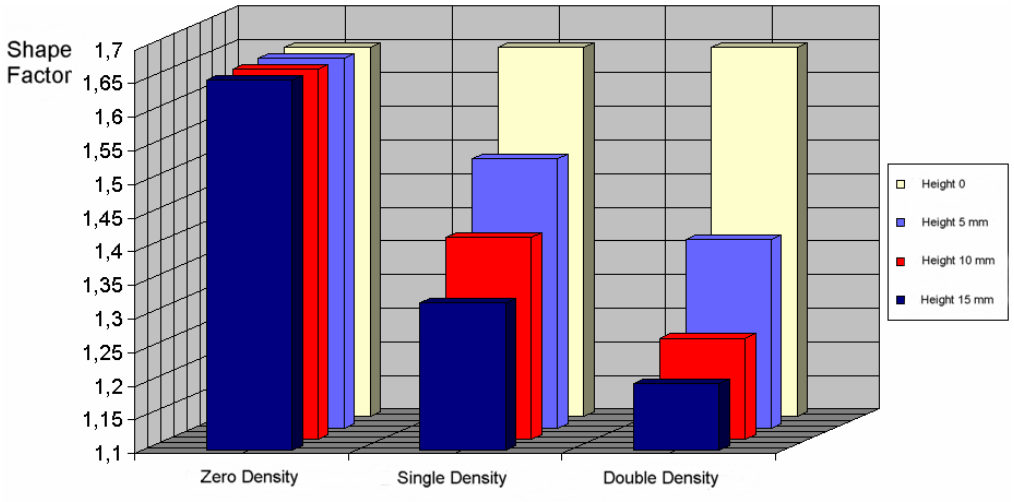

Fig. 11.21 - 3D-histogram of the shape factor function of density and height of the cylinders

Further considerations can be drawn from a further deeper analysis of Tables 11.2 and 11.3. For this reason, it is suitable to prepare a new table, which, for each condition (i.e. height and the density of the cylinders) shows, section by section, the difference between the thickness of the boundary layer and its thickness as to the smooth bottom, that can be called the differential thickness.

Table 11.7 - Differential thickness

	Section	**Rough 5 mm**	**Rough 10 mm**	**Rough 15 mm**
Single Density	1	10.8	16.2	25.7
	2	18.5	24.3	36.4
	3	21.1	31.2	45.9
	4	28.7	37.8	50.6

	Section	**Rough 5 mm**	**Rough 10 mm**	**Rough 15 mm**
Double Density	1	12.2	18.2	27.7
	2	19.2	26.8	38.4
	3	24.2	36.8	45.8
	4	30.5	38.9	48.7

This Table represents the direct influence on the boundary layer thickness of the cylinders, in their different heights and arrangements.

Then, it is possible to compare among them the values of the differential thickness obtained for the double and single densities in the corresponding sections and heights of the cylinders, getting the Table 11.8.

Table 11.8 - Ratio of the differential thickness between double and single densities

Section	Rough 5 mm	Rough 10 mm	Rough 15 mm
1	1.13	1.12	1.08
2	1.04	1.10	1.05
3	1.15	1.18	1.00
4	1.06	1.03	0.96
Mean	1.09	1.11	1.02
General Mean	1.07		

It is possible to compare subsequently the values of the differential thickness, at a parity of section and density of the cylinders, both between the values concerning the 10 mm high cylinders and the 5 mm high cylinders, as well as between the values concerning 15 mm high cylinders and the 5 mm high cylinders (Tab. 11.9).

Table 11.9 - Ratio of the differential thickness between the 10/5 and 15/5 cylinders

	10mm/5mm	Mean	General Mean	15mm/5mm	Mean	General Mean
Single Density	1.50	1.40	1.41	2.38	2.07	2.00
	1.31			1.97		
	1.48			2.18		
	1.32			1.76		
Double Density	1.49	1.42		2.27	1.94	
	1.40			2.00		
	1.52			1.89		
	1.28			1.60		

From the Table 11.8 it is evident that the ratios of the differential thickness obtained for the double and single densities in the corresponding sections and heights of the cylinders fluctuate all of them around a mean value of 1.07, with a maximum difference of about 10%. Besides, the partial means carried out when the height of the cylinders changes, give values of 1.09, 1.11, 1.02.

They do not seem to point out any specific trend. On the contrary, they seem to show that the influence of the cylinder density on the boundary layer thickness is substantially independent of their height. Therefore, the differences among the partial means, owing to the fact that they assume indifferently positive or negative sign, might be caused by accidental errors, which can be considered absolutely negligible, also considering the results achieved by the data processing illustrated in the work.

Moreover it is evident from Table 11.9 that the ratios of the differential thickness, at a parity of section and density of the cylinders, both between the case of the 10 mm high cylinders and the 5 mm high cylinders, as well as between the case of the 10 mm high cylinders and the 15 mm high cylinders and the 5 mm high cylinders, fluctuate around the value 1.41 for the first case, with a maximum difference of 9%, and around the value of 2.00 for the second case, with a maximum difference of 20%. Also in this case, they do not show a specific trend, and seem to point out that the influence of the height of the cylinders on the thickness of the boundary layer is substantially independent of their density. Also in this case, the differences between the partial means might be due to accidental errors.

In the light of such results, therefore, it is also possible to affirm that the height of the cylinders has more influence on the thickness of the boundary layer than their density.

11.5 Synthesis of the obtained results

In this chapter, a complete experimentation about the effects of a vegetated bottom on the local mean velocity distributions and the values of the thickness of an equilibrium boundary layer turbulent current is carried out. Particularly, the heights of the cylinders used to model the vegetation were 5 mm, 10 mm and 15 mm, and their arrangements were according to rectangular o square meshes.

The comprehensive synthesis of the performed measurements and elaborations about the effects of the height and the density of the cylinders on the behaviour of the current is the following:

- The increase of the flow resistances is a growing function both of the height of the cylinders and of their density.
- Owing to the increase of the flow resistances, it is necessary to increase opportunely

the slope of the canal bottom in order to obtain the condition of horizontal free surface.

- Because of the increase of the flow resistances, the boundary layer thickness turned out to be growing both with the increase of the height of the cylinders and with the increase of their density: moreover, the first effect proved to be more considerable than the second one.
- Likewise what happens in the cases of uniform motion currents with vegetation, the dimensional local mean velocity distributions show a sharp bend near the cylinders, caused by the greater resistance that the current meets on the spot near the cylinders compared to the upper zone where there are no cylinders. However, we must say that, owing to the particularly low density of the cylinders adopted, such detail seems to be unnoticeable in many working conditions and/or in many test sections. Particularly, it was possible to establish the existence of a limit ratio between the thickness of the boundary layer in a section and the height of the cylinders, above which the cylinders themselves are unable to produce visually such sharp bend: such ratio resulted equal to 2.9 for the single density and 3.6 for the double one.
- If we take into consideration all the local mean velocity distributions where no sharp bend appears, as well as the parts of the local mean velocity distributions placed higher than the cylinder tops, where, on the contrary, the sharp bend is visible, such dimensional distributions, made non dimensional with the boundary layer thickness and the external stream velocity, showed equilibrium characteristics in every kind of vegetation (that is cylinder height and density): this is a clear superimposition in all test sections concerning the same kind of vegetation. In summary, for such velocity distributions it is a question of "partial" equilibrium.
- The equilibrium conditions that occur moreover, depend on the type of vegetation (height and thickness of the cylinders), since the shape of the non dimensional local mean velocity distributions shows a clear and regular variability when such characteristic changes.
- It is possible to define a particular "Shape Factor" which sums up with a number the different conditions of "partial" equilibrium of the boundary layer.

12. TESTS ON A BOUNDARY LAYER CURRENT: NEW METHODOLOGY TO MAKE EXPERIMENTAL DATA NON DIMENSIONAL

In this chapter, a new methodology to make the local mean velocity profiles non dimensional is proposed. It foresees the division of the current in two layers:

- the first layer is characterized by the presence of vegetation
- the second layer is relative to the part of the current above the cylinders, that has been defined as "open current".

Therefore, a new origin of the coordinate system is defined, assuming as base starting, for the heights, the top of the cylinders, and, for the velocities, the value that the current presents at the top of the cylinders themselves, in each working condition and in each measurement section.

The researches carried out on the rigid vegetation had allowed to determine the velocity profiles in six types of currents, characterized by two different densities (single and double) and by three different heights of the cylinders (5, 10, 15 mm). The methodology which allows to define the excess velocity profile in the open current has been applied to each velocity profile of every section and in every working condition, by choosing from time to time the most suitable couple of values of y_e and u_e, where the values of y_e were those ones corresponding to the top of the cylinders, and the values of u_e were the ones corresponding to this height for each velocity profile.

By way of an example, Figs.12.1 and 12.2 show the dimensional profiles of the velocity excesses in the open current concerning the first section with cylinders 15 mm high, in the configuration single density and double density respectively.

Also the line corresponding to 90% of (u_0-u_e) is reported in the profile in Fig.12.1 and Fig. 12.2, being necessary for the subsequent processing.

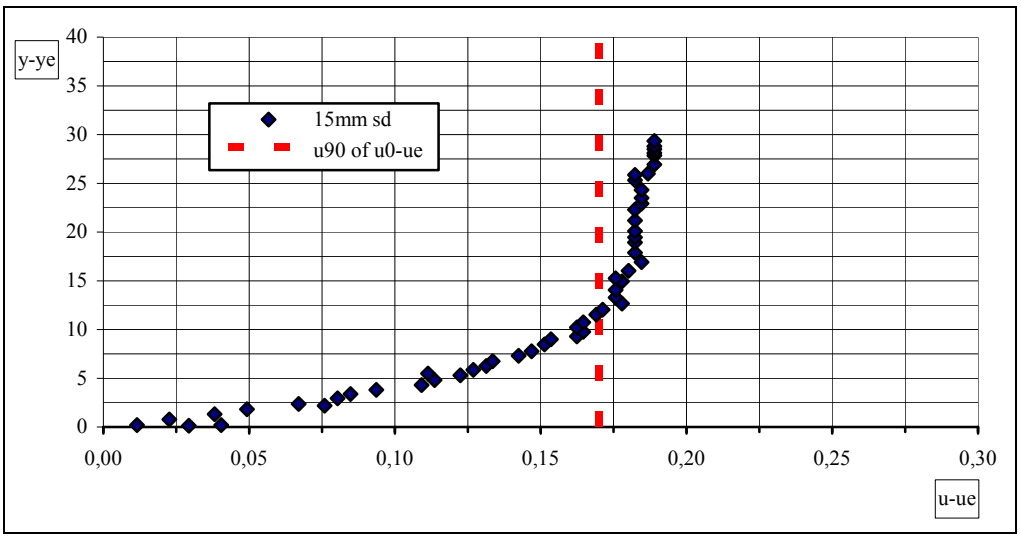

Fig. 12.1 - Shifting of the reference. Section 1, 15 mm single density

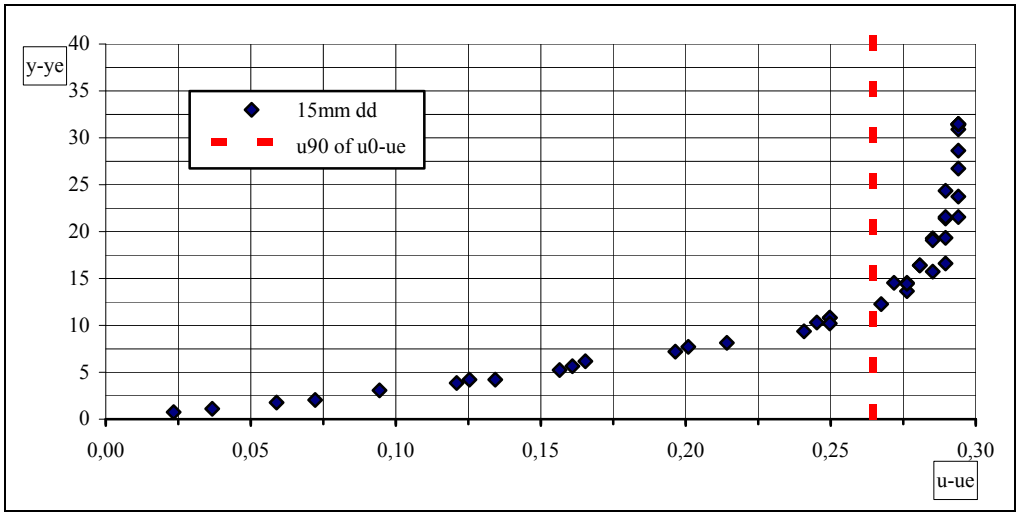

Fig. 12.2 - Shifting of the reference. Section 1, 15 mm double density

In these dimensional profiles of the velocity excesses in the current, the velocities were made non dimensional as to (u_0-u_e), and the heights as to the thickness corresponding to the 90% of (u_0-u_e) called δ'_{90}. In particular, it was chosen the value of δ' that might be obtained directly from all the profiles available.

The Figs. 12.3-12.5 show the non dimensional profiles of the velocity excesses in the open current, referred to the three vegetation heights (5, 10, 15 mm) respectively, in the single and double density configuration.

The examination of the profiles shows, for each height of the cylinders, their complete superimposition when the measurement section changes, and between single and double density too.

Of course, since this description concerns only the current above the cylinders, it turns out that it is possible to go over the partial imbalance seen in Chapter 11.

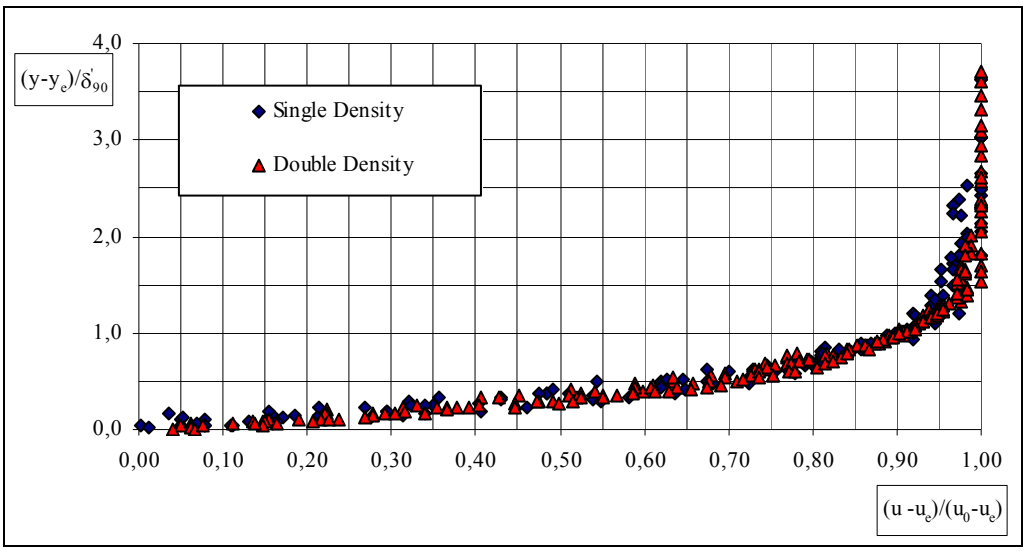

Fig. 12.3 - 5 mm velocity profiles

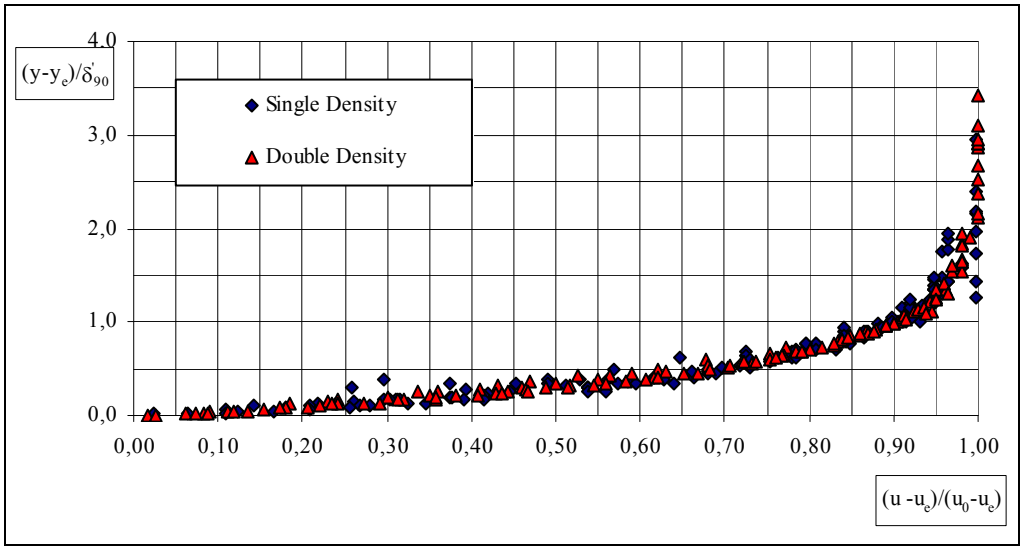

Fig. 12.4 - 10 mm velocity profiles

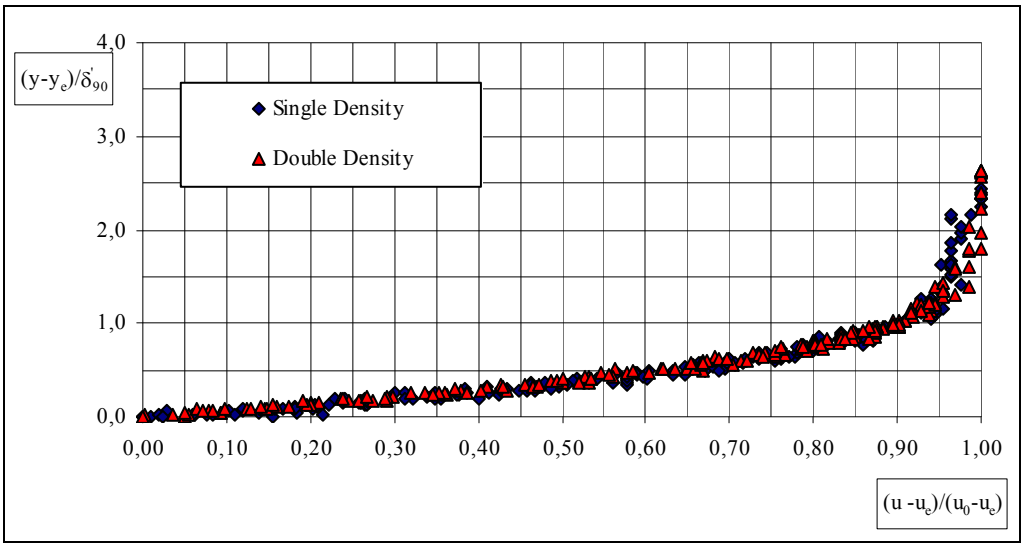

Fig. 12.5 - 15 mm velocity profiles

Finally, in Fig.12.6, a further superimposition of all the profiles in Figs. 12.3, 12.4, 12.5 has been carried out; it was observed that they are superimposed one upon another almost perfectly.

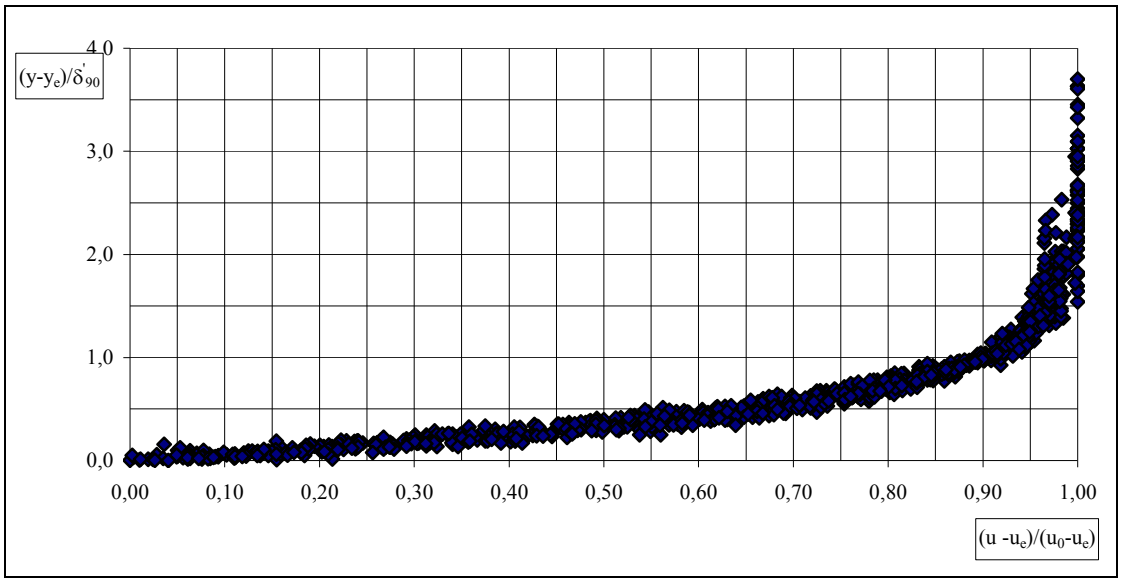

Fig. 12.6 - Superimposition of non dimensional velocity profiles

Therefore, the methodology of velocity excess in the open current allows to work always in a condition of total equilibrium, and above all to obtain a single condition of equilibrium independent of the height and the density of the vegetation model taken into consideration.

In Chapter 11 it was pointed out that the superimposition was not perfect in the low part of the non dimensional velocity profiles; while the non dimensional distribution of the velocity excesses in the open current is independent of the bottom vegetation, that is of the density and height of the cylinders.

13. TESTS ON A BOUNDARY LAYER CURRENT: MEASUREMENT POINT BETWEEN TWO CONSECUTIVE CYLINDERS

13.1 Description of tests

The experimental tests described in this paragraph are strictly linked to the previous ones, but they arise also from a review of the experimental works concerning the uniform or steady streams flowing down in channels with rigid vegetation where the distributions of the turbulence statistical quantities were obtained averaging in space as well as in time the measurements of the instantaneous velocity data collected in different verticals around the cylinders.

Now, it is experimentally verified the effect of a suitable shift of the measurement vertical around the cylinders, on the hydrodynamic characteristics of the flow.

In previous paragraph the instantaneous velocity data were measured in verticals located along the axis of the flow. On the contrary, now the data have been measured in the same test sections but in verticals located along one of the two rows of the cylinders placed near the axis of the flow, on both sides. In particular, for each density of the cylinders, in the middle between two consecutive cylinders, in order to compare velocities distributions with their consequences in the two different but correspondent verticals sets.

The measurements have been carried out keeping either previous fundamental hydraulic parameters or the equilibrium condition of the boundary layer unchanged.

13.2 Velocity measurements and relative processing

Some example of the obtained velocity distributions are shown in Figs. 13.1-13.4.

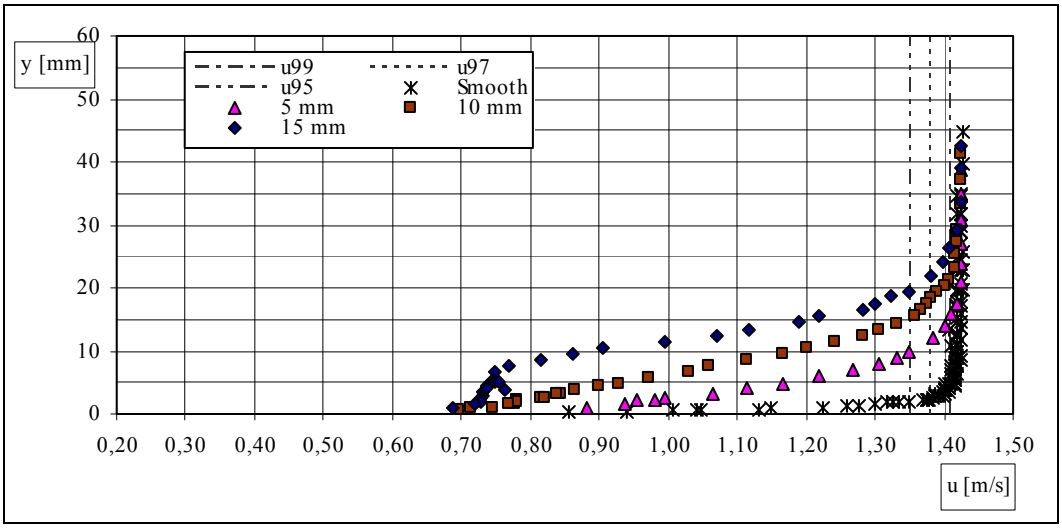

Fig. 13.1 - Local mean velocity distributions in test section n.1 (single density)

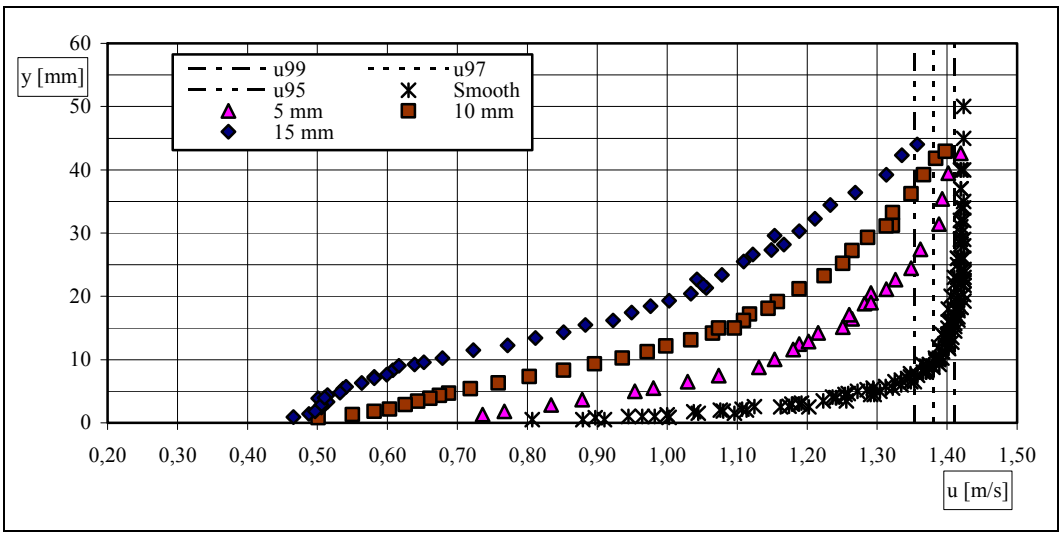

Fig. 13.2 - Local mean velocity distributions in test section n.4 (single density)

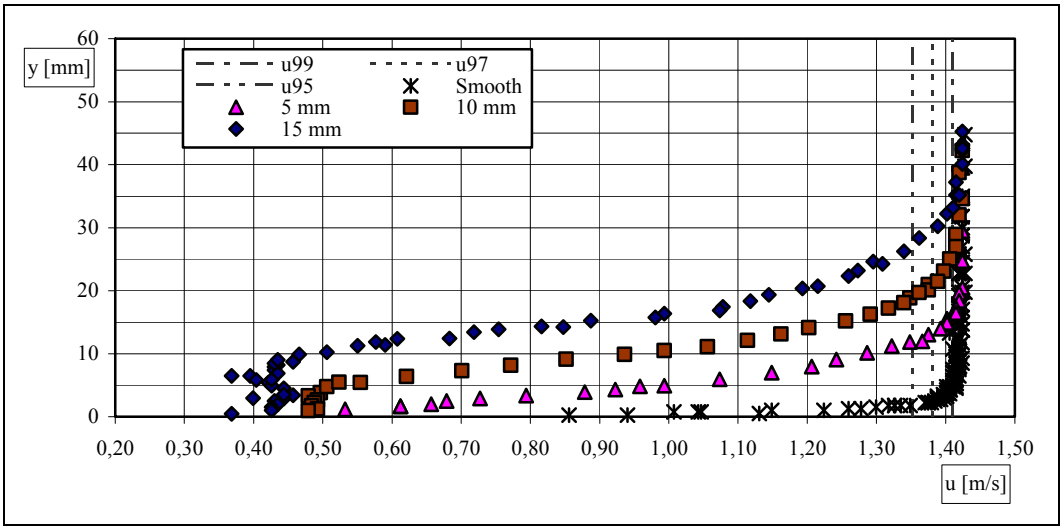

Fig. 13.3 - Local mean velocity distributions in test section n.1 (double density)

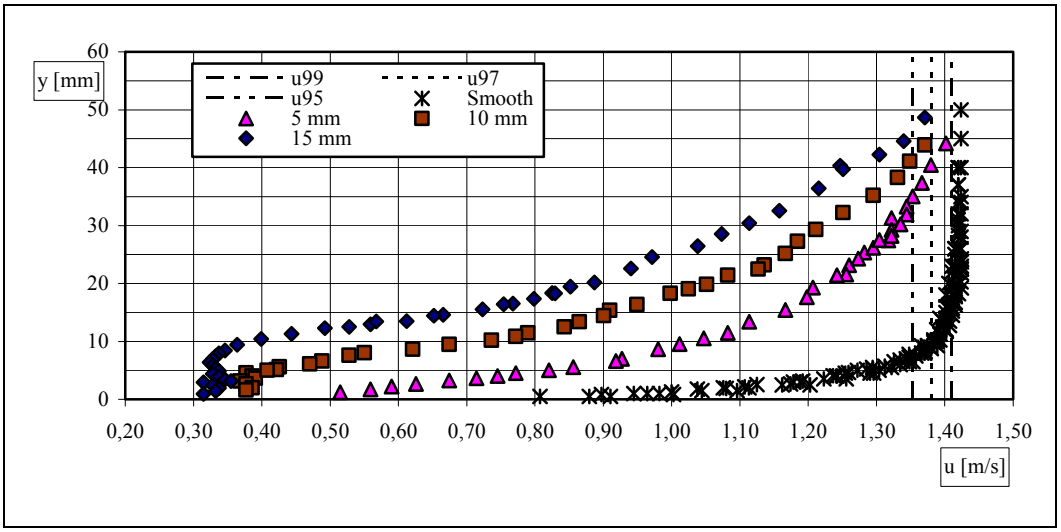

Fig. 13.4 - Local mean velocity distributions in test section n.4 (double density)

Starting from the local mean velocity distributions, the values of the thickness of the boundary layer have been obtained. These values are reported in bold face in the Tables 13.1 and 13.2 together with the corresponding ones shown in the Chapter 11, in order to make the comparison easier.

Table 13.1 - Thickness of the boundary layers (single density).

Thickness of the boundary layer	Smooth	Rough 5 mm	Rough 10 mm	Rough 15 mm
δ_{S1} (mm)	3,8	14,6-**16,5**	20,0-**22,8**	29,5-**27,2**
δ_{S2} (mm)	7,1	25,6-**22,7**	31,4-**30,4**	43,5-**39,5**
δ_{S3} (mm)	10,9	32,0-**33,0**	42,1-**45,0**	56,8-**51,7**
δ_{S4} (mm)	13,5	42,2-**41,3**	51,3-**53,2**	64,1-**59,2**

Table 13.2 -Thickness of the boundary layers (double density)

Thickness of the boundary layer	Smooth	Rough 5 mm	Rough 10 mm	Rough 15 mm
δ_{S1} (mm)	3,8	16,0-**16,3**	22,0-**25,4**	31,5-**34,2**
δ_{S2} (mm)	7,1	26,3-**28,0**	33,9-**35,4**	45,5-**46,0**
δ_{S3} (mm)	10,9	35,1-**41,0**	47,7-**49,4**	56,7-**55,9**
δ_{S4} (mm)	13,5	44,0-**52,7**	52,4-**54,7**	62,2-**57,1**

However, it is important to point out that, as in the foregoing experimentations, the direct reading of the δ_{99} is not possible in all the local mean velocity distributions: therefore, also in this case, it has been necessary to adopt a method of computing the δ_{99} based on the readings of the δ_{95}.

Obviously δ_{99} and δ_{95} are, respectively, the boundary layer thickness based on 99% and on 95% of the external stream velocity. This method has been carefully described in previous Chapter 11.

It is clear from the Table that it is not possible to point out a trend of the thickness values of the boundary layer, in each test section and in each flow condition, between the correspondent values couples. Therefore a first possible conclusion can be that shift of the measurement vertical around the cylinders does not give rise to meaningful changes of the boundary layer thickness values (the apparent differences are random measurement errors).

At this point, the local mean velocity distributions obtained for each test section and each flow condition can be changed into non dimensional ones, through the velocity in the external layer and the boundary layer thickness.

All non dimensional velocity distributions with cylinders presence are shown in Figs. 13.5, 13.6, 13.7, 13.8, 13.9, 13.10.

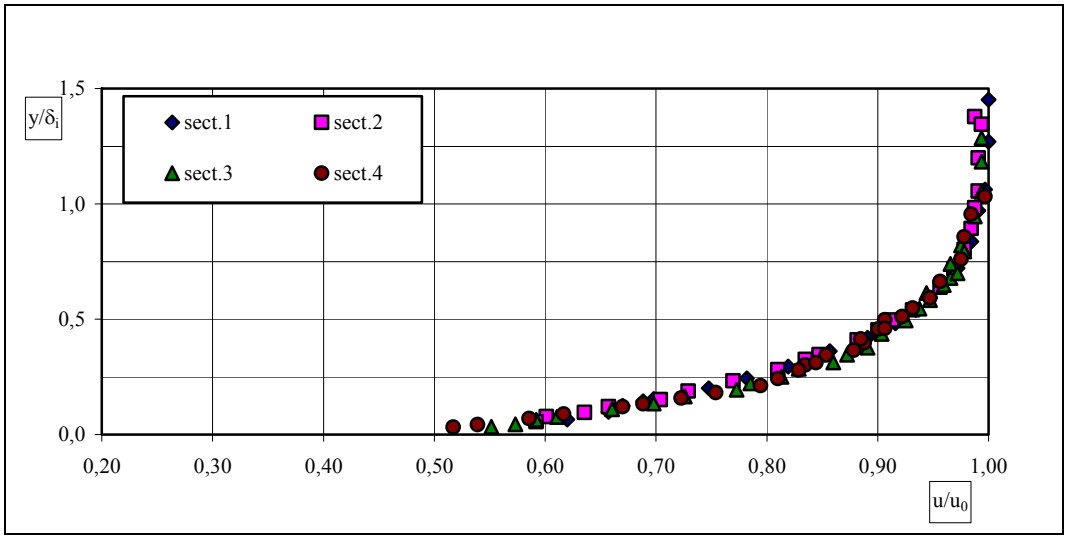

Fig. 13.5 - Non dimensional local mean velocity distributions: 5 mm single density

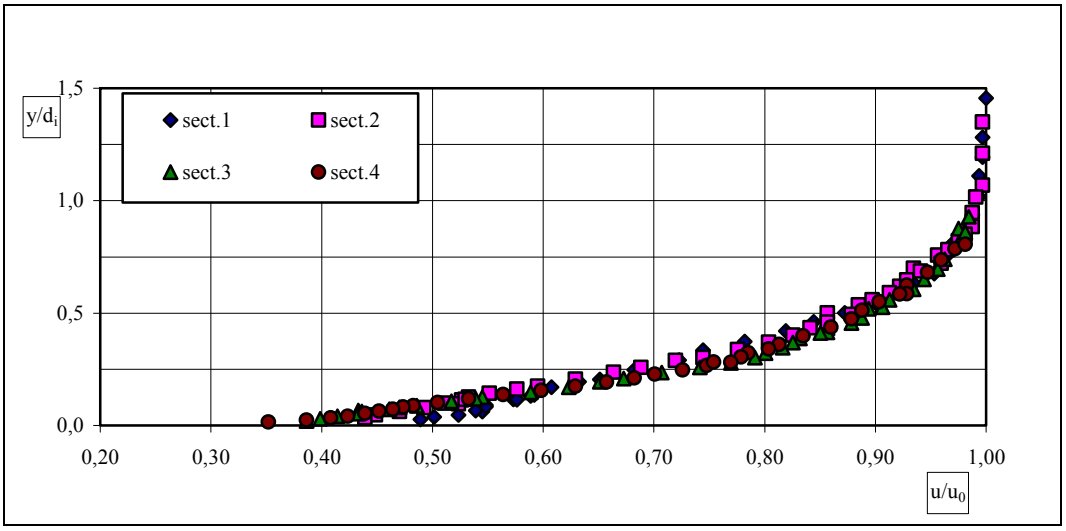

Fig. 13.6 - Non dimensional local mean velocity distributions: 10 mm single density

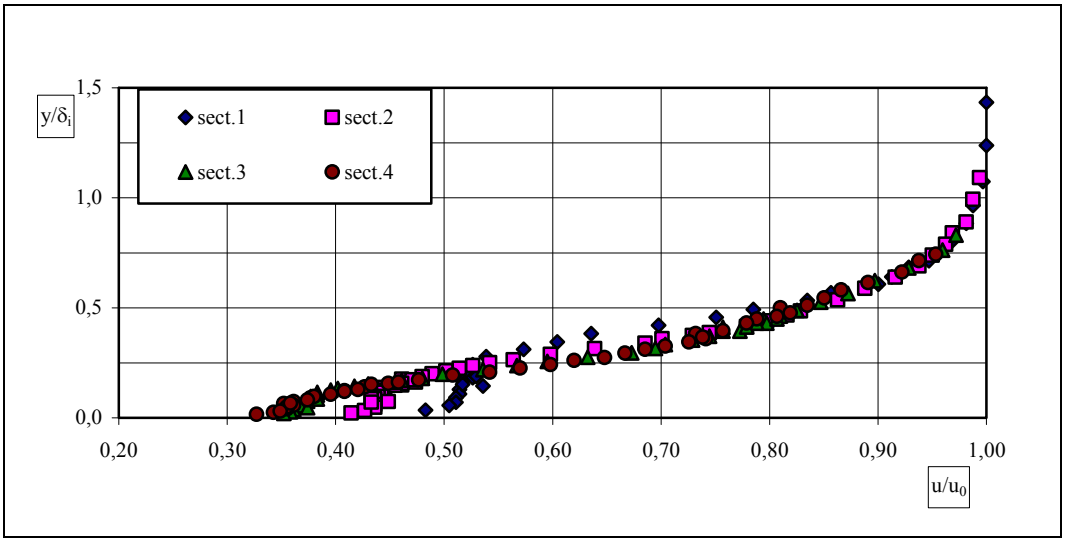

Fig. 13.7 - Non dimensional local mean velocity distributions: 15 mm single density

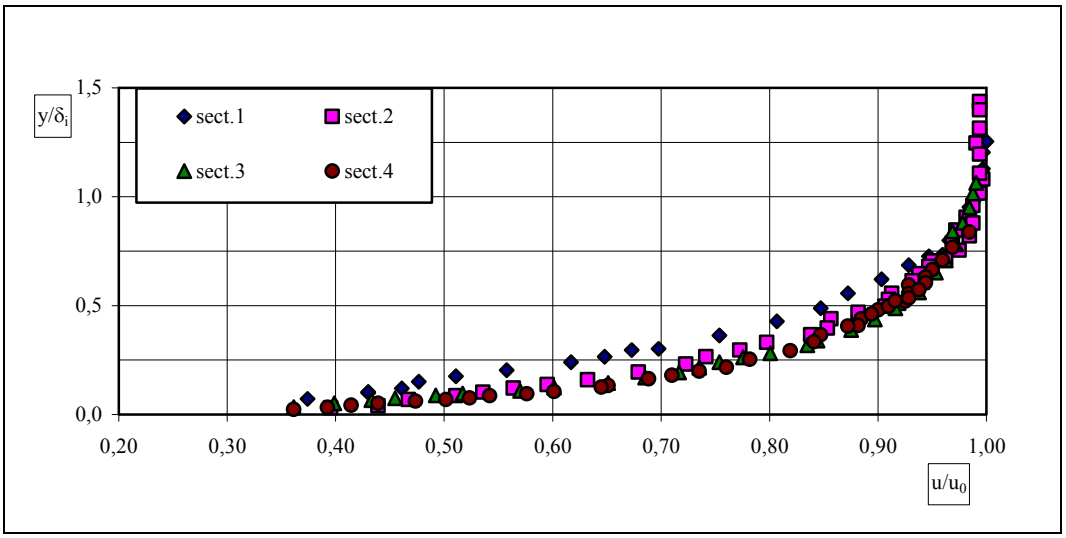

Fig. 13.8 - Non dimensional local mean velocity distributions: 5 mm double density

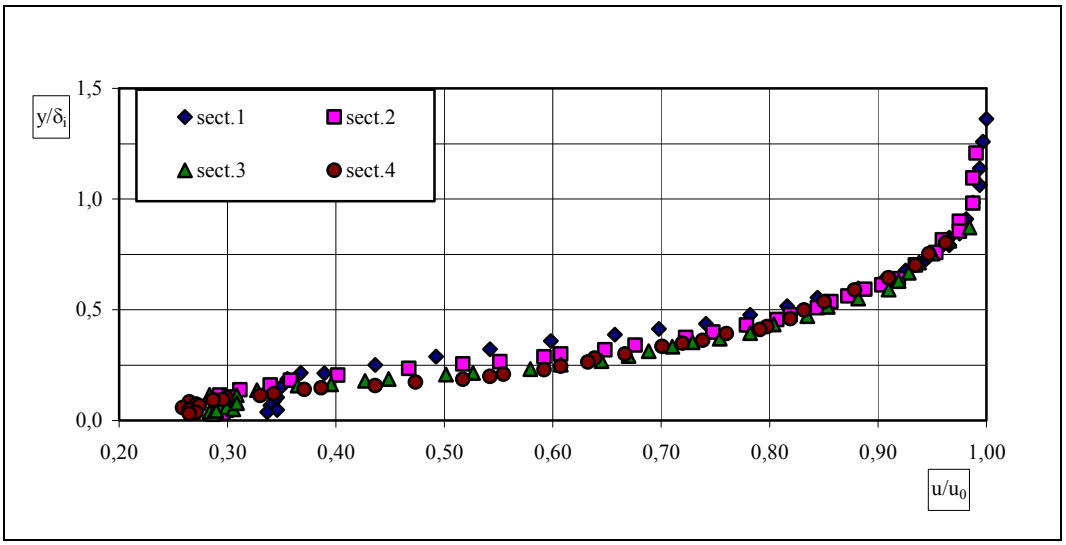

Fig. 13.9 - Non dimensional local mean velocity distributions: 10 mm double density

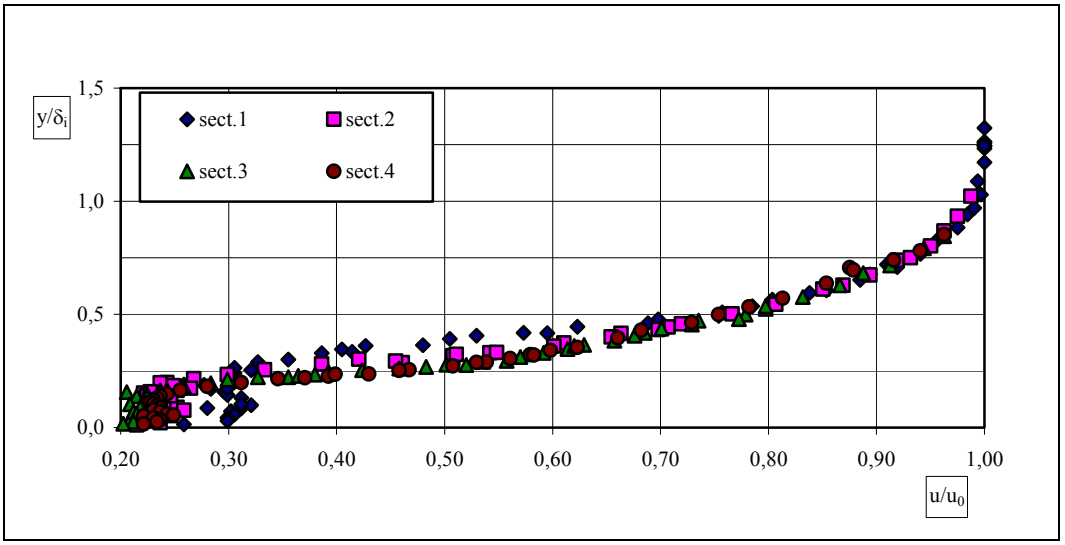

Fig. 13.10 - Non dimensional local mean velocity distributions: 15 mm double density

13.3 Processing of non dimensional local mean velocity distributions

While in the 5 mm case the non dimensional local mean velocity distributions relative to the four different test sections tend to be superimposed one upon another, showing a condition of "total" equilibrium of the boundary layer, in the 10 and 15 mm cases, on the contrary, it is clear that the non dimensional profiles tend to separate visibly and therefore to be only partially superimposed, showing a condition of "partial" equilibrium of the boundary layer, as it had been defined in previous Chapters.

In particular it is interesting to observe that, differently from Chapter 11 where the loss of the superimposition took place only below a certain value of the ratio y/δ, in these cases such loss of the superimposition sometimes take place also in the high part of the non dimensional profile.

Therefore it is possible to assert that shift of the measurement vertical around the cylinders gives rise to meaningful changes of the typology of the partial equilibrium boundary layer conditions that had been defined in previous Chapters: in fact this partial equilibrium regards not only the lower part of the non dimensional profile (as in previous Chapters was pointed out), but also its higher part.

In order to realize why in some sections there is not superimposition any longer, it is convenient to evaluate the ratios among the boundary layer thickness values and the heights of the cylinders: these ratios are reported in Table 13.3 in bold face, together with the corresponding ones already evaluated in Chapter 11, in order to make an easier comparison.

Table 13.3 - Ratio between thickness of the boundary layer and height of cylinders

	20 cm	**30 cm**	**40 cm**	**50 cm**
5 mm single density	2,92-**3,30**	5,12-**4,54**	6,40-**6,60**	8,44-**8,25**
10 mm single density	2,00*-**2,28***	3,14-**3,04**	4,21-**4,50**	5,13-**5,32**
15 mm single density	1,97*-**1,81***	2,90*-**2,63***	3,79-**3,45**	4,27-**3,95**
5 mm double density	3,20*-**3,25***	5,26-**5,59**	7,02-**8,19**	8,80-**10,53**
10 mm double density	2,20*-**2,54***	3,39*-**3,54***	4,77-**4,94**	5,24-**5,47**
15 mm double density	2,10*-**2,28***	3,03*-**3,06***	3,78-**3,73**	4,15-**3,81**

An asterisk marks the cases where such superimposition disappears.

As in Chapter 11, from the Table 13.3 it is possible to evaluate a limit value of the ratio, depending on the density of the cylinders, below which the anomaly pointed out in the non dimensional distributions appears. Such limit value has been estimated about 2,9 for the

single density, and about 3,6 for the double density.

It is interesting to observe that limit values are like the corresponding ones already estimated in Chapter 11. This result confirms the circumstance that, also if the specific trend of non dimensional distribution is not alike in the different considered verticals around the cylinders, in any case the main equilibrium or partial equilibrium characteristics of boundary layers on vegetated beds keep unchanged, apart from the chosen verticals series.

Besides, in the following Table 13.4 the ratios between the values of the Table 13.3 and the limit values previously estimated concerning single and double density are shown.

As it happened already in Chapter 11 it is possible to notice clearly that, where the ratio is about 1, the anomaly is scarcely visible; when the ratio decreases, the anomaly becomes more evident; and the smaller the ratio is the more evident the anomaly becomes. In short, it is possible to conclude that, in any case, according to the density of the cylinders, as long as the height of the cylinders is enough smaller than the thickness of the boundary layer, this one seems to be of "total" equilibrium; while, when the height of the cylinders is a considerable fraction of the thickness of the boundary layer, this one looses the characteristic of "total" equilibrium and assumes the opposite characteristic of "partial" equilibrium.

Table 13.4 - Ratio between values of the Table 13.3 and corresponding limit values

	20 cm	**30 cm**	**40 cm**	**50 cm**
5 mm single density	1,02-**1,14**	1,77-**1,56**	2,21-**2,28**	2,91-**2,85**
10 mm single density	0,69***-0,79***	1,08-**1,05**	1,45-**1,55**	1,77-**1,84**
15 mm single density	0,68***-0,63***	1,00***-0,91***	1,31-**1,19**	1,47-**1,36**
5 mm double density	0,89***-0,90***	1,46-**1,55**	1,95-**2,28**	2,44-**2,93**
10 mm double density	0,61***-0,70***	0,94***-0,98***	1,33-**1,37**	1,46-**1,52**
15 mm double density	0,58***-0,63***	0,84***-0,85***	1,05-**1,03**	1,15-**1,06**

Moreover, it is interesting to notice that, where the anomaly is evident, the dimensional local mean velocity distributions too show some irregularities at the height of the cylinders.

In Figs. 13.11 and 13.12 are reported together the four non dimensional local mean velocity distributions concerning the smooth plate and vegetated plate with 0 (smooth), 5, 10, 15 mm high cylinders respectively, relative to single and double density, after having eliminated from each distribution the points relative to the non equilibrium conditions.

It is clearly visible that in each figure the four distributions are not superimposed among themselves, but that they follow distinct laws.

Besides, if we compare the two figures, it is possible to observe that, apart from the

distributions concerning the smooth plate, which are the same in both, there is no superimposition even between distributions relative to the same height of the cylinders, but of different densities.

It is therefore possible to infer that the presence of vegetation has, in any case, an influence on the general trend of the non dimensional local mean velocity distributions, even when it does not influence the dimensional local mean velocity distributions at the height of the cylinders in an evident way. This influence is connected both with the height of the cylinders and their density.

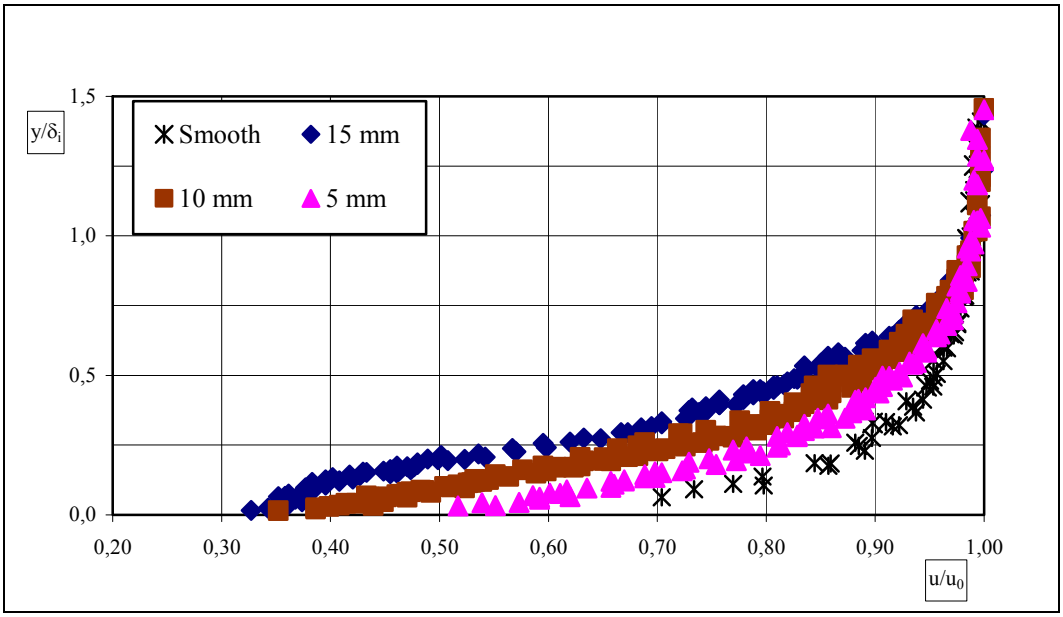

Fig. 13.11 - Non dimensional local mean velocity distributions (single density)

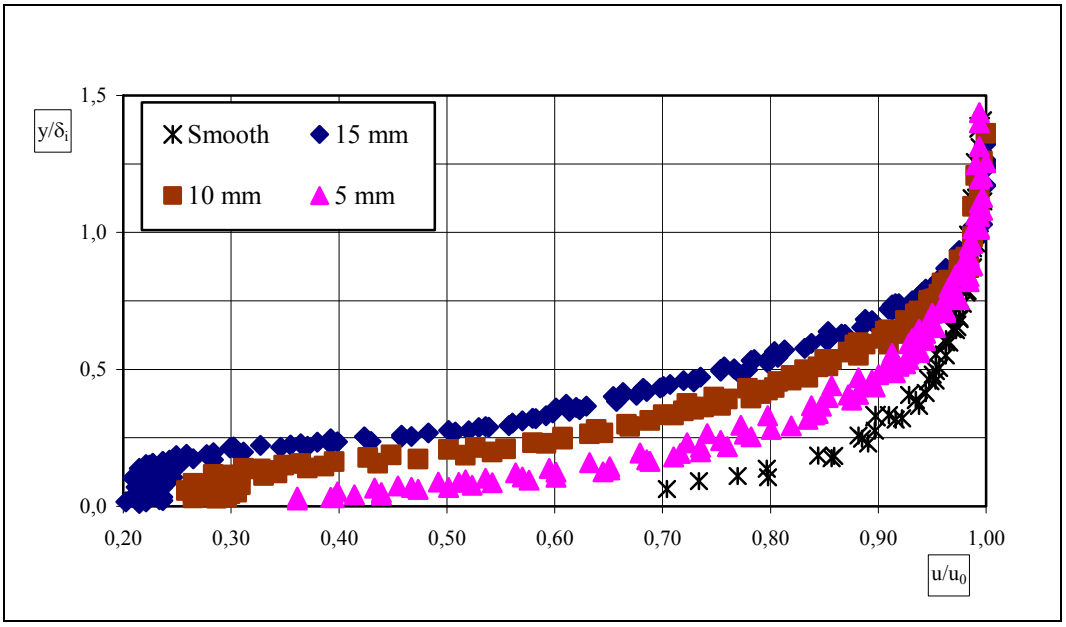

Fig. 13.12 - Non dimensional local mean velocity distributions (double density)

Finally, to complete the processing about the shape of the non dimensional local mean velocity distributions, the mean values of the ratios δ_{99}/δ_{97} for each height and density of the cylinders made possible to identify a "Shape Factor", which is a function both of the height and the density of the cylinders, shown in the following table. As in other cases, in the Table either values of the present measurements (in bold face) or the values relative to Chapter 11 are reported, in order to have an easy comparison between the "Shape Factor" values in both vertical sets around the cylinders.

Table 13.5 –Different Shape Factors for the various flow conditions

	Zero Density	**Single Density**	**Double Density**
Height 0	1,65-**1,65**	1,65-**1,65**	1,65-**1,65**
Height 5 mm	1,65-**1,65**	1,50-**1,38**	1,38-**1,30**
Height 10 mm	1,65-**1,65**	1,40-**1,27**	1,25-**1,19**
Height 15 mm	1,65-**1,65**	1,32-**1,22**	1,20-**1,12**

13.4 Comparisons with previous results

In previous Chapter 11 the effects of a rigid fully submerged vegetated bed on the hydrodynamics of a turbulent boundary layer developing on it have been experimentally investigated. In this paragraph the experimental measurements of the instantaneous velocities have been carried out in verticals placed along the axis of the flow, in order to verify the effects of a suitable shift of the measurement verticals around the cylinders on the hydrodynamic characteristics of the examined flow, and to make a suitable comparison.

The results of the comparison that can be drawn from the performed experimental measurements are the following ones:

- shift of the measurement verticals around the cylinders does not give rise to meaningful changes of the boundary layer thickness values;
- the local mean velocity distributions made non dimensional with the boundary layer thickness and the external stream velocity, show a "total" or "partial" equilibrium characteristics with every kind of vegetation (that is cylinder height and density). The loss of "total" equilibrium in a section depends on the ratio between the thickness of the boundary layer in the section and the height of the cylinders: the limit values of this ratio depends on the density type of vegetation (2,9 for the single density and 3,6 for the double one), and are the same apart from the measurements verticals positions;
- apart from the measurements verticals position, the equilibrium ("total" or

"partial") characteristics depend on the type of vegetation (height and thickness of the cylinders);

- apart from the measurements verticals position, it is possible to define a particular "Shape Factor" which sums up with a number the different conditions of "partial" equilibrium of the boundary layer;
- unlike what happens in cases of the measurements carried out in the axis of the flow, the equilibrium loss concerns either the lower part or the higher one of the non dimensional profiles;
- finally the "Shape Factor" values and the non dimensional profiles shapes depend on the measurements verticals position around the cylinders.

14. A SIMPLIFIED EXPERIMENTAL METHODOLOGY TO EVALUATE ABSOLUTE ROUGHNESS

14.1 Introduction

The knowledge of the resistance properties of vegetated surfaces is yet now one of the most important environmental fluid mechanics topics, due both to the lack of present knowledge about it and to the difficulty of the matter. Some papers are present in international literature about the argument (Bettess 2003, Kouwen et al. 1969, Kouwen & Unny, 1973, Kouwen & Unny, 1981, Lopez and Garcia, 1997, Stone & Shen, 2002), but much greater is the work to be done with respect to that already performed.

In fact, vegetation may be regarded as a kind of surface roughness. The main procedure to experimentally study in a laboratory the topic, is to use a very long channel with vegetated bottom and generate within it an uniform flow. The slope S of this channel necessary to generate this uniform flow can be introduced within one of the most frequently used formulas relating open-channel flow velocity V to resistance coefficients, as for instance the Manning formula, the Darcy-Weisbach one, or also the eldest Chézy one, in order to obtain the relative n, f, C resistance coefficients. Unfortunately the channel length needed to obtain such a result must be a very long one, due to the necessity of attain the uniform flow.

The previous observations induced us to conceive an alternative procedure in order to obtain the same result with less equipment resources.

In conclusion, in this chapter, a new way is presented of determining the resistance coefficients in a vegetated flow, and consequently also the absolute roughness of the bottom.

14.2 Generalities about resistance formulas and coefficients

In a recent review (Yen, 2002) it is observed that each resistance coefficient can be considered either as cross section coefficient or as reach one, and that the usual resistance formulas can be considered as reach formulas to apply to uniform flows. It is possible to apply them also to not uniform flows, although to a very short reach, practically to a single cross section: therefore, in this case, the resistance coefficient can vary in the subsequent cross sections of the flow.

Referring to the reach formulas, the most frequently used, relating open-channel flow velocity V to resistance coefficients, are the Darcy-Weisbach, Manning and Chézy ones:

$$(14.1) \qquad V = \sqrt{\frac{8g}{f}}\sqrt{RS}; \qquad V = \frac{1}{n}R^{2/3}S^{1/2}; \qquad V = C\sqrt{RS}$$

where f, n, and C are the Weisbach, Manning and Chézy resistance coefficients, and R = hydraulic radius, S = slope, g = gravitational acceleration. In case of cross section formulas, the slope S must be substituted by the head slope J**.** Comparing these formulas, it is possible to obtain the following expressions:

$$\sqrt{\frac{f}{8}} = \frac{n\sqrt{g}}{R^{1/6}} = \frac{\sqrt{g}}{C} \tag{14.2}$$

Among these resistance formulas, the authors choose the Darcy-Weisbach approach, because it is the most suitable for an exact evaluation of the flow resistances. Within this approach, the resistance coefficient f (called friction factor) is related to the absolute roughness, that here will be called ε, through the Colebrook-White formula:

$$\frac{1}{\sqrt{f}} = -K\log\left(\frac{\varepsilon/4R}{a} + \frac{b}{\mathrm{Re}\sqrt{f}}\right) \tag{14.3}$$

with Re Reynolds number defined as Re = 4VR/ν, and ν kinematic viscosity of the fluid.

The values of the constants a and b have been the object of many experimental surveys. In particular, in (Yen 2002) values for a and b, obtained by other researchers either for open channels with different aspect ratios or for wide open channels, are suggested. In Moody-type diagram, relative to circular full pipes, the values K = 2, a = 3.71 and b = 2.51 are used.

According to Marchi (1961) it is always possible to use the values of Moody-type diagram relative to circular full pipes also for open channels flows. This requires adoption of a suitable shape parameter ψ depending on the aspect ratio, so that the Colebrook-White formula becomes:

$$\frac{1}{\sqrt{f}} = -2\log\frac{1}{\psi}\left(\frac{\varepsilon/4R}{3.71} + \frac{2.51}{\mathrm{Re}\sqrt{f}}\right) \tag{14.4}$$

In particular, ψ assumes the value 0.83 for wide rectangular channels. The values of f so obtained are very similar to those suggested by Yen for wide channels.

14.3 Basic experiments on a boundary layer flow

The experiments, on which the elaborations performed here are based, are deeply described in chapter n.11 and chapter n.13. The experimental channels was described in chapter n.4. In any case, in order to make this chapter more clear for the reader, the main information about the matter will be here repeated together with new information necessary for the purpose of the chapter.

Measurements were performed either with a smooth or a vegetated bottom. In particular,

the vegetation was modelled by means of brass 4mm diameter cylinders with three different heights (5mm, 10mm, 15mm) placed according to two different regular geometries (respectively, a rectangular mesh 5*2.5cm^2 and a square mesh 2.5*2.5cm^2), pointed out synthetically as single and double density. Consequently, the projected area of vegetation per unit volume of water in the flow direction (Tsujimoto *et al.*, 1992) were, respectively, 3.2m^{-1} and 6.4m^{-1}. Combinations of three different heights and two different densities produced six different vegetated bottoms.

In all the seven considered flow conditions (smooth bottom and six different vegetated bottoms), the same experimental setting was considered. In particular, the height of the sluice gate was set at 7.49cm so that the depth in the vena contracta was at 4.62cm; the load on the vena contracta was at 10.34cm, and the resultant velocity of the free stream was at 1.424m/s.

Moreover, it was necessary to ensure the zero value of piezometric head gradient of the boundary layer, in each one of the seven considered flow conditions. This corresponded to hold the free surface of the current horizontal, at least in the first 50cm where the boundary layer developed. Therefore, it was necessary to suitably incline the channel, taking into account the vegetation model, whose possible increase in height and density would generate a corresponding increase of head losses, which would need to be balanced by a suitable increase of channel slope. The chosen slopes' values are reported in both the subsequent tables 3 and 4. The test sections were set at 20, 30, 40 and 50 centimetres from the channel inlet. In each test section two measuring verticals were considered, differently positioned with respect to the cylinders. The first one was set at the centre of either a rectangular or a square mesh. The second one was set along a cylinder row and at the centre of the lateral side of the same rectangular or square mesh. It is clear that in the case of a smooth bottom there was no need of such a second measurement location.

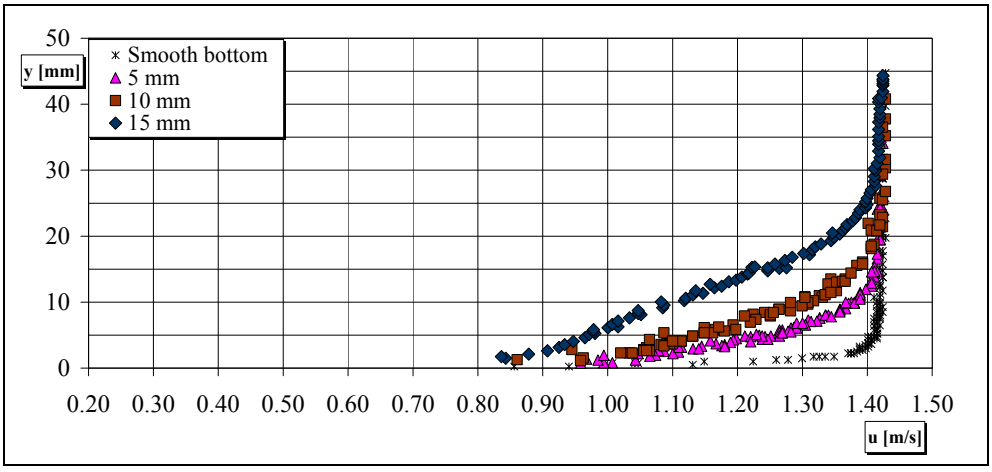

Fig. 14.1 - Local mean velocity distributions in test section n.1, central vertical (single density).

Either in the case of smooth or vegetated bottom, in each test section, along the chosen verticals, instantaneous velocities were measured in 20÷30 experimental points through a suitable LDA system, and in each point the local mean velocity was obtained.

Finally, in the figures 14.1 and 14.2, examples of the experimentally obtained local mean velocity distributions are reported.

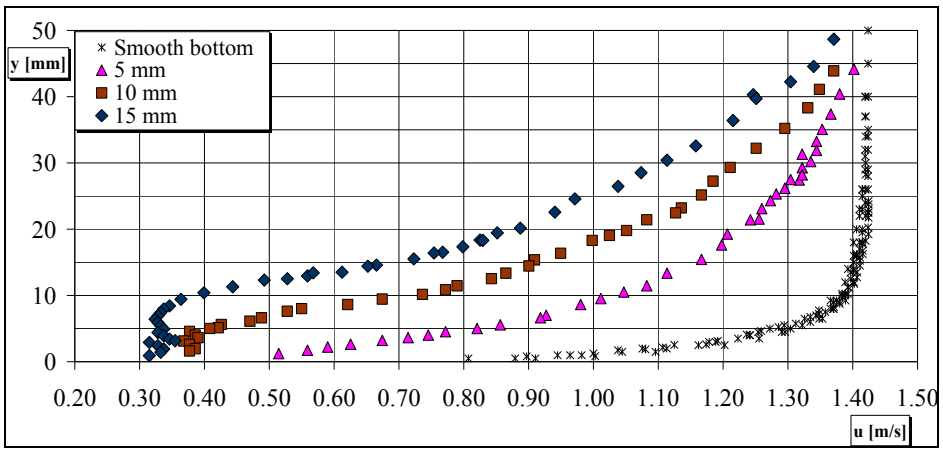

Fig. 14.2 - Local mean velocity distributions in test section n.4, lateral vertical (double density).

14.4 Control of flow rate experimental values

Once the experimental local mean velocity distributions had been obtained, some preliminary elaboration of the data were carried out.

First of all, the local mean velocity distributions were completed through two further values of the velocity, respectively relative to the bottom and to the free surface, which could not be obtained directly through the LDA measurements. These values were defined through suitable extrapolation techniques.

The second preliminary elaboration was to control, in each test section and in each flow condition, the flow rate experimental values per unit width q_u. This control was performed starting from the integral definition of the flow rate per unit width and transforming it in a summation:

$$(14.5) \qquad q_u = \frac{Q}{b} = \int_h V dh. \cong \sum_0^{h\,max} V_{mean} \cdot \Delta h$$

The summation was carried out with reference to each height step bounded by two following experimental points (included the bottom and the free surface) and the term V_{mean} represents the mean value of the superior and inferior velocity values in each summation step.

The result of the summation represents directly the unit flow rates in case of smooth bottom, while in the cases of vegetated bottom instead, the unit flow rates were obtained for

each vegetated bottom, through a mean between the results of the summation relative to central and lateral measurements.

The results of such a calculation are reported in the Table 14.1. In the same table, the column of theoretical flow rates represents the values computed directly multiplying the theoretical velocity in the vena contracta (1.424m/s) by the vena contracta cross section suitably reduced of the cross section relative to the cylinders. Moreover, also a column with the mean experimental flow rates among the four test sections of each considered flow condition are shown.

In the last column of the Table 14.1, the ratios between experimental flow rates and theoretical ones are reported. The maximum difference appears to be 2.5%: it can be attributed to experimental discrepancies. Therefore, the goodness of the fit between experimental and theoretical flow-rate values is sufficiently proved.

Flow rates are expressed per unit width, they show that the influence of lateral walls can be neglected similar to the wide channel case. Consequently in following calculations equation (4) with the Marchi's coefficient 0.83 will be considered.

Table 14.1 - Experimental and theoretical flow rates

		Experimental flow rates Q m^3/s				Theoretical flow-rates Q (m^3/s)	Experimental flow-rates means Q (m^3/s)	Ratio
		sec.1	sec.2	sec.3	sec.4			
Smooth bottom		0,00984	0,00988	0,00986	0,00983	0,00985	0,00985	1,000
Single Density	**5mm**	0,00981	0,00975	0,00974	0,00970	0,00968	0,00975	1,007
	10mm	0,00981	0,00974	0,00969	0,00975	0,00951	0,00975	1,025
	15mm	0,00958	0,00941	0,00931	0,00943	0,00934	0,00943	1,010
Double Density	**5mm**	0,00972	0,00966	0,00957	0,00956	0,00968	0,00962	0,994
	10mm	0,00952	0,00941	0,00924	0,00948	0,00951	0,00941	0,990
	15mm	0,00917	0,00895	0,00890	0,00939	0,00934	0,00910	0,975

14.5 Basic methodology to obtain the f friction factor starting from boundary layer measurements

In the following paragraphs the methodology to obtain the f friction factor starting from boundary layer measurements will be described. In fact, as the available stream is a boundary layer one, the flow is not uniform and the f friction factor values that can be obtained are the cross section ones, and define a cross section f(s) function. In subsequent paragraph it will be shown how to obtain the uniform flow reach value of f friction factor. This one will be subsequently used to obtain the absolute roughness ε and/or the Manning coefficient n of the considered kind of vegetated bottom.

Let us suppose to know the function f(s) relative to a certain kind of vegetated bottom and

to the specific stream flowing over. Taking into account the circumstance that also the flow depth h(s) and the flow velocity V(s) = q_u/ h(s) are functions of the same distance, it will be possible to write the Darcy-Weisbach equation (14.1) in the following way, where $\overline{V}$ is the mean velocity in cross section:

$$(14.6)\quad J(s)=\frac{f(s)}{4h(s)}\frac{\left[\overline{V}(s)\right]^2}{2g}$$

as in an wide rectangular cross section of flow depth h the hydraulic radius coincides with h. Now it is also possible to write:

$$(14.7)\quad J(s)=-\frac{dH(s)}{ds}=-\frac{d}{ds}\left\{\alpha(s)\frac{\left[\overline{V}(s)\right]^2}{2g}\right\}$$

where α is the Coriolis coefficient, which in boundary layers is also a function of s. In fact, the hydraulic head H is the sum of the piezometric head and the kinetic head: the first one is constant in all our boundary layers currents as their free surface are always horizontal.

Consequently, equations (14.6) and (14.7) give:

$$(14.8)\quad f(s)=-\frac{8gh(s)}{\left[\overline{V}(s)\right]^2}\frac{d}{ds}\left(\alpha(s)\frac{\left[\overline{V}(s)\right]^2}{2g}\right)=-\frac{4h(s)}{\left[\overline{V}(s)\right]^2}\frac{d}{ds}\left\{\alpha(s)\left[\overline{V}(s)\right]^2\right\}$$

Remembering now that $\overline{V}=q_u/h$ is the mean velocity in cross section and that consequently $\overline{V}$ is variable with s, whereas q_u is constant, rearranging of terms yields:

$$(14.9)\quad \begin{aligned} f&=-\frac{4h^3}{q_u^{\,2}}\frac{d}{ds}\left(\alpha\frac{q_u^{\,2}}{h^2}\right)=-4h^3\frac{d}{ds}\left(\alpha\frac{1}{h^2}\right)=-4h^3\left(\frac{1}{h^2}\frac{d\alpha}{ds}-\frac{2\alpha}{h^3}\frac{dh}{ds}\right)= \\ &=4h^3\left(\frac{2\alpha}{h^3}S-\frac{1}{h^2}\frac{d\alpha}{ds}\right)=8\alpha S-4h\frac{d\alpha}{ds}\end{aligned}$$

In previous equation, for sake of simplicity, the functional dependence on s has been discarded. Now, as it will be shown afterwards, a particular cross section can be identified where the condition dα/ds = 0 holds. Flow in this cross section most closely resembles uniform flow (α=const). In this section we assume that the simplified resistance equation, f = 8αS, is valid. The corresponding friction factor f is assumed to be a representative reach value of a uniform flow, having the same flow rate and water depth as the aforementioned selected channel cross section.

At this point the situation is the following one. The f friction factor value relative to the uniform flow can be computed through the simple formulation f = 8αS utilized in the suitable

cross section where dα/ds = 0. In order to obtain the unknown abscissa of this cross section and also the unknown value of α in the same cross section, it is necessary to known the analytical expression of the α(s) function. The value of α at the cross section will be obtained by interpolation of α values determined from velocity profiles in the test sections.

14.6 Calculation of α values, α(s) functions and f friction factor values

In the case of smooth bottom, as the velocity is the same along any horizontal line of the cross section, the expression of α can be easily transformed in an equation holding integrals of only one parameter (instead of surface integrals) which at last can be computed in the same way that in equation (14.5), i.e.:

$$(14.10)\quad \alpha = \frac{\int_0^{h\,max} V^3 dh}{h\overline{V}^3} = \frac{\sum_0^{h\,max} \frac{(V^i c^3 + V^{i+1} c^3)}{2} \cdot \Delta h}{h\overline{V}^3}$$

where V^i_c is the measured velocity at measurement point i.

In contrast, in the case of our model of vegetation, the flow velocity is variable along any horizontal line of the cross section, and therefore α can not be calculated as easily. To solve this difficulty, we make use of the available velocity distributions in the test sections in the following way.

First of all, if we consider any horizontal line in a cross section, it happens that the horizontal velocity distribution has an oscillating behaviour between a minimum value corresponding to lateral measurements and a maximum value corresponding to central measurements. Among the possible functions, the sine function is the most suitable that can represent this oscillating behaviour. Consequently, we can start from this equation:

$$(14.11)\quad \alpha = \frac{\int_0^{h\max} \overline{V^3}_{mean}\, dh}{h\overline{V}^3}$$

where the symbol $\overline{V^3_{mean}}$ is defined as the cubic mean of the velocity values along a horizontal line. In order to compute this term taking into account a sinusoidal velocity distribution between a minimum value (V_l) and a maximum value (V_c), it is necessary to start from the following representation of the horizontal velocity distribution: $V = V_0 + \Delta V \sin x$, where:

$$(14.12)\quad V_0 = \frac{V_c + V_l}{2} \qquad \Delta V = \frac{V_c - V_l}{2}$$

Consequently, it is possible to write in the generic point of the considered horizontal line:

$$\overline{V_{mean}^3} = \frac{1}{2\pi}\int_0^{2\pi}\left(V_0 + \Delta V \sin x\right)^3 dx =$$

(14.13)

$$= \frac{1}{2\pi}\int_0^{2\pi}\left(V_0^3 + 3V_0^2\Delta V \sin x + 3V_0\Delta V^2 \sin^2 x + \Delta V^3 \sin^3 x\right)dx = V_0^3 + \frac{3}{2}V_0\Delta V^2$$

Substituting now equation (14.12) in equation (14.13), it is possible to obtain, through simple calculations:

$$\overline{V_{mean}^3} = V_0^3 + \frac{3}{2}V_0\Delta V^2 = \left(\frac{V_c + V_l}{2}\right)^3 + \frac{3}{2}\left(\frac{V_c + V_l}{2}\right)\left(\frac{V_c - V_l}{2}\right)^2 = \frac{V_c^3}{2} + \frac{V_l^3}{2} - \frac{3}{16}\left(V_c - V_l\right)\left(V_c^2 - V_l^2\right) \quad (14.14)$$

Now, this expression must be inserted in equation (14.11) and this one must be suitably integrated obtaining:

$$\alpha = \frac{\int_0^{h\,max}\overline{V_{mean}^3}\,dh}{h\cdot\bar{V}^3} = \frac{\int_0^{h\,max}\frac{V_c^3}{2}dh + \int_0^{h\,max}\frac{V_l^3}{2}dh - \int_0^{hmax}\frac{3}{16}\left(V_c - V_l\right)\left(V_c^2 - V_l^2\right)dh}{h\cdot\bar{V}^3} \quad (14.15)$$

Finally, we transform integrals in summations obtaining:

$$\alpha = \frac{\sum_0^{h_{max}}\frac{(V^i{}_c{}^3 + V^{i+1}{}_c{}^3)}{2}\frac{\Delta h_i}{2} + \sum_0^{h_{max}}\frac{(V^i{}_l{}^3 + V^{i+1}{}_l{}^3)}{2}\frac{\Delta h_i}{2} - \sum_0^{h_{max}}\eta_j\Delta h_j}{h\cdot\bar{V}^3} \quad (14.16)$$

with:

$$\eta_j = \frac{3}{16}\left(V_{cj} - V_{lj}\right)\left(V_{cj}{}^2 - V_{lj}{}^2\right) \quad (14.17)$$

where j represent the generic height between two following measurement points. Finally, equations (14.16) and (14.17) allow calculation of α values in all the test sections of all the seven considered flow conditions. These values are reported in Table 14.2.

The values from the Table 14.2 are also presented in Figure 14.3. In this figure it is shown that the experimentally obtained α values can be interpolated through second order polynomials which start all from the same s_0 section placed at about 0.10m from the leading edge of the boundary layer. Up to this section, the α value may be considered equal to unity.

Table 14.3 shows the results of the aforementioned analysis: the second order polynomial curves coefficients a, b, c; the slope of the channel S; the abscissa s_0 of the test section where $d\alpha/ds = 0$; the height of the test section where $d\alpha/ds = 0$.

Table 14.2 - Coriolis α values for every flow conditions and in each test section

		Final α values			
		sec.1	**sec.2**	**sec.3**	**sec.4**
Smooth bottom		1,0081	1,0069	1,0127	1,0161
Single Density	**5mm**	1,0289	1,0416	1,0507	1,0590
	10mm	1,0470	1,0790	1,0998	1,1132
	15mm	1,0884	1,1411	1,1796	1,1833
Double Density	**5mm**	1,0343	1,0369	1,0458	1,0402
	10mm	1,0743	1,1027	1,1298	1,1071
	15mm	1,1371	1,1890	1,2178	1,1749

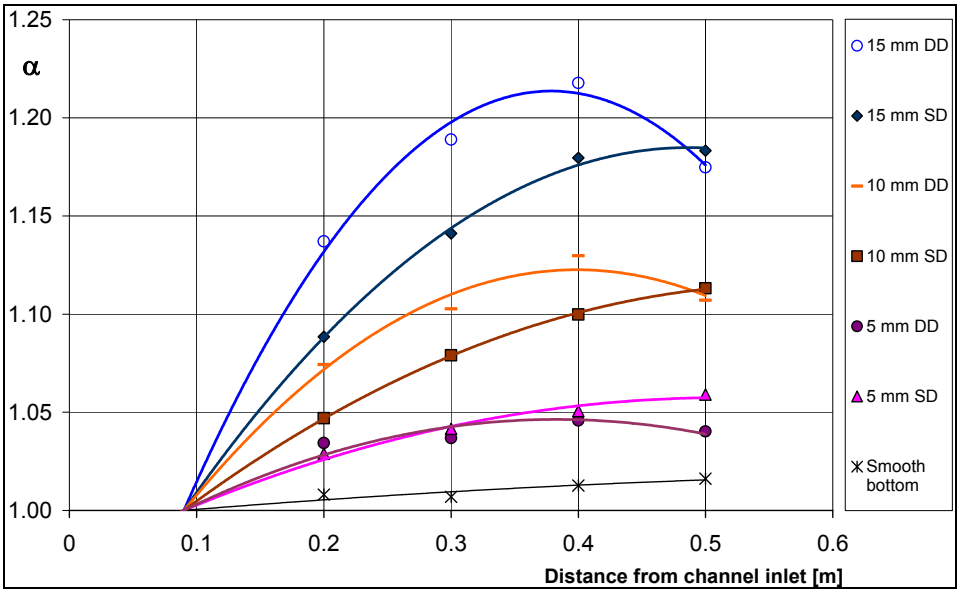

Fig. 14.3 - Values of parameter α and interpolating functions

Once the maximum values of α for each flow condition have been obtained, it is finally possible to use equation (14.9) to obtain the friction factor f values relative to the seven different considered bottoms. The results of such calculations are reported also in Table 14.3.

Table 14.3 - Interpolating curves coefficients for α values, consequent maximum values of same α and f correspondent values for each considered bottom.

		$\alpha=as^2+bs+c$			S	s_0 [m]	h_0 [m]	α [s=s_0]	f=8Sα [s=s_0]
		a	**b**	**c**					
Smooth bottom		-0,03630	0,05930	0,99500	0,0025	0,817	0,04814	1,01922	0,02038
Single Density	**5mm**	-0,31910	0,32820	0,97310	0,0092	0,514	0,05083	1,05749	0,07783
	10mm	-0,49900	0,55930	0,95280	0,0160	0,560	0,05507	1,10952	0,14202
	15mm	-1,17120	1,14140	0,90680	0,0227	0,487	0,05716	1,18489	0,21518
Double Density	**5mm**	-0,54110	0,41410	0,96710	0,0115	0,383	0,05050	1,04633	0,09626
	10mm	-1,28530	1,02520	0,91820	0,0205	0,399	0,05428	1,12263	0,18411
	15mm	-2,56320	1,94120	0,84610	0,0295	0,379	0,05727	1,21363	0,28642

14.7 Final calculations of n and ε values

Finally, starting from the obtained f values, and employing the aforementioned methodologies, it is possible to obtain the absolute roughness ε corresponding to the seven considered bottoms. In particular it is necessary to invert equation (14.4), with the shape parameter $\psi = 0.83$. The results of such calculations are reported in Table 14.4.

Table 14.4 - Bed's slopes and final f values and for each flow condition, and consequent absolute roughness

		$f=8\alpha i$ [$s=s_0$]	S	h_0 [m]	$\varepsilon/4h_0$ [$s=s_0$]	ε [$s=s_0$]
Smooth bottom		0,02038	0,0025	0,04814	0,000720	0,000139
Single Density	**5mm**	0,07783	0,0092	0,05083	0,049685	0,010102
	10mm	0,14202	0,0160	0,05507	0,145103	0,031961
	15mm	0,21518	0,0227	0,05716	0,257374	0,058847
Double Density	**5mm**	0,09626	0,0115	0,05050	0,075319	0,015215
	10mm	0,18411	0,0205	0,05428	0,210463	0,045692
	15mm	0,28642	0,0295	0,05727	0,358251	0,082069

15. CALIBRATION ON THE NEW METHODOLOGY

15.1 Experimental calibration of the methodology

In order to test the reliability of the arbitrary assumption relative to the choice $f = 8\alpha S$ where the condition $d\alpha/ds = 0$ holds and in general of the whole methodology, or in any case in order to calibrate the last one, further measurements have been performed using a much larger channel with varying slope, endowed with the single density 1.5cm high vegetation type.

The channel, deeply described in chapter n.5, has plexiglas walls and bottom, and is 40 cm large, 8 m long and its walls are 40 cm high.

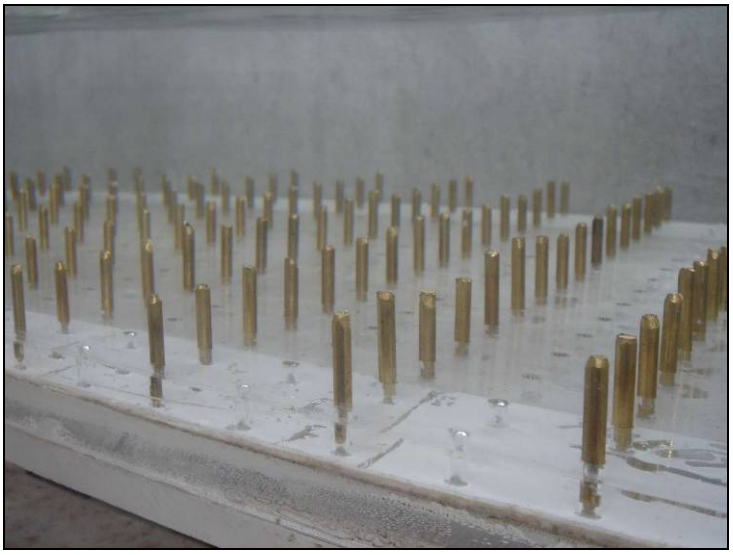

Fig. 15.1 - Vegetation chosen for the experimentation

Fig. 15.2 - Channel used for the experimentation

The measurement of the ε absolute roughness was performed giving to the bottom a suitable slope, and feeding it through an also suitable flow rate. As the channel is sufficiently long, it is always possible to obtain at its end a uniform flow. In case of supercritical flow the current attains the uniform flow naturally. In case of subcritical flow, the use of a sluice gate at the end allows it to attain the uniform flow.

The ε absolute roughness was then calculated through eq. (14.4) (where the second term of the parenthesis could be eliminated), measuring experimentally the other terms (slope and mean cross section velocity as ratio between flow rate and cross section area)

The first control that has been performed has been if the ε absolute roughness value would keep constant with the possible changing of the flow depth. In particular, it was decided to measure the roughness value in six different flow conditions: three in a subcritical flow and three in supercritical flows, always with different depths, in order to verify if the ε absolute roughness would keep constant.

Table 15.1 - Uniform flow conditions

Test n.	**Flow conditions**	**Slope**	**Flow-rate [l/s]**	**h_u [m]**	**V_u [m/s]**	**ε [m]**
1	subcritical	1%	33 l/s	0,0970	0,850	0,035
2	subcritical	1%	45 l/s	0,1155	0,974	0,035
3	subcritical	1%	22,6 l/s	0,0785	0,719	0,035
4	supercritical	2%	22,6 l/s	0,0644	0,876	0,033
5	supercritical	2%	33 l/s	0,0803	1,027	0,035
6	supercritical	2%	45 l/s	0,0954	1,178	0,035

In fact, the ε values coincide one another, within the experimental accidental errors, and consequently, their mean value has been considered as the true value (0.0347m).

This value has been subsequently compared with the correspondent value previously obtained through the boundary layer measurements (0.058847). The result has been that the true value appears to be a little less than the previous one, probably due to the already remembered arbitrary assumption. It is noteworthy that the difference between boundary layer measurements and the more reliable uniform flow measurements would appear at a first sight a little large, but really the presence of the logarithm in the Colebrook-White equation

strongly mitigates the actual consequences of the same difference.

Consequently, at least at this stage, the ratio (0.590) between the obtained true value and previous value computed through the new methodology has been assumed as a calibration constant for the same methodology.

Using this calibration factor, new values of the absolute roughness have been calculated either in the case of smooth bottom or in the six models of vegetated bottom. In Table 6 these calibrated values have been furnished. In the same table the correspondent n values are also referred, which have been obviously obtained starting from the f value and using eq. (14.2); but they will be used afterwards.

Table 15.2 - Final values of absolute roughness ε and Manning's n coefficients for the seven different considered vegetation conditions.

		$(f=8\alpha i)_{sl}$	ε_{sl}	ε_{unif}	$\varepsilon_{unif}/\varepsilon_{sl}$	ε_{sl} calibrati	n
Smooth bottom		0,02038	0,000139	-	-	0,000082	**9,30E-03**
Single Density	**5**	0,07783	0,010102	-	-	0,005957	**1,70E-02**
	10	0,14202	0,031961	-	-	0,018846	**2,24E-02**
	15	0,21518	0,058847	0,0347	0,590	0,034700	**2,68E-02**
Double Density	**5**	0,09626	0,015215	-	-	0,008972	**1,86E-02**
	10	0,18411	0,045692	-	-	0,026943	**2,49E-02**
	15	0,28642	0,082069	-	-	0,048393	**3,01E-02**

The ε value in the case of smooth bottom appears to be less than 0.1mm, that is correspondent to a condition of almost totally smooth bottom.

Finally, in figure 15.3, the obtained roughness of each vegetated bottom is reported as a function of the cylinders height and density, including also the case of smooth bottom. The experimental points are very well aligned along straight lines which join themselves in a single point on the abscissa axis. Probably the ε value is almost zero if the cylinders height is no more than 2 or 3mm, due to the presence of the laminar substratum. The two straight lines show an increasing trend with the cylinders height, more accentuated in case of double density with respect to single density. Besides the 3mm cylinders' height ε values can be computed, in relation to the two vegetation densities, through the following formulas, also reported within the diagram:

(15.1) $$\varepsilon = 2.874h - 0.0089$$

(15.2) $$\varepsilon = 3.942h - 0.0113$$

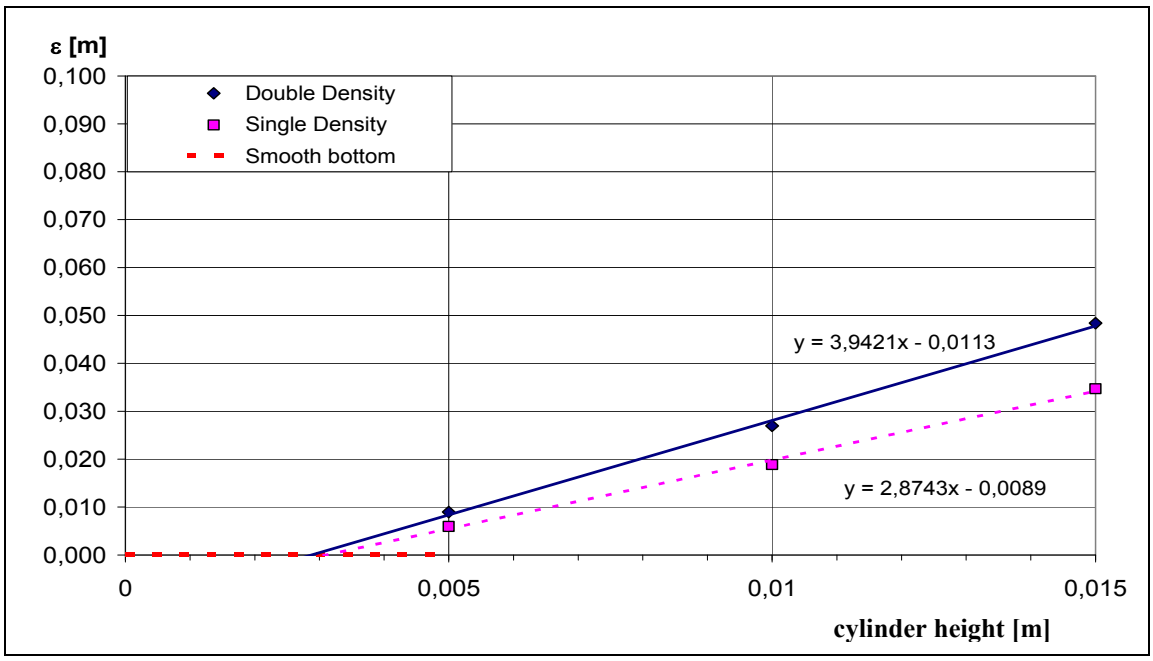

Fig. 15.3 - Absolute roughness values of the different bottoms and their interpolating functions.

15.2 Comparison with data from literature

As it has been already stressed, the very little value of absolute roughness obtained in the case of smooth bottom represents a first confirmation of the validity of the considered procedure.

But, in any case, another literature control has been performed with the Lopez and Garcia experimental data (1997). In particular, to perform such a comparison, a graph of Lopez and Garcia (figure 15.4) has been considered. This graph is relative to experiments carried out with rigid submerged vegetation realized through vertical cylinders always of 10cm height but of different densities and with currents heights of the order of 0,50m. In this graph, in the abscissa, the projected area of vegetation per unit volume of water in the flow direction (vegetation density) and in the ordinate the Manning's n values, are reported. For every value of vegetation density a single experimental point is plotted as a black point. These points appear to be aligned along a horizontal line till a value of about 0.025 for the vegetation density, and afterwards along an inclined line which is represented on the graph.

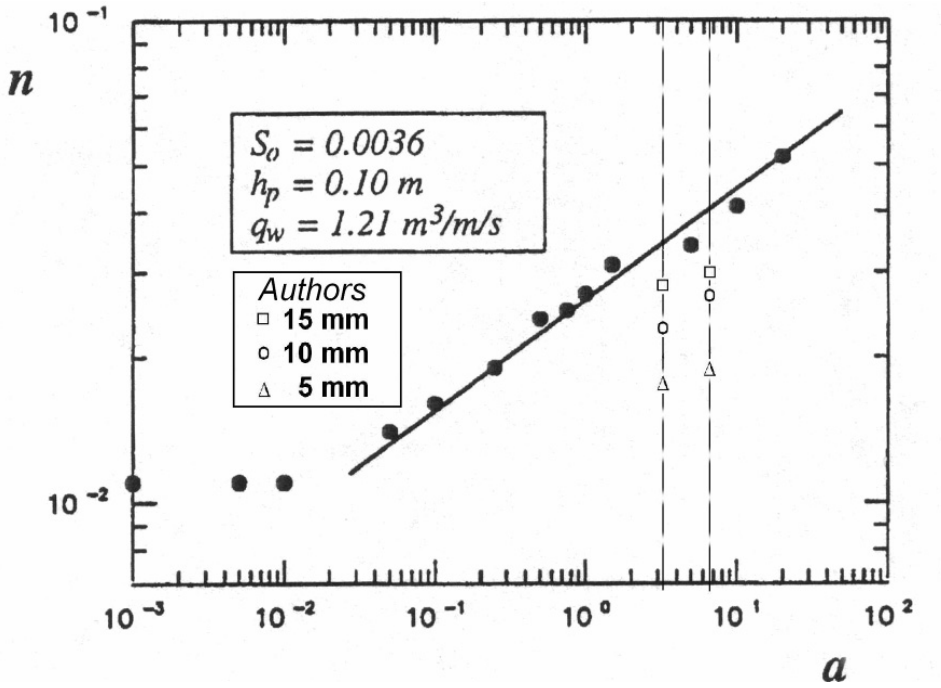

Fig. 15.4 - Comparison between Lopez and Garcia data and authors' data

In the cases of our measurements, the projected area of vegetation per unit volume of water in the flow direction is worth $3.2m^{-1}$ in the case of single density and $6.4m^{-1}$ in the case of double density. Two dotted vertical lines are representative of these values. In relation to the experiments carried out, six experimental points have been obtained, relative to both two densities' values and three cylinder' heights. For each one of these six different conditions, the values of the Manning's n reported in Table 14.4 (chapter n.14) have been represented through a specific point into the Lopez and Garcia graph. The obtained results are qualitatively comfortable. The Manning's n value depends mainly on the bottom roughness, so that, with equal cylinders density, the n coefficient must grow with the height of the cylinders. Figure 8 shows that for both cylinders densities, higher cylinders yield higher Manning's n values, and that the obtained roughness values from the current study remain always lower than the Lopez and Garcia interpolating line which corresponds to 10cm cylinder height.

But, if we would go deeper into the matter, it must be stressed that the comparison between authors' data and Garcia and Lopez data has been here carried out independently of the circumstance that the depth of the two considered currents is much different one another.

In order to take in consideration also this circumstance and attain a more significant comparison, in the next chapter some additional considerations will be made about significance of ε and n parameters and the influence of the depth of the current.

15.3 Significance of n and ε roughness parameters

It is a known feature of the Manning's n parameter that it depends not only on the bottom's nature but also moderately on the hydraulic radius of the considered water current. It was already Chow who proposed some consideration about this matter, that was substantially the following one.

<In planning problems, it was pointed out that n depends on the height of the current flow, on the shape of the section and on the channel slope, which would make impossible to supply a univocal solution of the measuring problem.

However, it is also clear that n is linked to the product of the current mean velocity by the hydraulic radius.

In particular, this relation is specific for a certain type of vegetation, and it seems to be independent of the shape of the section and the channel slope.

Practically speaking, it was noticed that the curves n-VR relative to channels characterized by different types of vegetation and different shapes of the section and slopes, group themselves in reference curves n-VR, each one relative to some entity of flow resistance (low, mean, high…) classified according to the type of vegetation and its height and density.>

It is to say that Chow expressed the variability of n for a fixed type of vegetation as a function of the VR product (practically a Reynolds number).

At present, the ε parameter is more and more used as a characteristic one for rough surfaces instead of the older n one. A fundamental hypothesis linked to the use of the ε parameter is that it really depends only on the surface characteristics (and for this reason it appears as a characterization of the same surface better than the n parameter). In this paper the ε parameter has been largely used, whereas the n parameter has been used only to make suitable comparisons with older literature.

The hypothesis of constancy of the ε parameter can explain the variability of the n parameter. Indeed, the joint use of equations (14.2) and (14.4) leads to the following new correspondence equation:

$$(15.3)\quad n = \frac{R^{1/6}}{2\sqrt{8g}\,\log\dfrac{14.84\psi R}{\varepsilon}}$$

Eq. (15.3) is wholly valid only if the term $2.51/Re\sqrt{f}$ is negligible with respect to the term $(\varepsilon/4R)/3.71$ within eq. (14.4), circumstance that happens practically always with vegetated bottoms. In case it is not, eq. (15.3) can be yet considered only approximately valid.

This equation clearly shows that, if, in a current with a fixed wall type but with different

hydraulic radius R values, the ε parameter can be considered constant, consequently the n parameter must depend on the hydraulic radius R. This is the first level conclusion.

Moreover it is possible to study the function n(R). An analytical study of this function, very simply performed through the study of the sign of its derivative, shows that this sign depends on the value of the ratio ε/R. More precisely the break value of this ratio is $14.84\psi/e^6$: if ε/R is less than this break value then n increases with increasing R, whereas if ε/R is larger than this break value then n lowers with increasing R. In the case of a large rectangular channel, the break value is 0.03. Consequently in case of common roughness or also of vegetation sparse and/or low (ε/R<0.03) the first situation holds, as many authors have pointed out, whereas in case of high and/or dense vegetation (ε/R<0.03) the second situation holds.

In particular, the ratio between the two n_{LP} and n_{auth} corresponding to the flow depths of Lopez and Garcia and to our flow depths can be obtained through the equation:

$$\frac{n_{LP}}{n_{auth}} = \left(\frac{R_{LP}}{R_{auth}} \right)^{1/6} \Bigg/ \frac{log(14.84\psi R_{LP} / \varepsilon)}{log(14.84\psi_{auth} / \varepsilon)} \tag{15.4}$$

This equation, due to the reciprocal error correction between numerator and denominator, can be considered almost exact also in case eq. (15.3) could be considered only approximately valid.

As for the statement of Chow about the dependence on the VR product, it must be stressed that, with constant ε, increases of hydraulic radius bear increases of velocity too.

Consequently it can be supposed that some little confusion between a dependence only on R and a dependence on the product VR could be happened.

15.4 Deeper comparison with data from literature

The considerations of the previous paragraph allow to deepen the comparison with the Lopez and Garcia data.

In fact the n values that were calculated in Table 15.2 were relative to our flow depths. In order to compare with the Lopez and Garcia data it is necessary to calculate the n values of the considered vegetated beds as if they were placed under the Lopez and Garcia currents, in particular taking into account the different depths of their currents.

The mentioned calculations are performed in the following Table 15.3.

Table 15.3 -Values of absolute roughness ε and Manning's n coefficients for the seven different considered vegetation conditions relative to Lopez and Garcia currents.

		n (our)	abs.rough.	R = h	ratio	n (L&G)
Smooth bottom		0,009300	0,000082	0,04814	1,169161	0,01087
Single Density	**5**	0,016992	0,005957	0,05083	0,981663	0,01668
	10	0,022371	0,018846	0,05507	0,893990	0,02000
	15	0,026796	0,034700	0,05716	0,834310	0,02236
Double Density	**5**	0,018640	0,008972	0,05050	0,951005	0,01773
	10	0,024901	0,026943	0,05428	0,855992	0,02132
	15	0,030113	0,048393	0,05727	0,793369	0,02389

In this Table, for completeness, also the (approximated) calculation for the smooth bottom is inserted. The single columns hold the following data:

The "n(our)" column holds the n values already calculated in Table 15.2 and which correspond to our flow depths.

The "abs rough" column holds the absolute roughness values already calculated in Table 15.2.

The "R=h" column holds the heights of our currents already considered in Table 14.4.

The "ratio" column is the core of the calculation. On the ground of the values in previous columns here are reported the ratios between the n values calculated with regard to Lopez and Garcia flow depths and the n values calculated with regard to our flow depths. This calculation is obviously performed using eq. (15.4) and is only approximated in case of smooth bottom. As it can be seen, these ratios are always less than unity, except in the case of smooth bottom where the ratio is more than unity; and both behaviours are wholly correspondent to the considerations of the previous paragraph.

In the last "n(L&G)" column are reported the final n values relative to the same our beds but correspondent to Lopez and Garcia flow depths. Obviously they appear more little than the previous ones, except the first one which appears larger.

The so obtained values are reported in the new diagram of figure 15.4.

Moreover the two interpolating (18) and (19) laws have been used to extrapolate the values of the absolute roughness ε to the case of 10cm high cylinders. The corresponding values are of 0.205m for the case of single density and of 0.383m for the case of double density. It is possible, always using eq.(21), starting from these values, to obtain the Manning's n values correspondent to Lopez and Garcia flow depths, which result of 0.034 for the single density and of 0.040 for the double density. Always in the Lopez and Garcia graph of fig. 9 also these two last points have been plotted (in red).

As final and exact comparison, it is possible to stress these following observations.

The n value of the smooth bottom is wholly correspondent to such a physical condition.

The n values of the vegetated bottoms are yet in agreement with the Lopez and Garcia data just in the sense already described in paragraph 15.2.

Finally, the two values of n obtained through extrapolation of the (15.1) and (15.2) laws for currents like the Lopez and Garcia ones flowing over their vegetated beds agree in a very perfect way with the experimental values of Lopez and Garcia.

All these comparisons and considerations relative to vegetated beds are performed using exact n values, which take in account all the relevant parameters (vegetation's density, vegetation's height, flow depth).

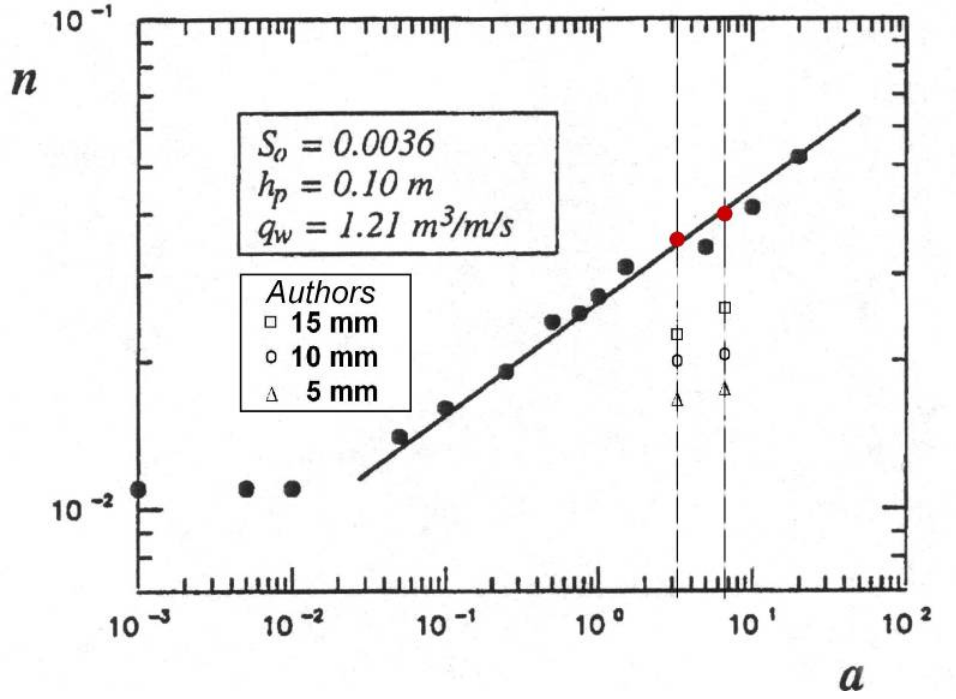

Fig. 15.5 - Lopez and Garcia graph with lastly calculated our points

16. SINGLE CYLINDER MEASUREMENTS

16.1 Introduction

In the previous chapters n.14 and n.15 a new procedure was proposed to experimentally measure the absolute roughness of vegetated river beds, which was no more based on the usual method of attaining uniform flow, but on measurements performed in boundary layer flows.

The main result was that this vegetated bed (obtained through vertical cylinders) could be considered as a rough surface whose equivalent roughness could be given by eq. (15.1) and (15.2) (in meters):

(15.1) $\varepsilon = 2.874h - 0.0089$

(15.2) $\varepsilon = 3.942h - 0.0113$

respectively in single and double density (defined in previous chapters), with h height of cylinders at least in the field 0.005-0.10m for h. The corresponding friction factors f (and consequently the ε values), in the considered current, had the values reported in the following Table 16.1.

Table 16.1 - Ratios between values of the friction factors f and absolute roughness ε relative to double and single density for the three different considered vegetation heights

Vegetation	$f_{s.d.}$	$f_{d.d.}$	f_{ratio}	$\varepsilon_{s.d.}$	$\varepsilon_{d.d.}$	ε_{ratio}
5 mm	0.07783	0.09626	1.2368	0.005957	0.008972	1.5061
10 mm	0.14202	0.18411	1.2964	0.018846	0.026943	1.4296
15 mm	0.21518	0.28642	1.3311	0.034700	0.048393	1.3946

where s.d and d.d. subscript is for “single density” and “double density”.

It is noteworthy that in double density the f friction factor values are not the double than in single density. In fact, if we compare one another either the f friction factors or the ε absolute roughness relative to the two densities with the same cylinders’ height, we can observe that they are not one the double of the other.

In particular the doubling of density should double the friction factor f in currents with the same depth and the same mean velocity. In the considered cases the two currents each time compared have almost the same depth and almost the same mean velocity, but they f values differ one another of a quantity much different than two times. Clearly the ε ratios differ from the f ratios due to the shape of eq. (14.4):

(14.4) $$\frac{1}{\sqrt{f}} = -2\log\frac{1}{\psi}\left(\frac{\varepsilon/4R}{3.71} + \frac{2.51}{Re\sqrt{f}}\right)$$

The circumstance that in double density the f friction factors are not the double than in single density could be explained through the mutual influence that cylinders aligned along a longitudinal line have one upon another. Moreover this conjecture can be considered as strengthened by the previous results relative to the locations of measurements verticals (chapter 13) which suggest that the influence zone of each single cylinder must be considered at least of the same order of magnitude than the distance among the same cylinders.

These considerations induced to investigate just about the influence zone of each single cylinder, in particular along the flow direction, so connecting also to the literature work about the single or few cylinders flow influence on currents flowing upon.

16.2 Organization of experiments

The experimentation announced in previous paragraph is based on the insertion of a single cylinder 1.5cm high (like the highest type of vegetation model carried out on the boundary layer flows in chapter n.11) in the bed of the experimental channel already considered in chapter n.15, and by using the whole acquisition system just calibrated.

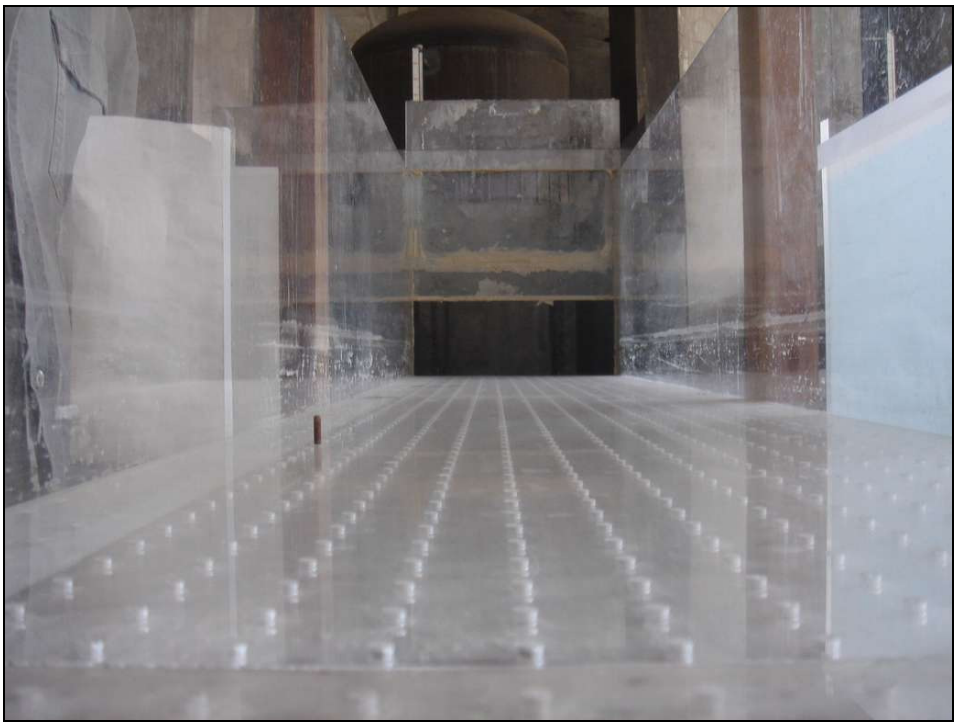

Fig. 16.1 - View of the single cylinder in the experimental channel

As already remembered, one of the advantages of using an LDA system is to have no interference with the flow, thus allowing a careful acquisition of the data. The acquisition speed was always of 2.000 data per second. Finally the time acquisition, that is a determining factor to reduce the fluctuations of the mean values to a minimum, has been yet fixed at 2 minutes and 15 seconds.

Finally, in order to obtain results comparable at all with those relative to experiences where absolute roughness values had been obtained, a very similar current type, characterized by a mean velocity of about 1.2m/s and a depth in measurements section of about 6cm, has been got ready in the channel.

Two series of statistical quantities, at first with the cylinder and then without it, in different points placed along verticals located downstream of this cylinder, at various distances from its axis (1.7cm, 2.2cm, 3.2cm, 5.2cm, 10.2cm, and 15.2cm), were acquired, so to get possible to compare the respective results.

16.3 Results of experiments

16.3.1 Distributions of local mean velocities

In the following figs. from 16.2 to 16.7, the distributions of local mean velocities are shown, relative to the six series of data acquisition. In each figure the distributions relative to the case without the cylinder and the case with the cylinder are superimposed.

It is evident that with the cylinder the velocities are lower than without it, especially at distances from the bed comparable with the height of the cylinder itself.

Moreover, it is also clear and even expectable, that the more the vertical of measurements is far from the cylinder the more the local mean velocities distribution gets closer to the distribution without the cylinder.

After the data acquisition in each point of the vertical in the two conditions with and without the cylinder, it was possible to calculate the areas of the two velocity distributions, and to compare their difference to the area obtained from the distribution without the cylinder.

These ratios are reported in the following diagram of Fig. 16.8, where it is possible to see how such ratio varies according to the distance from the cylinder.

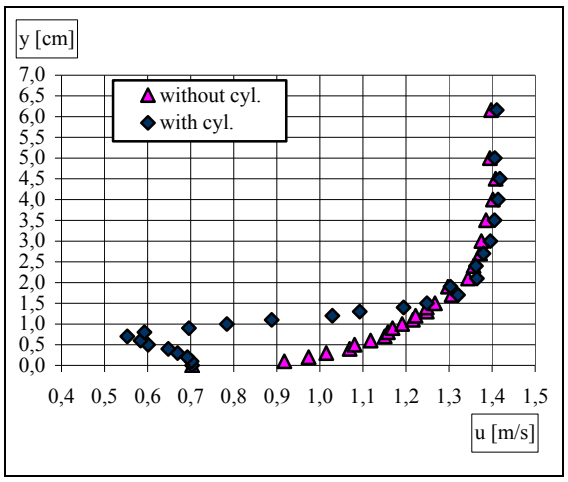

Fig. 16.2 - Distributions of local mean velocities at 1.7cm behind the cylinder

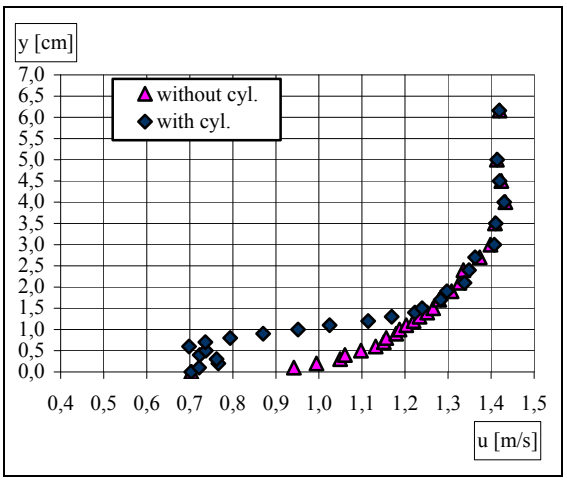

Fig. 16.3 - Distributions of local mean velocities at 2.2cm behind the cylinder

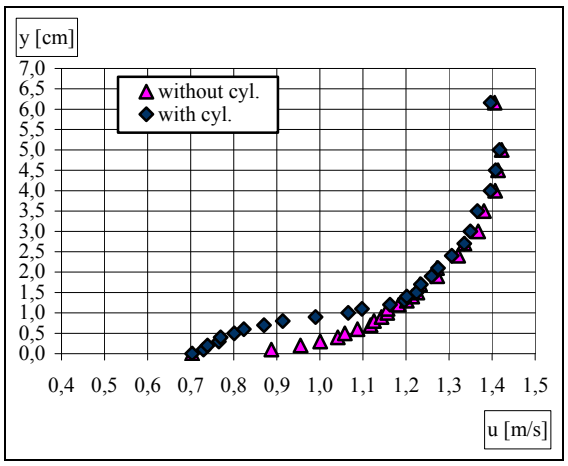

Fig. 16.4 - Distributions of local mean velocities at 3.2cm behind the cylinder

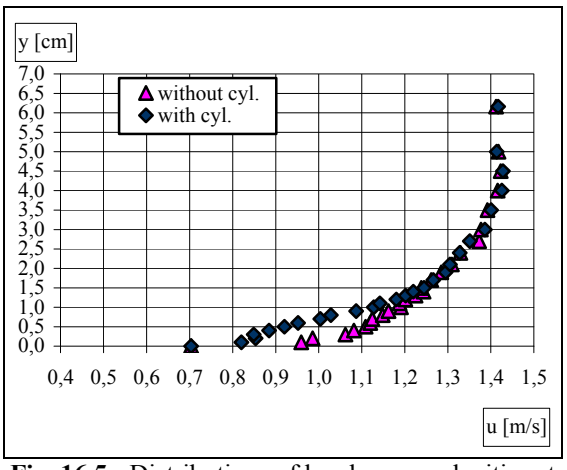

Fig. 16.5 - Distributions of local mean velocities at 5.2cm behind the cylinder

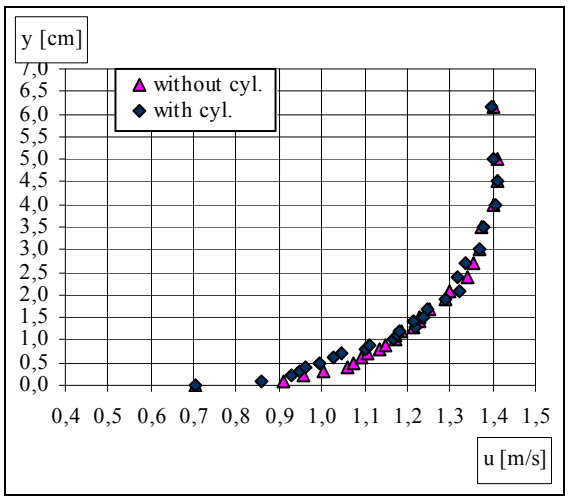

Fig. 16.6 - Distributions of local mean velocities at 10.2cm behind the cylinder

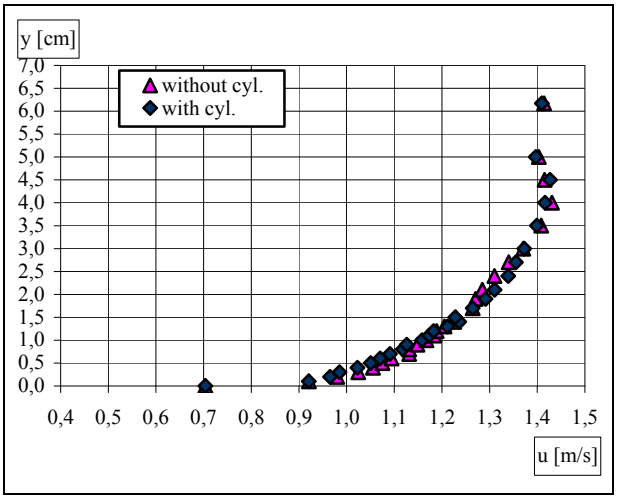

Fig. 16.7 - Distributions of local mean velocities at 15.2cm behind the cylinder

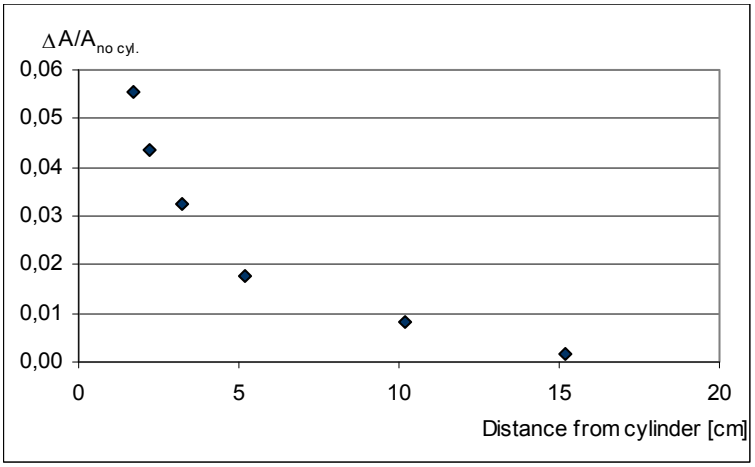

Fig. 16.8 - Relative difference of areas of mean velocity distributions against distance from the cylinder

Finally, from this diagram, it could seem that the perfect alignment of the two distributions, without and with the cylinder, would take place between 15cm and 20cm behind the cylinder.

16.3.2 Distributions of variances

In the following figs. from 16.9 to 16.14, the distributions of variances are shown, relative to the six series of data acquisition.

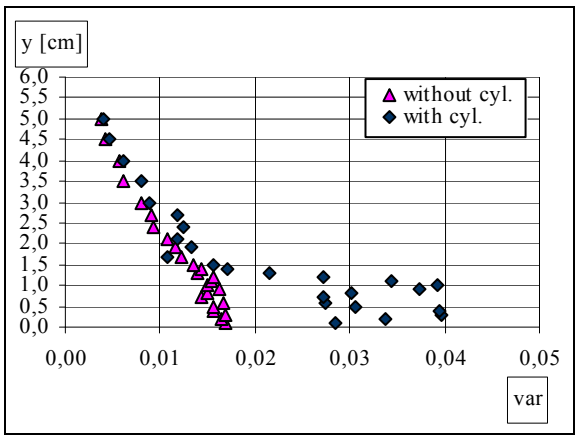

Fig. 16.9 - Distributions of variances at 1.7cm behind the cylinder

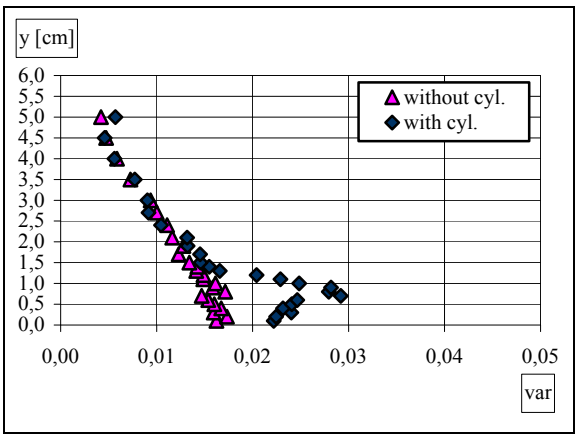

Fig. 16.10 - Distributions of variances at 3.2cm behind the cylinder

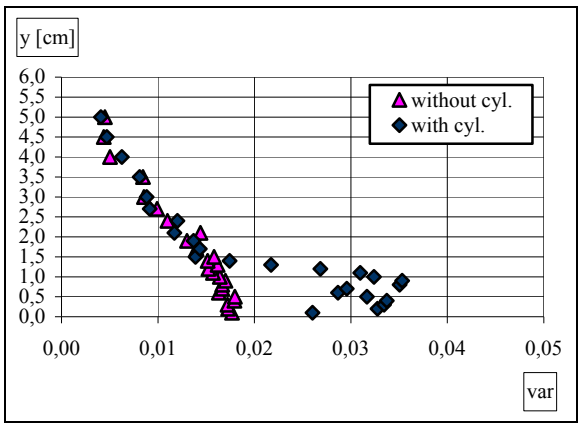

Fig. 16.11 - Distributions of variances at 2.2cm behind the cylinder

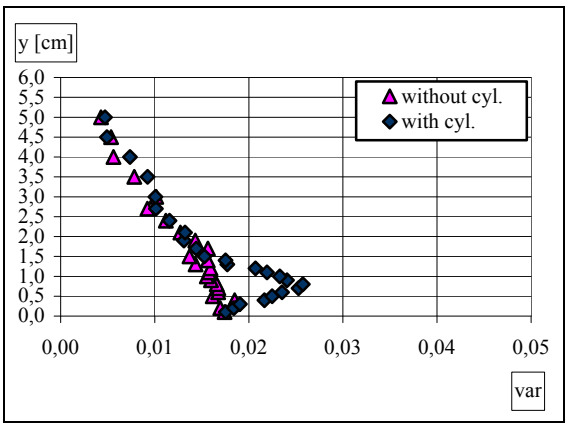

Fig. 16.12 - Distributions of variances at 5.2cm behind the cylinder

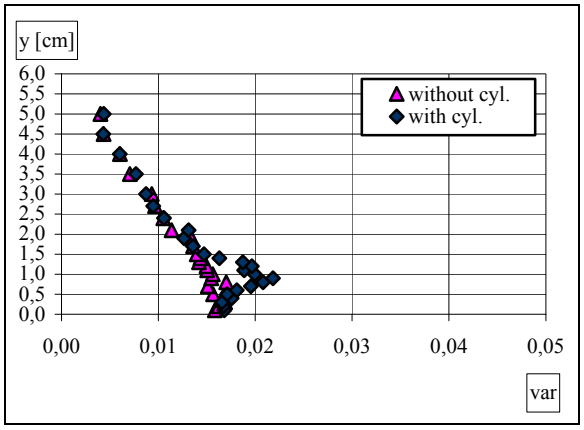

Fig. 16.13 - Distributions of variances at 10.2cm behind the cylinder

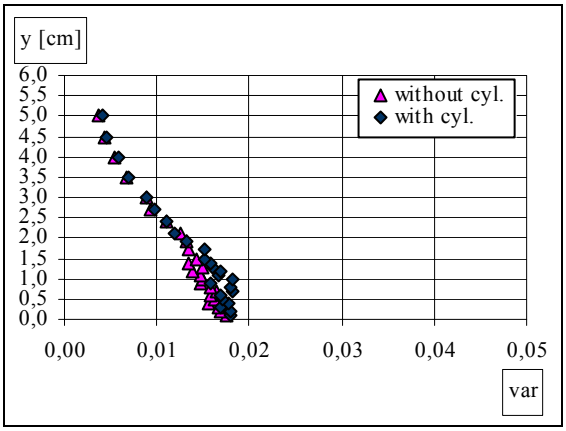

Fig. 16.14 - Distributions of variances at 15.2cm behind the cylinder

It is natural to expect that the variance increases with the approaching to the bed of the channel. Besides, we notice that in the presence of the cylinder there is a sudden rise in the variance values at the level of the cylinder itself.

In each figure the distributions relative to the case without the cylinder and the case with the cylinder are always superimposed. Here it happens that with the cylinder the variances are larger than without the cylinder, especially at distances from the bed comparable with the height of the cylinder.

Obviously here too this effect is the more less accentuated the more the vertical is far from the cylinder.

After the data acquisition in each point of the vertical in the two conditions with and without the cylinder, it was possible here too to calculate the areas of the two distributions of variances, and to compare their difference always to the area obtained from the distribution without the cylinder. These new ratios are reported in the following diagram of fig.16.15, by which it is possible to see how such ratio varies according to the distance from the cylinder.

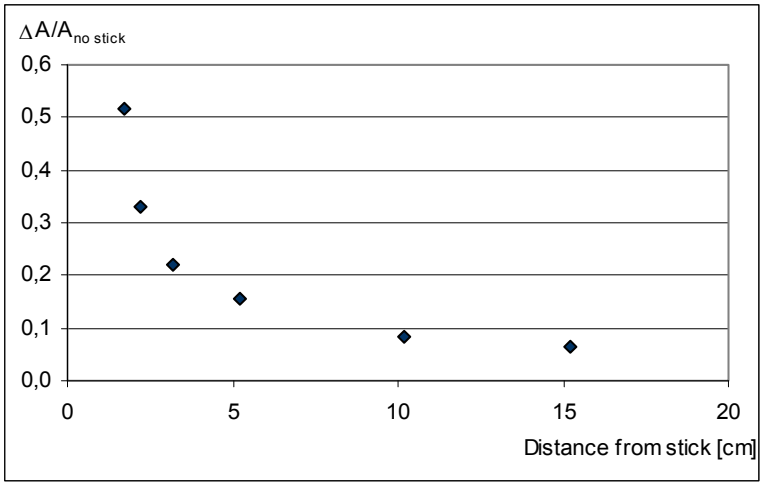

Fig. 16.15 - Relative difference of areas of fluctuation velocities variances distributions against distance from the cylinder

Here too, from this diagram, it could seem that the perfect alignment of the two distributions, without and with the cylinder, would take place perhaps at more than 20cm behind the cylinder.

16.3.3 Distributions of skewness

In the following figs. from 16.16 to 16.21, the distributions of skewness are shown, relative to the six series of acquisition.

In any case the distributions appear more irregular than the previous ones, certainly due to the circumstance that the time length of 2 minutes and 15 seconds for each run were fully sufficient for elaborating mean velocities and also fluctuation velocities variances, but were no more sufficient for elaborating the more complex skewness values with the same accuracy.

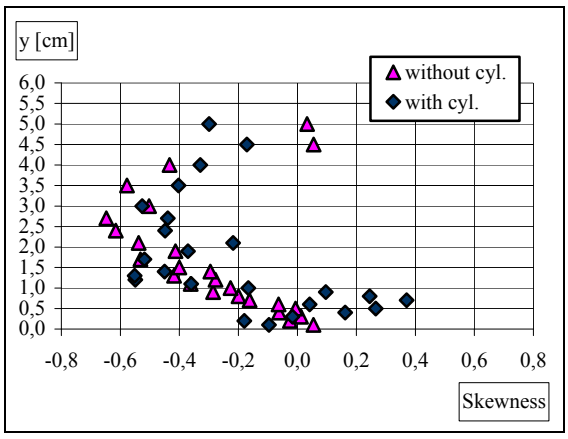

Fig. 16.16 - Distributions of skewness at 1.7cm behind the cylinder

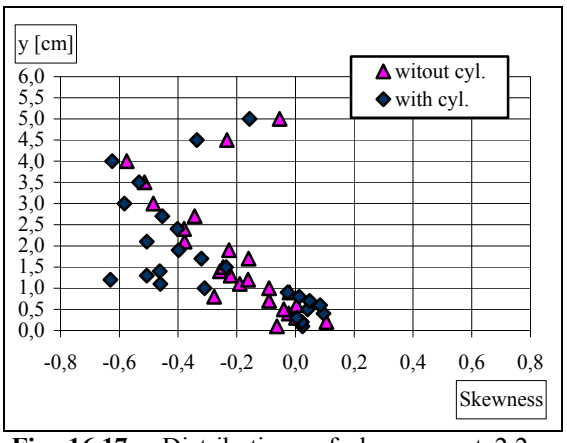

Fig. 16.17 - Distributions of skewness at 2.2cm behind the cylinder

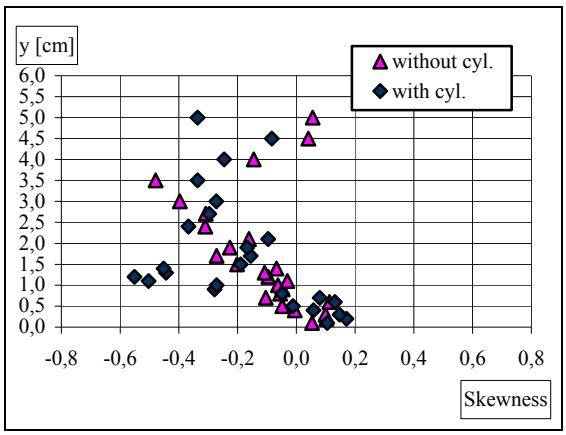

Fig. 16.18 - Distributions of skewness at 3.2cm behind the cylinder

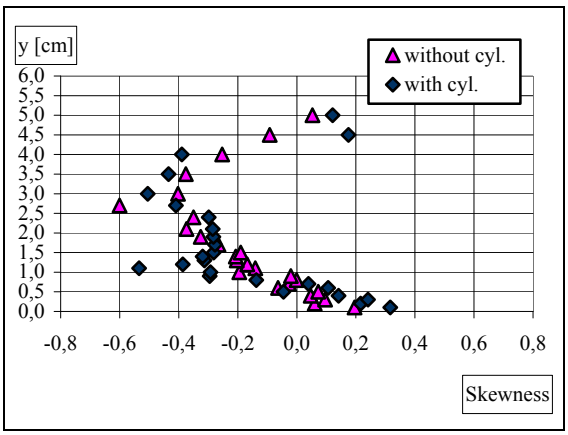

Fig. 16.19 - Distributions of skewness at 5.2cm behind the cylinder

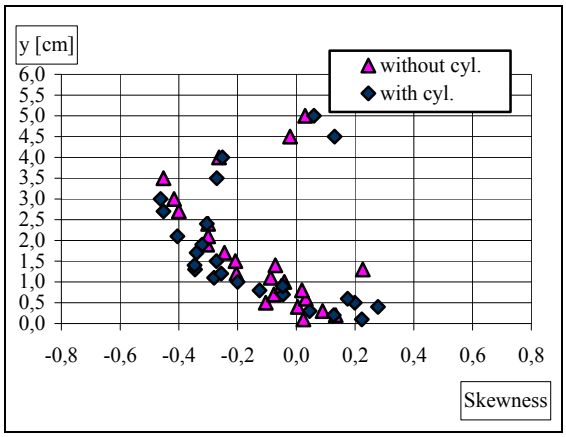

Fig. 16.20 - Distributions of skewness at 10.2cm behind the cylinder

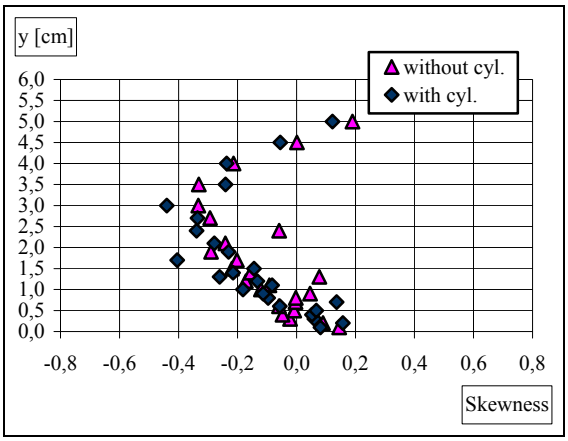

Fig. 16.21 - Distributions of skewness at 15.2cm behind the cylinder

But, also in presence of these less defined profiles, it appears however evident that the skewness values with and without the cylinder differ one from the other in correspondence of the cylinders' height, and that this difference tends to disappear at the largest distances from the same cylinder.

Here too, 15/20cm can be considered a distance where the phenomenon is finished.

More precisely, the difference between diagrams relative to conditions with the cylinder and without the cylinder is very clear especially between 10mm and 15mm height; only in the first section this difference is located between 5mm and 10mm height and is in the opposite side with respect the other ones.

16.3.4 Distributions of kurtosis

In the following figs. from 16.22 to 16.27, the distributions of kurtosis are shown, always relative to the six series of acquisition.

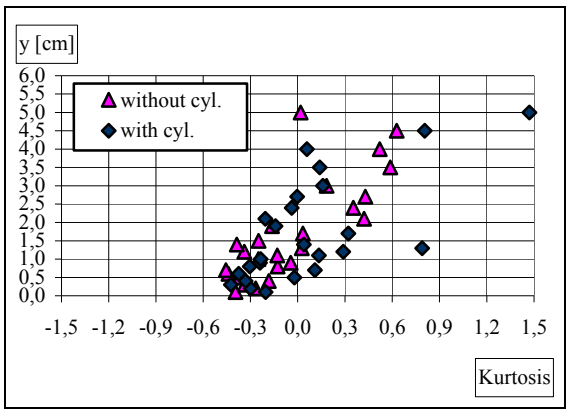

Fig. 16.22 - Distributions of kurtosis at 1.7cm behind the cylinder

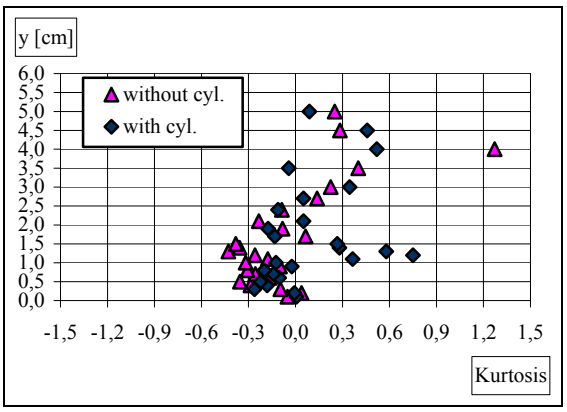

Fig. 16.23 - Distributions of kurtosis at 2.2cm behind the cylinder

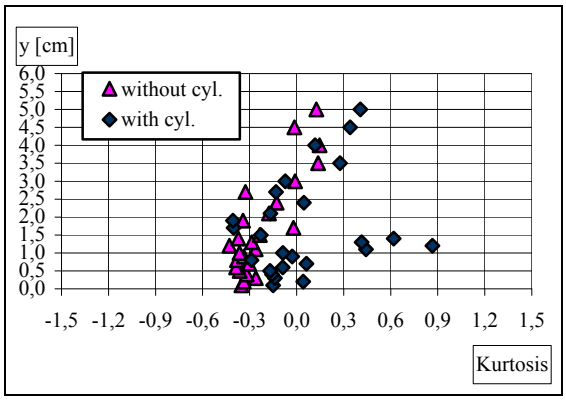

Fig. 16.24 - Distributions of kurtosis at 3.2cm behind the cylinder

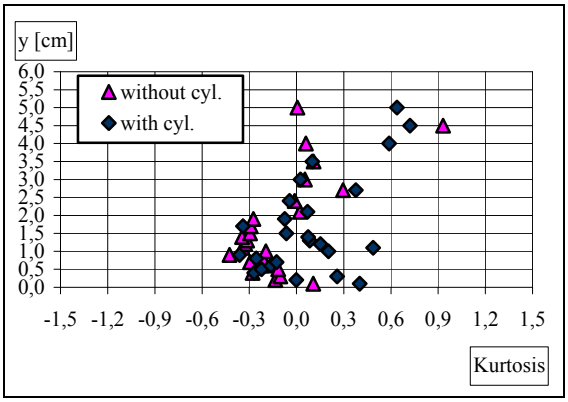

Fig. 16.25 - Distributions of kurtosis at 5.2cm behind the cylinder

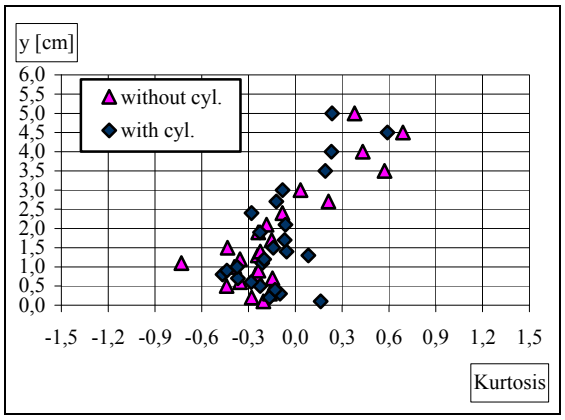

Fig. 16.26 - Distributions of kurtosis at 10.2cm behind the cylinder

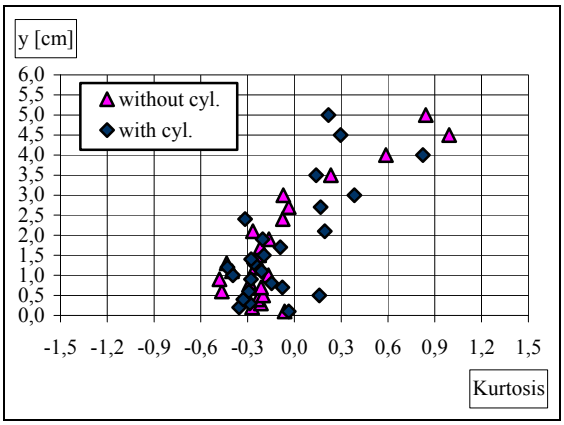

Fig. 16.27 - Distributions of kurtosis at 15.2cm behind the cylinder

Here too, as it is obvious, the distributions appear more irregular than the previous ones, due to the same circumstance than in relation to skewness.

Once more, 15/20cm can be considered a distance where the phenomenon is finished.

Finally, here too it appears however evident that the kurtosis values with and without the cylinder differ one from the other between 10mm and 15mm height, and that this difference tends to disappear at the largest distances from the same cylinder.

Here too the trend is not so clear in the first test section.

16.3.5 Distributions of integral length scales

Finally, in the following figs. from 16.28 to 16.33, the profiles of integral length scales are shown, always relative to the six series of acquisition.

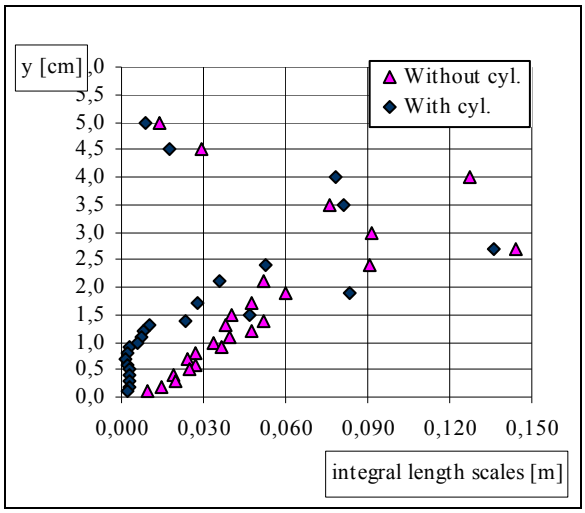

Fig. 16.28 - Distributions of integral length scales at 1.7cm behind the cylinder

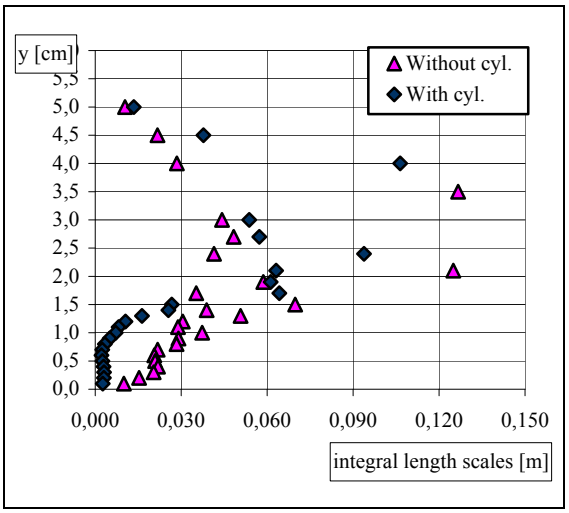

Fig. 16.29 - Distributions of integral length scales at 2.2cm behind the cylinder

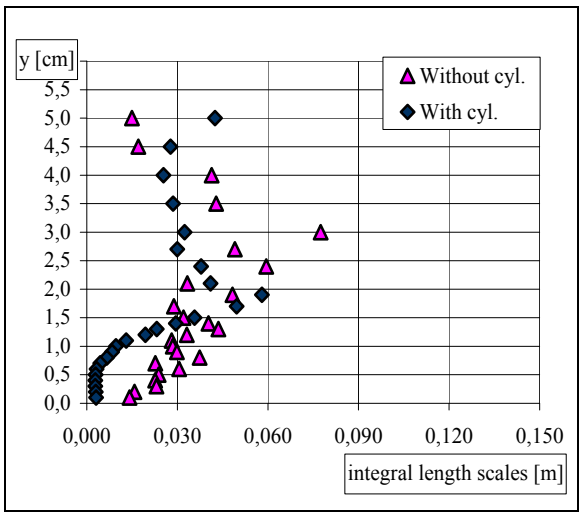

Fig. 16.30 - Distributions of integral length scales at 3.2cm behind the cylinder

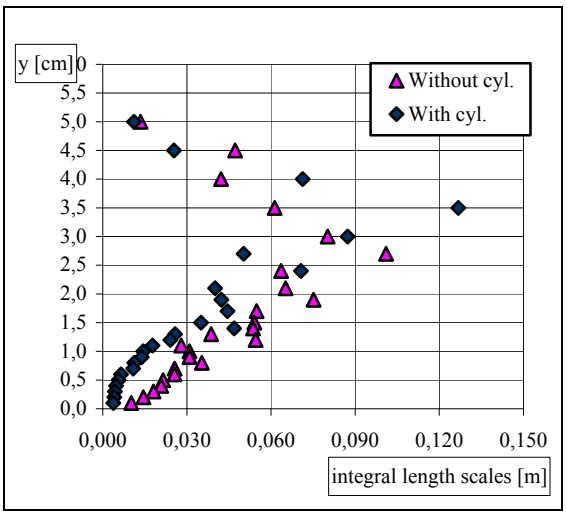

Fig. 16.31 - Distributions of integral length scales at 5.2cm behind the cylinder

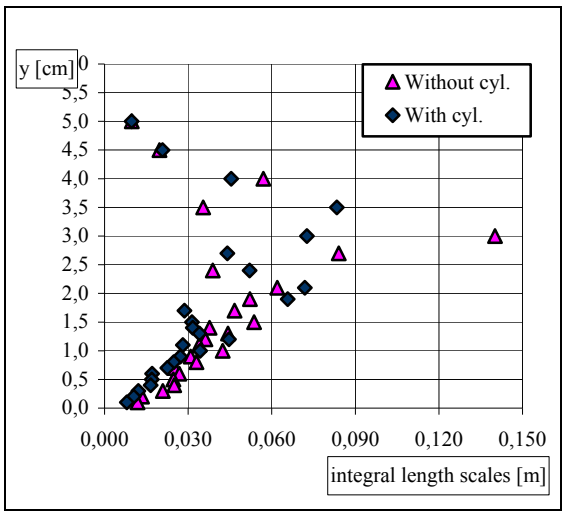

Fig. 16.32 - Distributions of integral length scales at 10.2cm behind the cylinder

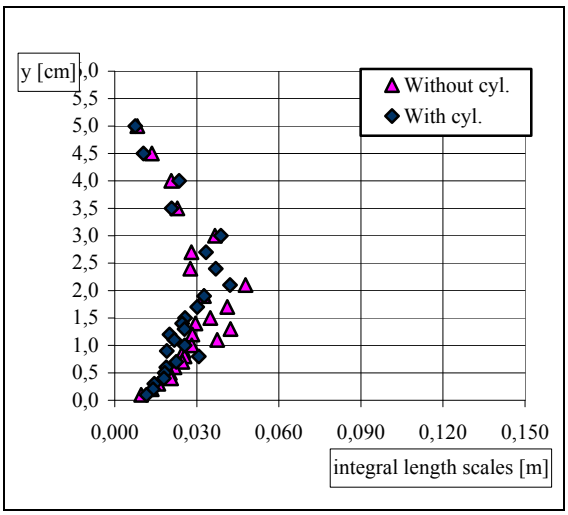

Fig. 16.33 - Distributions of integral length scales at 15.2cm behind the cylinder

First of all it is noteworthy to stress that the distributions appear less irregular than the skewness and kurtosis ones, as if the acquisition time of 2 minutes and 15 seconds would be this time sufficient for a correct elaboration. Lastly, it is evident that the phenomenon is finished yet at a distance of about 15/20cm.

Finally, here too it appears however evident that the integral length scales values with and without the cylinder differ one from the other this time in the whole height between 0mm and 15mm height, and that this difference tends to disappear at the largest distances from the same cylinder.

This time the trend is very clear also in the first test section.

16.4 Consequences of distributions' trend

In order to draw the suitable consequences from the considered distributions, it is first of all necessary to remember that the observed trends must be compared with the arrangements of the cylinders that were characteristic of the boundary layer measurements.

In those experiences the cylinders were arranged in rectangular or square meshes, with two of their four sides always aligned in the same direction of the flow (longitudinally). The distances between two subsequent cylinders were of 5cm in the so-called single density, and of 2.5cm in the so-called double density.

Now, comparing the two cases of single and double density for each different height of the cylinders, it could be considered presumable that, in absence of interference among the effects of the single cylinders, the actual resistances in the two cases would be the second one the double with respect to the first one. But double resistance would mean double values of

the f friction factor (as other hydraulic parameters were almost the same) and this circumstance was not verified.

The evident reason that can explain this behaviour is the interference between the wakes of the subsequent cylinders. Yet, as the distance between subsequent cylinders is of 5cm and 2.5cm respectively in single and double density, and as the longitudinal dimension of the influence area of each 15mm cylinder can be considered at least of the order of 15/20cm, it is possible to conclude that, referring to 15mm cylinders and to the considered flow type, in single density at least three cylinders are affected by the wake of a single one, and in double density even six cylinders are affected by the wake of a single one.

Now, when a cylinder is affected by the wake of a previous one, its own wake cannot develop in the same way than in absence of affection, and, as a consequence, the turbulent energy loss per unit volume of the two mixed wakes will not be the double with respect to the single wake. These considerations explain the not redoubling of the f friction factors.

Moreover, considering the shape of the distributions, it appears that the maximum effect of each wake is linked to what happens at a distance from the bed similar to the height of the cylinder. This behaviour is clearly evident in all distributions, perhaps except the integral length scales distribution.

Now, the f friction factors ratios shown in Table 16.1 with lower cylinders show that the effect of superposition of the wakes remains almost unaltered. This circumstance could be attributed just to the last remembered characteristic of the wakes, because almost the whole height of the cylinder does not take part in the phenomenon, but only its top: this interesting result allows to conjecture that also lowering the height of the cylinders its influence on the current would remain almost unaltered, as also experimental data just confirm.

17. EXPERIMENTAL TESTS ON UNIFORM FLOW WITH VEGETATED BOTTOM

17.1 Introduction

After having prepared the whole experimental plant, calibrated the acquisition system and implemented the Labview software necessary for the analysis of the statistic characteristics of the turbulence, and after the first tests with the presence of only one cylinder, it is possible, as we will show in this chapter, to proceed to the study of a current in uniform flow on a vegetated bottom.

The oversimplification adopted for the vegetation is rigid submerged, as well as the one chosen for the first tests carried on a boundary layer; in particular we chose a regular rectangular mesh with 2,5 side by 5,0 cm, already defined as "single density ", with cylinders 1,5 cm high.

The choice was suggested by the willingness to carry out a calibration of the methodology described in chapters n.14 and n.15.

Hereafter, we show the experimental tests carried out on uniform flows, pointing out:

- the local mean velocities in two different positions: coaxial to the mesh (defined "Stage A") and between two successive cylinders (defined "Stage B"), as carried out for the boundary layer currents;
- the fundamental statistical quantities of the turbulence (variance, skewness, kurtosis, integral length scales).

17.2 Description of the tests

As already shown in chapter n.15, the tests carried out on a uniform flow are six, with two different slopes of the channel (1% and 2 %) and three flow rates (22.6l/s, 33 l/s and 45 l/s). Besides, measurements in two different positions have been always carried out for each test:

- Coaxial to the mesh of the rigid vegetation;
- Between two consecutive cylinders.

For each test we obtained:

- the local mean velocities distribution;
- the variances distribution;
- the skewness distribution;
- the kurtosis distribution;
- the integral length scales distribution.

The measurement position is set at 5,50m from the inlet. This position was chosen as a consequence of appropriate tests about the flow profiles at different slopes and flow rate, in order to guarantee always the achievement of the uniform flow in the measurement section.

On the contrary, as regards the transversal section, differently from what made for the tests on smooth bottom, the measurement position is not at 12cm from the hydraulic left, but at:

- 7,50cm, in the case of acquisition coaxial to the mesh of cylinders;
- 6,25cm, in the case of acquisition between two successive cylinders.

Such a choice was due to the power of the laser, that might not work at its best, in the presence of excessive trouble, as the one created by the presence of the cylinders. Therefore, the use of an amplifier of signal was avoided, but took care of maintaining the current sufficiently inseminated, controlling the quality of the signal and the absence of ”drop-out” at every acquired point, through an oscilloscope.

The six tests are shown in Table 17.1.

Table 17.1 - Uniform flow conditions

Test n.	Flow conditions	Slope	Flow-rate [l/s]	h_u [m]	V_u [m/s]	ε [m]
1	subcritical	1%	22,6 l/s	0,0785	0,719	0,035
2	subcritical	1%	33 l/s	0,0970	0,850	0,035
3	subcritical	1%	45 l/s	0,1155	0,974	0,035
4	supercritical	2%	22,6 l/s	0,0644	0,876	0,033
5	supercritical	2%	33 l/s	0,0803	1,027	0,035
6	supercritical	2%	45 l/s	0,0954	1,178	0,035

17.3 Free surface profiles

In the figs from 17.1 to 17.6 the six flow profiles relative to the six considered hydrodynamic condition are shown.

The first three profiles are clearly of subcritical flows, and the last three profiles are clearly of supercritical flow.

In any case the test section location is indicated and it is clear that the same location has been always chosen in order to carry out the experimental survey on a practically uniform flow.

It is noteworthy that the condition of uniform flow has been attained in case of subcritical flow without using the final sluice gate. This circumstance was due to the particular combination of slope, flow-rate and absolute roughness of the performed experiments, but it is likely that it would not always happen.

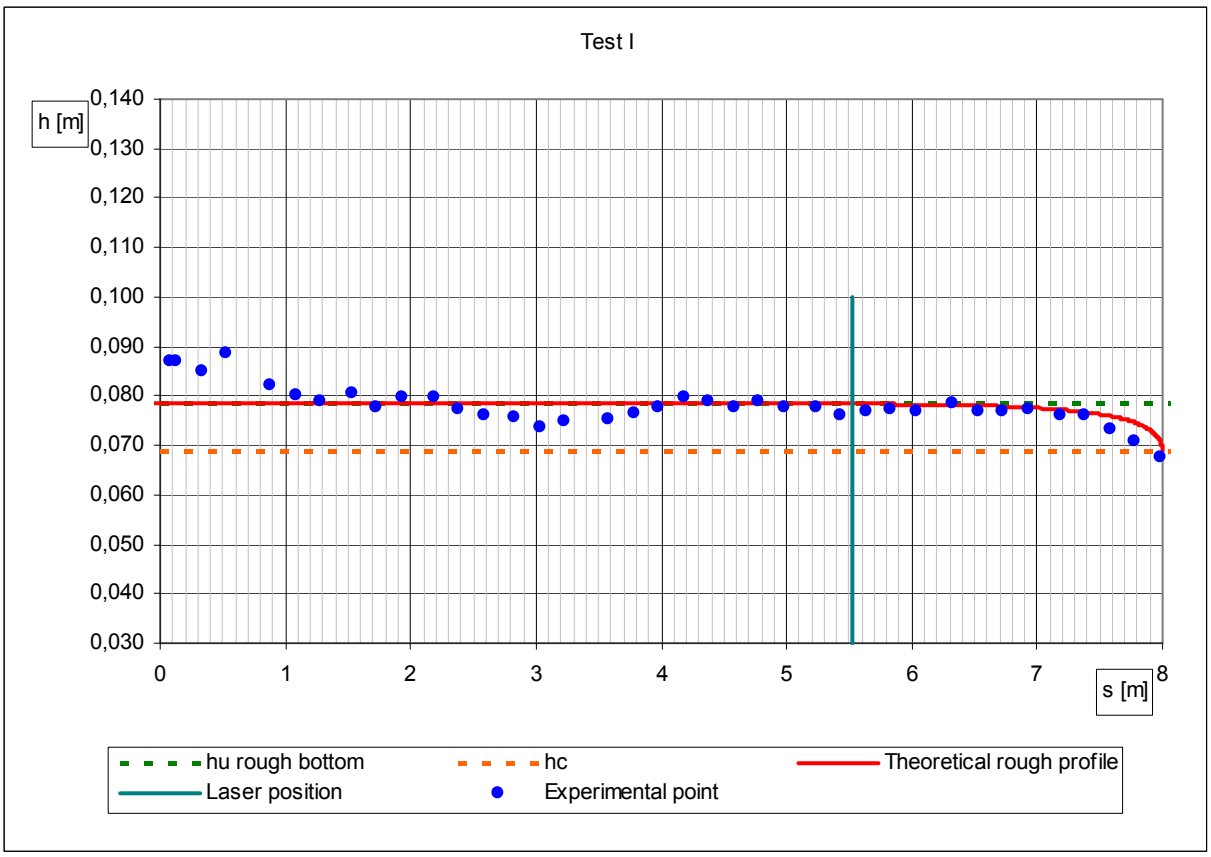

Fig. 17.1 - Free surface profile – Test I

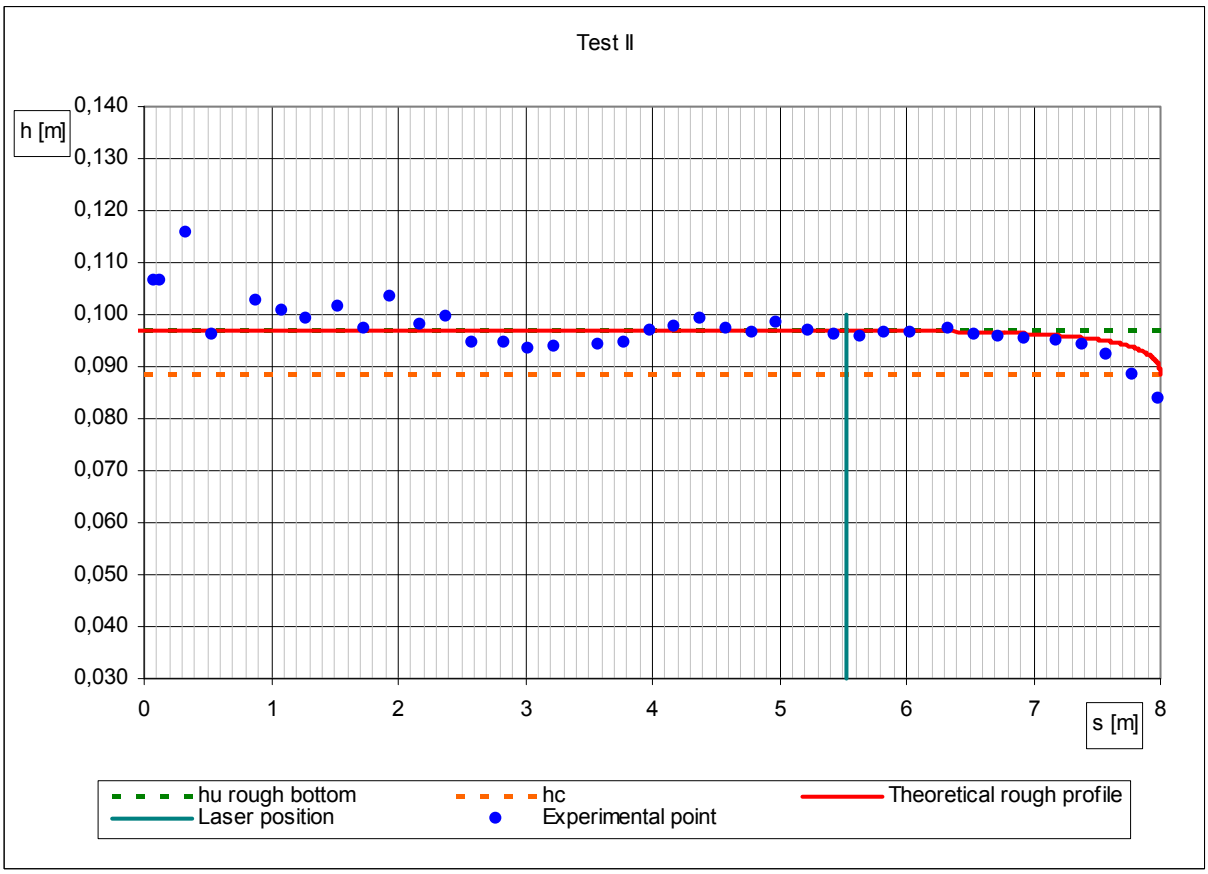

Fig. 17.2 - Free surface profile – Test II

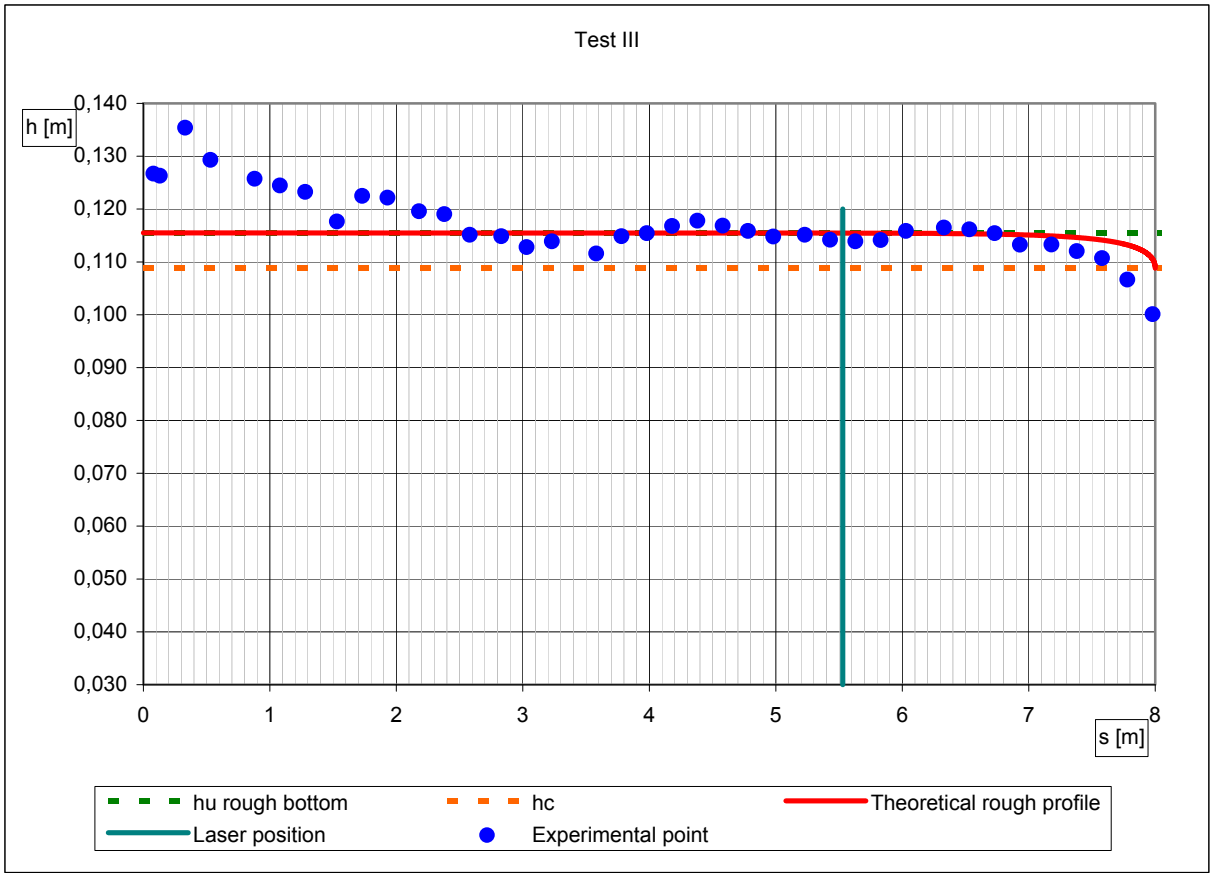

Fig. 17.3 - Free surface profile – Test III

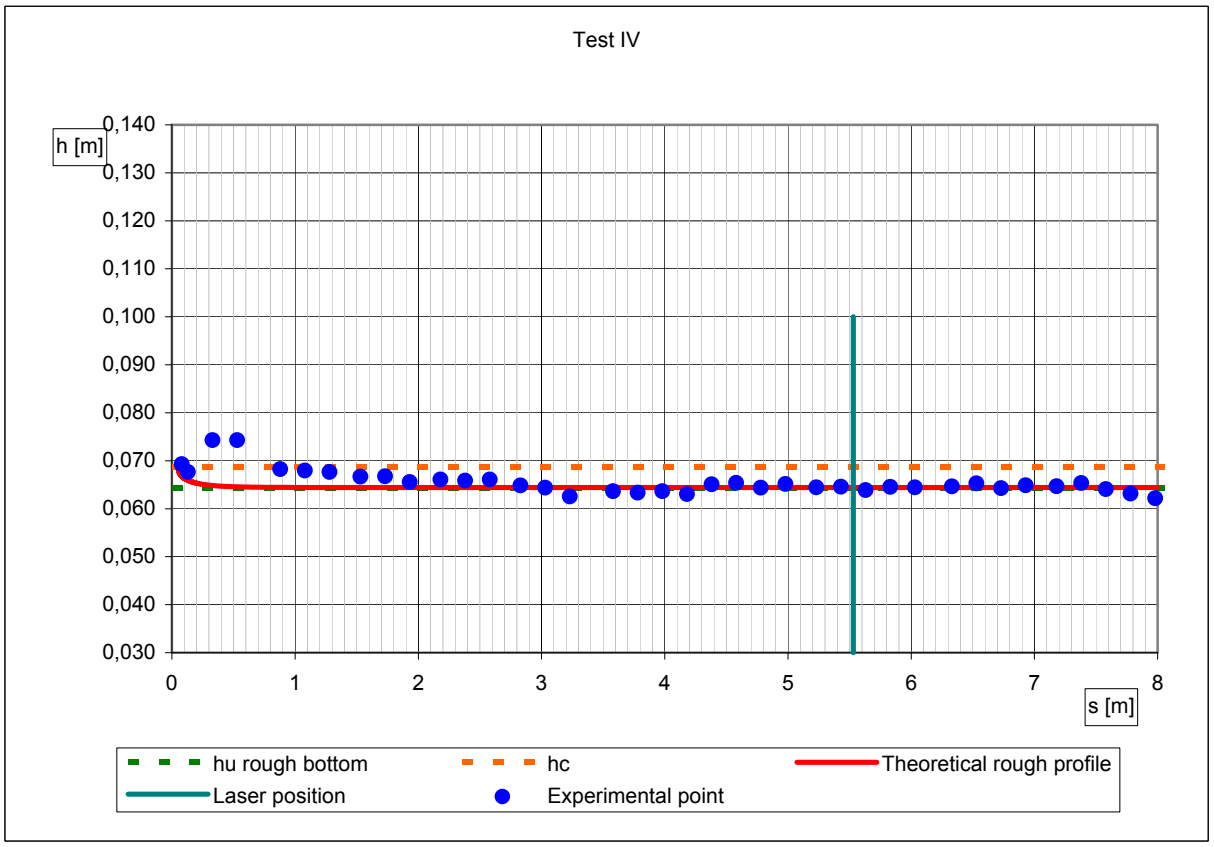

Fig. 17.4 - Free surface profile – Test IV

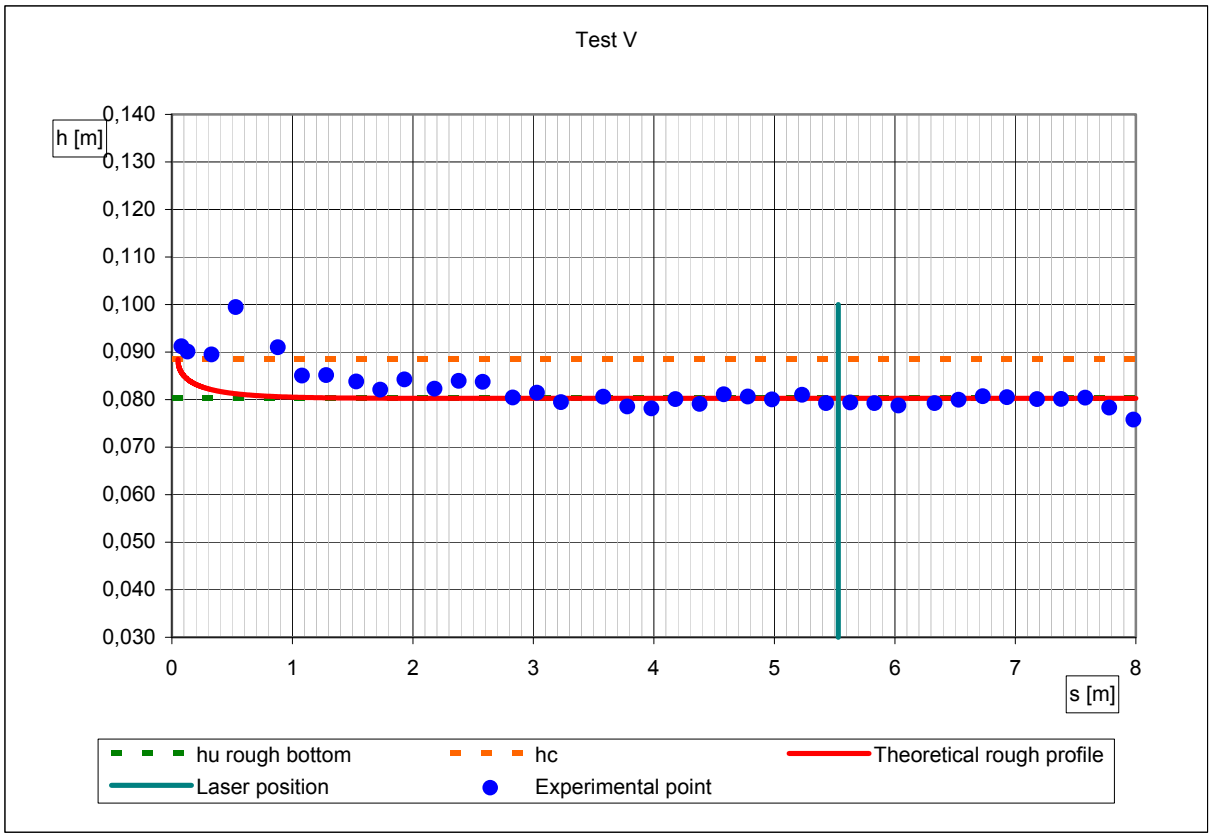

Fig. 17.5 - Free surface profile – Test V

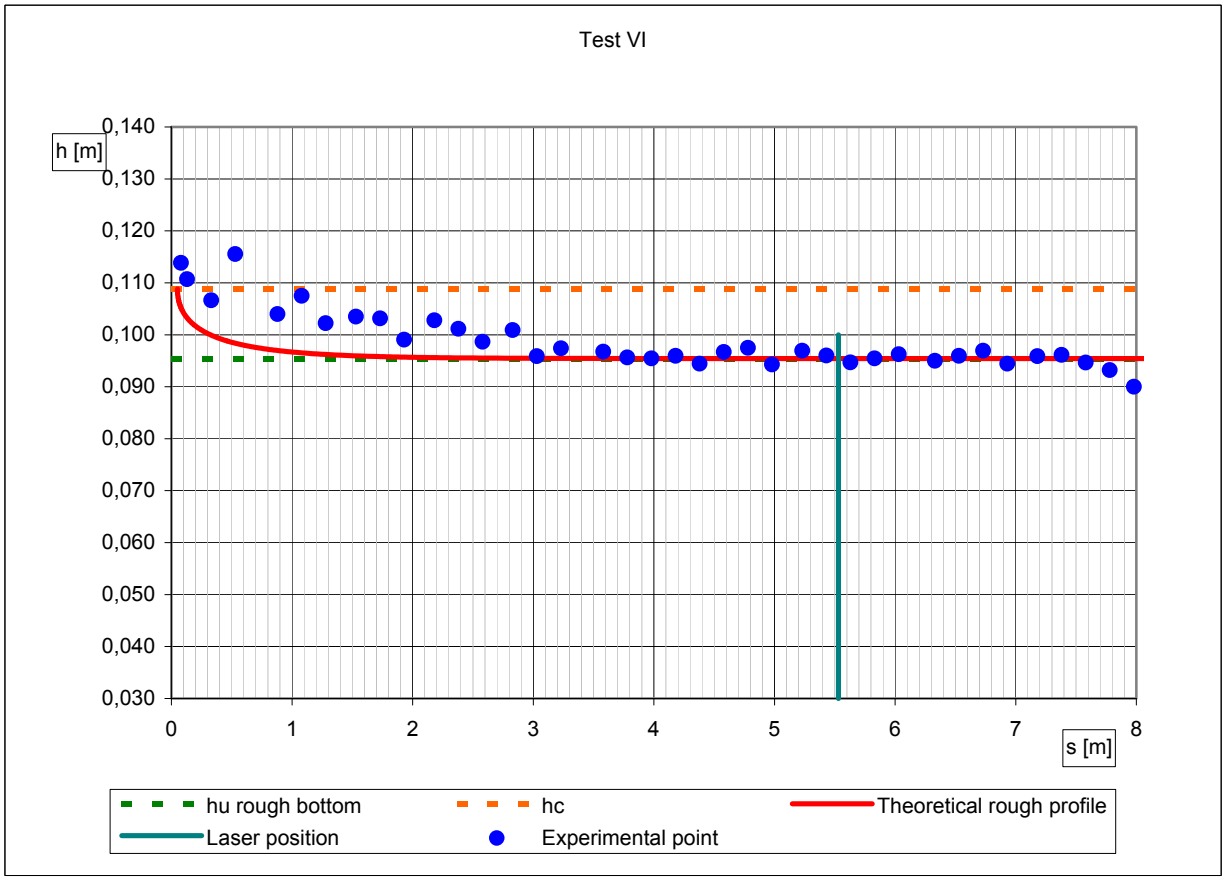

Fig. 17.6 - Free surface profile – Test VI

17.4 Local mean velocity distributions

The local mean velocity distributions relative to uniform flow conditions that have been examined show two common characteristics: i) a great regularity, independently of the hydrodynamic conditions (channel slope, flow rate, subcritical or supercritical flow); ii) in the part correspondent to the height of the cylinders (1.5cm) there is the presence of a little "discontinuity", when acquisitions are carried out at the centre of the rectangular mesh (Stage A) that is much more emphasized in comparison to when acquisitions are carried out behind a cylinder (Stage B).

Moreover in this second case (Stage B) the distribution of local mean velocities becomes practically vertical in the region behind the cylinder instead of going gradually towards the bottom, as it happens in Stage A.

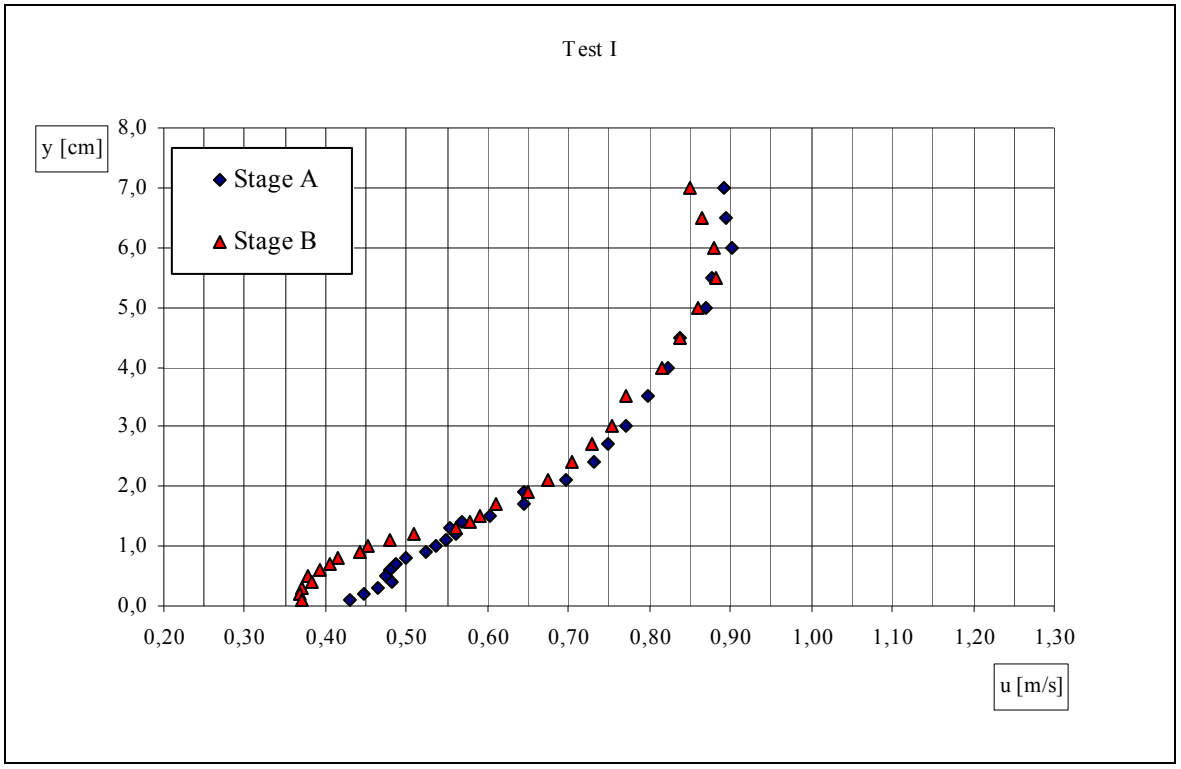

Fig. 17.7 - Local mean velocity – Test I

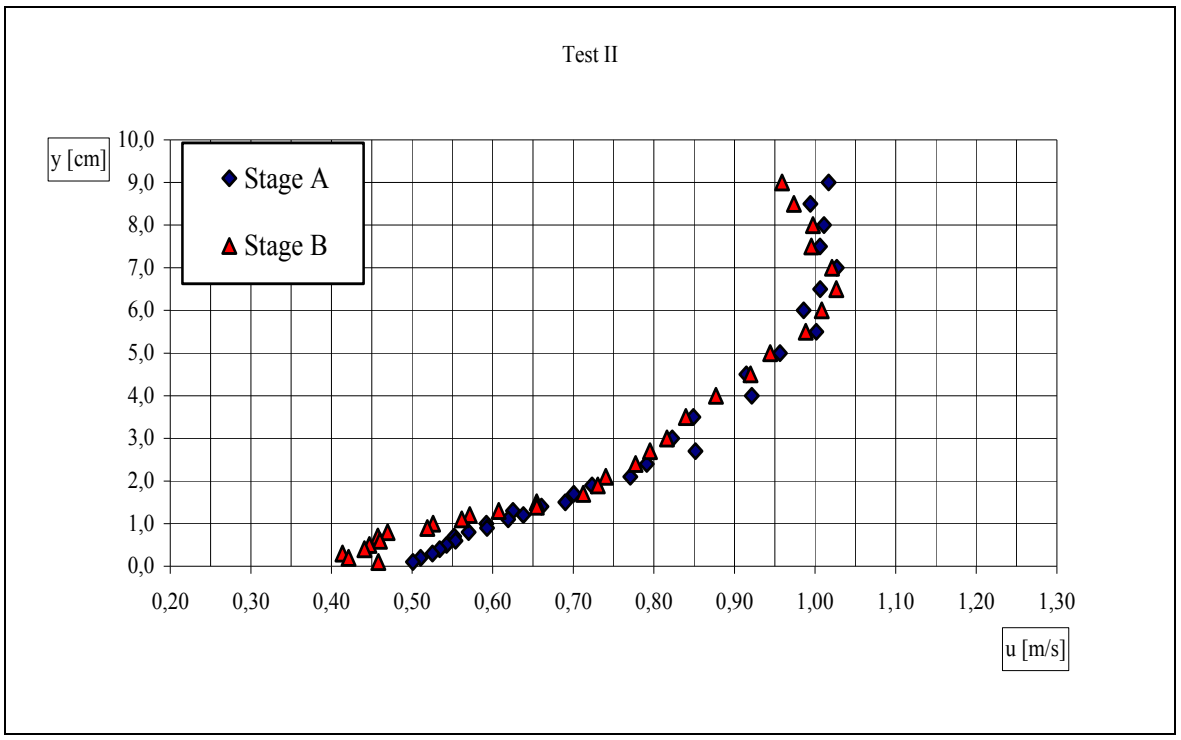

Fig. 17.8 - Local mean velocity – Test II

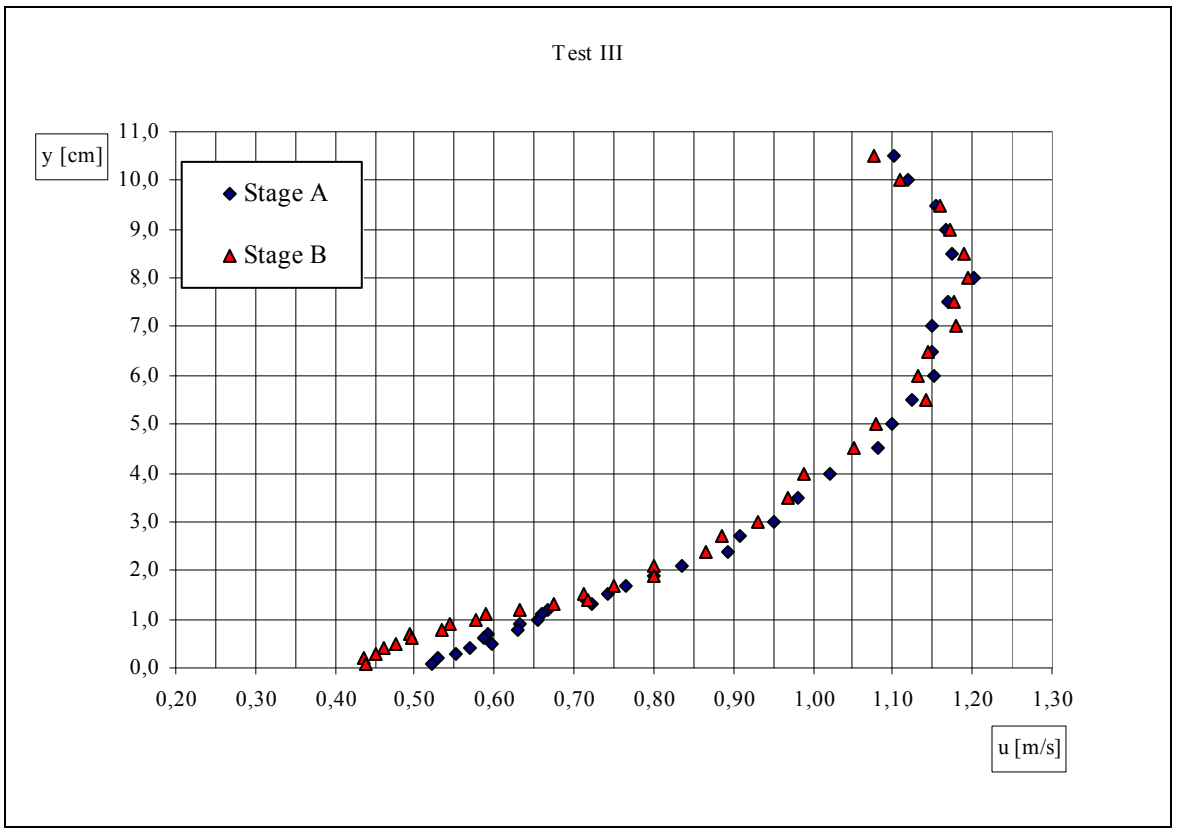

Fig. 17.9 - Local mean velocity – Test III

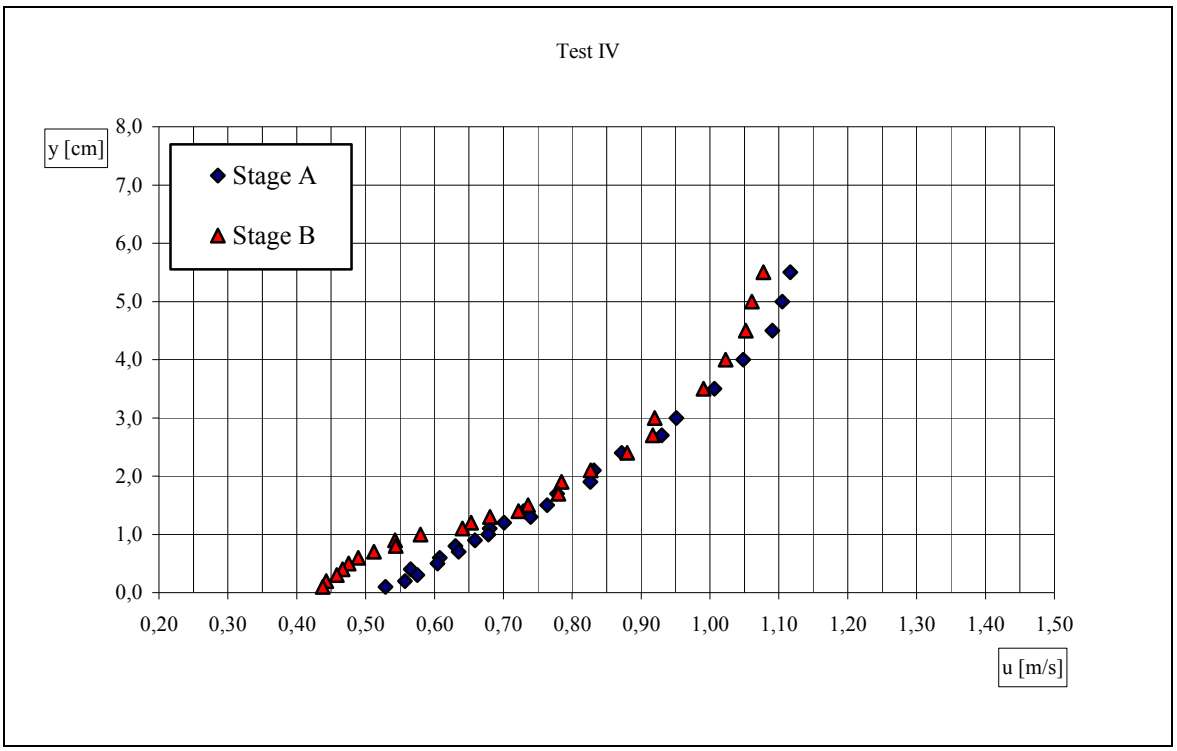

Fig. 17.10 - Local mean velocity – Test IV

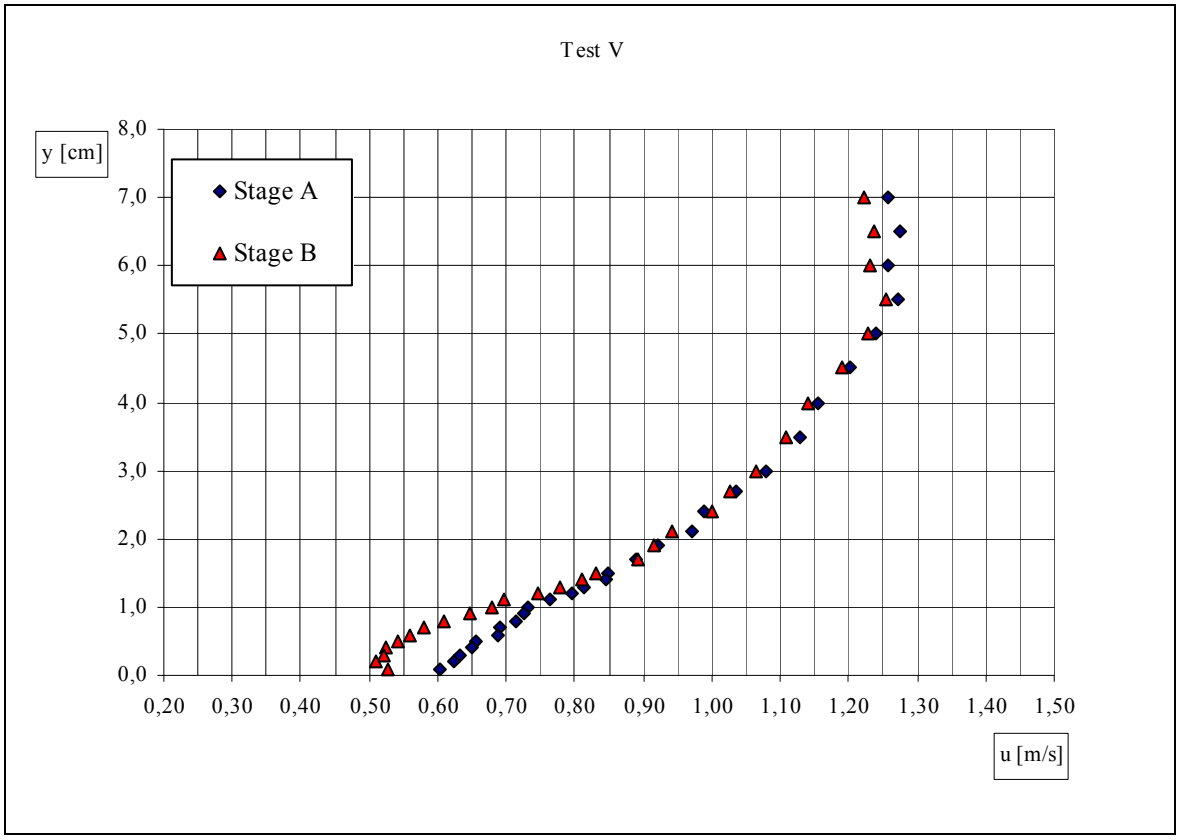

Fig. 17.11 - Local mean velocity – Test V

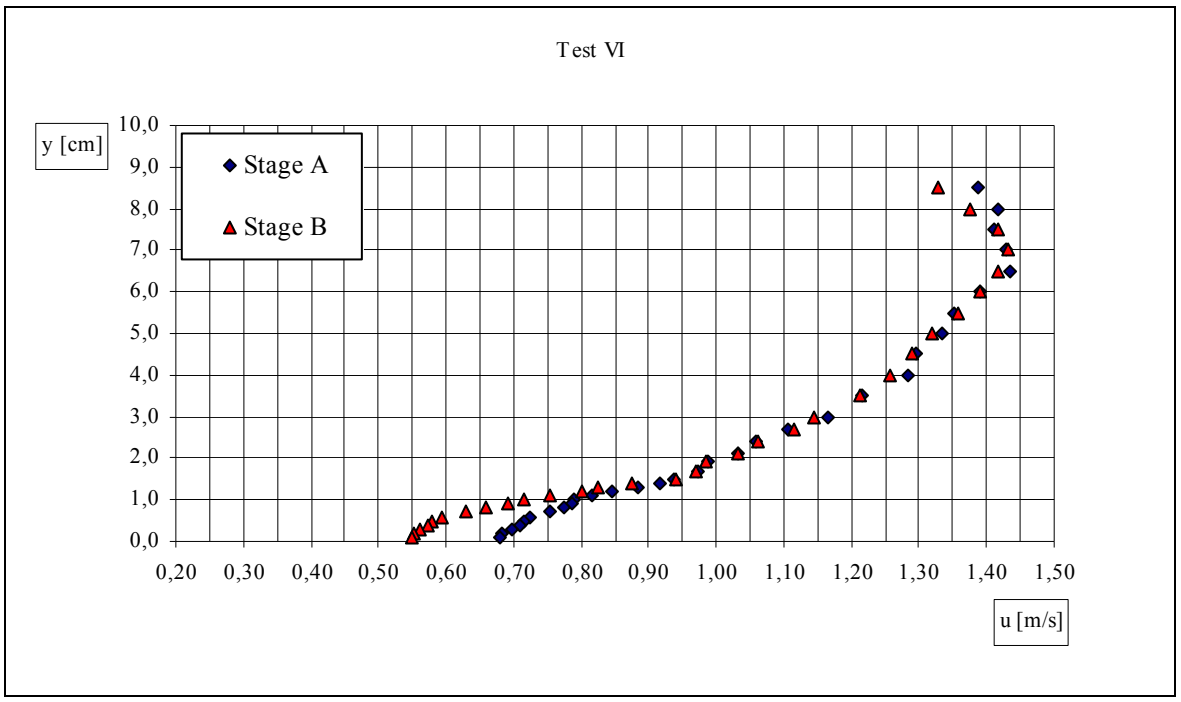

Fig. 17.12 - Local mean velocity – Test VI

17.5 Variance distributions

The Variance distributions relative to uniform flow conditions that have been examined show two common characteristics: i) a great regularity, independently of the hydrodynamic conditions (channel slope, flow-rate, subcritical or supercritical flow); ii) in the part correspondent to the height of the cylinders (1.5cm) there is the presence of a "peak", which appears more emphasized when acquisitions are carried out behind a cylinder (Stage B) in comparison to when acquisitions are carried out at the centre of the rectangular mesh (Stage A).

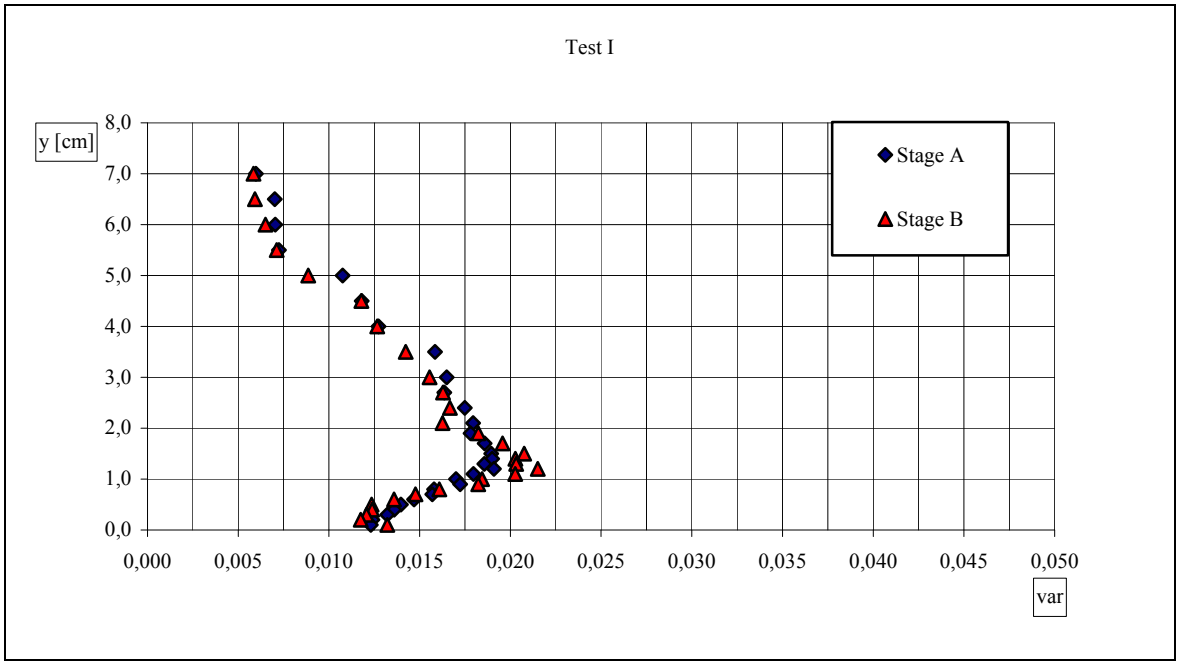

Fig. 17.13 - Variance – Test I

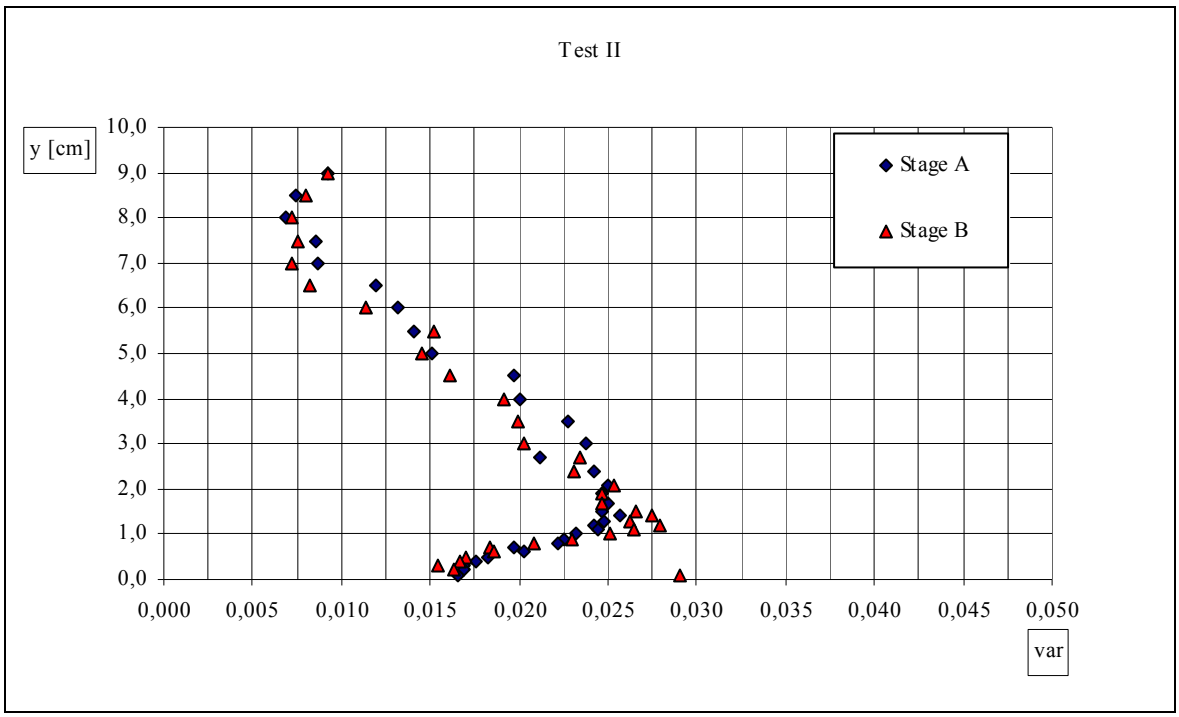

Fig. 17.14 - Variance – Test II

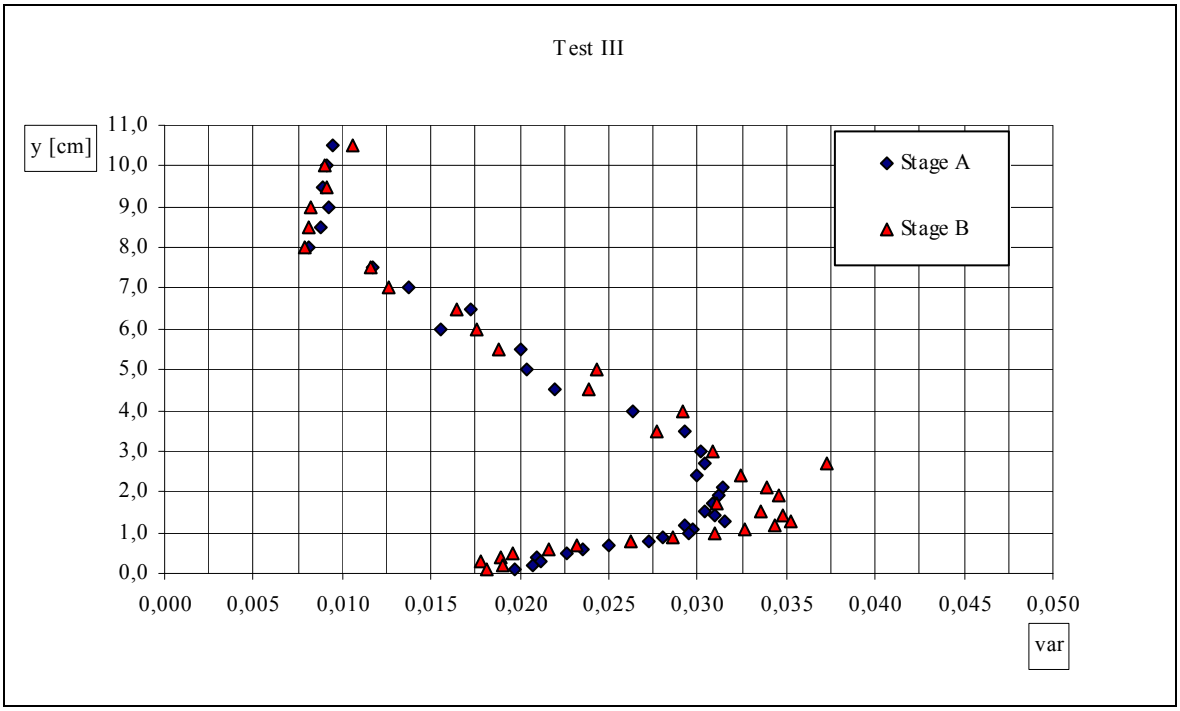

Fig. 17.15 - Variance – Test III

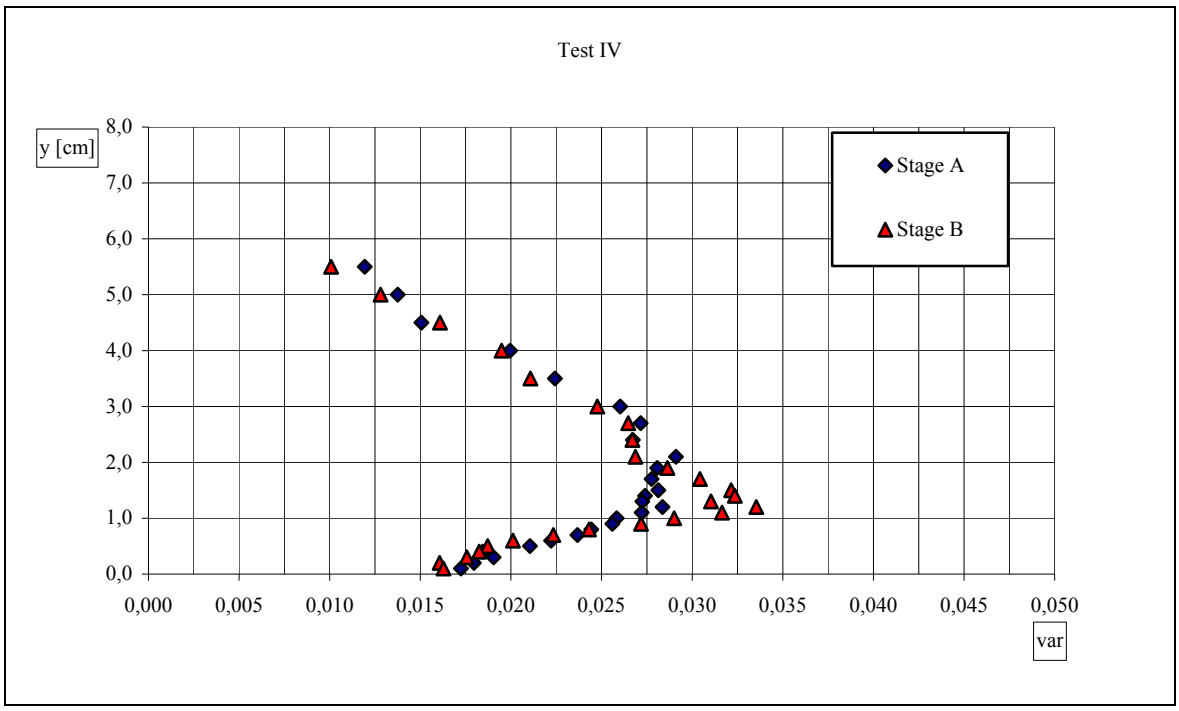

Fig. 17.16 - Variance – Test IV

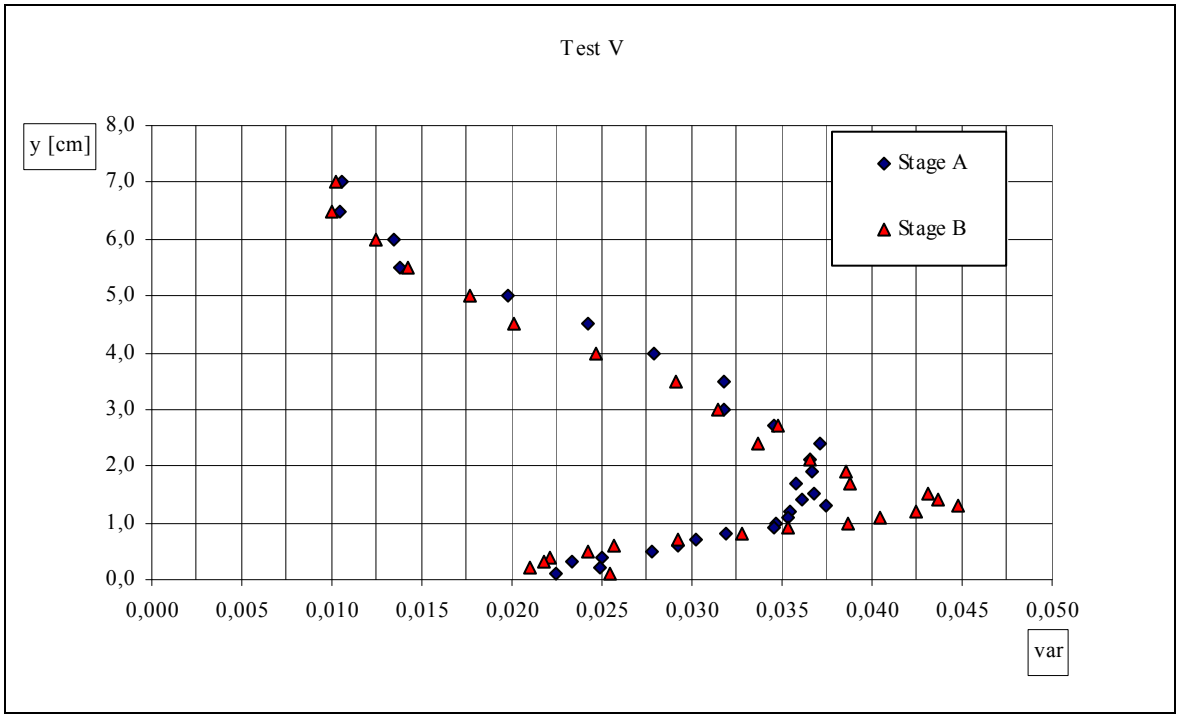

Fig. 17.17 - Variance – Test V

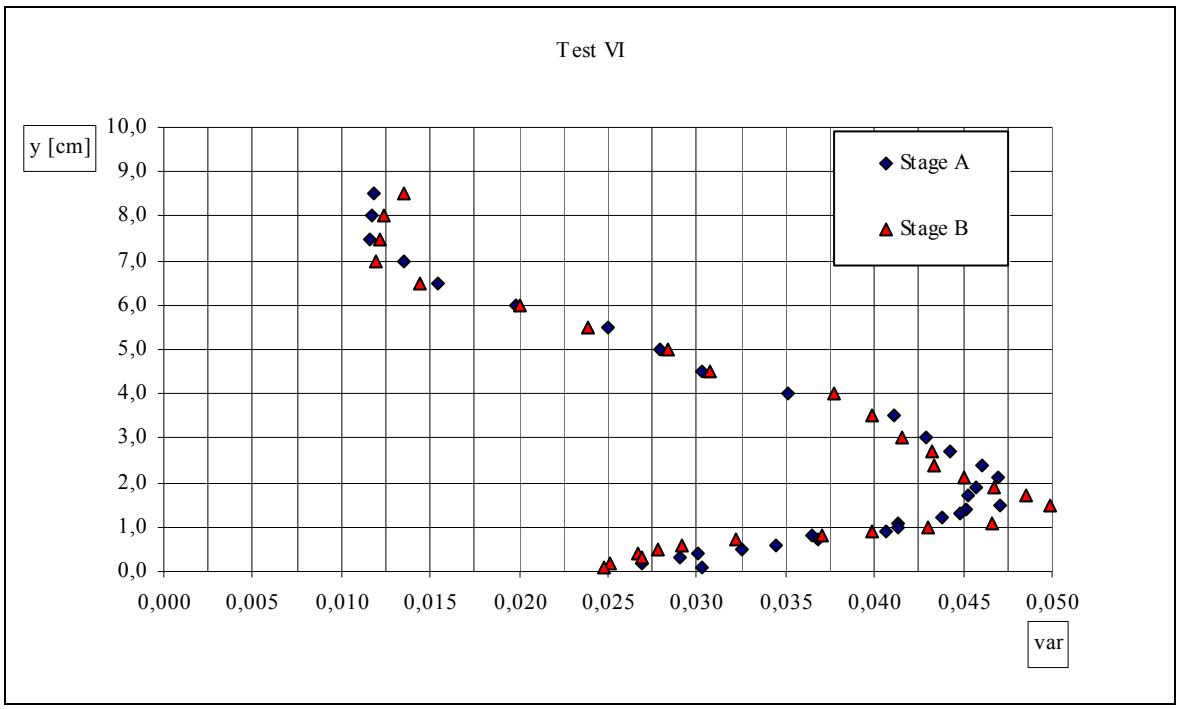

Fig. 17.18 - Variance – Test VI

17.6 Skewness distributions

The Skewness distributions relative to uniform flow conditions that have been examined show two common characteristics: i) a fair regularity, independently of the hydrodynamic conditions (channel slope, flow-rate, subcritical or supercritical flow); ii) some independence of the acquiring vertical location, in the sense that the distributions relative to Stage A appear not to differ from those relative to Stage B.

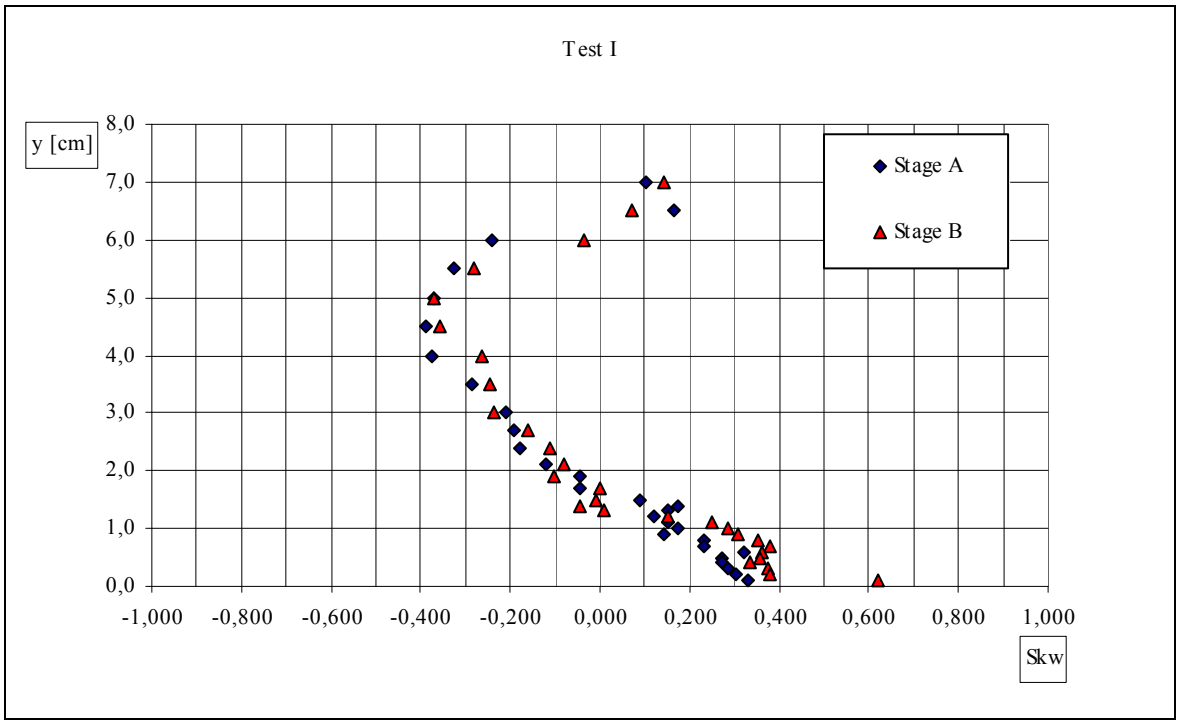

Fig. 17.19 - Skewness – Test I

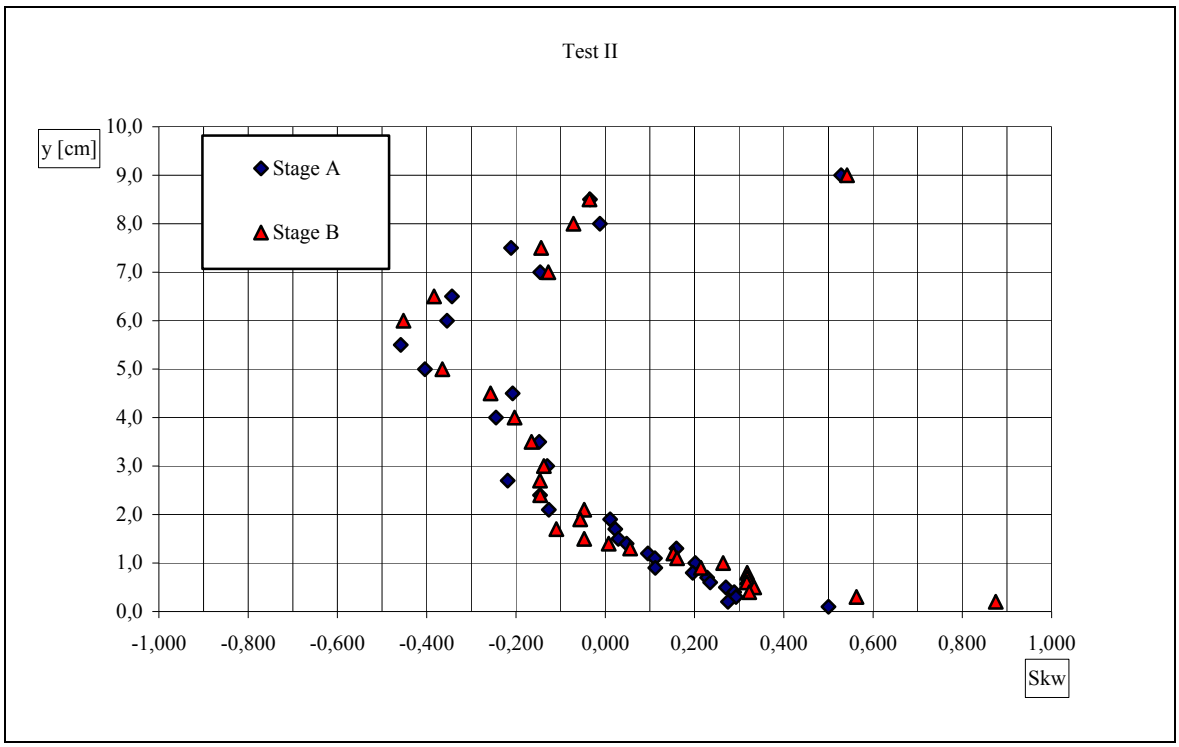

Fig. 17.20 - Skewness – Test II

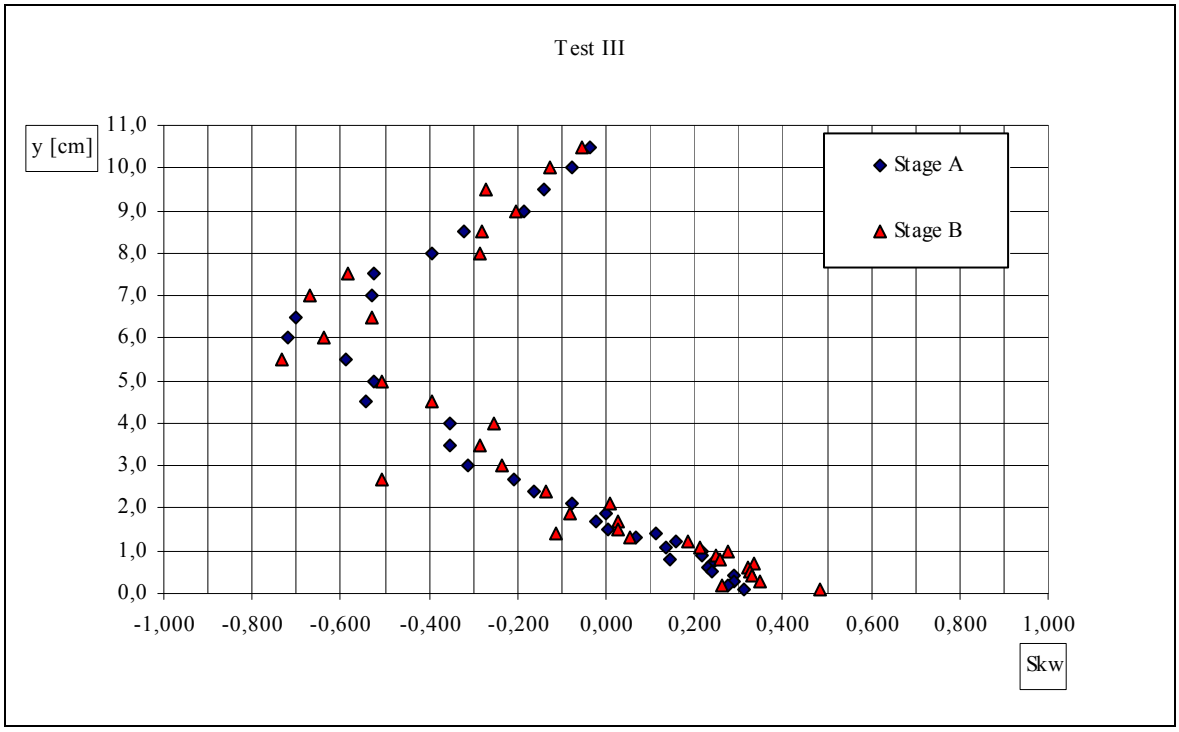

Fig. 17.21 - Skewness – Test III

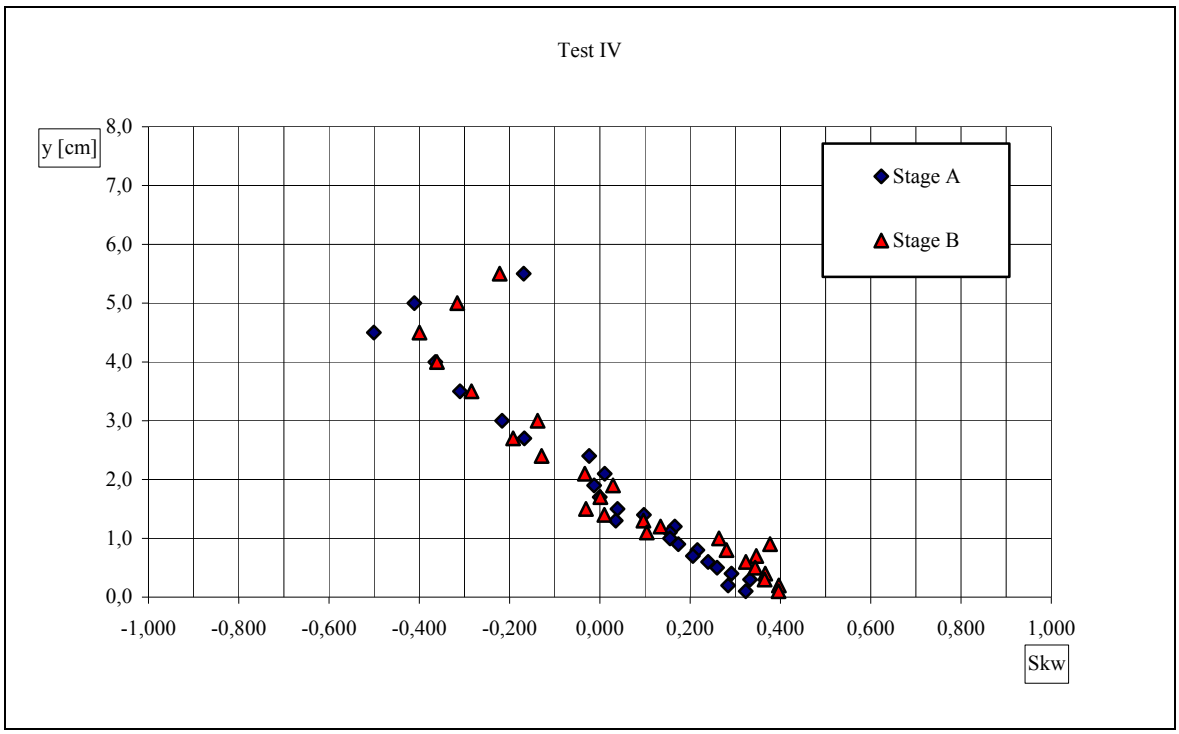

Fig. 17.22 - Skewness – Test IV

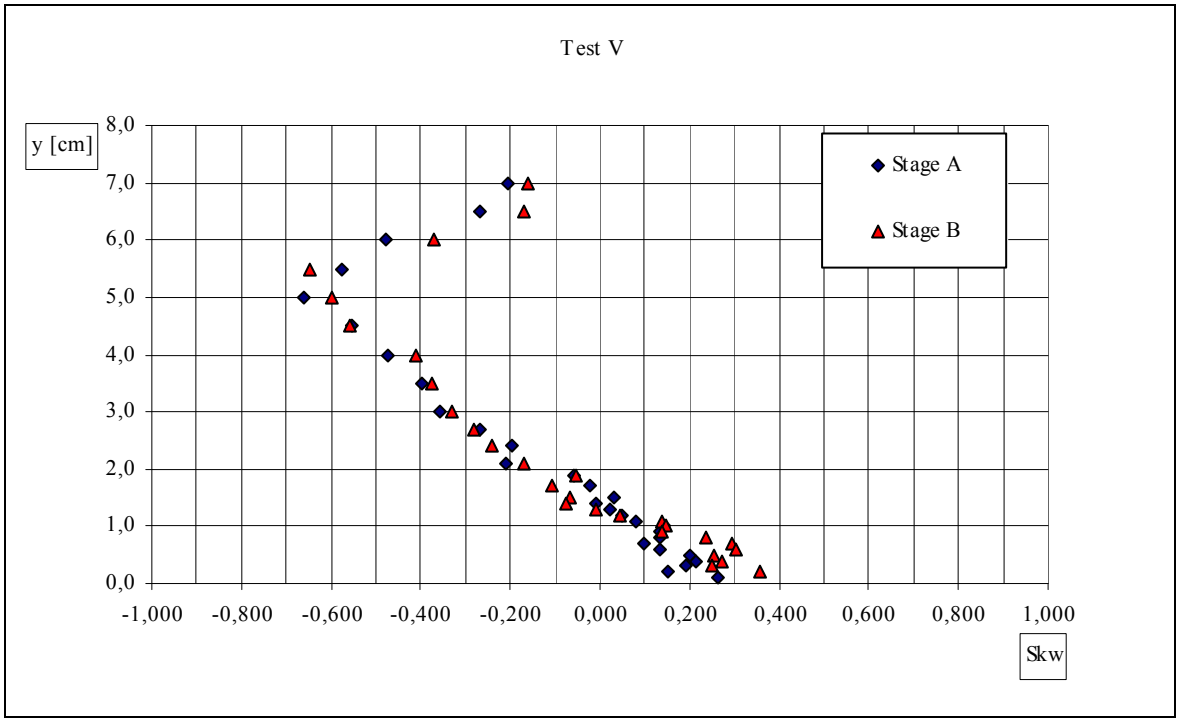

Fig. 17.23 - Skewness – Test V

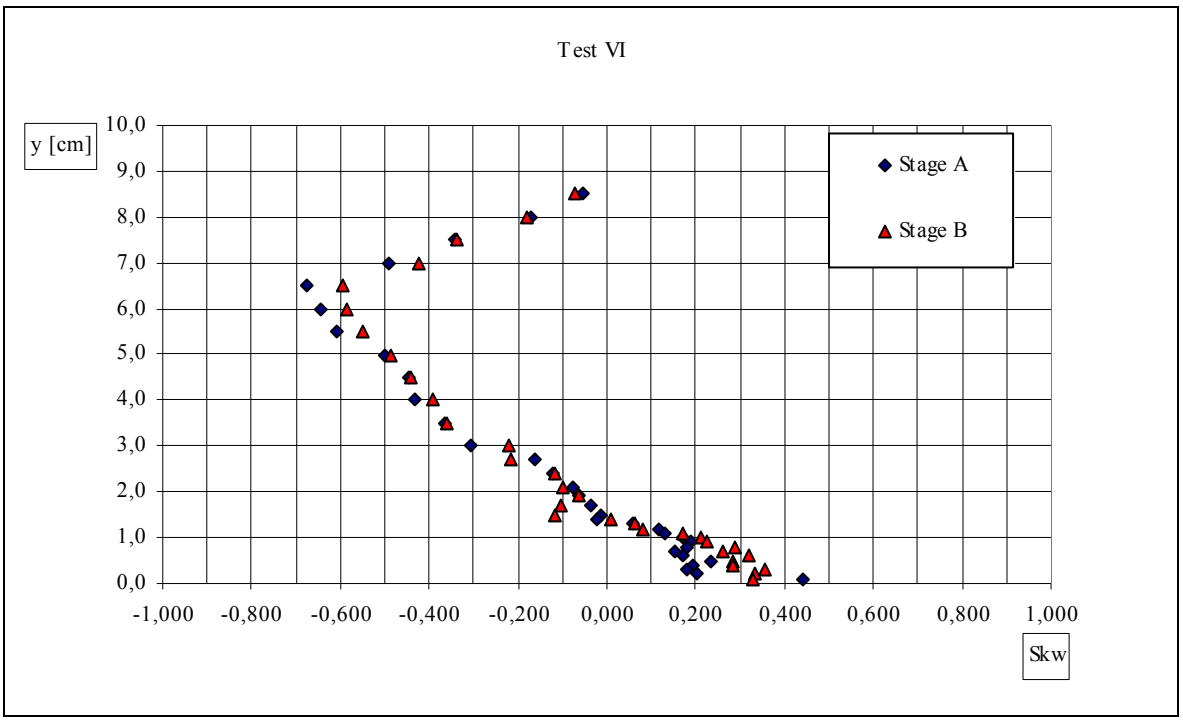

Fig. 17.24 - Skewness – Test VI

17.7 Kurtosis distributions

The Kurtosis distributions relative to uniform flow conditions that have been examined show two common characteristics: i) a great regularity, independently of the hydrodynamic conditions (channel slope, flow-rate, subcritical or supercritical flow); ii) some independence of the acquiring vertical location, in the sense that the distributions relative to Stage A appear not to differ from those relative to Stage B.

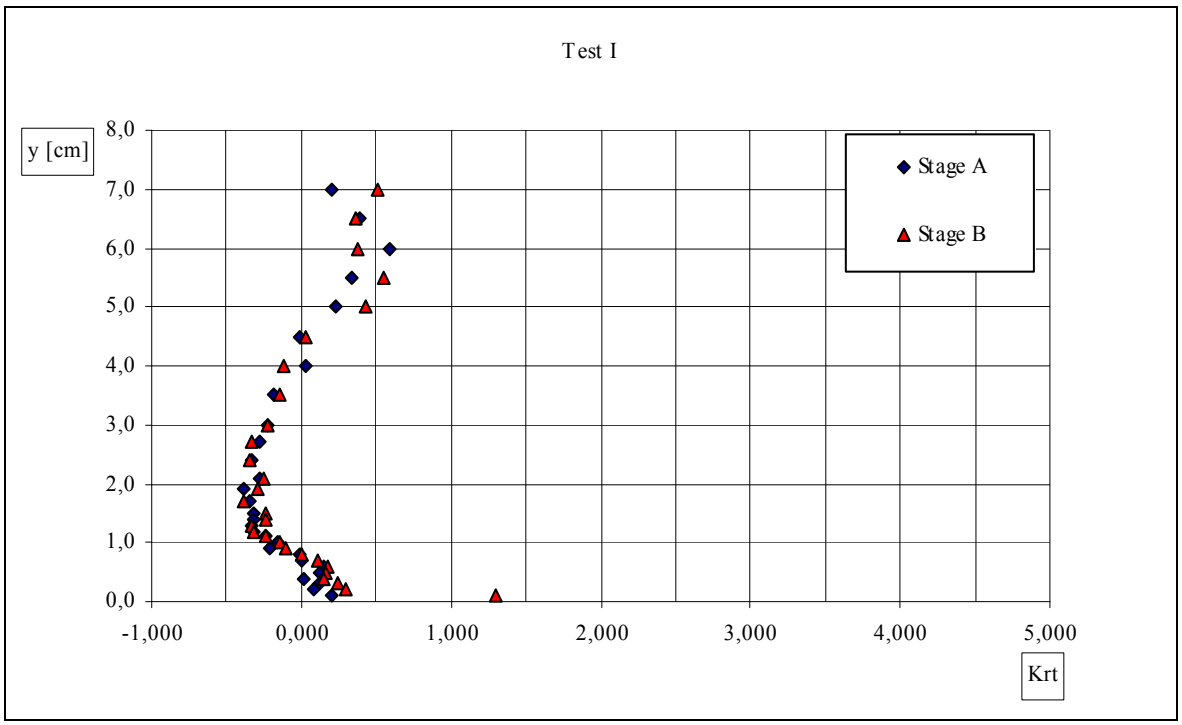

Fig. 17.25 - Kurtosis – Test I

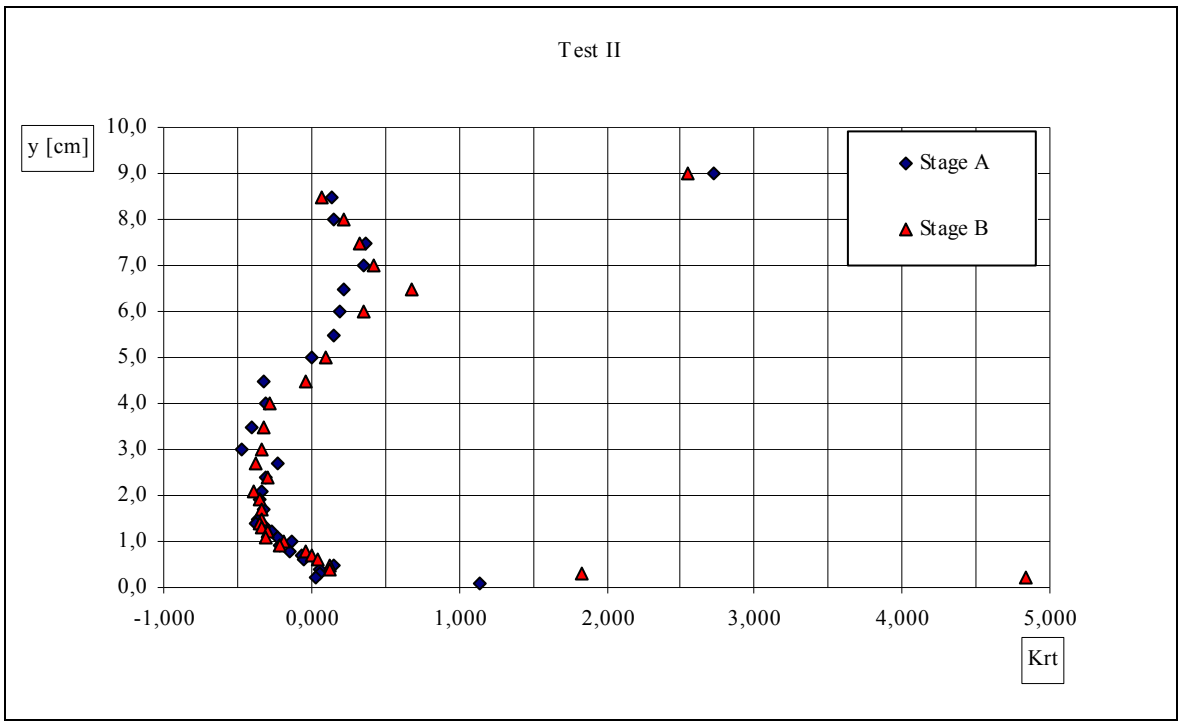

Fig. 17.26 - Kurtosis – Test II

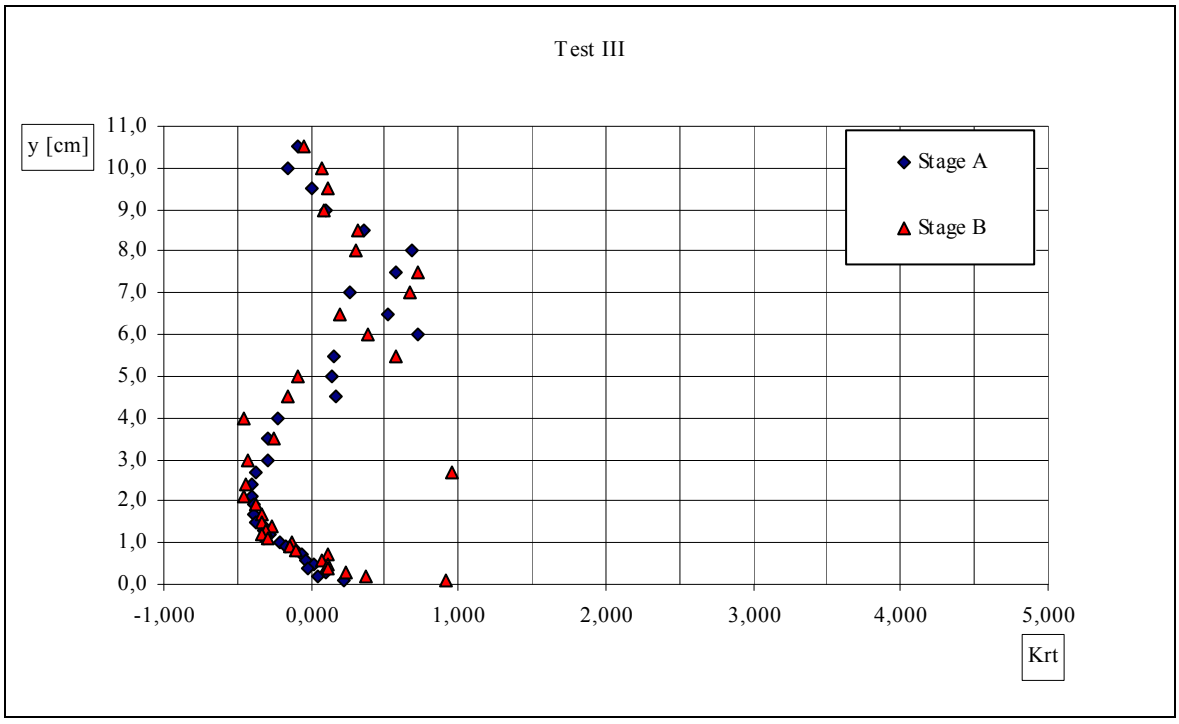

Fig. 17.27 - Kurtosis – Test III

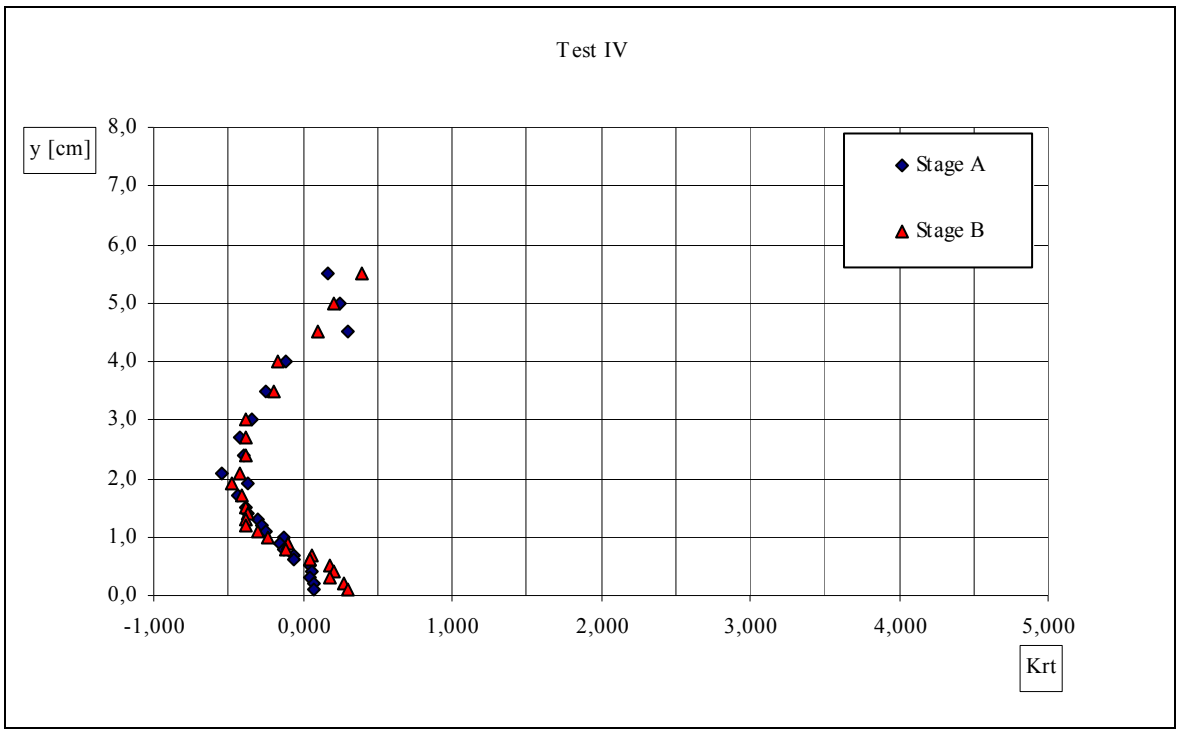

Fig. 17.28 - Kurtosis – Test IV

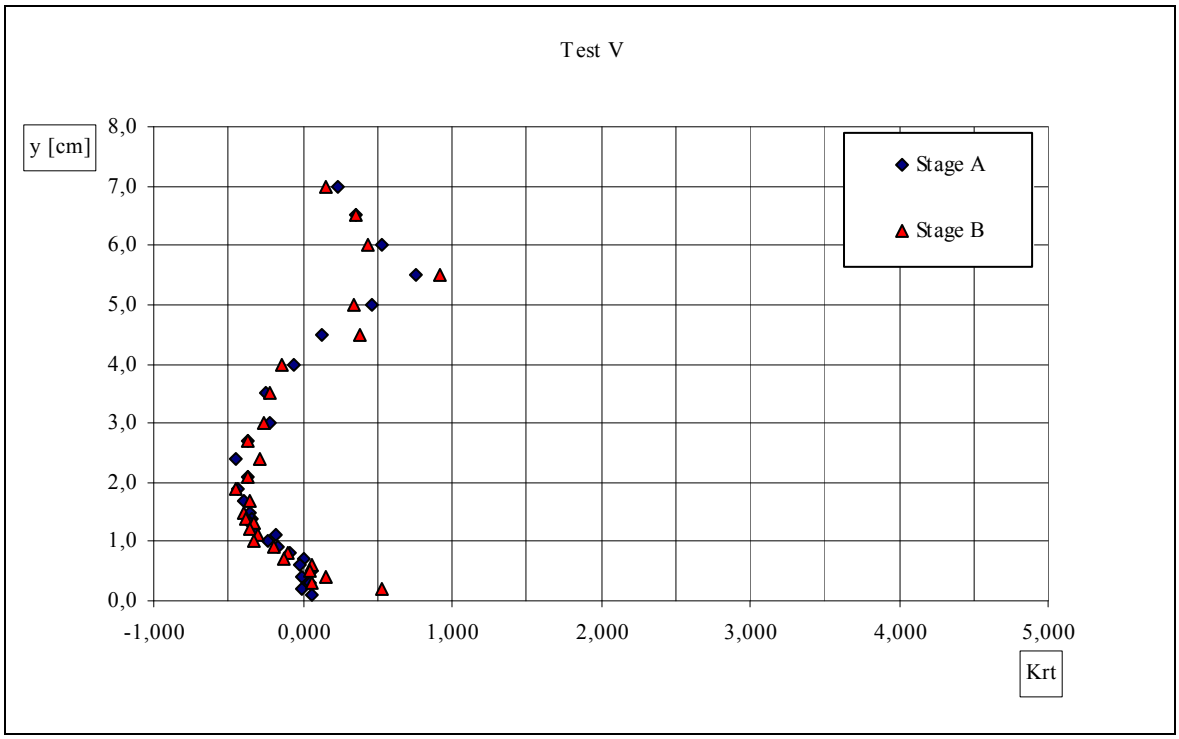

Fig. 17.29 - Kurtosis – Test V

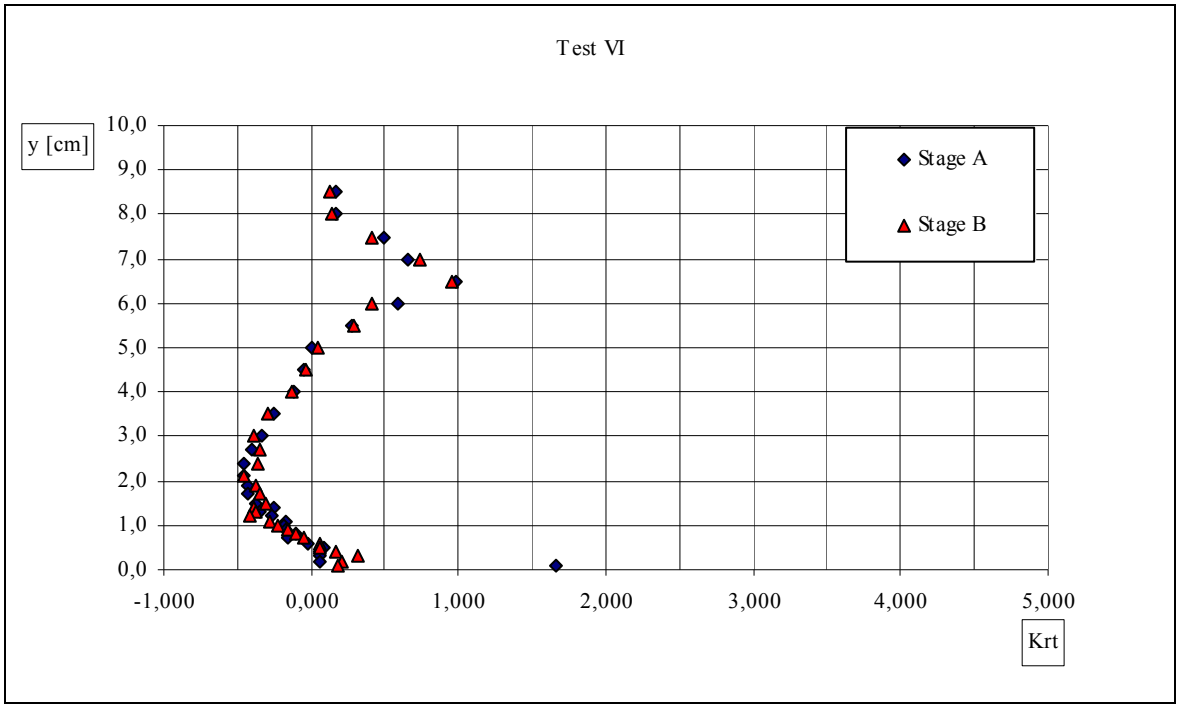

Fig. 17.30 - Kurtosis – Test VI

17.8 Integral length scales distributions

The integral length scales distributions relative to uniform flow conditions that have been examined show two common characteristics: i) a great regularity, independently of the hydrodynamic conditions (channel slope, flow-rate, subcritical or supercritical flow) this time only till the height of the cylinders; ii) an important dispersion on the contrary in the superior zone of the current.

Moreover in case of stage B the distribution of integral length scales becomes practically vertical in the region behind the cylinder instead of going gradually towards the bottom, as it happens in stage A. This characteristic is similar to what happens in local mean velocities distributions.

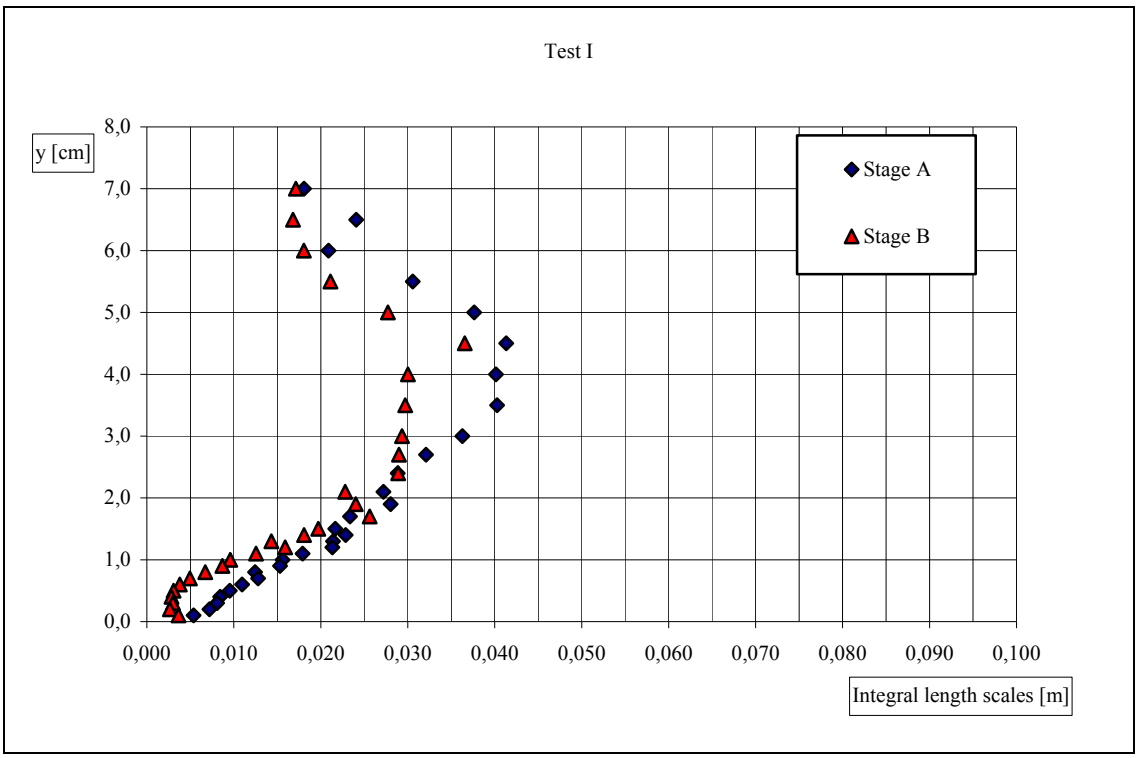

Fig. 17.31 - Integral length scales – Test I

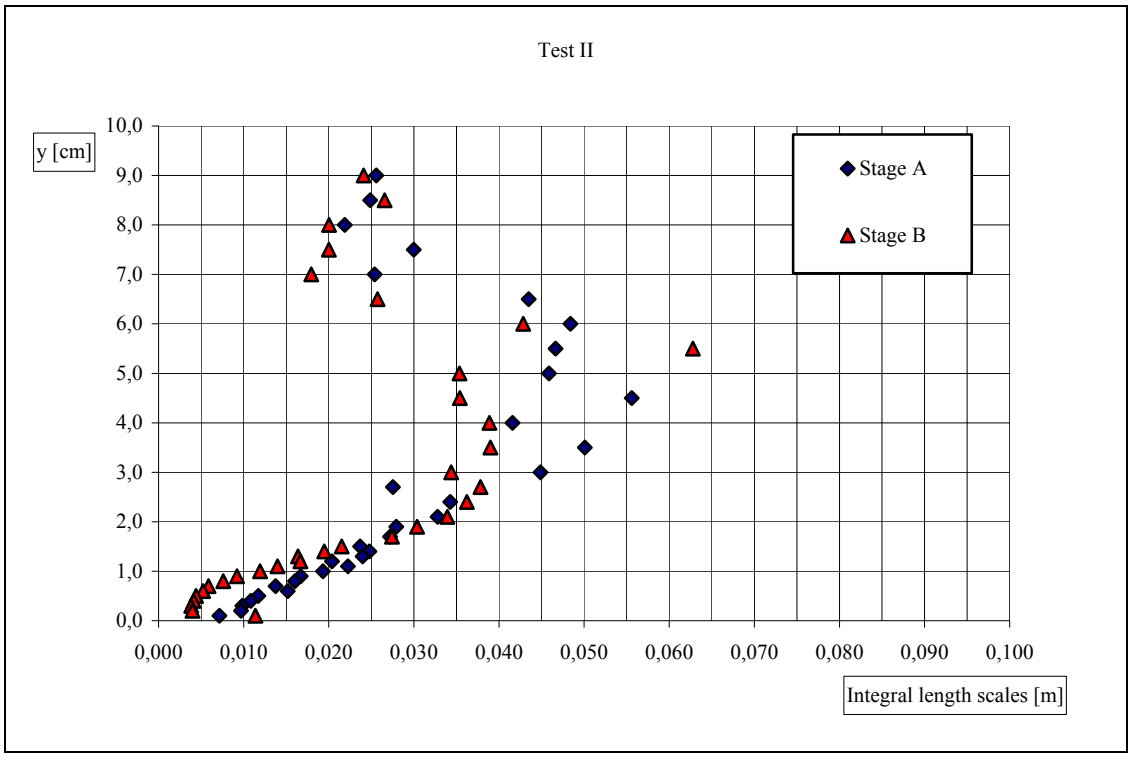

Fig. 17.32 - Integral length scales – Test II

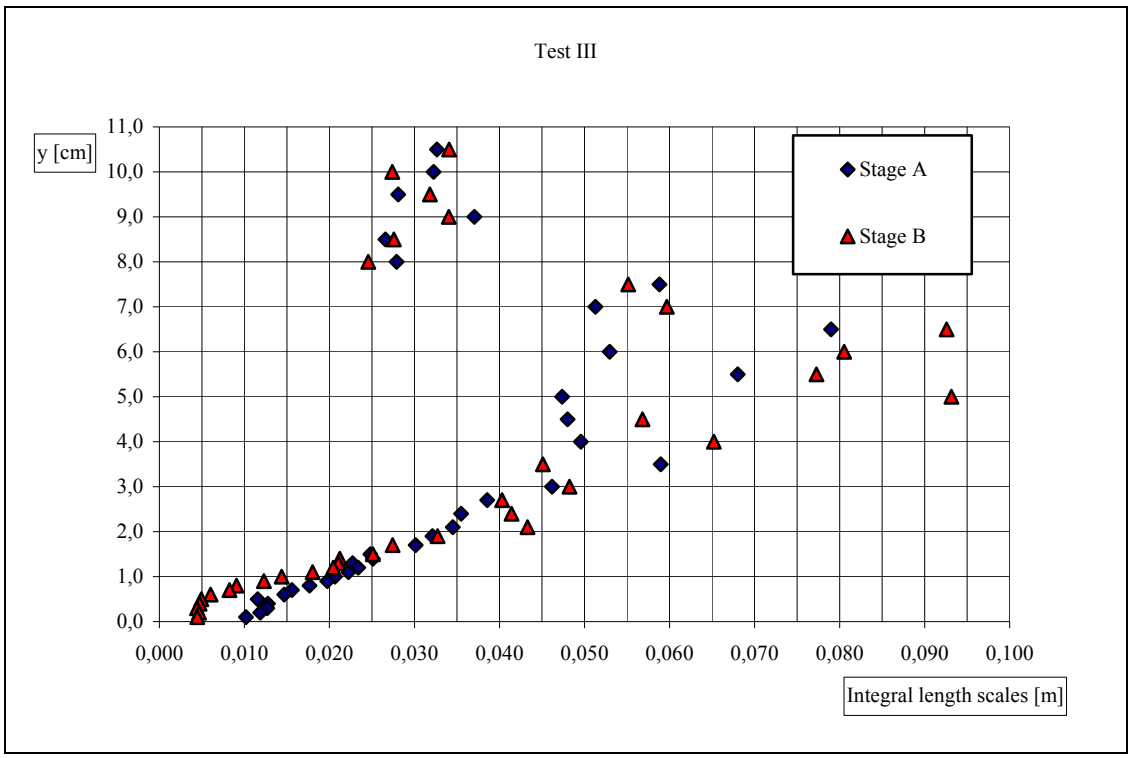

Fig. 17.33 - Integral length scales – Test III

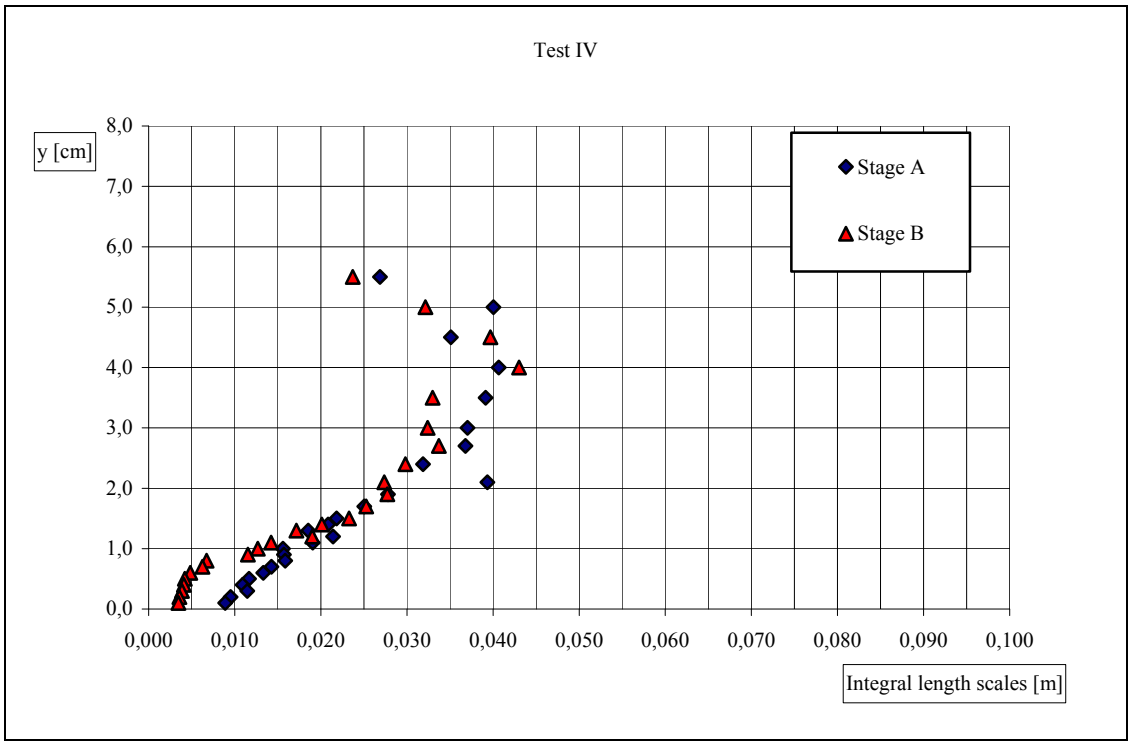

Fig. 17.34 - Integral length scales – Test IV

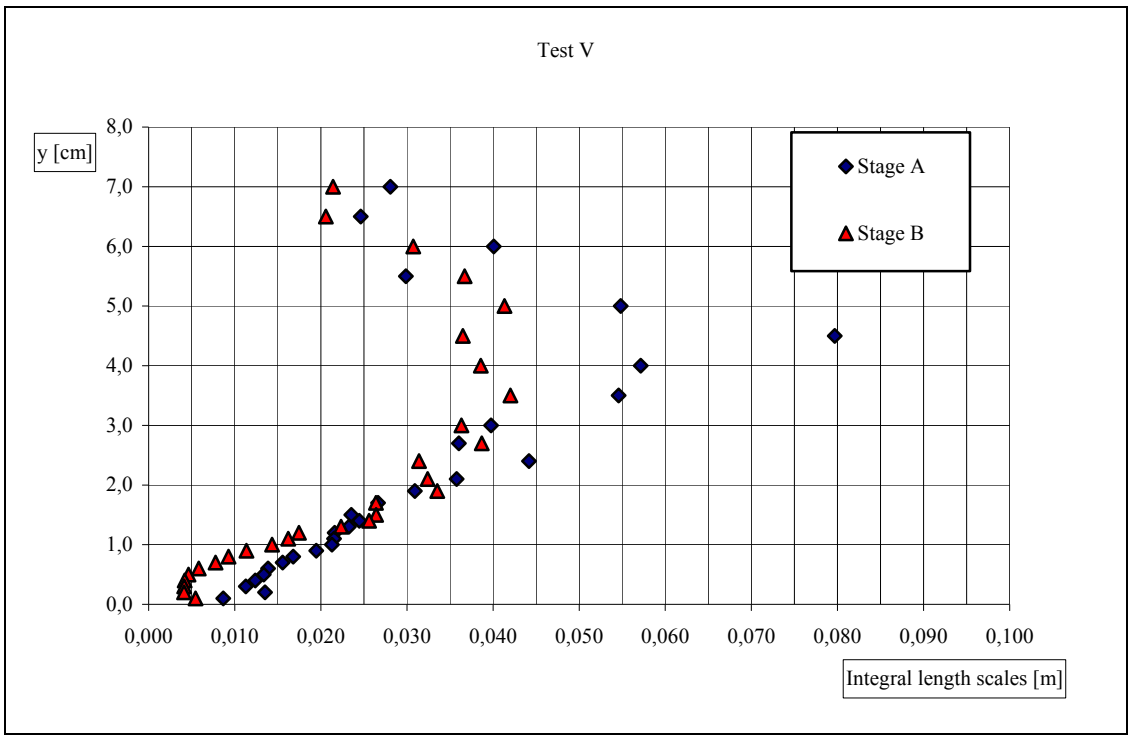

Fig. 17.35 - Integral length scales – Test V

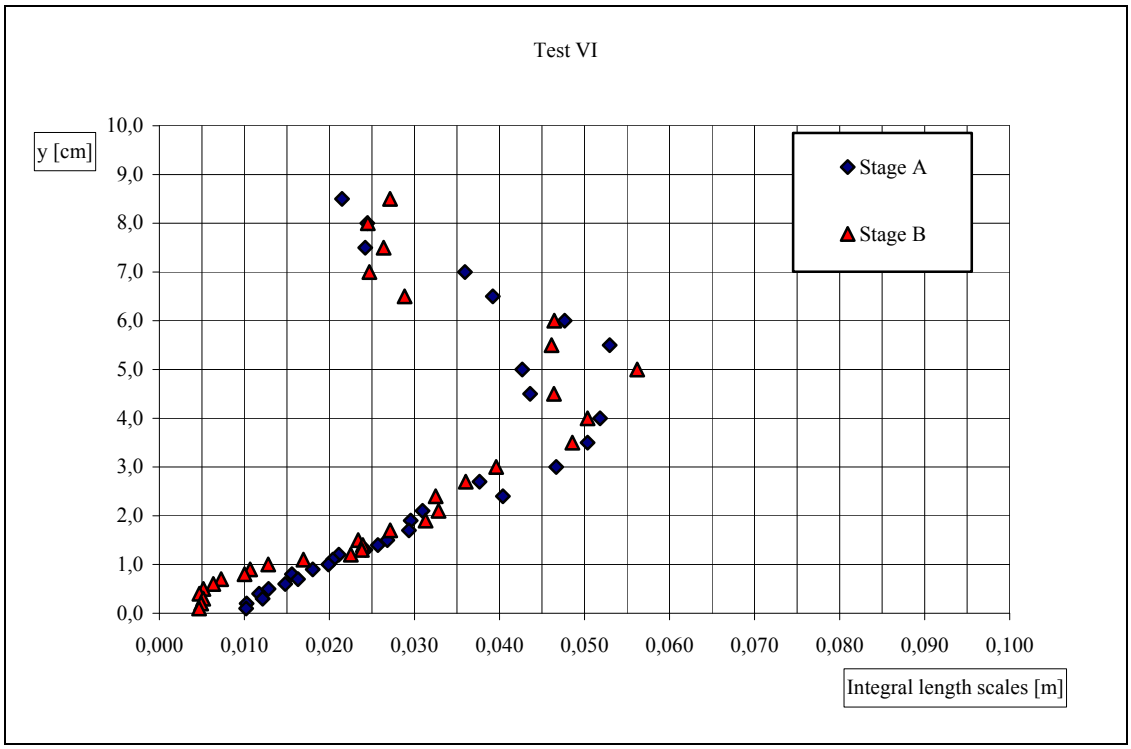

Fig. 17.36 - Integral length scales – Test VI

Generally speaking, the tests on uniform flow show better quality than those performed in the wake of the single cylinder, probably due to the greater uniformity of the same flow.

It is also noteworthy that some statistic characteristics, as local mean velocities, integral length scales and partially also the variances, are significantly sensitive to the location of the measurement vertical with regard to the cylinders location, whereas the other ones are almost not sensitive at all to this location. In this sense, it is possible to state that the first ones of the statistical characteristics appear more meaningful than the second ones in order to study this type of phenomenon.

18. CONCLUSIONS

The experimental research performed in this Doctoral thesis refers to a relatively new research field in international literature: i.e. the field of currents flowing over vegetated bottom.

This research has been mainly an experimental one.

Two different channels have been used, the first one already ready in the laboratory before the beginning of this thesis, and the second one wholly planned and build during this thesis.

The vegetation type was always of a submerged rigid shape, modelled through brass cylinders of different heights and/or densities.

The main measurements device was a Polythec LDA working in backscatter with frequency-shifter and frequency tracker system for processing the signals.

The main signal acquiring and elaborating device was a National Instruments DAQ and a LabView program developed during the thesis.

This research could deepen three different sides of the physical phenomenon (A, B, C).

A) The first side of the research is relative to a topic that appears to be new at all in international literature, in particular relative to the behaviour of water boundary layers flowing over a vegetated surface.

In order to limit the possible extension of the argument, either the possible boundary layers or vegetation types have been strictly selected. As for boundary layers, the type with zero piezometric head gradient has been chosen: this boundary layer type, in cases of smooth bottom, is characterized by so-called “equilibrium conditions”. As for vegetation, the rigid submerged vegetation has been taken into consideration. Six types of rigid submerged vegetation have been considered, always of sparse type.

A first result of the research has been that, in case of very sparse and very low vegetation, the boundary layer totally holds its equilibrium characteristics, typical as already said of boundary layers with zero piezometric head gradient flowing over a smooth bottom.

In cases of vegetation more dense and/or high, this characteristic behaviour holds only in the layers of the flow not directly obstructed by vegetation (partial equilibrium).

In any case the equilibrium conditions that occur depend on the type of vegetation (height and thickness of the cylinders), since the shape of the non dimensional local mean velocity distributions shows a clear and regular variability when such characteristic changes. Moreover it is possible to define a particular “Shape Factor” which sums up with a number the different

conditions of “partial” or “total” equilibrium of the boundary layer.

The second result was that it is possible to use a new data presentation methodology, which has been called “methodology of velocity excess in the open current”.

This methodology indeed allows to work always in a condition of total equilibrium, and above all to obtain a single condition of equilibrium independent of the height and the density of the vegetation model taken into consideration (the “Shape Factor” does not more change).

A third result regards the effects of a suitable shift of the measurement verticals around the cylinders on the hydrodynamic characteristics of the examined flow. This segment of the research has been carried out without using the methodology of velocity excess in the open current. The conclusions that can be drawn from the performed experimental measurements (and that obviously refer to the standard presentation methodology) are the following ones:

- shift of the measurement verticals around the cylinders does not give rise to meaningful changes of the boundary layer thickness values;
- the local mean velocity distributions made non dimensional with the boundary layer thickness and the external stream velocity, show a “total” or “partial” equilibrium characteristics with every kind of vegetation (that is cylinder height and density). The loss of “total” equilibrium in a section depends on the ratio between the thickness of the boundary layer in the section and the height of the cylinders: the limit values of this ratio depends on the density type of vegetation and are the same apart from the measurements verticals positions;
- apart from the measurements verticals position, the equilibrium (“total” or “partial”) characteristics depends on the type of vegetation (height and thickness of the cylinders);
- apart from the measurements verticals position, it is possible to define a particular “Shape Factor” which sums up with a number the different conditions of “partial” equilibrium of the boundary layer;
- unlike what happens in cases of the measurements carried out in the axis of the flow, the equilibrium loss concerns either the lower part or the higher one of the non dimensional profiles;
- finally the “Shape Factor” values and the non dimensional profiles shapes depend on the measurements verticals position around the cylinders.

B) The aim of the second side of the research was to present a simplified procedure of determining the resistance coefficients of water currents, and in particular of vegetated bottom currents. The proposed procedure allows the estimation of the f friction factor of a uniform

flow and consequently the ε absolute roughness of the its bed through experimental measurements carried out on a boundary layer stream. Consequently, instead of requiring a very long experimental channel, the whole procedure can be carried out within the boundary layer of the flow in a shorter experimental channel and the results can be extrapolated to the uniform flow.

The absolute roughness values obtained with the described procedure are reasonable either in case of smooth or vegetated bottom.

In a historic period in which vegetated bottoms will attain more and more importance in engineering practice, the possibility of obtaining such results through the use of simplified experimental facilities can play a positive role in the field of environmental hydraulics.

With regard to this topic, in the thesis is also stressed that the f friction factor values obtained doubling the density of the vegetated bottom do not double in comparison with the previous ones.

In those experiences the cylinders were arranged in rectangular or square meshes, with two of their four sides always aligned in the same direction of the flow (longitudinally). The distances between two subsequent cylinders were of 5cm in the so-called single density, and of 2.5cm in the so-called double density.

A specific part of the research has been developed in order to explain this behaviour. This part regarded the influence zone of each specific cylinder, and the results of the measurements performed with a single cylinder showed that this influence zone was so large to cover at least three subsequent cylinders with the minor (single) density and at least six cylinders with the redoubled density.

Consequently, when a cylinder is affected by the wake of a previous one, its own wake cannot develop in the same way than in absence of affection, and, as a consequence, the turbulent energy loss per unit volume of the two mixed wakes will not be the double with respect to the single wake. These considerations explain the not redoubling of the f friction factors.

C) The third side of the research regarded the more usual in international literature measurements on uniform flows.

In this case a very large experimental survey has been performed with one specific type of vegetated bottom, but letting flow over it six hydrodynamically different current types. In each different type two different measurements verticals were considered, differently positioned with respect to the cylinders.

For each measurement vertical about 30 measurement points were taken in consideration.

In each point the instantaneous velocities were considered, whose values were acquired at 2000Hz frequency for a time duration of 2 minutes and 15 seconds.

Starting from these very numerous experimental data, very deep statistics have been carried out.

In particular, for each experimental point were obtained:

i) local mean velocities;

ii) Variances, Skewness, and Kurtosis of the fluctuating velocities;

iii) the integral length scales of the turbulent flow.

In relation to some observation that had been made about the behaviour of the boundary layer current in relation to the position of measurements verticals, it is noteworthy that:

i) the shape of local mean velocities distributions changes with the position, as it happened also in boundary layer flow;

ii) the shape of the fluctuating velocities statistics (variance, skewness, kurtosis,) does not appear to change significantly with changing of position of the measurement vertical partially except the case of the variance (and this behaviour certainly requires a theoretical deepening);

iii) on the contrary, when the integral length scales (that also depend on turbulence characteristics) are observed, it is possible again to notice a clear different behaviour between the considered vertical locations (and this result makes yet more intriguing the result of point ii). In this sense, the local mean velocities and longitudinal length scales seem to be more meaningful than the moments in order to study this type of phenomenon.

But, in any case, beyond the previous observation, these statistics can constitute the basis for further deepening of the behaviour of channel flows over vegetated bottom.

REFERENCES

Ackermann J.D., and Okubo A., 1993, Reduced mixing in a marine macrophyte canopy, *Funct. Ecol*., **7**, pp.305-309

Balachandar, R. and Ramachandran S., 1999, Yurbulent Boundary Layers in Low Reynolds Number Shallow Open Channel Flows, *Journal of Fluids Engineering, Transactions of ASME*, **123** (2), pp.394-400 (jan)

Balachandar, R., Blakely, D., Tachie, M. and Putz, G., 2001, A Study on Turbulent Boundary Layers on a smooth Flat Plate in an Open Channel, *Journal of Fluids Engineering, Transactions of ASME*, **121**, pp.684-689 (sep)

Bandypadhyay, P.R., 1992, Reynolds Number Dependence of the Freestream Turbulence Effects on Turbulent Boundary layers, *AIAA Journal*, **30** (7), pp.1910-1912

Baptist M.J., V. Babovic, J. Rodriguez Uthurburu, M Keijzer, R.E. Uittenbogaard, A Mynett, and A. Vevey, 2006, On inducing equations for vegetation resistance, Journal of Hydraulic Research, accepted

Ben Meftah M., De Serio F., Malcangio D., Petrillo A. and Mossa M., 2006, Experimental study of flexible and rigid vegetation in an open channel, *Proceedings of River Flow 2006*, Lisbona, Portugal

Bettess, R., On the hydraulic roughness of vegetation in channels XXX *I.A.H.R., Congress Tessaloniki (Greece)* Theme C 25-30*, 2003*

Blair, M.F., 1983a, Influence of Free-Stream Turbulence on Turbulent Boundary Layer Heat Transfer and Mean Profile Development. Part I Experimental Data, *Transactions of the ASME Journal of Heat and Mass* Transfer, **105** (feb), pp. 33-40

Blair, M.F., 1983b, Influence of Free-Stream Turbulence on Turbulent Boundary Layer Heat Transfer and Mean Profile Development. Part II Analysis of results, *Transactions of the ASME Journal of Heat and Mass* Transfer, **105** (sep), pp. 41-47

Burke R.W., and Stolzenbach K.D., 1983, Free surface flow through salt marsh grass, *MIT-Sea Grant. Rep. MITSG 83-16*, Cambridge, Massachusetts, USA, 252

Carollo F.G., Termini D., and Ferro V., 2005, Flow resistance law in channels with flexible submerged vegetation, Journal of Hydraulic Engineering, 131(7), pp.554-564

Carollo F.G., Termini D., and Ferro V., 2005, Flow velocity measurements in vegetated channels, Journal of Hydraulic Engineering, 128(7), pp.664-673

Castro, I.P., 1984, Effects of Free Stream Turbulence on Low Reynolds Number Boundary Layers, *Transactions of ASME Journal of Fluid Engineering*, **106** (sep), pp.298-306

Charnay, G., Mathieu, J. and Comte-Bellot, G. 1976 Response of a turbulent boundary layer

to random fluctuations in an external stream, *The Physics of Fluids*, **19** (9) pp.1261-1272

Charney, G., Comte-Bellot, G. and Mathieu J., 1971, Development of a turbulent boundary layer on a flat plate in an external turbulent flow, *AGRD CCP*, 93-71, pp.27.1-27.10

Choi S. and Kang H., 2003, Reynolds stress modelling of vegetated open-channels flows, *Journal of Hydraulic Research*, **42**(1), pp.3-11

Chow Ven Te, 1959, Open-Channel Hydraulics, McGraw-Hill Classic Textbook Reissue Series

Clauser, F. H., 1956, The turbulent boundary layer, *Advances in Applied Mech*, **4**, pp.1-51

Coles, D., 1956, The law of the wake in the turbulent boundary layer, *Journal of Fluids Mechanics*, **1, pp.191**-226

Cui J. and Neary V.S., 2002, Large eddy simulation (LES) of fully developed flow through vegetation, *Proceedings of the 5th International Conference on Hydroinformatics*, Cardiff, UK

Cui J., 2000, Large-eddy simulation of turbulent flow over rough surfaces, PhD dissertation Mechanical Engineering, University of Iowa, Iowa City, Iowa, USA

De Felice, S. and Gualtieri, P., 2005, Interactions between turbulent Boundary Layer and rigid vegetated beds: Comparison among hydrodynamic characteristics in different points around the cylinders, *I.A.H.R. Congress, Seoul (Corea), 11*/16 september, pp.2434-2445

De Felice, S., Gualtieri, P. and Pulci Doria, G., 2004, Study of the interactions between turbulent boundary layer and vegetated beds through an LDA system, *A.I.VE.LA. National Conference*, Naples, Italy, www.aivela.org.

De Felice, S., Gualtieri, P., Pulci Doria, G, 2008, A simplified experimental method to evaluate equivalent roughness of vegetated river beds *International Congress on Environmental Modelling and Software 4th Biennial Meeting of iEMSs*, Barcellona (Spain), july 2008 – published on CD-ROM – 11 pages

De Felice, S., Gualtieri, P., Pulci Doria, G, 2009, Influence field of a single rigid submerged stick in a liquid current and its relations with a sticks array, *International Symposium on EchoHydraulics*, Concepcion (Chile), january 2009, in press

De Felice, S., Gualtieri, P., Pulci Doria, G, 2009, Experimental comparison through LDA between currents with submerged vegetation, *International Symposium on EchoHydraulics*, Concepcion (Chile), january 2009, in press

Dean, R.B., 1976, A single formula for the complete velocity profile in a turbulent boundary layer, *ASME Journal. of Fluid Engineering*, **98**, pp.723-727

Defina A. and Bixio A.C., 2005, Mean Flow and turbulence in vegetated open channel flow, *Water Resources Research*, **41**(7)

Evans, R.L. and Horlock, J.K. 1974 Calculation of the Development of Turbulent Boundary Layers With a Turbulent Freestream, *Transactions of the ASME Journal of Fluid Engineering*, 1974 (dec), pp.348-352

Evans, R.L., 1985, Freestream Turbulence Effects on Turbulent Boundary Layers in an Adverse Pressure Gradient, *AIAA Journal*, **23** (11), pp.1814-1816

Fenzl R. N., 1962, Hydraulic resistance of broad shallow vegetated channels, PhD Thesis, University of California at Davis, Davis, California, USA

Finnigan j., 2000, Turbulence in plant canopies, *Annual Review of Fluids Mechanics*, **32**(1), pp.519-571

Fischer-Antze T., T. Stoasser, P. Bates & N.R.B. Olson, 2001, 3D numerical modeling of open-channel flow with submerged vegetation, *Journal of Hydraulic Research* **39**(3) pp.303-310

Freeman G.E., R.E. Copeland, W. Rahmeyer, D.L. Derrick, 1998, Field determination of Manning's n value for shubs and woody vegetation, *Engineering Approaches to Ecosystem Restoration, Proc. Wetlands Engrg. And River restoration, Conf. ASCE*, New York, USA

Gad-el-Hak, M. and Bandyopadhyay, P.R., 1994, Reynolds number effects in wall-bounded flows, *Applied Mechanics Review* **47**(8) pp.307-365

George, W.K. and Casillo, L., 1997, Zero pressure-gradient turbulent boundary layer, *Applied Mechanics Review* **50**(11), pp.689-729

Ghisalberti M. and Nepf H., 2006, The structure of shear layer flow over rigid and flexible canopy, *Environmental Fluid Mechanics*, **6**, pp.277-301

Gioia G., and F.A. Bombardelli, 2002, Scaling and similarity in rough channel flows, *Physical Review Letters*, **88**(1), pp.14501-14504

Granville, P.S., 1976, A modified law of the wake for turbulent shear layers, *ASME Journal of Fluid Engineering*, **98**, pp.578-580

Greco, M. and Pulci Doria, G., 1983, Strato limite in una corrente originariamente turbolenta (Boundary Layer in a current with turbulent free-stream), *Simposio su l'Anemometria Laser-Doppler nella sperimentazione idraulica*, Roma, pp. 156-175

Green J.C., 2005, Modelling flow resistance in vegetated streams: review and development of a new theory, *Hydrological Processes*, **19**, pp. 1245-1259

Gualtieri, P. and Pulci Doria, G. 1998, A proposal of a physically based thickness definition and of a new mean velocities distribution law in a turbulent boundary-layer on the ground of LDA measurements, *13th Australasian Fluid Mechanics Conference,* Melbourne, pp. 845/848

Gualtieri, P. and Pulci Doria, G. 1999, Boundary Layer Intermittency Model, *Int. IUTAM Symp. on Geometry and Statistics of Turbulence Hayama Japan*, pp.379/384

Gualtieri, P. and Pulci Doria, G., 1997, Non dimensional distribution of longitudinal integral length scales in a turbulent boundary layer *FLUCOME '97 Congress Hayama Japan*, pp.161/166

Gualtieri, P. and Pulci Doria, G., 1998a, Skewness, Kurtosis and Length Scales experimental distributions laws based on a three bands model in a turbulent boundary layer, *Excerpta of Italian contributions to the field of hydraulic engineering*, **12** pp.155/194

Gualtieri, P. and Pulci Doria, G., 1998b, A proposal of a physically based thickness definition and of a new mean velocities distribution law in a turbulent boundary-layer on the ground of LDA measurements, *13th Australasian Fluid Mechanics Conference, Melbourne*, pp.845/848

Gualtieri, P. and Pulci Doria, G., 2001 A Correct Model of Variance, Skewness, Kurtosis in Boundary Layer with Turbulent External Layer, *14th Australasian Fluid Mechanics Conference Melbourne*, pp.259/262

Gualtieri, P. and Pulci Doria, G., 2003, A correct model of longitudinal integral length scales in boundary layer with turbulent external layer, *2nd International Conference on Heat Transfer, Fluid Mechanics, and Thermodynamics H.E.F.A.T., Victoria Falls Zambia*, produced on CD-ROM

Gualtieri, P., Pulci Doria, G. and Taglialatela, L., 2004a, Experimental validation of turbulent boundary layers in channels *3rd International Conference on Heat Transfer, Fluid Mechanics, and Thermodynamics H.E.F.A.T.,* Cape Town South Africa, June, produced on CD-ROM.

Gualtieri, P., Pulci Doria, G. and Tagliatatela, L., 2004b, Effect of vegetation on boundary layer with turbulent external stream, *2nd International Conference on Fluvial Hydraulics RiverFlow*, Naples, Italy, pp.381-388.

Gualtieri, P., Pulci Doria, G. and Tagliatatela, L., 2004c, Density vegetation influence on boundary layer, *15th Australasian Fluid Mechanics Conference on Fluvial Hydraulics AFMC*, Sydney, Australia, pp.195-198.

Gualtieri, P., Pulci Doria, G., De Felice, S. and Catapano, 2006 Studio tramite LDA degli effetti di un fondo fittamente vegetato su di uno strato limite turbolento (Study through LDA of the effects on a turbulent Boundary Layer of a densely vegetated bottom) *XXX Convegno di Idraulica e Costruzioni Idrauliche IDRA 2006*, 11/15 sept., Roma, Published on CD-ROM pp.1-14

Gualtieri, P., Catapano R., Pulci Doria, 2007, Experimental observations through LDA of a

current with almost rigid submerged vegetation *XXXII IAHR Congress "Harmonizing the Demands of Art and Nature in Hydraulics"* Venezia (Italy) – 1/6 july 2007 – Vol I Abstracts p.165 Proceedings on CD-ROM by CORILA Venezia Curatori: G. Di Silvio, S. Lanzoni

Gualtieri, P., Catapano R., Pulci Doria, 2008, Boundary layer development over a bottom covered with rigid submerged vegetation, within the Volume *Fluid Mechanics of Environmental Interfaces*, Editors C.Gualtieri and D.T.Mihailovic, Published by Taylor&Francis, Leiden, The Netherlands, pp. 241/298

Hancock, P.E. and Bradshaw, P., 1983, Influence of Free-Stream Turbulence on Turbulent Boundary Layers, *Transactions of the ASME Journal of Fluids Engineering*, **105** (sep), pp.284-289

Hancock, P.E. and Bradshaw, P., 1989, Turbulent structure of a boundary layer beneath a turbulent free stream, *Journal of Fluid Mechanics*, **205** pp.45-76

Hoffmann, J.A. and Mohammady, K., 1991, Velocity Profiles for Turbulent Boundary Layers Under Freestream Turbulence, *Transactions of the ASME Journal of Fluid Engineering*, **113** (sep), pp.399-404

Huffman, G. D., Zimmerman, D. R. and Bennett, W. A., 1972, The effect of Free-stream turbulence leel on turbulent boundary layer behaviour, *AGARDograph 164 Paper I-5,* pp.91-115

Huthoff F., Augustijn D.C.M. and Hulscher S.J.M.H., 2006, Depth-averaged flow in presence of submerged cylindrical elements, *Proceedings of River Flow 2006*, Lisbona, Portugal

Keijzer M., Baptist M., Babovic V. and Uthurburu J.R., 2005, Determining equation for vegetation induced resistance using genetic programming, *Proceedings of GECCO'05*, Washington, DC, USA

Kline, S. J., Lisin, A.V. and Waitman, B.A., 1960 Preliminary experimental investigation of effect of free-stream turbulence on turbulent boundary-layer growth, *N.A.C.A. TN D-368*, pp. 1-60

Klopstra D., Barneveld H.J., Van Noortwijk J.M. and Van Velzen E.H., 1997, Analytical model for hydraulic roughness of submerged vegetation, *Proceedings of the 27th IAHR Congress*, San Francisco, USA, pp.775-780

Kouwen, N., Unny, T.E. & Hill, H.M., Flow retardance in vegetated channels *Journal Hydraulic Division ASCE* 95(2), 329-342*,* 1969

Kouwen, N. & Unny, T.E., Flexible roughness in open channels *Journal Hydraulic Division ASCE* 99(5), 684-698, 1973

Kouwen, N. & Unny, T.E., Flow resistance in vegetated waterways *Trans. ASEE* 24(3) 684-

698, 1981

Kutija V. and Hong H.T.M., 1996, A numerical model for assessing the additional resistance to flow introduced by flexible vegetation, *Journal of Hydraulic Research*, **34**(5), pp.99-114

Lopez F. and Garcia M., 1997, Open-Channel Flow Through Simulated Vegetation: Turbulence Modeling and Sediment Transport, *US Army of Engineers Waterway Experiment Station Wetlands Research Program Technical Report WRP-CP-10*

Lopez F. and Garcia M., 1998, Open channel flow through simulated vegetation: Suspended sediment transport modeling, *Water Resources Research*, **34**(9), pp.2341-2352

Lopez F. and Garcia M., 2001a, Mean Flow and Turbulence Structure of Open-Channel Flow Through Non-Emergent Vegetation, *Journal of Hydraulic Engineering*, **127**(5), pp.392-402

Marchi, E., Il moto uniforme delle correnti liquide nei condotti chiusi ed aperti, *L'Energia Elettrica,* **23** (4)(5), 1961

Mc Donald, H. and Kreskowsky, J.P., 1974, Effects of free stream turbulence on the turbulent boundary layer, *International Journal of Heat and Mass* Transfer, **17** pp.705-716

Meier H.U. and Kreplin, H.P., 1980, Influence of Freestream Turbulence on Boundary-Layer Development, *AIAA Journal*, **18** (1), pp.11-15

Mejier D.G. and Van Velzen E.H., 1998, Prototype-scale flume experiments on hydraulic roughness of submerged vegetation, *Proceedings of the 28th IAHR Congress*, Graz, Austria

Mellor G.L., and Herring H.J., 1973, A survey of mean turbulent filed closure, *AIAA J.*, **11**, pp.590-599

Neary V.S., 1995, Numerical modelling of diversion flows, PhD dissertation, Civil and Environmental Engineering, University of Iowa, Iowa City, Iowa, USA

Neary V.S., 2000, Numerical model for open-channel flow with vegetative resistance, *IAHR's 4th International Conference on Hydroinformatics*, july 23-27, Cedar Rapids, Iowa, USA

Neary V.S., 2003, Numerical solution of fully developed flow with vegetative resistance, *Journal of Engineering Mechanics*, **129**(5), pp.558-563

Nepf H.M., and E.R. Vivoni, 1999, Drag, turbulence and diffusion in flow through emergent vegetation, *Journal of Geophysical Research*, 105(2), pp.479-489

Nezu I., and Nakagawa H., 1993, Turbulence in open-channel flows, Monograph, Balkema, Rotterdam, The Netherlands

Nezu I., Sanijou M. and Okamoto T., 2006¸ Turbulent structure and dispersive properties in vegetated canopy, *Proceedings of River Flow 2006*, Lisbona, Portugal

Nezu, I. and K. Onitsura, Turbulent structures in partly vegetated open-channels flows with LDA and PIV measurements *Journal of Hydraulic Research* 2001 no 6 vol.39 629-642, 2002

Patel V.C., and Yoon J.Y., 1995, Application of turbulence models to separated flows over rough surfaces, *Journal of Fluids Engineering* 117(2), pp. 234-241

Poggi D., Porporato A. and Ridolfi L., Albertson J.D., Katul G.G. 2004, The effect of vegetation on canopy sub-layer turbulence, *Boundary-Layer Meteorology*, **111**, pp.565-587

Prandtl, L., 1904, Űber Flüssigkeitsbewegungen bei sehr kleiner Reibung (On Fluid Motions with Very Small Friction), *Verhandlungen des III Internaztionalen Mathematiker Kongresses (Heidelberg 1904)*, Leipzig 1905

Pulci Doria, G. and Tagliatatela, L., 1990, Ipotesi di distribuzioni adimensionali di velocità media e di agitazione in correnti turbolente (An hypothesis about non dimensional distributions of local mean velocity and turbulent velocity fluctuations in turbulent streams) *Giornate di Studio per la celebrazione della nascita di Girolamo Ippolito*, Lacco Ameno, Italy, pp.223-245

Pulci Doria, G., 1991, Statistical quantities distributions and the use of the entropy concept *International Conference on Entropy and Energy Dissipation on Water Resources*, Maratea, Italy, pp.541-586

Raupach M.R. and Shaw R.H., 1982, Averaging procedures for flow within vegetation canopies, *Boundary Layer Meteorology*, **22**, pp.79-90

Raupach M.R., and Thom A.S., 1981, Turbulence in and above plant canopies, *Annual Review of Fluids Mechanics*, **13**, pp.97-129

Righetti m:, and Armanini A., 2002, Flow resistance in open channel with sparsely distributed bushes, *Journal of Hydrology*, **269**, pp.375-395

Robertson, J.M. and Holt, C., 1972, Stream turbulence effects on turbulent boundary layer, *Journal of Hydraulic Division Proceedings of the American Society of Civil Engineers*, **98** (HY6), pp.1095-1099

Rodi W., 1980, Turbulence models and their application: state of art paper, Monograph, IAHR, Delft, The Netherlands

Russo Spena, A., 1954, Contributo allo studio delle correnti di strato limite (A contribution to boundary layer streams research), *Printed by Stabilimento Tipografico Bavarese for the Istituto di Idraulica e Costruzioni Idrauliche,* Napoli, june, pp.3-35

Russo Spena, A., 1957, Correnti di strato limite lungo lastre scabre (Boundary Layer streams over a rough bottom), *L'Energia Elettrica*, **XXXIV** (1) pp.1-23

Schlichting, H. and Gersten, K., 2003, *Boundary Layer Theory (transl. by Mayes K.)*, 8th revised and Enlarged Edition 2000, Corrected Printing 2003, Springer-Verlag, Berlin-Heidelberg.

Schlichting, H., 1955, *Boundary Layer Theory (transl. by Kestin J.)*, Pergamon Press LTD, London

Shi Z., J. Pethick, and K. Pye, 1995, Flow structure in and above the various heights of a saltmarsh canopy: a laboratory flume study, *Journal of Coastal Research*, **11**, pp.1204-1209

Shimizu Y. and Tsujimoto T., 1994, Numerical analysis of turbulent open-channel flow over a vegetation layer using a k-ε model, *Journal of Hydroscience and Hydraulic Engineering,* **11**(2), pp.57-67

Smart G.M., M.J. Duncan, and J.M. Walsh, 2002, Relatively rough flow resistance equations, *Journal of Hydraulic Engineering*, **128**(6), pp.568-578

Speziale C.G., Sarkar S., and Gatski T., 1991, Modeling the pressure strain correlation of turbulence: an invariant dynamical systems approach, *Journal of Fluids Mechanics*, **227**, pp.245-272

Sreenivasan, K.R., 1989, Turbulent boundary layer, in "*Frontiers in Experimental Fluid Mechanics*", M. Gad-el-Hak (ed), pp.159-209

Stone B.M. and Tao Shen H., 2002, Hydraulic Resistance of Flow in Channels with Cylindrical Roughness, *Journal of Hydraulic Engineering*, **128**(5), pp.500-506

Tachie, M.F., Balachandar, R. and Bergstrom, D.J., 2003, Low Reynolds number effects in open-channel turbulent boundary layers, *Experiments in Fluids*, **35**, pp. 338-346, (jan)

Tachie, M.F., Balachandar, R., Bergstrom, D.J. and Ramachandran S., 2001, Skin Friction Correlation in Open Channel Boundar Layers, *Journal of Fluids Engineering, Transactions of ASME*, **123**, pp. 953-956, (dec)

Tachie, M.F., Bergstrom, D.J. and Balachandar, R., 2000, Rough Wall Turbulent Boundary Layers in Shallow Open Channel Flow, *Journal of Fluids Engineering, Transactions of ASME*, **122**, pp.533-541 (sept.)

Timoschenko S., 1955, Strenght of materials; Part I: Elementary theory and Problems, D. Van. Nostrand Company, Inc. pp. 137-165

Tsuijimoto, T., Shimizu, Y., Kitamura, T. and Okada, T., 1992, Turbulent open-channel flow over bed covered by rigid vegetation, *Journal of Hydroscience and Hydraulic Engineering*, **10**(2), pp.13-25

Tsujimoto T., and Kitamura T., 1990, Velocity profile of flow in vegetated-bed channels, *KHL Progressive Report, Hydraulic Laboratory, Kanazawa University*

Tsujimoto T., and T. Kitamura, 1998, A model for flow over flexible vegetation-covered bed, *Proc. Int. Water Resourches Engrg. Conf ASCE*, New York, USA, pp. 1380-1385

Tsujimoto T., Shimizu Y., Kitamura T. and Okada T., 1992, Turbulent open-channel flow over bed covered by rigid vegetation, *Journal of Hydroscience and Hydraulic Engineering,* **10**(2), pp.13-25

Uittenbogaard R., 2003, Modelling turbulence in vegetation aquatic flows, *Proceedings of Riparian Forest Vegetate Channels Workshop*, Trento, Italy

Wilson N.R. and Shaw R.H., 1977, A higher closure model for canopy, *Journal of Applied Meteorology,* **16**, pp.1197-1205

Yen B.C., 2002, Open channel flow resistance, *Journal of Hydraulic Engineering*, **128**(1), pp. 20-39